Materials characterization by synchrotron x-ray microprobes and nanoprobes

Lorenzo Mino

Department of Physics and Interdepartmental Centre NIS, University of Turin, via Giuria 1, 10125 Torino, Italy

Elisa Borfecchia

Department of Chemistry, Interdepartmental Centre for Crystallography CrisDi, and INSTM Reference Center, University of Turin, via Giuria 7, 10125 Torino, Italy and Haldor Topsøe A/S, Haldor Topsøes Allé 1, 2800 Kgs. Lyngby, Denmark

Jaime Segura-Ruiz

European Synchrotron Radiation Facility (ESRF), 71 Avenue des Martyrs, BP 220, 38043 Grenoble Cedex 9, France and Institut Laue-Langevin (ILL), 71 avenue des Martyrs, 38000 Grenoble, France

Cinzia Giannini

Institute of Crystallography, National Research Council (IC-CNR), via Amendola 122/O, 70126 Bari, Italy

Gema Martinez-Criado*

European Synchrotron Radiation Facility (ESRF), 71 Avenue des Martyrs, BP 220, 38043 Grenoble Cedex 9, France and Instituto de Ciencia de Materiales de Madrid (ICMM), Consejo Superior de Investigaciones Científicas (CSIC), Sor Juana Inés de la Cruz 3, 28049 Madrid, Spain

Carlo Lamberti†

Department of Physics and Interdepartmental Centre NIS, University of Turin, via Giuria 1, 10125 Torino, Italy, Department of Chemistry, Interdepartmental Centre for Crystallography CrisDi, and INSTM Reference Center, University of Turin, via Giuria 7, 10125 Torino, Italy, and The Smart Materials Research Center, Southern Federal University, Sladkova Street 174/28, 344090 Rostov-on-Don, Russia

(published 28 June 2018)

In recent years synchrotron x-ray microprobes and nanoprobes have emerged as key characterization tools with a remarkable impact for different scientific fields including solid-state, applied, high-pressure, and nuclear physics, chemistry, catalysis, biology, and cultural heritage. This review provides a comparison of the different probes available for the space-resolved characterization of materials (i.e., photons, electrons, ions, neutrons) with particular emphasis on x rays. Subsequently, an overview of the optics employed to focus x rays and the most relevant characterization techniques using x rays (i.e., x-ray diffraction, wide-angle x-ray scattering, small-angle x-ray scattering, x-ray absorption spectroscopy, x-ray fluorescence, x-ray-excited optical luminescence, and photoelectron spectroscopy) is reported. Strategies suitable to minimize possible radiation damage induced by brilliant focused x-ray beams are briefly discussed. The general concepts are then exemplified by a selection of significant applications of x-ray microbeams and nanobeams to materials science. Finally, the future perspectives for the development of nanoprobe science at synchrotron sources and free-electron lasers are discussed.

DOI: 10.1103/RevModPhys.90.025007

*gema.martinez.criado@csic.es
†carlo.lamberti@unito.it

 © 2018 American Physical Society

CONTENTS

I. Introduction 2
A. Importance of x-ray microprobes and nanoprobes 2
B. General comparison among different probes 5
1. Laser probes 5
2. Electron probes 6
3. Ion probes 7
4. Neutron probes 9
C. X-ray probes 9
1. The key role of synchrotron sources 9
2. The upcoming area of x-ray free-electron lasers 11
II. Focusing X-ray Optics 12
A. X-ray optics: General concepts 13
1. Basic resolution limits 13
a. Diffraction limit 13
b. Geometrical source demagnification 13
c. Imperfection effects on resolution 14
d. Efficiency and depth of field 14
2. Factors influencing the beam line design 14
B. Refractive optics 15
C. Reflective optics 15
D. Diffractive optics 15
E. Comparative summary and outlook 15
III. Space-resolved X-ray Analytical Techniques 16
A. Principal x-ray-matter interactions and related characterization methods 16
B. X-ray scattering: XRD, SAXS, and WAXS 18
C. X-ray absorption spectroscopy: XANES and EXAFS 20
D. X-ray fluorescence and other decay spectroscopies 20
E. Photoelectron spectroscopy 22
F. Multiple-particle coincidence techniques 24
G. Transmission full-field and scanning approaches 24
1. Full-field mode 24
2. Scanning x-ray microscope 25
3. Comparison between full-field and scanning modalities 25
H. The power of a multitechnique approach 25
I. Radiation damage effects: Physical basis, warnings, and strategies 26
IV. Selected Applications in Materials Science 30
A. Semiconductors 30
1. Group IV semiconductors 30
2. III-V semiconductors 31
3. II-VI semiconductors 34
4. Oxide semiconductors 35
5. Other (nonoxide) magnetic semiconductors 37
B. Metals 40
1. Chemical imaging of a single catalyst metal nanoparticle 40
2. Catalytic beds 42
C. Superconductors 43
1. Structural investigations of high-temperature superconductors 44
2. Direct-write x-ray nanopatterning of cuprate superconductors 44
D. Devices 46
1. MQWs for optoelectronic applications 46
2. Switching mechanism in memristive devices 48
3. Impurities in Si for solar cells 49
4. Quantum dots in field effect transistors 50
V. Conclusions and Perspectives 51
List of Symbols and Abbreviations 52
Acknowledgments 53
References 53

I. INTRODUCTION

A. Importance of x-ray microprobes and nanoprobes

Space-resolved characterization is a long-standing issue, being primarily related to the microscopy field. Its early origins are often dated back to the "Book of Optics" by the Arab polymath Alhazen (Ibn al-Haytham, 965–1040) (Ibn al-Haytham, 1989), first reporting on light reflection and refraction phenomena and on the possibility of employing visible light to magnify small objects (Sabra, 2007). The contemporary electron (Zewail and Thomas, 2010), scanning-probe (Kalinin and Gruverman, 2011), and x-ray microscopes (Sakdinawat and Attwood, 2010; Ice, Budai, and Pang, 2011), enabling real space imaging and characterization with state-of-the-art resolutions in the 10^{-9}–10^{-10} m length scale, are therefore the end of a one-millennium-long line in scientific and instrumental progress.

Different kinds of "probes" can be selected to obtain space-resolved structural or compositional information, including photons of different energies, electrons, neutrons, and ions. The advantages and drawbacks of each probe are briefly discussed in Sec. I.B. However, this review is focused on x-ray microbeams and nanobeams, which in recent decades have emerged as powerful and versatile characterization tools with high-impact applications in a wide range of scientific areas. This impressive development can be primarily ascribed to the interplay of three key factors, shown in schematic form in Fig. 1, reciprocally interacting in a positive-feedback loop: the impressive progress in x-ray-focusing optics and synchrotron brilliance, the rich interaction of x rays with matter, and the increasing demand for space-resolved probes.

The basic motivation is that a large number of materials, both natural and synthetic, exhibits heterogeneities on the micrometric and submicrometric scales. These features substantially influence chemical-physical properties of materials and their response and performance in the case of technological application: to fully characterize such samples a space-resolved approach is required, generally using a probe that is comparable (or smaller) to the size of the heterogeneities.

During the last two decades, remarkable results have been achieved in terms of both available brilliant x-ray sources (e.g., low emittance and diffraction-limited storage rings) and x-ray-focusing optics (see Sec. II). The increasingly demanding request for more and more advanced analytical tools, coming from several research areas, represents a driving force in the technical development of x-ray source performance and x-ray optics technology. Recent advances in these two key sectors are opening new possibilities for x-ray microbeam and nanobeam characterization.

The use of x rays appears to be particularly appealing owing to the richness of radiation-matter interaction (absorption, diffraction or scattering, fluorescence, imaging, etc.) and its peculiarities allow for unique characterization methods (see Sec. III). X-ray fluorescence (XRF) (Hubbell *et al.*, 1994; Fahrni, 2007; Wobrauschek, 2007; Pushie *et al.*, 2014; West *et al.*, 2014, 2015) for instance provides qualitative and

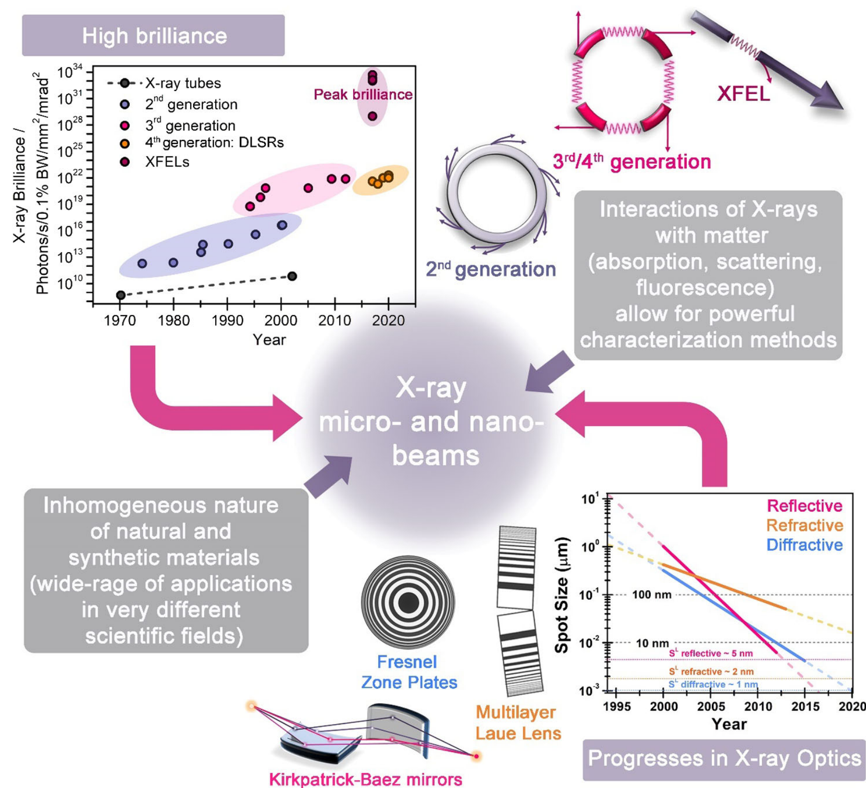

FIG. 1. Schematic representation of the key factors leading to x-ray microbeam and nanobeam science development: (i) the increasing demand for space-resolved probes to characterize heterogeneous samples down to the nanoscale, coming from very different research fields; (ii) the high brilliance currently achievable exploiting third- and fourth-generation synchrotron sources; (iii) the impressive progresses in x-ray-focusing optics; and (iv) the rich interaction of x rays with matter, providing unique characterization tools. The top left panel reports the time evolution for x-ray brilliance, distinguishing between x-ray tubes, different generations of synchrotron sources [dedicated second-generation sources after the early parasitic use, third-generation sources using insertion devices, fourth generation diffraction-limited storage rings (DLSRs)], and linear XFEL sources. For DLSRs, both current and foreseen values are reported (Weckert, 2015). For XFELs, peak-brilliance values are indicated as also reported in Table III to which the reader is referred for information about pulse duration and repetition rate.

quantitative information on elemental composition distribution, while using x-ray absorption spectroscopy (XAS) the local chemistry can be fully explored in terms of oxidation states, coordination numbers, local symmetries, and interatomic distances (van Bokhoven and Lamberti, 2016). X-ray diffraction (XRD) and scattering techniques have been employed almost since x-ray discovery as a direct structural probe, primarily in crystalline materials but also to investigate the different structural levels in disordered systems [e.g., wide-angle x-ray scattering (WAXS) or small-angle x-ray scattering (SAXS)]. In addition, new coherent diffraction methods such as 3D ptychography are recently emerging based on nanofocused illumination to provide quantitative mapping of the electron density distribution (Thibault, Guizar-Sicairos, and Menzel, 2015) (Kuppili *et al.*, 2017; Sala *et al.*, 2017, 2018; Pfeiffer, 2018).

X-ray microbeams and nanobeams are nowadays used in a wide range of multidisciplinary applications as shown in Fig. 2. Indeed, the ability of hard x rays to penetrate from micrometers to millimeters into most materials (e.g., in silicon the absorption length is 17.5 μm at 5 keV and 9.79 mm at 50 keV), simultaneously determining local composition, chemistry, and short-range or long-range structural order can be employed to characterize buried sample volumes and small samples in their natural or extreme environments, providing unprecedented insights in a multitude of scientific fields. The principal application fields include materials science, biology and protein crystallography, chemistry, solid-state physics, earth and planetary science, nuclear science, environmental science, archeology, paleontology, and cultural heritage conservation. Although this review is focused on materials science applications, which will be discussed in detail in Sec. IV, in the following we provide a brief overview of the most promising research branches with some groundbreaking results for the scientific fields previously listed.

Micro-XRF and micro-x-ray absorption near-edge structure (XANES) spectroscopies are currently established as versatile and powerful analytical tools for elemental and chemical mapping in biological systems at the cellular and intracellular levels. These methods have been employed to understand how cells uptake and segregate heavy metal impurities under normal and toxic conditions (Matsuyama *et al.*, 2009). Several studies were also performed to explore the role of transition metals in neurodegenerative disorders, such as Alzheimer's and Parkinson's diseases (Collingwood *et al.*, 2005; Chwiej *et al.*, 2008). Regarding x-ray microscopy and imaging methods, soft x-ray microscopy offers several advantages with respect to other approaches (e.g., electron microscopy) when applied

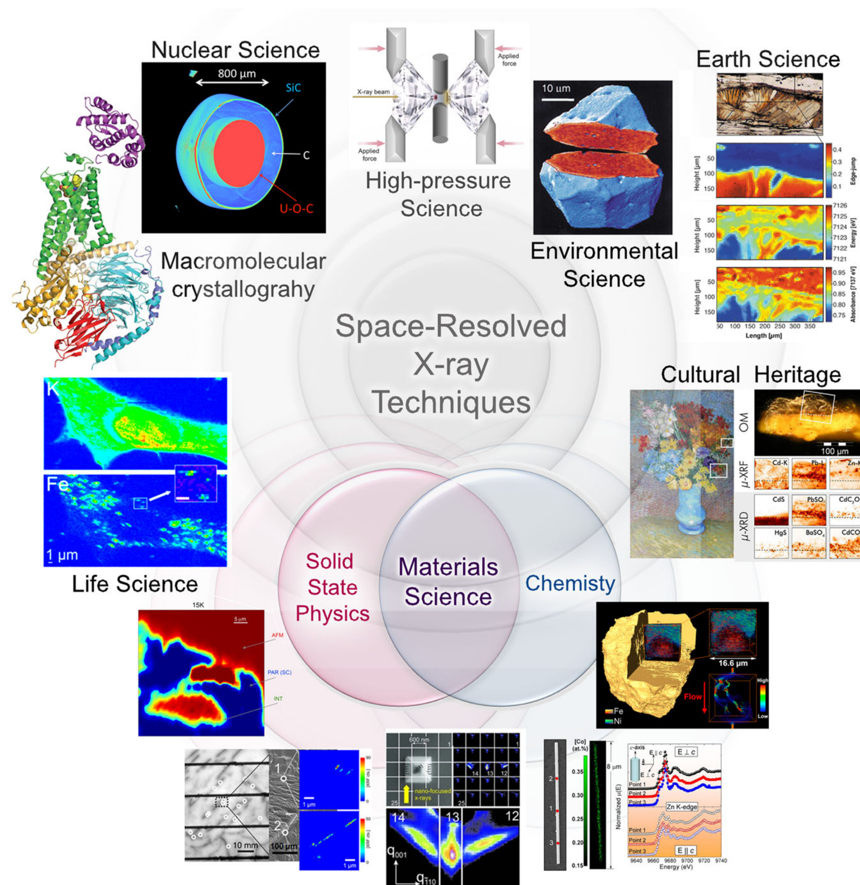

FIG. 2. Overview of the wide range of multidisciplinary applications which exploit x-ray microbeams and nanobeams. The reported illustrations representative of each application field are adapted with permission from the following sources, starting from top left, in clockwise order: nuclear science. From Ice and Specht, 2012. High-pressure science: previously unpublished. Environmental science. From Salbu *et al.*, 2001. Earth science. From Pascarelli *et al.*, 2006. Cultural heritage. From Van der Snickt *et al.*, 2012. Chemistry. From Meirer, Morris *et al.*, 2015. Materials science. From Segura-Ruiz *et al.*, 2011, Hanke *et al.*, 2008, and Kwapil, Gundel *et al.*, 2009. Solid state physics. From Ricci *et al.*, 2015. Life science. From Ortega *et al.*, 2007. Macromolecular crystallography. From Rasmussen *et al.*, 2011.

to biological samples. Within the water window (energy range between the absorption edges of carbon and oxygen at 284 and 532 eV, respectively), the method allows for visualization of unsectioned, frozen-hydrated cells, employing only their natural absorption contrast, with competitive imaging times as well as 3D resolutions on the order of tens of nanometers (Sakdinawat and Attwood, 2010). On the other hand, hard x rays are particularly suitable for tomographic inspection of biologically relevant samples, mainly due to their higher penetration depth into larger-scale structures (e.g., tissue and organs) (Sakdinawat and Attwood, 2010). Finally, x-ray microbeams offer several benefits for protein crystallography (Rasmussen *et al.*, 2007; Rosenbaum *et al.*, 2007; Sawaya *et al.*, 2007). The high photon flux available at third-generation sources allows for outstanding signal-to-noise ratio even when very small proteic crystals (easier to produce) are analyzed using intense microbeams and nanobeams. Moreover, if the beam divergence is small enough, a smaller beam size ensures very sharp diffraction spots, and different areas within the same crystal can be selected in turn for the analysis.

In geology and environmental sciences, space-resolved x-ray based analytic methods are widely employed. For instance, single-crystal XRD (Coppens *et al.*, 1992) is commonly applied to space-resolved structural investigations on microvolumetric single-crystal minerals, as well as to high-pressure or extreme conditions studies (Prewitt and Downs, 1998; Jacobsen *et al.*, 2005; Dera, 2010). X-ray scattering techniques, such as SAXS and WAXS, are particularly employed in the research of paracrystalline or amorphous mineral assemblages for the *in situ* monitoring of crystallization reactions (Meneghini, Gualtieri, and Siligardi, 1999; Pontoni *et al.*, 2003; Sankar *et al.*, 2007), and, recently, for nanoscale investigation of organic-mineral interactions (Gilow *et al.*, 2011). The unique capabilities of XAS spectroscopy have been extensively exploited in earth science (Brown *et al.*, 1988; Calas *et al.*, 2002; Chaboy Nalda, 2008), both for element-selective investigation of local structure and oxidation state (Borfecchia *et al.*, 2012; Mino *et al.*, 2014), and in the structural analysis of nonordered materials of geological interest, such as glasses, silicatic melts, metamictic minerals, fluid inclusions, polymers, and gels (Quartieri, 2003).

Several applications of x-ray spectromicroscopy methods are related to the dating, authentication, and restoration of artworks relevant to the cultural heritage and archaeological

TABLE I. Comparison of x-ray photons (x-ray microscopes and nanoprobes), visible photons (visible-light microscopes and lasers), electrons (SEM and TEM microscopes), ions, and neutrons as probes for (sub-)micrometric space-resolved characterization.

	Photons		Electrons			
	X rays	Visible	SEM	TEM	Ions	Neutrons
Wavelength range (m)	$0.001–5 \times 10^{-8}$	$4–8 \times 10^{-7}$	$6–80 \times 10^{-12}$	$2–4 \times 10^{-12}$	$1–10 \times 10^{-14}$[a]	$2–40 \times 10^{-10}$
Best spatial resolution (m)	5×10^{-9}	2×10^{-7}	$1–10 \times 10^{-9}$	10^{-10}	10^{-8}[a]	10^{-6}
Penetration depth (m)	$1–50 \times 10^{-6}$ ($E < 10$ keV) 2×10^{-2} ($E = 100$ keV)	$< 10^{-7}$ (in metals)	$< 10^{-8}$[b]	$< 10^{-7}$[b]	$5–100 \times 10^{-6}$	10^{-1}
Source brightness (particles s^{-1} cm^{-2} $sterad^{-1}$ eV^{-1})	10^{26}		10^{29}		10^{19}[c]	10^{24}
Vacuum needed	No		Yes		Yes[a]	No

[a]The wavelength range and the best resolution (Yao and van Kan, 2015) are provided for protons, which are the most commonly employed probes in ion beam analysis, under vacuum conditions. Analysis in air is possible, but the spatial resolution is strongly degraded.
[b]The penetration depth of electrons in condensed matter is strongly dependent on the electron kinetic energy; see Fig. 11.
[c]The brightness for ion sources is usually reported in pA μm^{-2} $mrad^{-2}$ MeV^{-1} (Liu *et al.*, 2015): 6×10^{18} particles s^{-1} cm^{-2} eV^{-1} $sterad^{-1} = 10^7$ pA μm^{-2} $mrad^{-2}$ MeV^{-1}.

fields (Sakdinawat and Attwood, 2010). These materials are particularly precious, so that sampling is usually forbidden or very limited in number and size (e.g., pigments in ancient paintings, glasses, ceramics). Thus, the low invasiveness at high spatial resolution of the combination of synchrotron-based Fourier transform infrared microspectroscopy and x-ray synchrotron-based microimaging techniques has allowed the study of a large number of historical materials (Cotte *et al.*, 2007; Janssens *et al.*, 2010; Farges and Cotte, 2016). A relevant example is the identification of an alternative degradation pathway of the pigment cadmium yellow (CdS) in the painting "Flowers in a blue vase" by Van Gogh with a combined micro-XRF, micro-XRD, micro-XANES, and micro-Fourier transform (FT) infrared (IR) investigation (Van der Snickt *et al.*, 2012). Likewise, the darkening of the yellow colors in Van Gogh's Sunflowers (Van Gogh Museum, Amsterdam) strongly debated over the past few decades was recently addressed by micro-XANES and micro-XRF (Monico *et al.*, 2015). The results evidenced the chemical alteration of chrome yellows in this iconic painting, outlining the regions with the highest risk of color change due to the instability of the pigment used.

In high-pressure research (Ariga *et al.*, 2011) very small sample volumes are commonly probed since the smaller the sample, the higher the pressure that can be achieved. In particular, diamond anvil cells (Liebermann, 2011) can exclusively operate with samples within the 10–100 μm length scales (Ice, Budai, and Pang, 2011) and consequently hard-x-ray microbeams able to penetrate the anvil material are crucial tools.

Finally, a reliable investigation of nuclear materials also requires x-ray microbeams (Ice and Specht, 2012; Carter *et al.*, 2013; Misra, 2014; Denecke, 2016), because of both their highly intrinsic heterogeneous nature and radioactive hazard (when handling nuclear materials their radioactivity is proportional to the sample volume, small samples are consequently preferred). For this reason several synchrotron beam lines have been specifically equipped to handle radioactive materials (Rothe *et al.*, 2012; Sitaud *et al.*, 2012; Llorens *et al.*, 2014).

B. General comparison among different probes

Several probes can be selected to obtain space-resolved structural, electronic, or compositional information. To provide the reader with a concise overview, typical values for the main parameters related to photon, electron, neutron, and ion probes are summarized in Table I.

In the next sections, the peculiarities of each characterization tool will be briefly discussed, highlighting the key strengths and weaknesses related to the use of x-ray photons for probing matter with micrometric and nanometric resolutions.

1. Laser probes

Laser and x-ray microprobes share many characteristics as both of them are based on photons, but the main difference between them is their wavelength range. Indeed, laser microprobes operate within a wavelength range of a few microns to around 200 nm, while x rays work within a 10–0.01 nm range. Moreover, laser beams are characterized by a much higher coherence than synchrotron x-ray sources; this gap, however, will be partially covered by fourth generation diffraction-limited storage rings (DLSRs) and x-ray free-electron laser (XFEL) sources.

Laser microprobes are much less expensive than large-scale facilities; however, being laboratory-scale instrumentation, their costs bear heavily on a single research group or department, while the cost of large-scale facilities is shared at a national or international level. The sources and optics employed in laser microprobes are easier to construct and therefore much cheaper than those for x rays. Furthermore, the former has a much better performance in terms of power (sources), efficiency, and correction of aberrations (optics) than the latter. However, apart from the price, the other strengths of laser microprobes are being narrowed by new

improvements in the x-ray optics and also in the near future by the DLSRs (Eriksson, van der Veen, and Quitmann, 2014), the compact light sources (Eggl *et al.*, 2016), and the x-ray free-electron laser (XFEL) (Emma *et al.*, 2010). The temporal modulation is another advantage of lasers with respect to x-ray sources. Lasers having pulses with full width at half maximum (FWHM) of several tens of femtoseconds (10^{-14} s) are commercially available, and more refined systems allow even attosecond (10^{-18} s) FWHM pulses (Wirth *et al.*, 2011). On the other hand, synchrotron sources provide x-ray pulses with typical FWHM of several tens of picoseconds. However, this aspect will also be improved by the XFEL sources, where the limit of a few femtoseconds will be reached (see Table III).

The long wavelength of laser microprobes has important drawbacks associated with it. The first one is related to the spatial resolution. For any optical element in the visible or x-ray wavelength range, there is a fundamental maximum resolution limited by diffraction (s_{DL}) according to the Rayleigh criterion (Als-Nielsen and McMorrow, 2001):

$$s_{\mathrm{DL}} = \gamma\lambda/\mathrm{NA}, \tag{1}$$

where λ is the wavelength and NA is the numerical aperture of the lens. γ is equal to 0.61 in the case of two-dimensional focusing by a round lens, whereas for a linear (or rectangular) lens, γ is equal to 0.5. Equation (1) gives the theoretical limit; however, the real limit for the maximum resolution is always higher due to defects in the real optics as well as further experimental issues such as alignment, vibrations, drifts, etc. Equation (1) shows that the resolution is better for shorter wavelengths. For instance, the best resolution achievable for laser microprobes is around 200 nm, while the record for x rays is 7 nm (Mimura *et al.*, 2010; Yamauchi *et al.*, 2011) (see Table IV). The spatial resolution for lasers can be improved to 20 nm by working in the near field conditions (Oshikane *et al.*, 2007), but it suffers from spurious effects due to modifications produced by the presence of a probe in the region near the sample. Thus, although several exciting approaches have emerged recently that can "break" the diffraction rule under certain circumstances (Mortensen *et al.*, 2010), the use of x rays provides unique advantages over near field imaging approaches (restricted to surfaces with small areas in the region within ~10 nm of the tip or nanoantenna) (Novotny and van Hulst, 2011), or far-field imaging techniques (that involve photoactivatable fluorophores) (Resch-Genger *et al.*, 2008) in terms of sample surface quality and information depths.

The beam penetration depth is energy and material dependent. In general, x rays have a much larger penetration than lasers. For instance, for a common semiconductor such as GaAs, the penetration depth for the 488 nm line of an Ar laser is ~125 nm, while for a 10 keV x-ray beam it is ~50 μm. This is a drawback of laser microprobes when relatively thick or buried samples are examined. Nevertheless, the surface sensitivity of laser-based studies may be useful for some specific applications.

There are two other major weaknesses of lasers with respect to synchrotron x rays. The first one is the energy tunability. Although dye lasers allow tuning the laser energy in a short range, they are far from the continuous and wider energy tunability offered by synchrotron radiation (SR) from IR to gamma rays. The second drawback is the elemental specificity provided by x rays, which can be replicated by lasers for certain chemical groups under resonance conditions [i.e., when the laser wavelength matches an electronic transition of some chemical groups present in the sample (Ricchiardi *et al.*, 2001; Bordiga *et al.*, 2003)], but is not a key characteristic of these microprobes.

2. Electron probes

Electron microscopes are probably the main competitor of x-ray microprobes. Many x-ray characterization techniques have a counterpart using electron probes: XRD versus electron diffraction, XAS versus electron energy loss spectroscopy (EELS), XRF versus energy-dispersive x-ray (EDX) spectrometry, x-ray emission spectroscopy (XES) versus electron probe microanalysis (EPMA).

The first advantage of electron microscopes is their price. Although electron-based instruments are in general more expensive than laser systems, they are still much cheaper than a SR-based microprobe and a single laboratory (if properly funded) can afford having dedicated scanning and transmission electron microscopes (SEM and TEM). Indeed, SEM and TEM facilities are widely spread in physics, chemistry, materials science, and engineering departments. From the technical point of view, a single electron microscope offers multiple characterization techniques, combined with an outstanding spatial resolution. Electrons accelerated into an electric potential U have an associated wavelength given by the de Broglie equation:

$$\lambda = \frac{h}{p} = \frac{h}{\sqrt{2m_0eU}}\frac{1}{\sqrt{1+eU/2m_0c^2}}, \tag{2}$$

where h is the Planck constant, p is the relativistic momentum of the electron, e and m_0 are, respectively, the charge and mass of the electron at rest, and c is the speed of light in the vacuum. Therefore, the de Broglie wavelength of electrons is much shorter than those of x rays for the typical acceleration potentials used in the microscopes. For instance, the 10 and 200 keV electrons used typically in SEM and TEM have wavelengths of, respectively, ~12.2 and ~2.5 pm. Accordingly, electron microprobes can be focused down to ~2 and <0.1 nm in SEM and TEM microscopes, respectively (Erni *et al.*, 2009; de Abajo, 2010). However, the final spatial resolution of electron microscopes depends not only on the electron probe size but also on the type of signal measured: transmitted electrons, secondary electrons, visible photons [cathodoluminescence (CL) (Salviati *et al.*, 2013)], emitted x rays, etc. When impinging electrons interact with the sample, they lose energy by random scattering within a teardrop-shaped volume known as the interaction volume shown in Fig. 3. This volume is material and electron-energy dependent, and its shape and extent can be estimated using Monte Carlo (MC) simulations. Each of the signals used in a specific method is generated from different electron interaction volumes (see Fig. 3) and, therefore, each technique has a different analytical resolution. Transmitted and diffracted electrons have the best analytical spatial resolution, followed by Auger and secondary electrons, as they are generated in the smallest volume near the surface (Fig. 3). Secondary fluorescence such as CL is generated over the

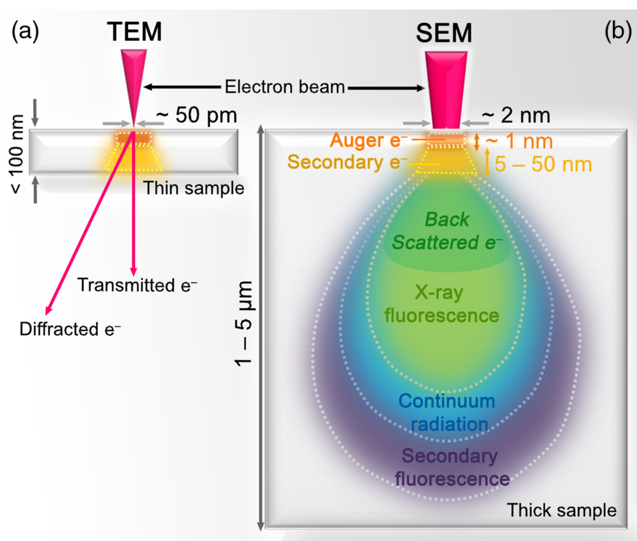

FIG. 3. Schematic representation of the teardrop-shaped interaction volume of the electron beam inside the sample. The different signals that can be measured in a (a) TEM or (b) SEM microscope are also indicated.

largest volume, even larger than continuum radiation, resulting in the poorest spatial resolution (Lim *et al.*, 2009).

High-energy electrons create core holes in the target material [see Fig. 10(a)], whose decay process allows getting insight into the chemical composition and oxidation state of the surface of the investigated sample. The radiative channel [see Fig. 10(b)] results in EPMA (Kuisma-Kursula, 2000; Scott, 2003; Cubukcu *et al.*, 2008), while the nonradiative ones result in Auger spectroscopy [Fig. 10(c)]. The former exploits the element specificity of the x rays emitted by an excited atom that, when collected at high-energy resolution, can discriminate different oxidation states and first-shell ligands of the excited element.

EPMA probes the occupied density of states and is analogous to the XES or particle-induced x-ray emission (PIXE) techniques that use x rays or protons as a primary beam. Two different detection systems can be used in EPMA: energy-dispersive spectrometry (EDS) (Gauvin, 2012; Newbury and Ritchie, 2013, 2015) or wavelength-dispersive x-ray fluorescence (WDXRF), often just named wavelength-dispersive spectrometry (WDS) (Fournier *et al.*, 1999; Tanaka, Takeguchi, and Furuya, 2008; Ritchie, Newbury, and Davis, 2012). EDS systems use solid-state detectors that measure the energy release of a single x-ray photon. They are characterized by a much faster acquisition rate since they simultaneously acquire the whole spectrum. Thus, this technique represents the ideal solution for a qualitative analysis over large area samples, where the time needed for the collection depends on both the square of the sample size and the square of the spatial resolution. The energy resolution is within the 100–200 eV range, which does not allow discrimination among different oxidation states and limits their use for element speciation purposes with a concentration higher than 0.1% (Cubukcu *et al.*, 2008). Instruments based on WDXRF use the Bragg diffraction of analyzing crystals for x-ray separation, resulting in an energy resolution of about 10 eV, and with a chemical detection limit better than 100 ppm. The main drawback of the WDXRF setup is that the energy of the emitted x-ray photons is scanned sequentially: this makes the data collection in the typical spectral range (0.5–20 keV) time consuming and requires different analyzer crystals of different d spacing to cover the whole energy range (Scott, 2003).

Despite these advantages, electron microscopes have various drawbacks that constrain their use in the characterization of several systems. Among them, we mention the need for sample preparation, which can be challenging and could even modify the intrinsic properties of the samples to be studied. TEM, for instance, needs very thin specimens (≤100 nm) relatively transparent to the electrons, requiring a careful and time-consuming sample preparation by sophisticated means such as focused ion beam (FIB) setups. Indeed, electrons strongly interact with matter via direct charge-charge Coulomb interactions and therefore information obtained from electron probe methods is intrinsically restricted to the first few nm from sample surfaces. The typical surface selectivity of electron probe methods can be considered either a unique advantage, when the primary interest is in surface features, or a strong obstacle, if aiming for a bulk characterization or for the analysis of buried or embedded volume portions. For instance, the penetration depth for a 10 keV x ray is $\sim 50\ \mu$m in GaAs, while it is only $\sim 1.8\ \mu$m for electrons with the same energy (Kanaya and Okayama, 1972). The use of intense electron beams or higher energies to increase the penetration depth can generate significant radiation damage, mainly because electrons are capable of transferring relatively large momenta to the sample (de Abajo, 2010). Another disadvantage is the need to operate under high vacuum, which strongly limits the use of different *in situ* environment setups. Finally, the lack of elemental selectivity in electron microscopes is a major drawback with respect to x rays, unless XRF or Auger spectroscopies are used as probes.

3. Ion probes

The interaction of ion beams with condensed matter concerns both the electrons and the nuclei and can be explained in terms of the basic concepts of atomic and nuclear physics (Wang and Nastasi, 2009; Avasthi and Mehta, 2011). In contrast to photons or electrons, ions with high kinetic energy deposit extremely localized densities of energy to the target. In this way, solids receive in an ultrashort time (from $\sim 10^{-17}$ to 10^{-15} s) and in a small volume (from $\sim 10^{-17}$ to 10^{-16} cm^3) a very high-energy density by the impact of just one high-energy ion (Ziegler and Biersack, 1985; Avasthi and Mehta, 2011). With the availability of ions from protons to uranium in the energy range of eV to GeV, it is possible to have penetration depths from a few nanometers, for low-energy heavy ions, to several tens of microns, for medium-energy (few MeV) light ions (Avasthi and Mehta, 2011).

Ion beams have been of increasing relevance in fundamental and applied research in different fields such as materials science, solid-state and applied physics, biology, geology, and cultural heritage. Their applications, driven by the beam characteristics, concern the materials synthesis (at very low beam energy), the modification of the matter properties,

and/or its characterization, or both cases, at intermediate and high beam energies (Avasthi and Mehta, 2011). The synthesis of thin films and the modification of materials with ion beams, although relevant in materials science, are not covered in this review.

High-energy beams (from a few MeV to a few hundred of MeV) are used for ion beam analysis (IBA) to investigate, in a nondestructive fashion, the elemental composition and the electronic properties of materials, in the μm- and sub-μm scale (Tsuji *et al.*, 2008, 2012; Avasthi and Mehta, 2011). Owing to the charged nature of ions, the use of electromagnetic optics is possible to obtain focused ion beams which are typically of a micrometric size, but can reach the 10 nm scale (Orloff, Swanson, and Utlaut, 1996; Sakai *et al.*, 2002; van Kan *et al.*, 2005; Karydas *et al.*, 2007; Tsuji *et al.*, 2008, 2012; Siegele *et al.*, 2009; Rothermel *et al.*, 2010; Fujita, Ishii, and Ogawa, 2011; Gordillo *et al.*, 2011; Kamiya *et al.*, 2011; Rout *et al.*, 2013; Kada *et al.*, 2014; Sorieul *et al.*, 2014). The actual spatial resolution depends on the lateral straggling of the ion beam in the sample, which depends on the ion mass and energy as well as on the sample nature. It has been demonstrated that it is possible to achieve spatial resolutions in the ~10 nm range with advanced focusing (Yao and van Kan, 2015) or collimation (Pezzagna *et al.*, 2011) techniques. Figure 4 describes how ion beams impinging on a material induce a complex cascade of physical processes which results in the emission of secondary radiation and particles.

These processes have provided various analytical techniques (Stensgaard, 1992; Breese, Jamieson, and King, 1996; Wang and Nastasi, 2009; Avasthi and Mehta, 2011) which have been classified according to the interaction mechanism (scattering, excitation, decay, photon emission, or reaction),

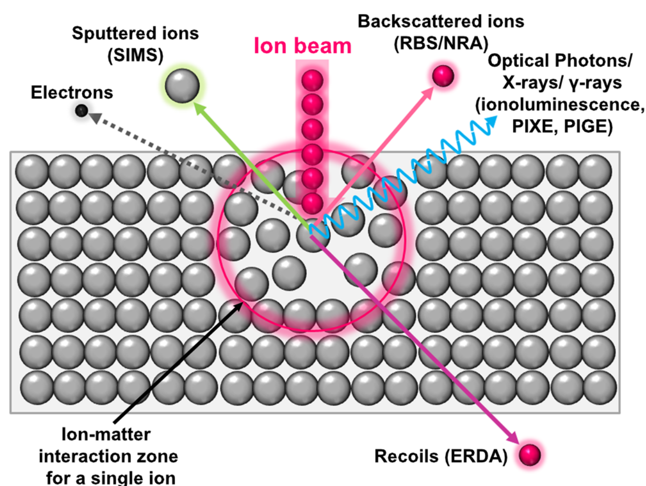

FIG. 4. Schematic representation of the different scattering, excitation, and decay phenomena that occur when an ion beam interacts with matter and the consequent IBA techniques: photon emissions [ionoluminescence, PIXE, and proton-induced or particle-induced γ-ray emission (PIGE), depending on the photon energy]; backscattered ions and nuclear reaction products in Rutherford backscattering spectroscopy (RBS) and nuclear reaction analysis (NRA), respectively; sputtered ions in secondary ions mass spectrometry (SIMS); and nuclei recoils in elastic recoil detection analysis (ERDA).

and on the mode of detection of the reaction products. The most relevant methods among the IBA techniques are briefly summarized in the following.

PIXE consists of the detection of x rays of different energies emitted by a material as a consequence of an electronic transition between a core or valence electron into a core hole generated by particle (proton) bombardment (Johansson, Akselsson, and Johansson, 1970; Lefevre *et al.*, 1987; Ryan *et al.*, 1990; Johansson, Campbell, and Malmqvist, 1995; Adams, Janssens, and Snigirev, 1998; Ryan, 2000); see Fig. 4. PIXE probes the occupied density of states and is analogous to the XES or EPMA techniques that use x rays or electrons as a primary beam; see Figs. 10(a) and 10(b). Compared to electron-based x-ray analytical techniques, such as EDS, PIXE offers much higher sensitivities (lower detection limits) because the intensity of the background x rays (Bremsstrahlung radiation) is 3 orders of magnitude lower in PIXE than in EDS. Analogous techniques to PIXE are particle-induced (or proton-induced) γ-ray emission (PIGE) and ionoluminescence [(IL), also known as ion-beam-induced luminescence (IBIL)], where the experimental setup detects the γ rays emitted by the sample nuclei or the visible or UV light emitted by the sample atoms, respectively, upon excitation with the ion beam.

Secondary ions mass spectrometry (SIMS), see Fig. 4, is intrinsically a destructive method consisting of the composition depth profile of materials by sputtering the surface with a focused primary ion beam and recording ejected secondary ions (Pachuta and Cooks, 1987; Benninghoven, 1994; Zalm, 1995). The m/q ratios of these secondary ions are determined with a mass spectrometer to obtain the elemental, isotopic, or molecular composition of the surface to a depth of 10 to 20 Å. SIMS is usually considered as a qualitative technique, although quantification is possible with the use of standards. Remarkably, the elemental detection limit of SIMS ranges from parts per million to parts per billion. Recent advances allowed imaging of nano-objects with SIMS (Passarelli and Winograd, 2011; Vickerman, 2011; Senoner and Unger, 2012; Gilmore, 2013).

Rutherford backscattering (RBS), see Fig. 4, is used to determine the compositional depth profile by measuring the elastic backscattering of a beam of high-energy ions (usually α particles or, less commonly, protons) impinging on a sample (Galindo *et al.*, 2010).

RBS is also known as high-energy ion scattering (HEIS, $E > 1$ MeV); this nomenclature is used to differentiate the technique as a function of the beam energy and thus of the surface sensitivity of the analysis: medium-energy ion scattering (MEIS, $E \sim 50$–300 keV) (Baer *et al.*, 2013) and low-energy ion scattering spectroscopy (LEIS, $E \sim 1$–3 keV) (Niehus, Heiland, and Taglauer, 1993; Brongersma *et al.*, 2007; Cushman *et al.*, 2016), being progressively more surface sensitive. RBS (or HEIS), MEIS, and LEIS are particularly responsive to heavy elements in light matrices.

The fraction of the ion beam not contributing to RBS will progressively slow down in the target material until its energy is sufficiently low to interact with the nuclei. This interaction can result in a nuclear reaction yielding new unstable nuclei that decay via the standard α, $\beta^{\pm}$, or γ channels, typical of the hit nucleus. The detection of those nuclear decay products

results in the nuclear reaction analysis (NRA) technique which provides isotope specific elemental profiling especially sensitive to light elements such as hydrogen (Fukutani, 2002; Wilde and Fukutani, 2014). The depth sensitivity of NRA is obtained by changing the beam energy and thus its stopping power.

Elastic recoil detection analysis (ERDA), see Fig. 4, exploits the elastic interaction between the ions of beams and the atoms of the target samples that are forward scattered and collected after the sample (David, 1992; Assmann *et al.*, 1994). The technique, also known as forward recoil scattering (or spectrometry), provides the depth profile of the elemental analysis of thin films and is particularly sensitive to light elements in heavy matrices.

4. Neutron probes

Neutron probes have also been extensively employed (Cheetham and Wilkinson, 1992; Mezei, 1997; Sosnowska and Willis, 1999; Arrighi and Higgins, 2004; Wilson, 2005; Melnichenko and Wignall, 2007; Alonso *et al.*, 2008; Manke *et al.*, 2011; Willumeit, 2011) due to their specific capabilities that complement x-ray and electron-based methods. They include, for example, sensitivity to hydrogen (Neumann, 2006), isotope specificity, and magnetic interaction (Fitzsimmons *et al.*, 2004; Kozhevnikov *et al.*, 2011). With regards to penetration depth, cross sections for neutron-matter interaction (mainly with atomic nuclei) are significantly weaker than for x-ray photons, making them ideal bulk probes.

In standard neutron experiments, typical beam sizes are within the 0.1–10 mm range. To push down the available spatial resolution, to date specific optics have been developed using several approaches (Erko, 2008), e.g., Bragg diffraction (Mikula *et al.*, 1986), reflection [in mirrors (Sears, 1989), Kumakhov lenses (Kumakhov and Sharov, 1992), or capillary optics (Chen *et al.*, 1992)] and refraction, in compound refractive lens (Eskildsen *et al.*, 1998; Beguiristain *et al.*, 2002; Shimizu, 2006).

However, a major obstacle in the (sub)micrometric characterization of materials with neutrons, apart from the technical limitation in manufacturing the focusing devices, is the relatively low flux provided by present neutron sources, i.e., on the order of 10^{15} $\mathrm{n\,cm^{-2}\,s^{-1}}$ for reactor-based sources, while it can slightly exceed 10^{17} $\mathrm{n\,cm^{-2}\,s^{-1}}$ for spallation sources. The corresponding typical brightness for neutron sources is circa 2 orders of magnitude lower than for x rays produced by third- and fourth-generation synchrotron facilities; see Table I. The low incident flux makes the fabrication of neutron-focusing devices for submicrometric resolution even more challenging. Notwithstanding these difficulties, submicrometric beams have been reported in recent years using thin-film waveguides based on the resonant beam coupling principle (Guthrie, 2015; Salmon and Zeidler, 2015).

C. X-ray probes

1. The key role of synchrotron sources

As already introduced in the previous sections, x-ray-based methods offer outstanding possibilities for nondestructive imaging and characterization at the (sub)micrometric scale, overcoming many limitations imposed by other available probes. Their strengths include the availability of several, often complementary, contrast mechanisms (e.g., absorption, emission and scattering, diffraction, phase contrast, and polarization), the simple sample preparation procedures, and the possibility to perform experiments under *in situ* or *operando* conditions. Indeed, x rays, especially in the hard-x-ray energy range, exhibit relatively low cross sections for their interaction with matter, making them ideal nondestructive characterization tools, applicable in air, water, and other environments. Low cross-section values also imply high penetration depths through matter, thus offering the opportunity of 3D analysis.

Another key feature is the possibility to achieve outstanding performance in terms of flux and brightness using third- and fourth-generation synchrotrons (see Fig. 1). The relationship between space-resolved characterization at the (sub)micrometric scale and highly brilliant x-ray sources is straightforward. Indeed, the space-resolved approach implies that only a micrometric-sized sample volume is probed, thus resulting in a very low signal compared with standard analysis averaged on macroscopic volumes. High brilliance with low emittance sources is therefore crucial to obtain satisfactory data quality in terms of signal-to-noise ratio and spatial resolution within a reasonable acquisition time.

Also table-top x-ray microscopes (Adam, Moy, and Susini, 2005; Takman *et al.*, 2007; Bertilson *et al.*, 2009; Muller *et al.*, 2014) and laboratory x-ray microbeam setups (Altamura *et al.*, 2012; Sibillano *et al.*, 2014) have been recently demonstrated and, using novel rotating-anode generators, brilliancies up to 4×10^9 $\mathrm{photons\,s^{-1}\,mm^{-2}\,mrad^{-2}}$ can be achieved with laboratory instrumentation (Altamura *et al.*, 2012). However, even with the best high-brilliance laboratory microsources, the beam spot size is usually still some tens of micrometers in diameter (Altamura *et al.*, 2012). Therefore, the production of highly intense microbeams and nano-x-ray beams is mostly oriented to synchrotron large-scale facilities because of several factors.

From a scientific point of view, such sources can allow one to probe deeply into inner grains embedded in materials, buried heterostructures, small particles, or microdomains by simultaneously characterizing many properties *in situ*. The microstructure and nanostructure in 2D and 3D can be fully revealed, and its evolution during dynamical processes (such as materials deposition and gas phase chemical reactions) and under operating conditions (e.g., temperature cycling, high electric fields) can be monitored (Wang, Chen-Wiegart, and Wang, 2014; Harks, Mulder, and Notten, 2015; Huang *et al.*, 2015).

From an instrumental or technical perspective, low-emittance synchrotron sources (coming DLSRs and modern third-generation synchrotrons, see Table II) deliver very small, well-collimated, and extremely intense electron beams, providing nanometer lateral resolution (today down to sub-5 nm) (Doring *et al.*, 2013) with several orders of magnitude more photon flux than lab sources (Schroer and Falkenberg, 2014), ranging from the soft- to the hard-x-ray energy regimes. So far, current SR sources have been characterized by quite different beam properties in the vertical and horizontal directions. Whereas the diffraction limit is achieved in the vertical direction even for hard x rays, the horizontal source size and divergence is much larger than the diffraction limit.

TABLE II. Comparison of the key features of some selected SR facilities. A more complete list of synchrotrons with further details about microbeam and nanobeam setups of the specific beam lines is available in the Supplemental Material (729).

	Synchrotron radiation facilities							
	ESRF	APS	Spring8	SLS	PETRA-III	DLS	MAX-IV	SIRIUS
Full name	European Synchrotron Radiation Facility	Advanced Photon Source	Super Photon Ring	Swiss Light Source	Positron-Elektron-Tandem-Ring-Anlage III	Diamond Light Source	Machine run by MAX-lab of Lund University	The name refers to the most brilliant star in the sky
Location	Grenoble, France	Lemont, IL, USA	Hyogo, Japan	Villigen, Switzerland	Hamburg, Germany	Didcot Oxfordshire, UK	Lund, Sweden	Campinas, Brazil
Synchrotron light source generation	Third	Third	Third	Third	Third	Third	Fourth	Fourth
Number of operative beam lines	43	48	47	17	14	30	14	20
Nominal energy (GeV)	6	7	8	2.4	6	3	3	3
Current (mA)	200	100	100	400	100	500	500	500
Circumference (m)	844	1104	1436	288	2304	565.3	528	518.4
Emittance (nm rad)	3.8	3.0	3.0	5.5	1.2	3.22	0.33	0.25

However, in the coming DLSRs the horizontal beam size and divergence match the intrinsic divergence of the undulator radiation. As a result, optimal diffraction-limited focusing could be used by matching the aperture of the nanofocusing optics to the lateral coherence length of the x rays falling onto its aperture. Thus, only the coherent fraction of the x-ray beam will be efficiently focused. Accordingly, the largest fraction of the beam will be used for nanofocusing, making DLSRs highly efficient for x-ray scanning microscopy, where high signal-to-noise ratio and minimal exposure time are demanded. In summary, synchrotrons easily fulfill key source requirements that are instead hardly achievable with laboratory-based instrumentation, such as low emittance, high photon flux, energy tunability, spectral purity, and high stability.

As represented in Fig. 1, the improvement of x-ray source brilliance (B) in the recent decades has been impressive. Moving first from x-ray tubes ($B = 10^7$–10^9 photons/s/0.1%BW/mm^2/mrad^2) to the first synchrotron ($B \approx 10^{12}$ photons/s/0.1%BW/mm^2/mrad^2), and subsequently through the different generations of synchrotron sources, including low emittance and DLSRs, B values of the order of 10^{22} photons/s/0.1% BW/mm^2/mrad^2 were obtained (Liu et al., 2014; Susini et al., 2014; Tavares et al., 2014). The Hamburg XFEL, operating with 3000 pulses s^{-1}, exhibits an average B value of 1.8×10^{24} photons/s/0.1%BW/mm^2/mrad^2 that will become 1.6×10^{25} photons/s/0.1%BW/mm^2/mrad^2 once the target 27 000 pulses s^{-1} mode will be operational, with a peak brilliance higher than 10^{33} photons/s/0.1%BW/mm^2/mrad^2 (Altarelli, 2011; Altarelli and Mancuso, 2014); see Table III. These brilliances are expected to further increase in the near future. Brilliance time evolution is well reproduced by an exponential growth curve with an estimated doubling time of 10 months (Eriksson, van der Veen, and Quitmann, 2014).

At the same time, an exponential reduction of the achievable spot size has been reported, with a typical halving time of 22 months (Endo et al., 2011). Such a trend for the more common and more promising x-ray-focusing devices is demonstrated in Fig. 1. Over the last two decades, the available spot size has improved drastically down to 5 nm x-ray beams (Doring et al., 2013), owing to the progress in optical design, fabrication technology, online metrology, and wave front diagnosis tools, thus pushing the space resolution fully inside the nanotech realm (Ice, Budai, and Pang, 2011; Martinez-Criado et al., 2013).

The x-ray optics field represents an extremely active research area, and the microfocusing and nanofocusing of x rays, with an index of refraction slightly smaller than unity, are challenging tasks. In principle, the focusing can be achieved simply by using a pinhole, but the resulting x-ray photon flux at the sample would be too low for most practical purposes. Narrow apertures are efficient only if the beam divergence on the aperture exceeds the diffraction-limited divergence. Consequently, pinhole-based focusing schemes have been employed almost exclusively in combination with condensing optics.

However, state-of-the-art space resolutions are nowadays mostly achieved using advanced focusing devices based on x-ray refraction, reflection, and diffraction as well as combined

TABLE III. Comparison of the key features of some selected x-ray free-electron laser facilities.

	XFEL facilities				
	LCLS	SACLA	European XFEL	FERMI	SwissFEL
Full name	Linac Coherent Light Source	Spring-8 Angstrom Compact Free-electron Laser	European X-Ray Free-electron Laser	Free-electron laser Radiation for Multidisciplinary Investigations	Swiss Free-electron Laser
Location	California, USA	Japan	Germany	Italy	Switzerland
Number of light flashes per second	120	60	27 000	50	100
Pulse duration (fs)	2–100	2–20	2–100	150–180	2–200
Minimum wavelength of the laser light (nm)	0.15	0.08	0.05	4	0.1
Maximum electron energy (GeV)	14.3	6–8	17.5	1.5	5.8
Length of the facility (km)	3	0.750	3.4	0.3	0.74
Number of experiment stations	3–5	4	6, upgradeable to 10	3, upgradeable to 6	2
Peak brilliance (photons/s/mm^2/mrad^2/0.1% bandwidth)	2×10^{33}	1×10^{33}	5×10^{33}	$> 10^{29}$	1.3×10^{33}

schemes [e.g., a Kirkpatrick-Baez mirror and multilayer zone plate (Doring *et al.*, 2013)]. These optics are specifically designed to optimally exploit the high brilliance and reduced emittance of third- and fourth-generation synchrotron sources (Bilderback, Elleaume, and Weckert, 2005) and include Fresnel zone plates (Vila-Comamala *et al.*, 2011), compound refractive lenses (Evans-Lutterodt *et al.*, 2007), Kirkpatrick-Baez mirrors (Yamauchi *et al.*, 2011; Da Silva *et al.*, 2017), and tapered capillaries (Bilderback and Fontes, 1997; Bilderback, 2003). A detailed description of x-ray optics working principles and a comparative overview of different available solutions is reported in Sec. II.

Finally, in addition to the impressive developments of the x-ray sources in terms of both brilliance and performance of x-ray-focusing devices, rapid technical progress is ongoing for the whole instrumentation required in a (sub)microprobe setup. For instance, monochromators have been specifically designed to easily switch between monochromatic and white-beam operation modes, as well as to preserve a stable focal spot position during the energy scan (Yamazaki *et al.*, 2013; Kristiansen *et al.*, 2015). Moreover, recent advances in x-ray detector technology (e.g., fast-readout large area detectors with high dynamic range and low-noise characteristics) (Gruner, 2010; Ryan *et al.*, 2010) enable enhanced sensitivity with shorter acquisition times.

2. The upcoming area of x-ray free-electron lasers

Future directions in materials research at the micrometer and nanometer length scales are expected to be strongly impacted by the even much higher photon flux, brilliance, and coherence of the radiation at the XFELs. These sources will provide a unique radiation with a drastic increase in brilliance and extremely short x-ray pulses that are ideal for ultrafast pump and probe studies (Fletcher *et al.*, 2015; Minitti *et al.*, 2015; Stankus *et al.*, 2016). XFELs are also ideally suited for nanobeam technologies, such as x-ray microscopy applied to time-resolved studies in the femtosecond domain (Schropp *et al.*, 2013a, 2013b). However, special attention must be paid because the peak intensity of their focused beams will be well above the damage threshold of any material; see Sec. III.I. The problem can be partially overcome by freezing the sample in time using the femtosecond pulse duration instead of cryogenically cooling the sample, as recently developed using coherent x-ray diffraction with XFELs (Kimura *et al.*, 2014).

The first soft Free Electron Laser in Hamburg (FLASH) (Schreiber *et al.*, 2012; Honkavaara, 2017) and hard Linac Coherent Light Source (LCLS) (Bostedt *et al.*, 2016) FEL facilities were realized in 2005 at the Tesla Test Facility (TTF) and in 2009, at the Stanford Linear Accelerator Center (SLAC), respectively. Nowadays, several x-ray facilities have been planned or commissioned: FERMI (Italy), SWISS-FEL (Switzerland), European XFEL (Germany), POL-FEL (Poland), MAXIV-FEL (Sweden), LCLS (USA), SACLA (Japan), PAL-XFEL (South Korea), and Beijing FEL (BFEL, China). FERMI (Allaria *et al.*, 2016) was the first lasing-seeded FEL facility in the world, based on the high-gain harmonic generation principle (Yu *et al.*, 2000) which upconverts, within the FEL, a coherent seed source into a higher harmonic. In 2012, FERMI was also the first FEL to offer an x-ray laser beam with variable polarization, from linear to circular.

In order to identify the major scientific breakthroughs connected with the diffusion of FELs, it is fundamental to know which is the wavelength range covered by the source, but also several other characteristics such as peak brilliance and time structure (key features to implement “diffract-destroy” or “pump-probe” experimental schemes), photon polarization, and longitudinal and spatial coherence. Table III compares selected x-ray FEL facilities, available worldwide, in terms of the number of light flashes per second, also called the repetition rate, the minimum pulse duration, the minimum wavelength of the laser light, the maximum electron energy, the length of the facility, the number of experimental stations, and peak brilliance.

A broad class of dynamic phenomena, to be studied far from equilibrium, is accessible thanks to the unique combination of relevant FEL properties: wavelength tunability, multiple polarization, tunable femtosecond pulses, complete coherence, and enormous peak brightness. For a more complete description of the physics of x-ray free-electron

lasers, the reader is referred to recent specific reviews on this topic (Bostedt et al., 2016; Pellegrini, Marinelli, and Reiche, 2016). Primary application areas for FEL research include (i) ultrafast processes in condensed matter and chemistry under extreme conditions (Wernet et al., 2015), (ii) light conversions to other forms of energy (McNeil and Thompson, 2010), and (iii) damage-free coherent imaging and scattering experiments to follow the dynamics of nanostructures (Carnis et al., 2014). The first two fields are particularly relevant in chemistry (Di Cicco et al., 2011), biology and materials science (Edwards et al., 2005), and solid-state physics, especially dealing with materials for energy, femtosecond magnetism (Hellman et al., 2017), phase transitions in correlated material, and catalysis (Bencivenga et al., 2015; Popova-Gorelova and Santra, 2015). The third one is expected to produce groundbreaking contributions in structural biology and solution chemistry (Rajkovic et al., 2011). Regarding structural biology, more than 90% of existing protein structures have been determined by x-ray diffraction, and modern structural genomic and proteomic programs demand high-throughput crystallographic pipelines, although only about 5% of known sequences have been structurally determined. According to recent statistics from the Joint Center for Structural Genomics (http://www.jcsg.org), only 9.8% of expressed proteins generate crystals of sufficient size and quality for x-ray screening (Holton and Frankel, 2010). In this respect, the use of smaller crystals (~1 μm) with FEL x-ray sources has proven to be extremely effective (Batyuk et al., 2016).

In the last decade, we have assisted to an increasing number of x-ray coherence-based experiments, realized at dedicated SR beam lines, with holography (Eisebitt et al., 2004), ptychography (Dierolf et al., 2010; Sala et al., 2018; Pfeiffer, 2018), and coherent diffraction imaging (Nugent, 2010) to mention the most used techniques (see also Sec. III.B). These methods rely on the use of coherent x rays to explore matter independently of its crystallinity, following the pivotal idea, theoretically conceived by Sayre (1952), to perform crystallographic studies without a crystal. The intrinsic high brilliance and coherence and ultrashort pulse duration offered by FEL sources will allow, within the same experiment, to waive the stringent limitations of crystallography, and consequently to explore soft and hard matter, or a combination of organic and inorganic materials. Furthermore, the same properties will enable the realization of extremely small nanobeams, potentially exploitable to probe the ultrafast dynamics of a process at the nanoscale. This unique combination of spatial and temporal resolutions with the coherence of the beam will allow the exploration of matter under extreme conditions and characterization of structure and dynamics of novel materials, by inspecting their functional mechanisms at the atomic scale in real time.

II. FOCUSING X-RAY OPTICS

As already mentioned in Sec. I.A, the development of effective strategies for microfocusing and nanofocusing, even in the critical x-ray spectral range, is a key factor in the field of x-ray-based space-resolved characterization. Several routes have been explored and developed in the last two decades for x-ray microscopes and microprobe setups (Martinez-Criado et al., 2013; Suzuki and Terada, 2016; Tada and Ishiguro, 2017).

Nowadays, x-ray beams with spot sizes ranging from a few micrometers down to tens of nanometers are available using three categories of devices: refractive (Sec. II.B), reflective (Sec. II.C), and diffractive (Sec. II.D) optics. The classification is based on the physical phenomenon exploited for x-ray beam focalization (see Fig. 5). Currently, most of these optical elements are installed on SR beam lines and even on commercial laboratory instruments (Altamura et al., 2012; Sibillano et al., 2014). However, much effort is still put into their optimization in terms of beam size, efficiency, stability,

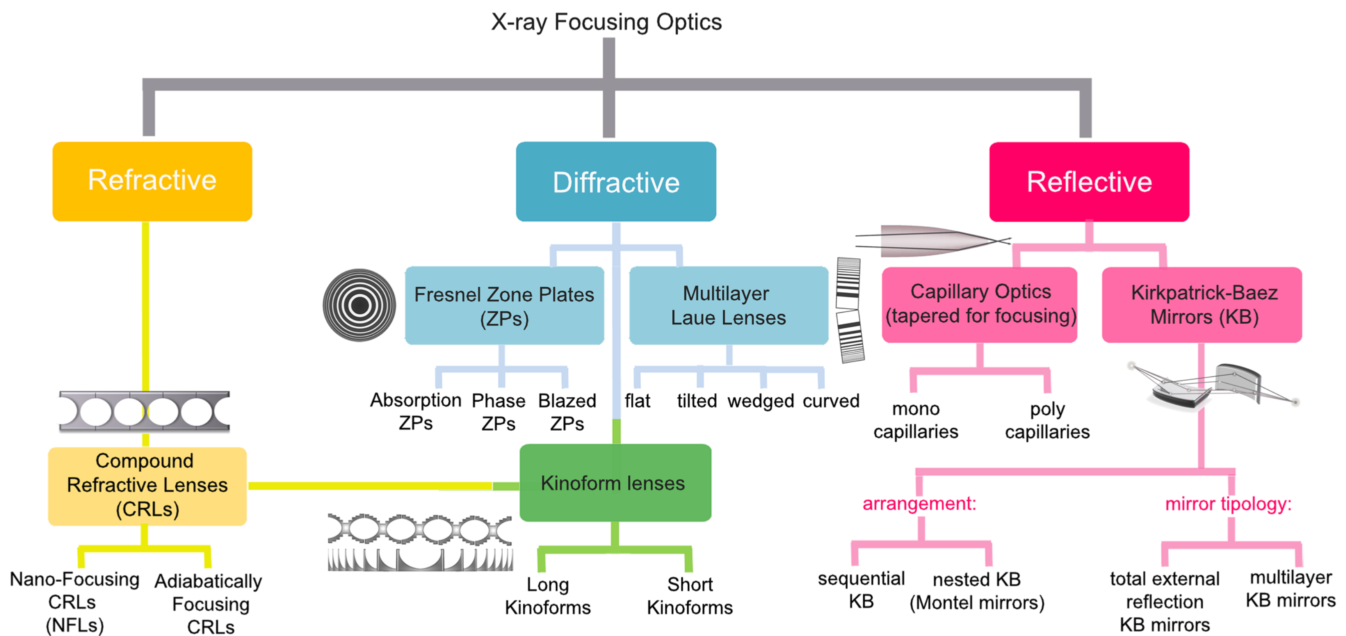

FIG. 5. X-ray focusing optics classification. The three principal categories (refractive, reflective, and diffractive optics) and the most common typologies for each category are indicated.

and manufacturing process. A close interplay between nanoengineering and fabrication capabilities, state-of-the-art metrology for the performance evaluation, and advanced theoretical modeling recently allowed breaking the 10 nm barrier. The race toward 1 nm resolution is now begun, with all the related groundbreaking scientific implications and opportunities. The possibility of hard-x-ray characterization at 1 nm resolution has been identified among the key objectives for a full exploitation of the onerous investment in major synchrotron facilities (Yan *et al.*, 2010).

In the following, Sec. II, after a brief overview about the basic optical principles, the most common and promising focusing optics are discussed, while the principal operation modes for x-ray microscopy and microbeam techniques are reported in Sec. III.G.

A. X-ray optics: General concepts

1. Basic resolution limits

We first describe some basic optical principles as well as parameters commonly employed to characterize and compare the different optics for x-ray focusing.

Let us consider the ideal case of optical demagnification using a thin lens (i.e., whose thickness can be neglected in comparison to its focal length), in the geometry shown in Fig. 6.

Using the parallel ray approximation, the object (or source S) and image (s) distances, indicated in Fig. 6(a) as p and q, respectively, and the lens focal length f are related by the Gaussian lens (or thin lens) equation:

$$\frac{1}{f} = \frac{1}{p} + \frac{1}{q}. \tag{3}$$

With an opening angle of θ [see Fig. 6(a)], the numerical aperture NA of the optical system can be expressed as

$$\mathrm{NA} = n \sin\theta = n \times \sin\left[\arctan\left(\frac{D}{2f}\right)\right], \tag{4}$$

where n is the index of refraction at wavelength λ of the medium interposed between the object and the image, and D is the geometrical aperture of the lens (Greivenkamp, 2004). Alternatively, considering the focus-to-infinity case ($S \to \infty$, and therefore $f = q$) represented in Fig. 6(b), the numerical aperture NA_∞ can be approximated using Eq. (5):

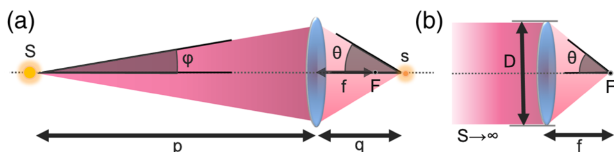

FIG. 6. (a) Schematic of the geometry for optical demagnification, described for a thin lens by the Gaussian lens formula (3). The object (or source S) and image (s) distances are indicated with p and q, respectively, while the lens focal length is f (F being the focal point). The lens opening angle is referred to as θ. (b) Definition of numerical aperture in the focus-to-infinity ($S \to \infty$) case. The geometrical aperture of the lens is indicated with D.

$$\mathrm{NA}_\infty = \lim_{S\to\infty} \mathrm{NA} = n\frac{D}{2f}. \tag{5}$$

Several factors restrict the resolution of real x-ray optics: the principal ones are hereinafter listed and briefly commented on.

a. Diffraction limit

The transverse resolution s_{DL} of any x-ray optical element is limited by diffraction and can be estimated by the Rayleigh criterion (Als-Nielsen and McMorrow, 2001), see Eq. (1), or alternatively by the Abbe resolution (Ditchburn, 1991):

$$s_{\mathrm{DL}} = \frac{\lambda}{2\mathrm{NA}}, \tag{6}$$

where λ is the wavelength and NA is the numerical aperture of the lens. The γ factor of Eq. (1) is equal to 0.5 for a linear (or rectangular) lens and to 0.61 in the case of 2D focusing by a round lens.

Although, in principle, spatial resolutions in the nanometer scales could be reached using hard x rays, the major restriction in x-ray optics remains the low achievable NA, due to the weak interaction of hard x rays with matter. This becomes evident from the definition of n as a complex number (Bordiga *et al.*, 2013):

$$n = 1 - \delta + i\beta, \tag{7}$$

where δ and β are real numbers that account for the dispersion and the absorption, respectively. In the hard-x-ray energy range, δ is a positive value on the order of 10^{-5} in solid materials and 10^{-8} in air. The imaginary part β can generally be neglected in comparison to δ, $\beta \ll \delta$. As a consequence, assuming $n \approx 1$ in Eq. (4), $\mathrm{NA} \approx \theta$ is obtained. Numerically, assuming a working wavelength of 1 Å, $\mathrm{NA} \approx 0.06$ is necessary to reach a diffraction-limited resolution $s_{\mathrm{DL}} = 1$ nm. A major effort in the development of fabrication strategies has been undertaken in the last decade to increase the achievable NA for x-ray nanofocusing optics. For example, recently a new manufacturing technique allows the fabrication of high-NA multilayer Laue lenses with focal spot sizes below 10 nm (Bajt *et al.*, 2018). Actually, a high resolution tip-tilt positioning system was developed last year for the next generation of multilayer Laue lens- (MLL)-based x-ray microscope (Xu *et al.*, 2017).

b. Geometrical source demagnification

In addition to the diffraction limit, the focusing optics is restricted by geometrical source demagnification s_G, defined according to Eq. (8):

$$s_G = \frac{Sq}{p}, \tag{8}$$

where S is the size of the source, q is the distance from the focusing element to the focal spot, and p is the distance from the source to the focusing element (the same notation as introduced in Fig. 6). Equation (8) highlights how increasing the source distance p from the focusing element a smaller focal size (lower s_G) can be obtained. Consequently, the development of extra-long beam lines allows higher source-size

demagnifications [e.g., the 1 km long beam line of Spring-8 (Yumoto *et al.*, 2005)].

c. Imperfection effects on resolution

Real optics are also limited by imperfections such as aberrations, mirror shape errors, roughness or nonuniformities, and further experimental instabilities such as vibrations and drifts (Tucoulou *et al.*, 2008; Honnicke *et al.*, 2011). For simplicity, all these effects can be included in a global resolution limit, namely, s_I.

In conclusion, several factors contribute to limiting the final point spread function s: the diffraction limit (s_{DL}), the geometrical source demagnification limit (s_G), and the imperfection-related limit (s_I). The resulting FWHM resolution can be approximated as a convolution of all these terms:

$$s \approx \sqrt{s_G^2 + s_{\mathrm{DL}}^2 + s_I^2}. \quad (9)$$

d. Efficiency and depth of field

Most of the real focusing devices do not transmit the entire incident photon flux into the focal spot. The transmission efficiency ε is defined as the intensity ratio between the beam transmitted by the focusing optic (I_t) and the incident beam (I_0):

$$\epsilon = \frac{I_t}{I_0}. \quad (10)$$

Reflective systems ($0.5 < \varepsilon < 0.9$) are more efficient than refractive and diffractive ones ($0.1 < \varepsilon < 0.4$). For refractive systems, this is due to absorption, while for the diffractive ones it is due to the scattering of I_0 into other diffraction orders (both positive and negative), which do not contribute to the first-order focus by the order-sorting aperture.

While the terminology efficiency is often used for Fresnel zone plates and mirror optics, the term transmission is commonly employed for refractive optics, although both cases describe the loss of photon flux. Another usual parameter is the gain, which describes the increase in intensity in the focal spot of the optical element compared to a pinhole with equivalent size.

The longitudinal resolution, also named depth of field (DoF), defines the distance along the optical axis in which all objects are sharply imaged on the image plane and it can be expressed according to Eq. (11):

$$\mathrm{DoF} \sim \frac{\lambda}{\mathrm{NA}^2}, \quad (11)$$

where λ is the wavelength and NA is the numerical aperture of the lens. The DoF value sets practical constraints on the sample thickness.

2. Factors influencing the beam line design

Besides the specific features of each operation method, and relative strengths and weaknesses discussed in Sec. III.G, the achievable spatial resolution with both full-field and scanning-probe setups is influenced by several factors. Once the operation mode has been selected, the practically achievable x-ray-beam features (and therefore the achievable spatial resolution) primarily depend not only on the electron and x-ray-beam properties (size and emittance), but also on the x-ray wavelength and the type and quality of the optical elements employed.

With regard to the energy dependence of the focusing performance, in the hard-x-ray range longer focal lengths (up to more than 1 m) and larger DoF values (up to a few mm) are achievable, in comparison to soft-x-ray microscopes and microprobes. This is an asset for *in situ* experiments using furnaces or high-pressure cells. In addition, the use of a shorter wavelength is favorable for x-ray diffraction and scattering studies which combine the investigation of both wide- and small-angle scattering signals.

The beam size (degree of coherence) can be reduced (increased) by scaling down the source size or by increasing the demagnification ratio. The latter strategy can be realized by either reducing the focal distance or setting up the microscope at a larger distance from the source.

The focal distance variation is peculiarly advantageous under operation with refractive lenses (see Sec. II.B), where both the NA and the demagnification ratio can be simultaneously increased, thus reducing the diffraction-limited spot size and increasing the intensity gain in the focus.

Optimization of the working distance and, consequently, of the resulting beam line length is an alternative strategy for the reduction of achievable spot size. Several third- and fourth-generation (DLSRs) synchrotron facilities are nowadays developing long beam lines (typical lengths in the 100–1000 m range) based on small horizontal secondary sources (~25 μm slit). Since typical synchrotron sources present an elliptical shape with a large aspect ratio, such a configuration produces a nearly circular focus. Such a scheme allows not only to fully exploit the source size in both vertical and horizontal directions (Mimura *et al.*, 2007; Somogyi, Polack, and Moreno, 2010; Chen *et al.*, 2014; de Jonge, Ryan, and Jacobsen, 2014; Martinez-Criado *et al.*, 2016), but also to keep working distances sufficiently large to accommodate *in situ* experiments.

Although a smaller beam size in principle can also be obtained with more complex optical arrangements on a shorter beam line, several practical factors discourage such an approach. Minimizing whenever possible the number of x-ray optical components directly implies an improvement in the beam stability. Several undesired effects are strongly attenuated by reducing the optical components, e.g., mirror slope errors, absorption in refractive elements, thermal drifts, vibrations, etc. (Tucoulou *et al.*, 2008). However, recently, the possibility of introducing an appropriate x-ray phase plate into the optical path to correct residual aberrations of a refractive x-ray lens was successfully tested (Seiboth *et al.*, 2017). This method could be applied generally to solve the x-ray focusing problem originated from surface errors of reflective optics, zone deformations in diffractive optics, and accumulated surface errors in larger refractive lens stacks.

Another relevant issue to be carefully considered is the possible radiation damage (see Sec. III.I), which is critical, for example, in the case of specific sensitive specimens (e.g., biological samples). The use of dedicated sample cryosystems (e.g., liquid nitrogen cryocoolers) (Chen *et al.*, 2014; Deng *et al.*, 2015) and/or the selection of particular focusing devices (Falcone *et al.*, 2011) have to be considered in these cases.

In conclusion, besides the "minimum spot size–maximum flux" criterion, the selection of a specific instrumental design is substantially influenced also by components availability, simplicity of use and flexibility, and global cost of the apparatus.

B. Refractive optics

Two main differences exist between x rays and visible light concerning refraction effects. First, for x rays, the deviation from a unit in the index of refraction, indicated as δ in Eq. (7), is on the order of 10^{-5}, and therefore negligible in comparison to the values assumed for visible light in glass ($n \sim 1.5$, $\delta \sim 0.5$). As a consequence, the focal length of a single x-ray lens, assuming a typical radius of curvature of 2 mm, is about 100 m, which is clearly too long for most practical applications. However, stacking several single lenses one behind another and forming what is generally referred to as a compound refractive lens (CRL), a shorter focal length of manageable size can be obtained (Snigirev *et al.*, 1996).

The second principal effect specifically derives from the negative values of the refractive index in the x-ray spectral range, i.e., $\delta > 0 \rightarrow n < 1$. As a consequence, the lenses for x-ray focusing have to be manufactured in a biconcave shape (Snigirev *et al.*, 1996, 1998), instead of the biconvex profile generally adopted in optical focusing lenses.

In the Supplemental Material (729) more details about the operation principles and the main characteristics of refractive focusing devices are reported in Sec. S-I. Moreover, the advanced strategies explored to achieve submicrometric resolution (e.g., nanofocusing refractive x-ray lenses, adiabatically focusing compound refractive lenses, and refractive lamellar lens) are also briefly discussed.

C. Reflective optics

Mirrors operating in normal-incidence geometry (usually adopted for visible light) are totally ineffective for x rays, due to the extremely low reflectivity and a grazing-incidence configuration must be applied. Total external reflection takes place according to Snell's law below a critical incidence angle $\theta_c = \delta^{1/2}$ (Bordiga *et al.*, 2013), where δ is the deviation from unity of the real part of the refraction index; see Eq. (7). Under such conditions (typical glancing angles of milliradiants), the whole incident wave is reflected, making wide-band-pass high reflectivity possible for x rays. Some penetration in the reflective medium still persists at its boundary, even if no energy flows across the interface. The incident beam propagates in the reflecting medium in the form of an evanescent wave, which slightly reduces the reflectivity, characterized by an exponential damping in amplitude that causes its extinction typically within the first nanometers of the mirror surface.

Reflective x-ray focusing optics represent an attractive achromatic alternative to refraction-based strategies previously discussed. The most common reflective devices in different geometries and approaches are extensively used worldwide in dedicated beam lines, especially for wide-band-pass applications. A more detailed description of capillary optics, Kirkpatrick-Baez mirrors (Kirkpatrick and Baez, 1948), total external reflection Kirkpatrick-Baez mirrors, multilayer Kirkpatrick-Baez mirrors, and nested Kirkpatrick-Baez mirrors is reported in Sec. S-II of the Supplemental Material (729).

D. Diffractive optics

X rays, as for every form of electromagnetic waves, are diffracted by gratings when the grating spacing is on the order of their wavelength. Typical lattice spacing in crystals (in the Å range) nicely fulfills this condition. Crystals can be therefore imaged as diffraction gratings with the atoms acting as slits or nodes. As repeatedly mentioned before, the related XRD methods are among the most powerful and widespread structural x-ray analytical tools.

Recent advances in nanofabrication capabilities, electron-beam lithography, and thin-film deposition allowed the fabrication of artificial gratings with typical spacing sufficiently reduced (although at least 1 order of magnitude higher than in crystals) to change the direction of an x-ray beam, thus suitable for application in x-ray optics.

In Sec. S-III of the Supplemental Material (729) a brief description of the most common diffractive optics is provided, pointing out their relative advantages and disadvantages when employed as x-ray-focusing devices, as well as the state-of-the-art achievements in terms of resolution and efficiency. Fresnel zone plates (Baez, 1961), multilayer Laue lenses, and the hybrid refractive-diffractive kinoform lenses are concisely outlined. A more extensive discussion of the matter can be found in Sec. S-III of the Supplemental Material (729) and elsewhere in specialized literature; see Erko, Aristov, and Vidal (1996).

E. Comparative summary and outlook

As discussed in the previous sections, a broad variety of x-ray optics and new combinatorial strategies have been developed in the last two decades for focusing x rays into microbeams or nanobeams. The selection of the approach and design for use depends on several specific factors, e.g., the kind of characterization method and information researched, experimental arrangement (bandwidth, photon energy, efficiency, coherence properties), sample nature and environment, and source features. It is practically impossible to indicate the best solution for x-ray focusing: each approach is generally designed to optimize a limited subset of performance-determining parameters (e.g., minimum spatial resolution, maximum efficiency, quick and easy alignment, reduced data acquisition time, or a well-established fabrication procedure, which commonly implies a lower cost).

Nevertheless, to provide the reader with a conclusive comparative overview on such a number of x-ray optics, the characteristics of the main focusing devices are summarized in Table IV. For the three macrocategories of refractive, reflective, and diffractive optics, the state-of-the-art values of the key parameters for application to advanced space-resolved characterization are reported.

The most evident and natural indicator of the performance of x-ray optics, even for a nonexpert audience, remains the achieved (and theoretically achievable) spot size. For this reason, Fig. 7 represents a general time evolution of the minimum hard-x-ray spot size during the last two decades, distinguishing among refractive, reflective, and diffractive optics.

Without claiming to generalize, considering Table IV and Fig. 7, it is possible to point out some key advantages related to

TABLE IV. Summary of the characteristics for the principal x-ray-focusing optics (refractive, reflective, and diffractive optics). For some parameters (numerical aperture NA, spectral bandwidth $\Delta E/E$, efficiency) only indicative information or typical variation ranges are reported, due to their high sensitivity to specific working conditions. Otherwise, when possible (i.e., in the case of working energy range E, the best resolution achieved, the ultimate theoretical resolution limit), specific values are reported, and the related literature source is quoted.

Parameter	Refractive x-ray optics	Reflective x-ray optics	Diffractive x-ray optics
NA	Limited (A_{eff})	Limited (θ_c)	High (limited by manufacture)
E	<1 MeV (Snigirev and Snigireva, 2008)	<80 keV (Suzuki, Takeuchi, and Terada, 2007)	<25 keV (Morgan et al., 2015)
$\Delta E/E$	10^{-3}	10^{-2} (multilayers), white beam (mirrors)	10^{-3}
Best resolution achieved	50 nm ($E = 21$ keV) (Schroer et al., 2005)	7 nm (20 keV) (Mimura et al., 2010; Yamauchi et al., 2011)	8 nm ($E = 22$ keV) (Morgan et al., 2015)
Ultimate resolution limit	~2 nm (Schroer and Lengeler, 2005)	~5 nm (Yamauchi et al., 2011)	~1 nm (Yan et al., 2007)
Efficiency	20%–30%	70%–90%	20%–30%
Chromaticity	$f \approx 1/\lambda^2$	Achromatic	$f \approx 1/\lambda$
Geometry	On axis	Grazing incidence, Bragg condition	On axis

each category of x-ray-focusing optics. The refractive optics are particularly suited for hard-x-ray microscopy due to their compactness and robustness (mechanical and thermal). Furthermore, their on-axis arrangement provides easier alignment and operation avoiding any change in the beam direction (Snigirev and Snigireva, 2008), while the focal length can be easily tuned by adding or removing individual optical elements in compound systems. Moreover, CRLs are around 10^3 times less affected by surface roughness with respect to mirror optics.

To date, spatial resolutions down to 50 nm have been reached (Schroer et al., 2005) and, notwithstanding a time-dependent spot-size reduction less pronounced than in the reflective and diffractive optics case, sub-10-nm hard-x-ray beam sizes are expected to be achieved using adiabatically focusing lenses.

The more striking advantage of the grazing incidence devices, such as capillaries and total external reflection Kirkpatrick-Baez mirrors, with comparison to both refractive and diffractive optics, is their intrinsic achromaticity. These devices can operate over a wide energy range maintaining a stable spot position and size, which is a crucial advantage for spectroscopic and wide-band-pass analytical methods. Currently an *in situ* wavefront-correction approach allowed one to overstep the bottleneck related to imperfections in mirror figuring, producing an x-ray beam focused down to 7 nm at 20 keV (Mimura et al., 2010).

Very small spot sizes have also been demonstrated with diffractive optics. The most common are zone plates (ZPs)

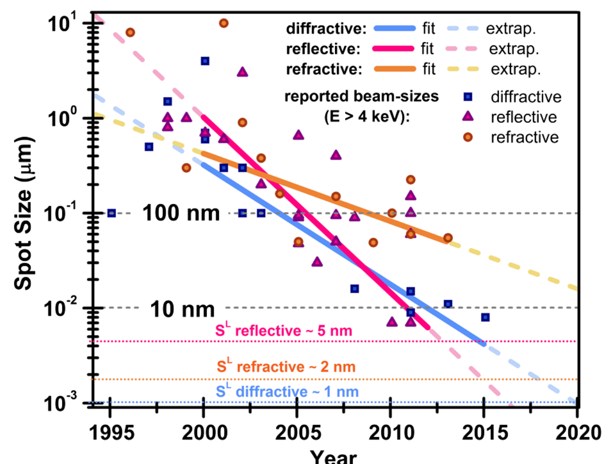

FIG. 7. Time evolution of the minimum hard-x-ray ($E > 4$ keV) spot size during the last two decades and extrapolation for the near future, distinguishing among refractive (orange circles and line), reflective (magenta triangles and line), and diffractive (blue squares and line) optics. Data were sorted from the values published in a suitable series of reports, while the trend lines are obtained upon monoexponential fits (notice the logarithmic scale for the ordinate axis). The dashed parts of the trend lines indicate the extrapolations for the very next future. The ultimate resolution limits (S^L) for the three categories are also indicated as dotted horizontal lines.

which are in-line devices, therefore very compact and relatively easy to use. The best performances are usually achieved in the soft-x-ray energy range. The hard-x-ray regimen demands challenging ultrahigh aspect ratios. Recently, using a zone-doubling approach aspect ratios larger than 20 have also been demonstrated. MLL structures have recently demonstrated a 12×24 nm^2 focusing at 12 keV (Nazaretski et al., 2016) and even a 8 nm focus has been reached using wedged MLLs (Morgan et al., 2015). It is also worth noticing that in the case of diffractive optics the lower resolution limit [~1 nm (Yan et al., 2007)] has been determined, with respect to reflective and refractive approaches.

For the extremely bright x-ray free-electron lasers, nanofocusing devices are also needed, but they must withstand the intense x-ray pulses without getting damaged. So far diamond Fresnel ZPs (David et al., 2011), beryllium refractive lenses (Schropp et al., 2013a), and reflective mirrors (Yamauchi et al., 2015) have been successfully employed.

III. SPACE-RESOLVED X-RAY ANALYTICAL TECHNIQUES

A. Principal x-ray-matter interactions and related characterization methods

The radiation-matter interaction in the x-ray range is extremely rich and has been extensively employed for material characterization (Lifshin, 2008; Willmott, 2011). An exhaustive discussion of the physics beneath these interactions is beyond the scope of this review; however, a brief analysis of key phenomena is included to show the potentialities for current developments in x-ray-based space-resolved characterization.

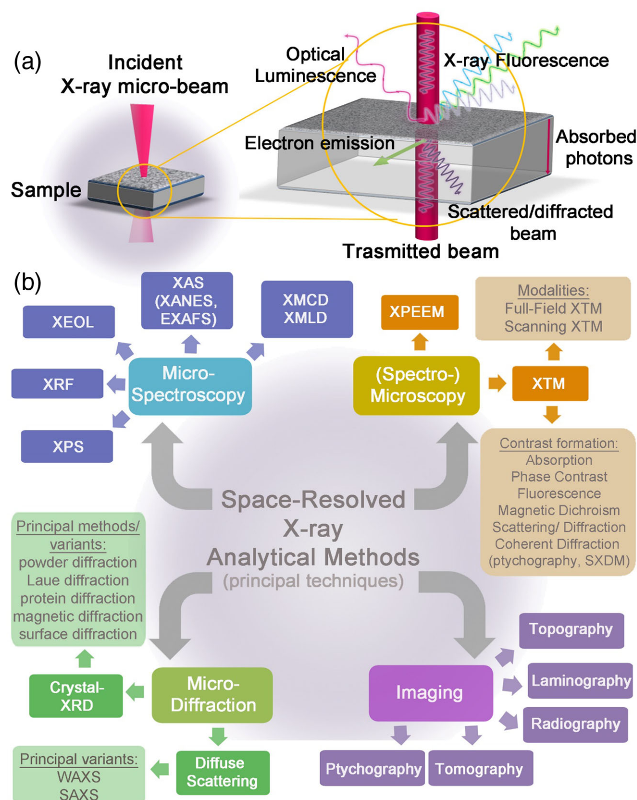

FIG. 8. (a) Schematic representation of the principal x rays and matter interactions. (b) Classification of most popular x-ray-based space-resolved analytical tools with micrometric and submicrometric resolution; four main categories are represented: microspectroscopy, microdiffraction, (spectro)microscopy, and imaging. For graphical reasons only the "micro-" prefix is reported although nowadays the majority of these analytical techniques can provide information at the submicrometric scale. The most common variants, methods, and operation modalities per each category are reported as well.

A schematic representation of the principal x-ray interactions with matter is reported in Fig. 8(a). The incident beam is primary absorbed [according to the Lambert-Beer law (Lambert, 1760; Beer, 1852)] or scattered by the sample. The radiation not absorbed nor scattered is transmitted through the sample. At typical x-ray energies, the absorption of a photon generally promotes the expulsion of a core electron (photoelectric effect). The resulting core hole can be filled by electrons from outer shells, whose excess energy is released either by the emission of characteristic x-ray fluorescence (XRF) or by the ejection of Auger electrons. In general, XRF decay is dominant for high-atomic number (Z) elements, while the probability of the Auger effect increases with a decrease in the difference of the corresponding energy states, and it is the highest for the low-Z atoms (Henke, Gullikson, and Davis, 1993).

More complex secondary deexcitation channels are also possible in specific materials after x-ray-induced photoionization, yielding to x-ray-beam-induced luminescence and current phenomena (Bianconi, Jackson, and Monahan, 1978; Goulon *et al.*, 1983; Emura *et al.*, 1993; Vyvenko *et al.*, 2002).

The classification of x-ray-based characterization techniques, with an emphasis on space-resolved analytical tools with micrometric and submicrometric resolution, is not an easy task. The richness and diversity of x-ray probe-matter interactions directly reflect in a variety of methods, and, correspondingly, of definitions (and related acronyms). Here the following classification in four main categories is proposed, as highlighted in Fig. 8(b):

- microspectroscopy methods,
- microdiffraction methods,
- microscopy and spectromicroscopy methods, and
- imaging methods.

Microspectroscopy and microdiffraction methods represent the space-resolved extension down to the microscale and nanoscale of standard spectroscopic or diffraction-based techniques. Most x-ray-based characterization techniques are in fact performed in a nonlocal, global-averaging fashion and the resulting information is obtained via spatial averaging over macroscopic length scales (Stangl *et al.*, 2009). However, using x-ray microbeams, inhomogeneous, or micrometric-sized samples as well as specific regions of interest (ROI) within a complex matrix can be investigated selectively.

The main microspectroscopy techniques relying on x-ray absorption are micro- and nano-XAS [XANES, and recently also extended x-ray absorption fine structure (EXAFS)] and polarization dependent methods, e.g., micro- and nano-XML (C)D [x-ray magnetic linear (circular) dichroism]. Other widespread microspectroscopic tools are micro-XRF, micro-XEOL (x-ray-excited optical luminescence) and micro-XPS (x-ray photoelectron spectroscopy), based on x-ray fluorescence, optical luminescence, and electron photoemission, respectively. In recent years, even the integration of very advanced spectroscopic approaches such as RIXS (resonant inelastic x-ray scattering) in synchrotron microprobe and nanoprobe setups is starting to be considered (Cotte *et al.*, 2011).

The general definition of microdiffraction and nanodiffraction is commonly used to indicate both microcrystallographic methods and microdiffuse scattering techniques, where the x-ray elastic scattering from low-ordered nanocrystals or disordered noncrystalline systems is investigated (WAXS and SAXS).

The available information strictly depends on specific analytic methods (Sec. III). A comparative summary of peculiar information achievable using different microspectroscopy and microdiffraction methods is provided in Sec. III.H, where the potentialities of a multitechnique approach are presented.

The distinction between microspectroscopy and diffraction and x-ray microscopy and spectromicroscopy is quite fine. What primarily identifies the microscopy methods is their ability to provide a highly magnified image of the investigated sample, in semantic analogy to visible-light microscopy. Consequently, the experimental arrangement and data acquisition and reduction routines related to an x-ray microscope (XRM) are optimized to achieve the best imaging performances. The term "spectromicroscopy" is typically used to describe microscopic imaging techniques in which the image contrast is given by spectroscopic features. The acquired images are then related to a specific energy of the spectroscopic probe. Otherwise, referring to "microspectroscopy" the emphasis is on the spectroscopic datum, obtained from a micrometric or submicrometric portion of the sample.

Summarizing, spectromicroscopy yields data as a function of the spatial coordinates in correspondence to a fixed probe energy coordinate (i.e., an "image"), whereas microspectroscopy

investigation outputs a function of the probe energy for fixed values of the spatial coordinates. The natural extension of both spectromicroscopy and microspectroscopy approaches would be to get the full spectroscopic and spatial information in the same measurement, thus obtaining data as a function of the energy and spatial coordinates simultaneously. In that limit, the distinction between the two analytical approaches is overcome. This combinatorial scheme is emerging in principal synchrotron facilities, and the definitions of x-ray microscope and x-ray microprobe for microspectroscopy and diffraction are often used as synonyms.

Analogous considerations can be done for microdiffraction methods and XRD-based microscopy techniques. In the first case, the setup is primarily designed to record the diffracted intensity as a function of the transferred wave vector (thus obtaining space-resolved diffractograms), while in the second one x-ray elastic scattering processes are exploited as a contrast mechanism in the micrograph formation, typically involving a Fourier transform operation to move from the reciprocal space to the direct space.

Owing to the advances in x-ray sources and optics performance, several typologies of XRMs have been established in recent years. Basic operation modalities of transmission XRM include full-field mode and scanning mode (see Sec. III.G), using different contrast mechanisms (e.g., absorption, phase contrast, magnetic dichroism, and diffraction). In addition, high-sensitivity elemental mapping can be obtained by detecting XRF signals (Falcone et al., 2011). Recently, lensless approaches have also been explored in coherent diffraction microscopy (Chapman and Nugent, 2010).

Under ultrahigh vacuum conditions, the photoelectrons emitted upon x-ray absorption can be detected, obtaining few-nm resolution images with a series of magnetic or electrostatic electron lenses [x-ray photoemission electron microscope (XPEEM) (Leung, Brash, and Hitchcock, 2010; Falcone et al., 2011; Cheng and Keavney, 2012)]. Other XRM schemes have been developed for specific applications, e.g., x-ray-beam-induced current (XBIC) microscopy provides unique insight into the electrical activity of impurities and defects in semiconductors (Trushin et al., 2010), and XEOL-based microscopy can be employed in luminescent systems (Larcheri et al., 2009; Martinez-Criado et al., 2012a).

The last category here proposed for x-ray-based space-resolved characterization techniques includes the imaging methods. Again, the boundaries for this group are roughly defined and substantially overlapped with other types. Here the definition "imaging" includes the techniques generally devoted to projective image formation. A popular example of a 2D imaging technique is radiography, routinely used for security scans and massively employed for medical inspection since x-ray discovery. Advanced alternatives, such as fluoroscopy or angiography, are nowadays employed as powerful medical diagnostic tools.

The change from a parallel beam to a nanofocused beam illumination allows for adjustable geometric magnification. Thus, projection micrographs and tomograms can be recorded with quantitative density contrast and pixel size down to 50 nm (Villanova et al., 2017).

Several approaches, which found widespread application across many research fields, are propagation-based imaging or inline holography in combination with computed tomography (holotomography) (Cloetens et al., 1999; Bleuet et al., 2010; Jiang et al., 2010; Sakdinawat and Attwood, 2010; Stockmar et al., 2015; Robisch et al., 2016) and confocal or x-ray-triangulation methods (Larson et al., 2002; Poulsen, 2004). Other methods have been explored for application in particular research areas, which in general highly benefited from the use of SR. Synchrotron-based laminography (Helfen et al., 2005), for instance, provides high-resolution nondestructive 3D imaging of ROIs in flat but laterally extended objects and devices [sensors, flip-chip devices, and other microelectronic systems (Helfen et al., 2006)]. Another example is x-ray topography, a nondestructive diffraction-based technique mainly employed for imaging defects and microstructure of crystals, with spatial resolution in the micrometer to centimeter range (Tanner and Bowen, 1980; Weissman, Balibar, and Petroff, 1984).

B. X-ray scattering: XRD, SAXS, and WAXS

Elastic x-ray scattering is an extremely powerful method to explore materials across several length scales. This is pretty intuitive in crystals, where it relies on the famous Bragg formula (Bragg and Bragg, 1913)

$$\lambda = 2d \sin\theta \tag{12}$$

which relates the incident photon wavelength λ, the sample interplanar distances d, or relevant scales to probe, to the scattering angle θ, where diffraction occurs in the reciprocal space.

Let us introduce the scattering vector or wave-vector transfer $\boldsymbol{q}$ as the difference between incident ($\boldsymbol{k}_i$) and scattered ($\boldsymbol{k}_s$) wave vectors: $\boldsymbol{q} = \boldsymbol{k}_s - \boldsymbol{k}_i$. Since the scattering process is elastic, its modulus q depends on the wavelength λ and the scattering angle θ or, alternatively, on the size d of the scattering object (length scale):

$$q = |\boldsymbol{q}| = 2k \sin\theta = \frac{4\pi}{\lambda}\sin\theta = \frac{2\pi}{d}. \tag{13}$$

Table V provides the typical q values, in Å^{-1}, corresponding to scattering objects of different length scales in the mesometric (1000–100 nm), nanometric (10 nm), and atomic (1–0.1 nm) regimes. Large length scales, such as nanometric or mesometric distances, have to be monitored at small or ultrasmall q; small interplanar distances, atomically small, have to be measured at large q, eventually using very short λ. These regimes are identified in the literature as ultrasmall- (uSAXD or uSAXS), small- (SAXD or SAXS), and wide- (WAXD or WAXS) angle x-ray diffraction or scattering, respectively.

TABLE V. Experimental techniques used to probe scattering objects of different sizes (d) and related scattering vectors, reported in Å^{-1}.

Technique	d (nm)	q (Å^{-1})
uSAXS or uSAXD	1000	0.000 63
SAXS or SAXD	100	0.006 3
SAXS or SAXD	10	0.063
WAXS or WAXD	1	0.63
WAXS or WAXD	0.1	6.3

When the lattice extension of a crystal is locally lost or reduced, as in the case of polymers or nanocrystals, which can be partly crystalline and partly amorphous, or for those materials which have a structure that locally deviates from the perfect crystal structure, it is worth discussing SAXS (Glatter, 1979; Portale and Longo, 2013) and WAXS (Bras *et al.*, 2003; Cammarata *et al.*, 2008; Giannini *et al.*, 2013; Graewert and Svergun, 2013). The total scattering here includes diffuse scattering, which derives from the disordered portion of the sample, and adds to the Bragg diffraction. A pure Bragg diffraction pattern encodes information on the crystalline part of the sample only and is related to the squared discrete structure factor of the crystal; a total scattered pattern contains information on crystalline and amorphous or disordered sample components and is computed by the squared continuous structure factor. Typically, when total scattering techniques are used, the scattered intensity, measured in the reciprocal space, can be transformed into a pair distribution function (PDF) (Bozin, Juhás, and Billinge, 2013; Lamberti *et al.*, 2016), which contains all the interatomic distances, i.e., direct space information. Therefore, the PDF will allow one to measure nanometric or mesometric interatomic distances and morphology, if extracted from SAXD or SAXS data, or atomic distances or length scales if extracted from WAXD or WAXS data. The combination of SAXS and WAXS techniques is ideal to explore materials with hierarchical order such as, for example, polymer-based fibers (Diaferia *et al.*, 2016), nanostructured carbons (Fang *et al.*, 2013), and catalysts with hierarchical pore structure (Yu, Su, and Cheng, 2007; Fan *et al.*, 2008; Serrano, Escola, and Pizarro, 2013).

Figure 9 shows a disordered assembly of nanospheres, with size a, illuminated by an x-ray beam of spatial coherence ξ. For an x-ray source of transverse dimension D, located at a distance R from the sample, the coherence length is computed as (Born and Wolf, 1999)

$$\xi = R\lambda/D. \tag{14}$$

If the spatial coherence length of the x-ray beam is smaller than the size assembly ($\xi \ll a$), as in Fig. 9(a), the objects are incoherently illuminated and the scattering 2D pattern and its related 1D profile contain few peaks depending on the size and shape of the objects. When the spatial coherence length of the x-ray beam is equal to the size assembly ($\xi \sim a$), as in Fig. 9(b), i.e., for a coherently illuminated assembly, the 2D pattern and related 1D profile are speckled. The speckles in the diffraction pattern, whose dimension depends on λ and a, encode information on the actual position of the scattering objects. In this case, the information which is extracted from the diffraction pattern is not purely morphological (size and shape of the objects); from the speckles the "structure" of the disordered assembly can be determined (Giannini *et al.*, 2016). The seminal idea of diffraction with coherent x rays was due to Sayre (1952), who proposed to use crystallographic methods in the absence of crystals. The real implementation took almost 50 years (Miao *et al.*, 1999) as required by the synergic combination of coherent SR x-ray beams, proper optics for microprobes and nanoprobes, microscopy, and crystallography. Coherent diffractive imaging (CDI), as it was called, is a lensless technique which, at least in principle, could allow the observation of matter down to atomic

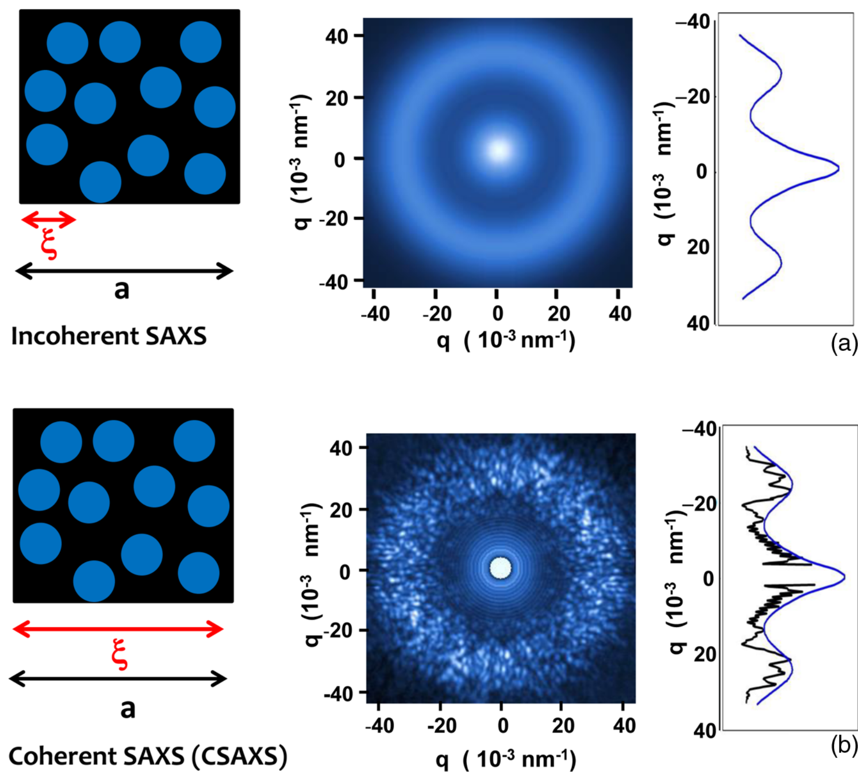

FIG. 9. (a) Incoherently illuminated assembly of nano-objects, relative 2D and 1D scattering patterns. (b) Coherently illuminated assembly of nano-objects, relative 2D and 1D scattering patterns.

resolution without limitation on the sample thickness and the crystallinity state. Differently from crystallography, the need for the periodicity of the crystal lattice, i.e., the coherence of the structure, is replaced by the coherence of the x-ray beam. *A posteriori* diffraction data have to be phase retrieved by proper mathematical algorithms to extract the sample structural information. Algorithms (Miao, Sayre, and Chapman, 1998; Rodenburg, Hurst, and Cullis, 2007; Fienup, 2013) behave as "virtual lenses," not affected by aberrations, and therefore allowing for a diffraction-limited resolution. In this context, ptychography (Dierolf *et al.*, 2010; Sala *et al.*, 2017, 2018; Pfeiffer, 2018) is a coherent imaging technique in which the sample is illuminated by a coherent beam and scanned at positions with some degree of mutual overlap. For each scanning point a far-field diffraction pattern is recorded by a pixel-array detector. The overlapped illumination allows a robust reconstruction thanks to the additional constraints that are provided to the phase retrieval problem. In this regard, the method is interesting for x-ray phase-contrast imaging and metrology applications based on the sample induced modulation and subsequent computational demodulation of a random or periodic reference interference pattern (Zdora *et al.*, 2017).

C. X-ray absorption spectroscopy: XANES and EXAFS

X-ray absorption spectroscopy is a powerful tool to study the local geometric and electronic structure of matter. XAS allows one to fully explore the local chemistry of both crystalline and amorphous materials in terms of oxidation states, coordination numbers, and interatomic distances, and it is particularly interesting owing to its chemical selectivity (Boscherini, 2013; Mino, Agostini *et al.*, 2013).

The technique is based on the acquisition and analysis of the x-ray absorption coefficient $\mu(E)$ as a function of the incident photon energy E in the region around the absorption edge of an element present in the sample. The region including a few tens of eV before and after the edge is usually called x-ray absorption near-edge structure (XANES) for hard x rays or near-edge x-ray absorption fine structure (NEXAFS) for soft x rays. It mainly reflects the unoccupied atomic levels of the absorbing species and can be divided into preedge, edge, and postedge parts. This spectral region is very sensitive not only to the interatomic distances, but also to symmetry of the coordinated atoms, distribution of charges, and potential around the absorbing atom (Mino, Agostini *et al.*, 2013).

A few tens of eV after the edge the EXAFS region starts and can be extended up to more than 1 keV. The spectrum in this energy range is a picture of how the photoelectron extracted from the absorbing atom probes the surrounding atomic environment. The EXAFS signal results in a series of oscillations, which have a relatively low intensity with respect to the edge jump. The EXAFS analysis provides information about the interatomic distances, the coordination numbers, and the Debye-Waller factors, which are related to thermal and static disorder (Borfecchia *et al.*, 2013; Mino, Agostini *et al.*, 2013; Mino, Gianolio *et al.*, 2013).

In a XAS experiment the ideal specimens are uniform thin foils or well-ground powders; however, the preparation of uniform samples is sometimes difficult. In recent years spatially resolved XAS has also emerged as an indispensable method to study nanostructured materials and individual nano-objects.

A full-field approach in transmission (Sec. III.G.1) can be used only for samples with appropriate thickness. On the contrary, scanning micro-XAS or nano-XAS (Sec. III.G.2) can be applied to wide varieties of specimens and can also exploit the fluorescence and electron-yield detection modes. The former method is very useful for its high sensitivity in trace element analysis, while the latter can provide surface-sensitive information.

For micro-XAS or nano-XAS acquisitions, a high stability in terms of sample and beam position is crucial. Commonly, there are two kinds of instability sources: high frequency instability (vibrations) and low frequency instability (drifts). The vibrations from the sample mounting result in deterioration of the spatial resolution, making a rigid support mandatory. On the other hand, the drift of the microbeam and nanobeam with respect to the sample position is mainly due to thermal and/or mechanical instability coming from the optical components (e.g. double-crystal monochromator). The beam position must be kept constant during the energy scan with a tolerance smaller than the beam size, consequently achromatic x-ray optics (Sec. II.C) are preferred for these experiments. One possible way to lower the impact of the thermal drift is the reduction of the measurement time. Therefore, high flux undulator sources located on low-emittance electron storage rings are highly desirable to perform micro-XAS and nano-XAS experiments.

D. X-ray fluorescence and other decay spectroscopies

Figure 10 summarizes the different physical processes and related spectroscopies resulting from the creation of a core hole by a high-energy beam (x ray, e^-, or p^+). The primary process is the creation of a core hole and the emission of a primary electron, Fig. 10(a). If we are dealing with an x-ray beam, measuring the response (intensity of the transmitted beam, intensity of the fluorescence or electron yields) by scanning the energy of the x-ray beam results in XAS, providing insight into the unoccupied density of states

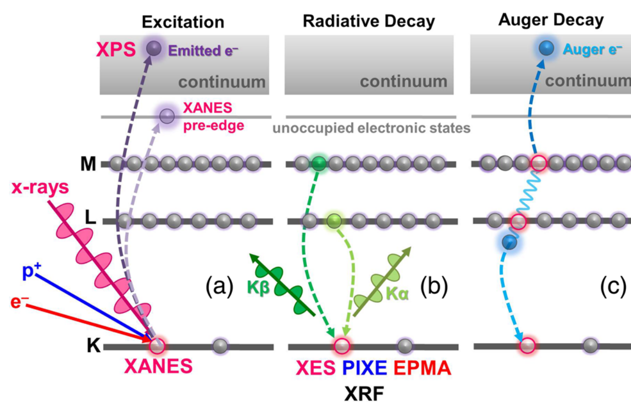

FIG. 10. Schemes of the different processes and related spectroscopies resulting after the interaction of a high-energy beam with matter: (a) excitation process, core hole creation; (b) radiative and (c) Auger decay channels.

(DOS); see Sec. III.C. Moreover, being the x ray absorbed in the process, all its energy $h\nu$ is transferred to the sample and the kinetic energy E_k of the emitted electron is linked to its binding energy by Einstein's photoelectric equation, scanning E_k (at fixed incoming photon energy) provides insight into the occupied DOS (XPS spectroscopy, Sec. III.E). Independently of the nature of the exciting beam, such an excited state may undergo a radiative [Fig. 10(b)] or Auger [Fig. 10(c)] decay process. The measurement of the energy of characteristic photons results in XRF spectroscopy, which is a fingerprint of the elemental composition because of the specificity of the $K\alpha$ and $K\beta$ emission lines (Deslattes *et al.*, 2003). The XRF nomenclature holds independently of the nature of the exciting beam (Potts *et al.*, 2002; West *et al.*, 2014, 2015). When the energy of the fluorescence photons is determined with high resolution, valence-to-core transitions $K\beta'$ and $K\beta_{2,5}$ allow one to discriminate the different oxidation states of transition metals and among different first (Seenivasan *et al.*, 2013) and even second (Gallo *et al.*, 2014) shell ligands. Related techniques are named as follows: EPMA for e^- beams, PIXE for p^+ (or ion) beams, and XES for x-ray beams (Nilsson and Pettersson, 2004; Glatzel and Bergmann, 2005; Bergmann and Glatzel, 2009; Mino, Gianolio *et al.*, 2010; Singh, Lamberti, and van Bokhoven, 2010; Pollock and DeBeer, 2015; Toyoshima and Kondoh, 2015). In the latter case, the energy of the incoming photons can be tuned to some specific preedge feature of the XANES spectrum, resulting in resonant XES, also known as RIXS (Kotani and Shin, 2001; Gallo and Glatzel, 2014). XRF allows an accurate identification of the elemental composition of the sample (detection limits down to a few ppb). Such analysis may be quantitative when the complex phenomena of beam penetration in the sample and x-ray absorption and reabsorption from the sample are properly considered (Sitko, 2009; Mino, Agostino *et al.*, 2010).

In the case of XRF, the allowed transitions that electrons can undergo from initial to final state are specified by the following electric-dipole selection rules:

$$\Delta n \neq 0, \quad \Delta l = \pm 1, \quad \Delta j = 0, \pm 1 \quad (j = l + m_s). \qquad (15)$$

A general empirical relationship between the wavelength of an x-ray characteristic line with the atomic number of the corresponding element is given by Moseley's law (Moseley, 1913)

$$\frac{1}{\lambda} = k(Z - \sigma)^2, \qquad (16)$$

where k is a constant for a particular spectral series and σ is a screening constant for the repulsion correction due to the other electrons in the atom. The larger the atomic number Z, the more complex becomes the XRF. The ratio of the number of emitted characteristic x rays to the total number of inner-shell vacancies in a particular atomic shell that give rise to it is called the fluorescence yield of that shell. The fluorescence yield is the probability that a vacancy in an atomic shell or subshell is filled through a radiative transition. For light elements ($Z < 20$) Auger electrons are predominantly produced during the relaxation on K shell ionization ($\sigma < 0.2$), while the medium to heavy elements are preferentially relaxing by a radiative manner. So, both Auger and XRF processes have Z-dependent probabilities that are complementary: the Auger yield is high for light elements and the fluorescence yield is high for heavy elements.

Compared to EDS typically used in scanning electron microscopy, XRF presents several experimental configurations such as total reflection XRF (TXRF), confocal XRF, energy-dispersive XRF, and wavelength-dispersive XRF. TXRF is a surface elemental analysis technique often used for the ultradiluted investigation of particles, residues, and impurities on smooth surfaces, for example, in the semiconductor industry for wafer surface contamination control. An incident beam impinges upon a sample at angles below the critical angle of total external reflection for x rays, resulting in reflection of almost 100% of the excitation photons. Because of its unique configuration, the main advantage of TXRF over conventional XRF is the reduced measurement background contributions by elimination of sample scattering which results in higher elemental measurement sensitivity. The confocal geometry uses two focusing optics for enhanced XRF elemental analysis and depth profiling. An excitation optics focuses a small x-ray beam onto the specimen, whereas a detection optics (polycapillary) collects fluorescent x rays from the sample. Specifically, elemental concentrations are measured within the small probe volume (confocal volume) defined by the intersection of the output focal spot of the excitation optics and the input focal spot of the collection optics. Thus, the polycapillary focusing optics act as spatial filters to eliminate background radiation from the sample and increase detection sensitivity for sample elements of interest. An energy-dispersive XRF system directly records the different energies of the emitted x rays, while counting and plotting the relative numbers of x rays at each energy. The WDXRF method physically separates the x rays according to their wavelengths, using a diffraction device such as a crystal or multilayer to isolate a peak and to obtain higher energy resolution. Thus, the detector does not need to be capable of energy discrimination, simplifying the pulse processing compared to dispersive XRF.

There is a useful figure of merit relevant to XRF called the detection limit that describes the lowest level of elemental concentration at which an instrument can be used for qualitative and quantitative analysis. Thus, a step forward would be 4D compositional capabilities (chemical imaging with space and time resolutions) with better detection limits at future XFEL facilities to access ultrafast phenomena (kinetics, photocatalysis, rapid fluctuations, and chemical reactions).

If during the radiative decay process visible photons are also emitted, we talk of XEOL, which is an x-ray photon in–optical photon out technique similar to photoluminescence. Rather than detecting the deexcitation process of electrons excited from the valence band into the conduction band, XEOL probes the deexcitation process after a deep core-level electron excitation by an x ray into the conduction band. Thus, XEOL monitors the optical luminescence (UV-vis-NIR) excited by an x-ray photon energy, which can promote a specific core-level electron of a given element of interest to bound, quasibound, and continuum states, providing elemental and, in some cases, site selectivity. The energy absorbed is partially transferred to optical deexcitation channels, resulting in radiative recombinations. XEOL can also be used to track the modulation of the absorption coefficient as a function of

excitation energy $\mu(E)$ called optical XAFS or photoluminescence yield (Martinez-Criado *et al.*, 2006). However, such a detection scheme is not straightforward owing to normalization, thickness, and self-absorption effects.

Because of the high energy of the incident x rays, and the subsequent core-level photoelectrons created, the XEOL process is a complex phenomenon that can be generally described as follows: (i) a core hole is created within femtoseconds by the annihilation of an x ray, (ii) the core hole is immediately filled by electrons from shallower levels via Auger or XRF decay, (iii) the new shallower core holes left behind are filled by even shallower core or valence electrons that generate a cascade process, (iv) the energetic photoelectrons and Auger electrons create more electrons and holes in their tracks as they travel through the absorbing medium and lose energy through inelastic scattering (thermalization), (v) electrons and holes (i.e., in semiconductors) thermalize at the bottom of the conduction band and top of the valence band, respectively (still relatively fast, i.e., subpicosecond), and (vi) electrons and holes in their respective bands radiatively recombine by a direct and/or indirect (with the assistance of a phonon) mechanism to produce luminescence with photon energy close to the band gap with a short lifetime (on the order of nanoseconds to subnanoseconds). In addition, defects such as impurities can produce intense optical emissions with photon energies significantly lower than the band gap and a relatively long lifetime (hundreds of nanoseconds to microseconds). Thus, in comparison to conventional UV-visible-NIR photoluminescence, XEOL can be site specific because the core level is characteristic of a given element involving energy transfer via secondary processes to the optical channel (thermalization of electrons and holes). The extent of this x-ray energy conversion to optical photons depends on the nature of the excitation channel (K or L shell, etc.), and the nature of the material, e.g., crystallinity, morphology, size, and proximity effects (quantum confinement, surface, and interface). Applied typically to organic and inorganic materials (for example, fluorescent proteins, phosphors, and semiconductors), XEOL has traditionally been a soft-x-ray technique that suffers from poor spatial resolution and long carrier diffusion length. Recently, owing to the key role of quantum confinement in limiting carrier dynamics, it has become particularly attractive for optical imaging of nanostructures (Martinez-Criado *et al.*, 2012c). When an x-ray microbeam or nanobeam is positioned at different points on a sample, and a XEOL spectrum recorded at each point, maps are produced that show the optical properties spatially resolved. Besides, by changing the x-ray-beam energy, more detailed depth-resolved optical information can be obtained.

Furthermore, time-resolved (TR) optical luminescence is a key tool for the disentanglement of the different mechanisms involved in the creation and relaxation processes of the electronic excitations. TR-XEOL can be performed at third-generation synchrotron sources thanks to their intrinsic pulsed time structure with up to subnanosecond pulse duration (Martinez-Criado, Segura-Ruiz, Alen *et al.*, 2014). Combining space, time, and energy resolutions, XEOL potential will further increase when exploited at x-ray free-electron laser sources and DLSRs in various research fields.

E. Photoelectron spectroscopy

Photoelectron spectroscopy (PES) consists of the measurement of the number of electrons emitted by the sample as a function of their kinetic energy (T) as a consequence of the absorption of a photon from an incoming monochromatic beam of energy $h\nu_0$. The phenomenon is described by Einstein's formula for the photoelectric effect (Egelhoff, 1987; Schattke and Van Hove, 2003; Miron and Morin, 2011; Bagus, Ilton, and Nelin, 2013; Margaritondo, 2013; Susi, Pichler, and Ayala, 2015; Weiland *et al.*, 2016)

$$T = h\nu_0 - \phi, \tag{17}$$

where the electron work function (ϕ, that is the minimum energy required to promote electron from sample to vacuum) is determined by measuring T, with $h\nu_0$ fixed and known. Depending on the type of incoming radiation, we are dealing with XPS (Nordling, Sokolowski, and Siegbahn, 1957; Sokolowski, Nordling, and Siegbahn, 1957) or ultraviolet photoelectron spectroscopy (UPS) (Turner and Jobory, 1962). Using Koopmans' theorem (Koopmans, 1934), that approximates ϕ to the former potential energy of the ejected electron ($\phi = -\varepsilon_0$), the PES spectra can be directly interpreted in terms of occupied DOS: core and valence DOS for XPS and UPS, respectively. This approximation neglects the fact that the remaining electrons adjust their distributions when ionization occurs and neglects the effects due to electron correlation. In most cases, the two neglected terms are of opposite sign and partially compensate, so that the overall error is relatively low (Hehre *et al.*, 1986; Michl and Bonačić-Koutecký, 1990).

According to Eq. (17), XPS provides the values $\phi\ (\sim -\varepsilon_0)$ of the core orbitals of the atoms present at the sample surface. Since such ε_0 are element specific, XPS can be used for the elemental speciation of the sample surface, being the integrated intensity of the XPS peaks proportional to the concentration of the specific element within the sampled region. XPS can consequentially provide a quantitative analysis of the surface composition (Powell and Seah, 1990; Tilinin, Jablonski, and Werner, 1996; Biesinger *et al.*, 2010); for this peculiarity it is also known by the alternative acronym ESCA (electron spectroscopy for chemical analysis).

As PES techniques detect electrons, we are dealing with surface sensitive techniques, probing the first few monolayers of the sample that usually require ultrahigh vacuum conditions, typically 10^{-12} bar. However, few synchrotron radiation beam lines are equipped with sophisticated electron lenses and differential pumping systems that allow exposing the surface to a local pressure as high as 10^{-3} bar of the desired atmosphere and extracting electrons from that surface and transferring them into the electron analyzer (Rupprechter and Weilach, 2007, 2008; Salmeron and Schlogl, 2008; Knop-Gericke *et al.*, 2009; Beaumont *et al.*, 2013; Starr *et al.*, 2013; Knudsen, Andersen, and Schnadt, 2016). The spectroscopy performed on such beam lines is named as "environmental PES" in the literature. Of interest is also the recent development of thin membranes that are partially transparent to electrons but that cannot be penetrated by molecules, such as graphene oxide (Kolmakov *et al.*, 2011).

XPS laboratory instruments are equipped with soft-x-ray sources, most commonly with Mg ($h\nu_0 = 1253.6$ eV) or Al

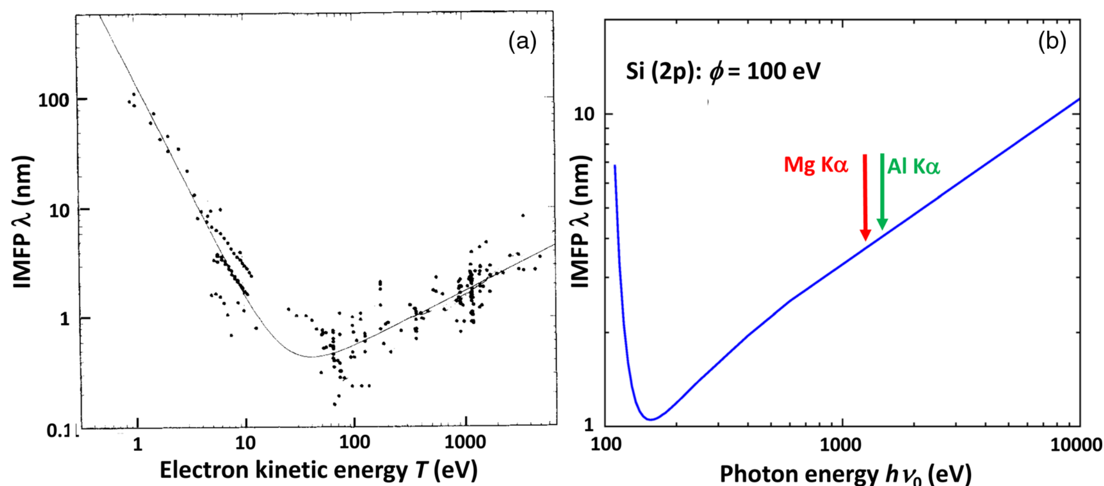

FIG. 11. (a) Compilation of IMFP measurements for different materials as a function of the electron kinetic energy T (scattered dots). The curve represents the empirical least squares best fit to Eq. (18) over all the reported data. Adapted from Seah and Dench, 1979. (b) IMFP for Si($2p$) photoelectrons in silicon as a function of photon energy. Adapted from Weiland et al., 2016.

($h\nu_0 = 1486.6$ eV) anodes while most of the UPS laboratory instruments use He discharge lamps ($h\nu_0 = 21.22$ eV). Besides laboratory instruments, in recent decades both XPS (Thiess et al., 2004; Kobayashi, 2005; Rubio-Zuazo and Castro, 2005; Takata et al., 2005; Ceolin et al., 2013; Miron and Patanen, 2014; Woicik, 2016) and UPS (Roman et al., 1992; Matsui et al., 1998) beam lines were developed at synchrotron sources.

Synchrotrons are attractive sources because they provide a superior incident photon flux, a higher energy resolution, and tunability of the exciting photon energy. The significant improved energy resolution (from about 300 meV using monochromatized Al or Mg $K\alpha$ down to 50 meV) allows identifying slightly different surface species and, for small adsorbed molecules, even to resolve the fine structure due to the excitation of molecular vibrations (Fuhrmann et al., 2004, 2005; Denecke, 2005). The high photon flux makes environmental PES possible and reduces the required acquisition time per spectrum down to a few seconds, which gives access to the time-resolved investigation of surface processes *in situ*. On the other hand, it also enables the investigation of very small coverages down to below 0.1% of a monolayer, facilitating the characterization of minority species.

The incident energy $h\nu_0$ can be optimized to the requirement of a particular experiment, maximizing or minimizing the surface sensitivity or the photoionization cross section of the substrate or the adsorbate. Indeed, as the x-ray penetration length in materials is much larger than the photoelectron inelastic mean free path (IMFP, λ), the information obtained in a PES experiment concerns the fraction of the sample from where photoelectrons may escape, typically $\sim 2\lambda$ from the surface. λ is strongly dependent on the kinetic energy T of the electron and less strongly on the sample density and chemical composition of the sample; see Fig. 11(a). λ is very high (up to several tens of nm) in the low T region ($T <$ few eV), rapidly decreases reaching a minimum of less than 1 nm in the $10 < T < 150$ eV region (the exact minimum depends on the sample), and then progressively slowly increases up to around 10 nm in the keV region. One of the most used empirical equations to estimate λ vs T is (Seah and Dench, 1979)

$$\lambda = \frac{A}{T^2} + B\sqrt{T}. \tag{18}$$

The first term in Eq. (18) dominates for low T values and it is more dependent on the nature of the investigated material as the parameter A ranges from 30 to 640 nm eV^2 moving from organic to inorganic compounds. For $T > 150$ eV, only the second term contributes to λ (the B parameter ranges between 0.054 and 0.096 nm eV$^{-1/2}$ for the different class of materials). The data reported in Fig. 11(a) imply that we can obtain the $\phi = h\nu_0 - T$ value of a given element in a specific matrix, changing the used monochromatic beam $h\nu_0$ and thus changing the kinetic energy of the measured electron T according to Eq. (17) and thus tuning the escape depth of the electrons by more than 1 order of magnitude. Figure 11(b) exemplifies this concept in the case of the XPS electron emitted from the ($2p$) level of silicon, reporting the λ value as a function of the selected excitation energy $h\nu_0$. For $h\nu_0$ values very close to the ϕ value of Si($2p$), 100 eV, T is very small and thus λ very high [see Fig. 11(a)]. Increasing $h\nu_0$, λ exhibits a minimum of about 1 nm and then starts increasing: at the Mg (Al) $K\alpha$ λ is just below (above) 4 nm, reaching values higher than 10 nm for $h\nu_0 = 10$ keV.

Consequently, the enhanced bulk sensitivity of hard-x-ray PES combined with the tunable photon energy of a synchrotron source provides the opportunity for nondestructive, depth-dependent measurements via the collection of different PES spectra at different $h\nu_0$ values.

When photoemitted electrons are discriminated not only by their kinetic energy, but also by their momentum we are referring to angle-resolved photoemission spectroscopy (ARPES) (Damascelli, Hussain, and Shen, 2003; Eschrig, 2006; Hasan and Moore, 2011; Margaritondo, 2013; Richard, Qian, and Ding, 2015). ARPES experiments usually use $h\nu_0$ values in the UV region, allowing reconstructing the DOS of the valence band of solids in the reciprocal space.

Until the late 1980s, PES experiments were forced to average the surface and interface properties over areas with a typical size of a few mm^2 (Margaritondo, 2013). The

situation changed due to both the increased brilliance of the third- and fourth-generation SR sources and the improvement in the x-ray optics, described in Sec. II, allowing x rays to be efficiently focused. As a result photoemission spectromicroscopy became an established technique (Margaritondo and Cerrina, 1990; Tonner et al., 1992; De Stasio et al., 1996; Marsi et al., 1997; Kiskinova et al., 1999; Barbo et al., 2000; Gunther et al., 2002; Escher et al., 2005; Biesinger et al., 2010; Horiba et al., 2011; Schneider et al., 2012; Patt et al., 2014).

F. Multiple-particle coincidence techniques

Multiple-particle coincidence techniques are very powerful approaches to correlate different types of information using concurrent experiments (Morin et al., 1998; Ikonen, 2010; Arion and Hergenhahn, 2015). In these approaches, more than one particle involved in the ionization process (electrons, photons, ions) is recorded and analyzed simultaneously. Depending on which particle is detected concurrently, there are several tools: electron-ion coincidence (PEPICO), ion-ion coincidence (PIPICO), electron-ion-ion coincidence (PEPIPICO), ion-neutral coincidence, and electron-electron coincidence. A particular case of the electron-electron coincidence technique is the so-called threshold photoelectron coincidence spectroscopy (TPEsCO), where a tunable light source is applied to scan across the different ion states while recording initially near zero kinetic energy electrons, frequently named threshold electrons (Baer and Tuckett, 2017). The progress of electron-electron coincidence spectroscopy gained relevance with the exploitation of the so-called “magnetic bottle” spectrometers, allowing (4π) collection efficiency and good detection efficiency also at very low kinetic energies (Eland et al., 2003). Although lasers remain the best solution to study one-electron valence ionization, SR sources offer the only practical alternative to examine deep valence levels (which commonly has a multielectron nature) and inner-shell photoionization. For example, final-state trication spectra and electron distributions generated by soft-x-ray single-photon triple ionization of rare gas atoms were obtained at BESSY-II (Berlin) (Eland et al., 2008). An alternative tool to conventional coincidence techniques is the so-called covariance mapping, which is performed at FEL facilities. By means of this technique, we are no longer limited to a low ionizing radiation flux, which typically reduces the acquisition time for the same amount of coincident events (Frasinski et al., 2013; Zhaunerchyk et al., 2013). Another approach commonly applied in surface science is photoelectron–Auger-electron coincidence spectroscopy, where the identification of the individual intermediate states can be obtained by recording both the Auger electron and the photoelectron emitted in the decay process. In solids, by using the angular-resolved Auger electron, the photoelectron coincidence approach allows the investigation of the core ionization mechanism with l and m_l quantum numbers selectivity (Stefani et al., 2004). Finally, a potent coincidence scheme is the so-called cold target recoil ion momentum spectroscopy (COLTRIMS) (Dorner et al., 2000), which aims at yielding a kinematically full picture of a decay involving three and more particles, relying on a system of ring electrodes, which guide and focus the charged particles.

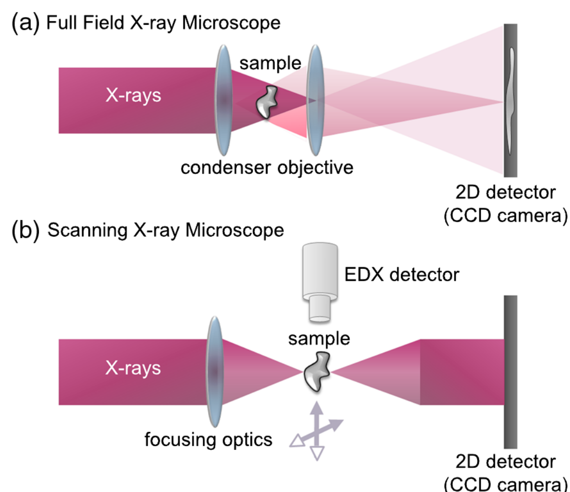

FIG. 12. Optical scheme of the (a) full-field x-ray microscope and (b) the scanning x-ray microscope.

G. Transmission full-field and scanning approaches

Several layouts for x-ray microscopy and (sub)microbeam probe methods can be found currently in operation, depending on manifold factors, as, e.g.,

- x-ray energy (soft versus hard),
- specific setup (surface versus bulk sensitive), and
- intrinsic nature of the sample and/or specific signal detected.

However, despite the rich variety of available layouts, each offering specific capabilities, two main operation schemes can be identified (Fig. 12): full-field and scanning modalities (Sakdinawat and Attwood, 2010).

1. Full-field mode

The full-field approach employs an optical arrangement that resembles, under several aspects, the classical visible light and transmission electron microscopes. A condenser optic is employed to illuminate the sample while an objective lens produces a magnified image of the sample into a fast charge-coupled device (CCD) camera (Guttmann et al., 2009) (typical speed values are on the millisecond time scale) (Labiche et al., 2007). Higher magnifications can be achieved by positioning the sample close to the focal distance (projection XRM). The projection of the object formed on the 2D detector shows a magnification that is given by the ratio between the objective optic-detector and source-objective optic distances. This flexible scheme can be easily used for absorption or phase-contrast imaging. Additionally, by collecting a series of projections at different sample rotation angles, the 3D electronic density of the sample is retrieved using tomographic reconstruction algorithms.

So far modified transmission x-ray microscopy (TXM) strategies (Sakdinawat and Attwood, 2010) have demonstrated improved resolution, using higher diffraction orders (with an efficiency reduction) or a compound zone plate. Also, there have been relevant enhancements in phase-sensitive approaches based on different accessible contrast mechanisms such as the Zernike phase, differential interference, and a spiral phase. In scanning TXM (STXM), the synchrotron light is focused by the zone plate to a small spot on the sample and raster

scanned in 2D, while collecting the transmitted x rays. STXM is routinely applied to generate maps of the projected local absorption of the sample. The smallest spot size is usually obtained by spatially coherent illumination and using a high-precision scanning stage. Another mode of operation, often referred to as spectromicroscopy, involves scanning of the incoming photon energy to achieve spectral information for elemental and chemical speciation. Today we can find several modalities such as time-resolved TXM, 3D-resolved polarization-dependent XAS using TXM, strain-dependent TXM, etc. State-of-the-art TXMs have been applied to various research fields including biological, environmental, and material studies.

2. Scanning x-ray microscope

In the scanning mode x-ray focusing optics are used to form a (sub)micrometric beam (nanoprobe or microprobe) through which the sample is raster scanned and maps are built on a pixel by pixel basis (Martinez-Criado *et al.*, 2012b). This approach that is the most common choice in microspectroscopy or diffraction multitechnique beam lines allows simultaneous (or at least alternative, depending on the specific experimental conditions) acquisition of multiple signals using suitable detectors. For instance, XRD, XRF, and/or XAS can be combined for a multipropose structural or compositional characterization at the submicrometric level (Martinez-Criado *et al.*, 2016); see Fig. 13.

3. Comparison between full-field and scanning modalities

Interestingly, full-field and scanning modalities are complementary in terms of relative advantages and drawbacks (Falcone *et al.*, 2011).

The full-field transmission scheme provides a shorter acquisition time and a relatively simpler instrumental design compared to the scanning-probe setup. However, the objective lens behind the sample strongly limits the efficiency, so that only a reduced percentage of the photon flux arriving at the sample effectively contributes to the final image formation. As a consequence, a full-field microscope compared to a scanning microprobe requires a higher photon dose to achieve comparable performances, with potential higher radiation damage effects; see Sec. III.I.

Moreover, full-field microscopes are generally limited in acquiring additional structural information (XRD), although XANES-based imaging in transmission mode has been demonstrated (Ade and Stoll, 2009; Guttmann *et al.*, 2012; Suzuki and Terada, 2016).

Conversely, the scanning setups are more efficient in terms of x-ray photon doses (i.e., a high trade-off between x-ray photon flux and signal-to-noise ratio) and suitable for multimodal imaging. As a drawback, they are slower. The typical scan requires from a few minutes to some hours, depending on the number of sampled points. Stricter requirements in terms of source brilliance and coherence to maintain a reasonable acquisition time are also imposed. In addition, the raster scan of the sample required in scanning mode implies the use of xyz translation stages, which can affect the effective lateral resolution due to sample positioning inaccuracy. Nevertheless, the information availability in the case of scanning modality is not restricted to transmission imaging and can be extended to parallel data collection on different secondary effects [XRF, total electron yield (TEY), XEOL, etc., see Fig. 13]. Moreover, a low-noise area detector can be placed in transmission mode for inline microdiffraction analysis. However, to maximally benefit from these capabilities, complex instrumentation (multielement fluorescence detectors, large area CCD cameras, optical lenses, etc.) and a careful design of the whole experimental setup is required (Fig. 13), in comparison to the simpler layout of full-field microscopes.

H. The power of a multitechnique approach

X-ray-based characterization tools introduced in the previous sections provide crucial microscale and nanoscale information exploiting the unique features of modern synchrotron sources (low-emittance third-generation DLSRs and XFELs). Further enhancements in the level of available information can be obtained by combining different characterization methods.

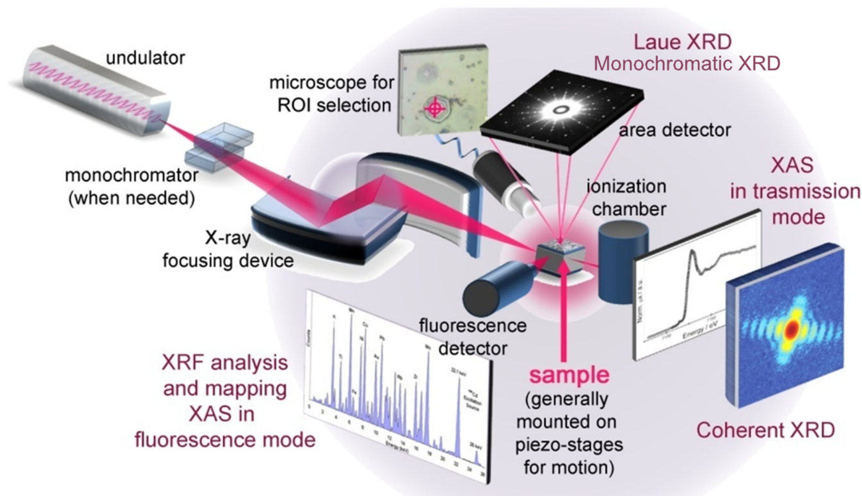

FIG. 13. Schematic model of a prototype scanning nanoprobe or microprobe beam lines dedicated to multitechnique space-resolved characterization.

A smart selection of x-ray techniques applied simultaneously can answer many key questions generally asked in materials science (e.g., element analysis, oxidation state, local structure, crystallographic orientation, microstructural features, such as grain size and phases, etc.), due to the high complementarity that such methods exhibit.

In particular, imaging methods match well with diffraction techniques since they operate directly in real space rather than in reciprocal space. Likewise, in contrast to diffraction, the investigation of absorption modulations can provide local structural information without requiring the existence of long-range ordering.

By monitoring the subsequent deexcitation processes (XRF, XPS, XEOL, XBIC, etc.), insight into even trace elemental composition and chemical features at several sample depths can be achieved.

Finally, scattering-based methods remain the more suitable choice in the case of direct (in principle nonelement selective) structural characterization of the different hierarchical levels of complex materials (structure refinement in crystals, phase identification, grain size, strain distributions, etc.).

The use of synchrotron micro-x-ray and nano-x-ray beams therefore combines several unique possibilities in a concurrent fashion:

- surface or bulk escape depths;
- element, site, and orbital selectivity with simultaneous access to K absorption edges and XRF emission lines of light, medium, and heavy elements due to the source energy tunability in a large multi-keV range;
- structural probe;
- chemical trace sensitivity owing to the high source brilliance;
- accessibility to different timing modes; and
- orientation effects by polarization selection rules.

Previous considerations demonstrate well the common trend in developing multitechnique microprobe and nanoprobe beam lines. Indeed, once an x-ray microbeam or nanobeam with suitable properties is achieved, the surrounding experimental arrangement is generally designed to optimize the flexibility in the detection modalities and to allow in a "single shot" a combination of the highest possible number of analytical methods. The schematic representation of an ideal scanning nanoprobe or microprobe multitechnique beam line is shown in Fig. 13.

A key element of the microprobe setup is the optical system employed to focus x rays, typically emitted by one or more undulators (they ensure higher brilliance and lower horizontal divergence compared to bending magnets or wigglers). For wide-band-pass applications, the pink beam (deflected by a mirror) or white beam (directly emitted from the undulator) is focused by the x-ray lens. Otherwise, when required, a monochromator is employed to select the beam energy, with particular attention to the stability of the focal point position while scanning the energy. The sample is typically mounted on a piezostage for high-precision positioning, while an optical microscope coupled to a camera, or to an electron microscope (Yin et al., 2016), is often employed to visualize or locate the ROI (or the sample itself).

Several kinds of signals can be detected, mainly using CCD cameras and energy- or wavelength-dispersive detectors, suitably arranged around the sample. The transmitted beam is detected for different spectroscopy (e.g., micro-XAS in transmission mode) and microscopy (TXM) applications. The fluorescence signal is acquired for XRF microspectroscopy or spectromicroscopy or micro-XAS. The detection of the x-ray scattered intensity, mainly via 2D detectors, is behind the microdiffraction methods (micro-Laue XRD, polycrystalline micro-XRD, microdiffuse scattering, far-field coherent diffraction, etc.). Specific methodologies and instrumentation can be exploited to resolve volume elements along the path of the penetrating x-ray beam with micrometric resolution (e.g., differential aperture microscopy).

In Fig. 13 the "electron part" (emitted photoelectrons, Auger and secondary electrons, with related detection system) is omitted. The reason is surely not its scarce relevance. The direct detection of photoelectrons as a function of their kinetic energy is the basis for micro-XPS and XPEEM techniques. Moreover, the electron-yield measurement (total, TEY, or partial) is employed to evaluate the XAS signal when the x-ray fluorescence cross section is particularly inefficient (e.g., soft-x-ray XAS for low-Z elements) and/or for surface sensitive studies.

The main problem when working with electrons is their extremely high cross section in interactions with matter (direct Coulomb interaction). This implies that the sample itself and the whole sample-detector path have to be maintained under ultrahigh vacuum conditions (see Sec. III.E). The vacuum system required is generally difficult to integrate in the multipurpose setup shown in Fig. 13 and electron-based characterization techniques are generally performed in dedicated beam lines, eventually equipped with XRF detectors.

I. Radiation damage effects: Physical basis, warnings, and strategies

The remarkable improvements in both the brilliance of third- and fourth-generation synchrotrons and the x-ray optics (see Figs. 1 and 7, respectively) are pushing the photon density on the sample to unprecedented values, which makes radiation damage (RD) a major concern (Henderson, 1995; Fayard et al., 2009; Holton, 2009; Howells et al., 2009; Hau-Riege, 2011; Hopkins and Thorne, 2016).

The most critical situation concerns experiments investigating living cells (Hemonnot et al., 2016) and biological macromolecules (Hedman et al., 1985; Garman, 2010), where RD has been a problem and a research topic for decades sufficiently relevant to justify an *ad hoc* international series of conferences: the *International Workshop on X-ray Radiation Damage to Biological Crystalline Samples* that reached its 9th edition in 2016 (Garman and Weik, 2017).

The situation becomes even more severe when experiments are performed at FELs (Nass et al., 2015), where the "measure before destroy" strategy is commonly adopted. It consists of a single shot-by-shot experiment, where data from every FEL pulse are collected before the destruction of the sample [due to the Coulomb explosion caused by the expulsion of multiple electrons from the sample, Fig. 14(b)], and a new fresh sample is replenished before the next pulse (Chapman et al., 2011; Alonso-Mori et al., 2012; Boutet et al., 2012; Kern et al., 2012; Frank et al., 2014; Liekhus-Schmaltz et al., 2015; Valenza and Seidler, 2016; Opara et al., 2017).

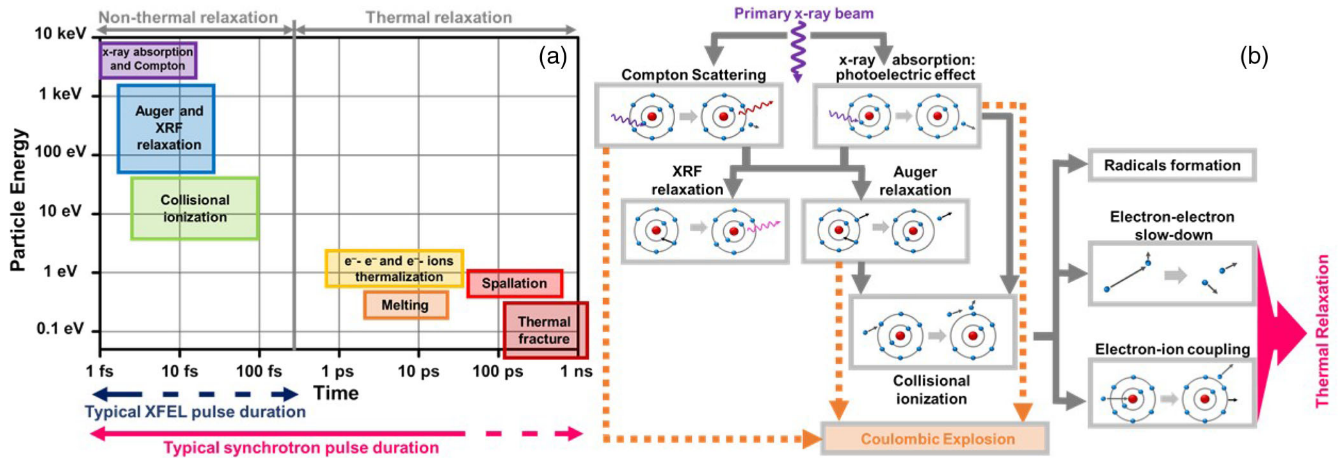

FIG. 14. Schematic representation of the cascade channels of energy transfer involved in the process of interaction between an intense hard-x-ray beam and condensed matter. (a) Classifies the different channels in a qualitative (energy, time) plane. (b) Depicts the physical processes involved in the main channels. In (a) also represented are the typical FEL (blue arrow, 2–200 fs, see Table III) and synchrotron (red arrow 20 ps—1 ns) pulse duration. From London *et al.*, 2001.

Besides, RD has been observed in organic semiconductor thin films during grazing incidence diffraction experiments (Neuhold *et al.*, 2012) and in poly(methylmethacrylate) thin films analyzed by UPS (Okudaira *et al.*, 1998). The rates of chemical transformation by RD of different polymers in XPEEM and STXM data collections at the Advanced Light Source (ALS) synchrotron using a 300 eV soft-x-ray beam have been measured quantitatively using $C(1s)$, $N(1s)$, and $O(1s)$ NEXAFS spectroscopy. The critical doses for chemical modifications, as monitored by changes in the NEXAFS spectra, were found to be highly dependent on the polymer nature, being 80 ± 12, 280 ± 40, and 1230 ± 180 MGy for poly(methyl methacrylate), fibrinogen, and polystyrene, respectively (Wang *et al.*, 2009). At 300 eV, 1 MGy $= 6.242^{*}\rho$ eV/nm^3, where ρ is the polymer density in g cm^{-3}.

Inorganic hard condensed matter is generally much less sensitive to x-ray doses, although exceptions are reported in the literature, some of them being summarized in the following. The aggregation and photoreduction of Pb^{2+} cations into Pb nanocrystals has been observed in borosilicate glass by time-resolved SAXS (Stanley *et al.*, 2014). Morphological changes in Li-ion batteries have been observed in TXM experiments (Nelson *et al.*, 2013). Structural RD was observed in silicon-on-insulator and in SiGe on silicon-on-insulator samples irradiated with a 250 nm beam size at 11.2 keV (Polvino *et al.*, 2008). RD was evidenced by the irreversible degradation of the (008) Bragg peak with time. They found that the magnitude of the RD decreases when moving away from the center of the irradiated volume, but that it is still appreciable at a distance of almost 1 order of magnitude larger than the beam size. CsI, CsI(Tl), Gd_2O_2S(Tb), Gd_2O_2S(Eu), Y_2O_2S(Eu), and Y_2O_2(Eu) thin films underwent changes in the photocurrent and scintillation light yield of several percent for accumulated doses of up to 5×10^{11} photons mm^{-2} in the 9–18 keV energy range (Tremsin *et al.*, 2001). Si-SiO_2 metal-oxide-semiconductor (MOS) capacitors and gate-controlled diodes, built on high resistivity n-doped Si with different crystal orientations, have been irradiated with 12 keV beam at the Deutsches Elektronen-Synchrotron (DESY) DORIS III synchrotron with doses in the range 100 kGy to 100 MGy (Zhang *et al.*, 2012). It was observed that the surface densities of oxide charges and interface traps at the Si-SiO_2 interface and the surface-current densities are gate voltage, orientation, and dose dependent. Both the normal state resistivity and the critical temperature of superconducting $Bi_2Sr_2CaCu_2O_{8+\delta}$ (Bi-2212) whiskers increased after a 6 h irradiation by a synchrotron μ beam (1.7×5.3 μm^2) at 17 keV (Aldica *et al.*, 2011). The RD effects on cultural heritage artifacts were recently reviewed (Bertrand *et al.*, 2015).

It must be considered that the relatively scarce literature on the RD induced by synchrotron beams on nonbiological materials probably does not mean that such effects are improbable. When detected, commonly synchrotron users only publish data acquired below damage threshold. It might even be possible that a fraction of the published results may be affected, at least to some extent, by RD problems that were not spotted.

In a few limited cases, RD is exploited for specific purposes such as radiation therapy for the space-resolved treatment of tumors (Prezado *et al.*, 2009), or the controlled modification of materials' properties: the redox and clusterization of silver nanoparticles (NP) in silicate glasses (Isaji *et al.*, 2012); the transition from the insulating antiferromagnetic state to the metallic ferromagnetic state in $Pr_{0.7}Ca_{0.3}MnO_3$ mixed oxide (Kiryukhin *et al.*, 1997); the monoclinic to tetragonal phase transition in $YBaFe_4O_7$ oxide (Duffort *et al.*, 2014); and innovative maskless x-ray nanopatterning approaches aimed to realize electrical devices with nanometer feature dimension; see Sec. IV.C.2.

The cascade channels of energy transfer involved in the process of interaction between an intense hard-x-ray beam and condensed matter, that may lead to RD, are schematically represented in Fig. 14 (London *et al.*, 2001; Hau-Riege, 2011). Figure 14(a) classifies the different channels in the plane having as abscissa the time scale of the processes and as ordinate the energy of the involved particles (photons, electrons, ions, or phonons). In the short time scale [up to about 100 fs in Fig. 14(a)] the processes are of pure electronic nature and do not involve any thermal motion of the ions; here

the ordinate values refer to the energy of the single electron or photon involved in the process. At longer time scales [from about 1 ps in Fig. 14(a)] thermalization processes among electrons and ions occur. The ordinate values refer here to the order of magnitude of the energy of the particles involved in the process, considering that these are collective effects involving a high number of particles.

Figure 14(b) displays the cascade of energy release channels involved in the process. The energy release of the primary hard-x-ray photons to the matter can be either partial, via an inelastic scattering and the emission of an electron in the Compton effect, or total, via the photoabsorption process and the emission of a photoelectron with kinetic energy given by Eq. (17). After a Compton event, the inelastically scattered photon is further subjected to the same possible events as for the primary beam: additional Compton scattering or definitive absorption process [the corresponding arrows not being drawn in Fig. 14(b) for simplicity]. The core hole, generated after the photon absorption, will be filled by valence electrons with the emission of an XRF or an Auger electron, the former decay channel being more probable for high-Z atoms and the latter for low-Z atoms. XRF photons can then be absorbed by higher shells of the same element or by core shells of lighter elements eventually present in the sample. Electrons emitted in Compton, photoelectric, or Auger processes will generate secondary ionization events by collision with atoms.

At larger time scales, we have the thermalization processes among electrons and between electrons and ions that finally result in a local increase of the sample temperature that is successively transferred from the illuminated region through neighbor regions by thermal conduction (via electrons or atoms and ions), and eventually through macroscopic mass motion (convection) when the sample environment consists of liquid or gas phases. The consequent local gradients in temperature, pressure, and ionization state, close to the irradiated matter, may result in stress gradients in the sample that in turn may yield to phase transformations, amorphization, thermal fracture, spallation (that is the internal rupture of the material followed by matter ejection due to large tensile stresses generated when the pressure wave is reflected from the free surface of the material), or even melting. In case the lattice structure is still intact, atomic heat conduction will take place through phonons. Typically, mass transport phenomena proceed through hydrodynamic and acoustic mechanisms and are slow processes on the time scale considered in Fig. 14(a). Note that the expansion in materials is limited by the sound speed and occurs on a time scale of hundreds of ps [Fig. 14(a)] (London et al., 2001; Hau-Riege, 2011).

In biological samples or in samples containing organic components (metal-organic frameworks, polymers, organic semiconductors, colloidal NPs, zeolites with template molecules, etc.) the collision ionization process may result in free-radical formation such as hydroxyl ($OH^{\bullet}$) and hydrogen radicals. The successive migration of such chemically reactive species may generate radiation-induced damage far away from the irradiated region.

The x-ray pulse length [2–200 fs for XFELs and 20 ps–1 ns for synchrotrons, see Fig. 14(a)] defines the duration of the energy deposition process during which x-ray photons couple with the electrons of the sample. The absorbed energy is successively redistributed over various degrees of freedom through the interaction of electrons, ions, and phonons as described (Fig. 14). In the case of FELs, the pulse length is so short (Table III), and the number of photons per pulse is so high that the electrons emitted by the sample via Compton, photoelectric, and Auger processes may be so high as to result in the Coulombic explosion of the fraction of the sample in close proximity with the illuminated volume [dashed orange arrows in Fig. 14(a)] (Neutze et al., 2000; Jurek, Faigel, and Tegze, 2004).

Computer simulations of the fundamental processes shown in Fig. 14 are performed with three different approaches depending on the energy and time values of the process. The x-ray inelastic scattering, photon absorption, XRF, and Auger relaxation processes and collisional ionization are usually simulated via a MC approach where, starting from a high number of primary x rays (typically 10^6), and using the known energy-dependent atomic photoabsorption and scattering cross sections (Henke, Gullikson, and Davis, 1993), the paths of primary and secondary photons and electrons are simulated in a probabilistic manner (London et al., 2001; Moukhametzianov et al., 2008; Dettmar et al., 2015; Torsello et al., 2018). MC simulations produce a quantitative space and time-dependent description of the distribution of the particles (photons, electrons, and ions) and ultimately a distribution of dose. MC methods are accurate in following the electrons down to energies of around 100–200 eV, where the interaction cross sections are so strong that the electrons are expected to remain almost localized (London et al., 2001).

To model the behavior of lower energy electrons, a better description of the electron-matter interaction is required. In this the intermediate energy and time-scale [see Fig. 14(a)] simulations are usually performed with a molecular dynamics approach that is able to track the position and the momentum of individual atoms, ions, and electrons (Silvestrelli et al., 1997; Jeschke, Garcia, and Bennemann, 1999; Gambirasio, Bernasconi, and Colombo, 2000; Neutze et al., 2000; London et al., 2001; Bergh, Timneanu, and van der Spoel, 2004; Jurek, Faigel, and Tegze, 2004; Gnodtke, Saalmann, and Rost, 2009; Froideval et al., 2011; Hau-Riege, 2011). At lower energies [longer time delays, see Fig. 14(a)] temperature mapping, thermal ion motion, and eventual melting, spallation, or cracking effects can be simulated by a finite-element approach (Nicholson et al., 2001; Aldica et al., 2011; Pagliero et al., 2014; Mino, Bonino et al., 2017; Mino, Borfecchia et al., 2017; Wallander and Wallentin, 2017).

As an example, Fig. 15 reports the effect of the x-ray induced heating of an InP nanowire (NW) obtained from a time-resolved and steady-state 3D finite-element modeling. Figure 15(a) reports the 3D representation of the model, where a 2-μm-long InP NW, with a diameter of 100 nm and oriented along the x direction, is supported on a 54-nm-thick insulating silicon nitride support and is illuminated by a 10-keV x-ray beam coming from the top (z axis) modeled with a Gaussian intensity profile with a full width at half maximum of 100 nm. The finite-element mesh was defined to be denser in the nanowire and in the section of the substrate near the nanowire, with about 10 nm distance between nodes, indicated with dots in the figure. Figure 15(b) reports the time evolution (from 0.1 to 5 ns) of the temperature gradient in the NW viewed in the (x, z) plane after irradiation of a single x-ray pulse of 0.1 ns

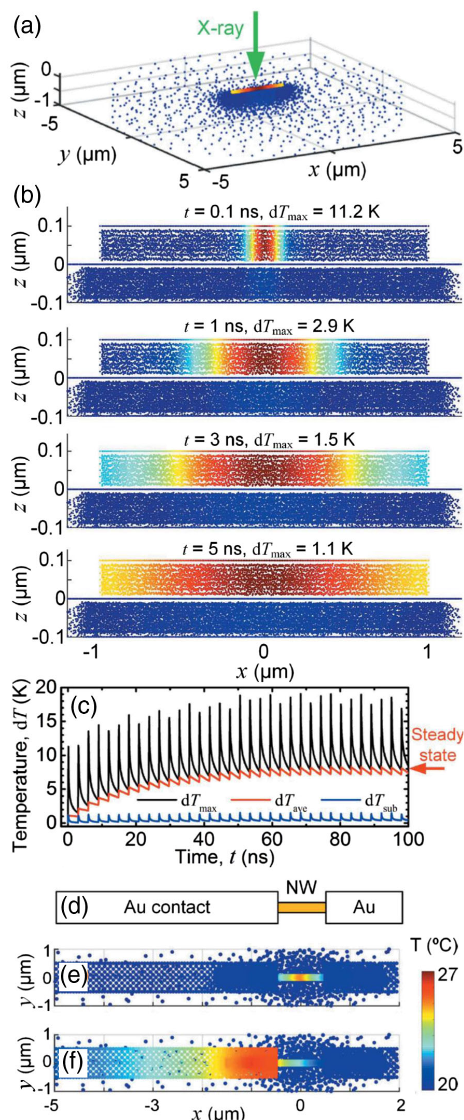

FIG. 15. Finite-element modeling of the temperature increase inside an InP NW supported on a Si_3N_4 membrane (a)–(c) after exposure to x-ray pulses of length 0.1 ns (photon energy = 10 keV; flux = 10^{12} photons s^{-1}; power = 1.6 mW). (a) 3D representation of the model; each node in the finite-element mesh is indicated with a dot. (b) Simulated temperature increase dT (relative to RT) after absorption of a single x-ray pulse (3000 photons) in the 0.1–5.0 ns interval after beam exposure. The color scale is different for each time. (c) Effect of a pulse repetition with period 3 ns on the local NW temperature at the beam position (black); the average NW temperature [orange (light gray), the arrow indicates the value obtained in a steady-state simulation]; the substrate temperature [blue (dark gray)]. (d)–(f) Simulated temperature in the InP NW contacted with 100-nm-thick gold contacts, as viewed along the z axis (beam direction). (d) Drawing of the sample. Temperature gradients obtained at a steady-state condition by impinging the x-ray beam at the center of the NW (e) or at the left interface between InP and Au (same color scale). Adapted from Wallander and Wallentin, 2017.

length (3000 photons). The heat transferred by the photon-matter interaction is efficiently transported within the NW and the temperature becomes almost homogeneous after about 5 ns, while the heat transport to the insulating substrate is small in this time scale. Figure 15(c) reports the effect of a pulse repetition with a period of 3 ns on the time evolution of the local NW temperature at the beam position of the average NW temperature and of the substrate temperature (black, orange, and blue curves, respectively, corresponding to black, light, and dark gray in the gray scale version). Figures 15(d)–15(f) refer to simulations performed by contacting the InP NW with two gold contacts from both sides. Here the heat transfer from the NW to the surroundings is much more efficient than in the previous case. Interesting is the fact that when the beam hits the contact region between Au and InP [Fig. 15(f)], a slightly higher local temperature is reached than in the case in which the beam hits the central part of the NW [Fig. 15(e)]. This is due to the fact that, when the beam hits the gold contact, much more energy is released to the overall sample because gold is a much more efficient x-ray absorber.

The authors concluded that, in the absence of a significant heat transfer to the substrate, the temperature increases by 55 K in air and far beyond the melting temperature in vacuum. Changing the size of the x-ray focus at constant flux produces a marginal effect on the sample temperature. The key strategy for reducing the x-ray-induced heating is to improve the heat transfer to the surroundings (Wallander and Wallentin, 2017).

An additional example of the use of the finite-element method in determining the sample temperature of an irradiated sample is reported in Fig. 31(b) where the role of the pulsed origin of SR is highlighted.

Summarizing, a list of useful guidelines follows: (i) RD strongly depends on the nature of the investigated material, being more severe in the following order: living cells > biological tissues > organic compounds > inorganic compounds. However, there is no general rule that can predict the maximum dose that can be received by a particular sample before being subject to RD effects. (ii) A protocol allowing one to determine the dose threshold should be defined to guarantee that the measurements are always performed on an undamaged sample; see, e.g., Jeffries et al. (2015). In this regard, beam lines should be equipped with calibrated filters able to progressively reduce the photon flux on the sample by several orders of magnitude. For solid samples, the use of rotating and/or fast translating sample holders (supported by smart acquisition protocols) will allow one to change the sampling point before the maximum dose is reached. For liquid samples liquid jet setups (Salassa et al., 2010) are effective in reducing the dose per molecule. (iii) The sample environment should be optimized to maximize the heat exchange between the sample and the environment (Wallander and Wallentin, 2017); this includes the use of cryostats, high-heat-conducing sample holders, and a He atmosphere whenever possible. Unfortunately, such care is less efficient in cases where RD is mainly due to radical formation during irradiation (Meents et al., 2010), where cryogenic temperatures are efficient only in limiting the region where reactive radicals can migrate. (iv) RD depends on the energy of x rays (being larger at lower energies and just above element absorption edges): for scattering techniques high-energy experiments are preferred; when high-Z elements are present in the sample, the ideal energy is just below the corresponding edge. Such a solution may be inaccessible for spectroscopic techniques, where the energy is determined by the experiment. (v) The smallest is the spot size and the worst is

the RD problem; consequently, the beam should not be smaller than what is needed. (vi) In x-ray diffraction microscopy experiments RD scales with the inverse fourth power of the resolution (Howells et al., 2009), implying that the maximum measured q must be chosen carefully.

IV. SELECTED APPLICATIONS IN MATERIALS SCIENCE

Among the vast amount of literature reporting the characterization of advanced materials with micro-x-ray and nano-x-ray beams in Sec. IV we report relevant cases studies where the different focusing optics (Sec. II) and the different characterization techniques (Sec. III) have been used to shed light on the structural and electronic properties of the investigated materials. Examples have been sorted distinguishing applications on different classes of materials: semiconductors (Sec. IV.A), metals (Sec. IV.B), and superconductors (Sec. IV.C). The final Sec. IV.D has been devoted to the characterization of devices. For brevity, this selection is far from being exhaustive, in terms of both the selected examples (e.g., Sec. IV.B deals only with metal nanoparticles, neglecting alloys) and of the categories of materials (e.g., graphenes, carbon nanotubes, glasses, polymers, ceramics, etc., are missing). Notwithstanding these limitations, we believe that the set of selected examples provides a comprehensive overview of the possibilities that are offered in the field of space-resolved characterization of materials at large-scale facilities.

A. Semiconductors

1. Group IV semiconductors

SiGe quantum dots have been chosen as a case study for the group IV semiconductor category because they are prototypical for investigating the fundamental aspects leading to the formation and evolution of self-assembly (Grutzmacher et al., 2007; Leite et al., 2008; Zhang et al., 2010). Technologically, the evident compatibility of SiGe/Si(001) quantum devices with the state-of-the-art Si technology makes the SiGe system interesting for electronic applications, mainly for metal-oxide-semiconductor field-effect transistor (MOSFET) and complementary metal-oxide-semiconductor (CMOS) devices (Oberhuber, Zandler, and Vogl, 1998), as well as for hybrid superconductor-semiconductor devices, such as resonant supercurrent transistors (Katsaros et al., 2010). Moreover, the SiGe/Si(100) system exhibits interesting potentialities in the fields of optoelectronic (Chaparro et al., 1999; Grutzmacher et al., 2007), spintronics (Tyryshkin et al., 2005), and quantum computing (Wang, 2002) devices based on Si.

SiGe islands grown by liquid phase epitaxy on a Si(001) substrate are ideal model systems to test the capabilities of x-ray microbeams and nanobeams to study individual nano-objects. In fact, depending on the germanium content, the island size can be accurately tuned in the range 3 μm–50 nm (Dorsch et al., 1998). Adjusting the time of the different growth stages, islands with well-defined morphologies can be obtained, moving from simple flat islands with side facets less steep than (111) to more complex objects, consisting of square-based truncated pyramids with (111) side facets and (001) top facets (Hanke et al., 2004). Compositional, structural, and elastic features of self-organized SiGe/Si (001) islands were systematically investigated at the micro-XRD beam lines of the European Synchrotron Radiation Facility (ESRF) (Hanke et al., 2008; Mocuta et al., 2008; Diaz et al., 2009; Rodrigues et al., 2009; Scheler et al., 2009; Dubslaff et al., 2010), adopting the x-ray reciprocal-space mapping (RSM) method (Metzger, Schulli, and Schmidbauer, 2005) supported by finite-element method (FEM) simulations (Wiebach et al., 2000) for the determination of the lattice displacements.

The 5×3 μm^2 x-ray beam delivered by beam line ID01 (ESRF) was used to investigate SiGe/Si(001) samples characterized by island sizes in the 3–200 nm size (Mocuta et al., 2008). They employed the scanning x-ray diffraction (SXD) approach, see Fig. 16(a), to map the location of the islands on the sample by monitoring the intensity of the SiGe(004) Bragg peak. SXD combines a high resolution in Q space, acquiring the intensity distribution around a Bragg peak, with a μm resolution in real space (Stangl et al., 2009).

Figure 16(b) shows RSM data collected from SiGe islands around the (004) reciprocal lattice point. The left panel refers to a low spatial-resolution RSM (averaging over around 10^3 islands), while the middle and right panels refer to high spatial-resolution RSM collected on two individual islands at different stages of the growth process: a fully developed truncated pyramid (IL1) and a flat island (IL2). The top insets report the corresponding SEM micrographs.

FEM simulations provided both the Ge distribution and the strain distribution in $Si_{1-x}Ge_x$ islands (Mocuta et al., 2008). The fully developed island (IL1) exhibits a lower germanium content ($x = 0.046 \pm 0.002$) in the bottom part of the pyramid, and a higher content ($x = 0.053 \pm 0.002$) in the top part, being the concentration step located at $1/3$ of the island height. Conversely, the flat island (IL2) has the $2/3$ top part missing, indicating that IL2 represents an intermediate growth stage of IL1. The identification of the growth mechanism, starting from flat islands that evolve to truncated pyramids, and their in-depth structural characterization could be determined only with a SXD imaging approach at a high-brilliance synchrotron equipped with microbeams. Indeed, the contribution to the total scattering of flat islands, representing only about 3% of the islands (corresponding to only 1% of the scattering volume), is completely negligible in an ensemble-averaging experiment; see the left part of Fig. 16(b).

The x-ray spot size employed in the study discussed (5×3 μm^2) did not allow spatial discrimination of possible substructures within the single island. A step further in terms of x-ray-beam performances was achieved at the beam line ID13 of the ESRF (Hanke et al., 2008), where refractive silicon x-ray lenses (see Sec. II.B) allowed focusing down to 0.2 μm FWHM enabling detailed SXD scans inside individual micrometer-sized semiconductor dots. By illuminating diverse (111) SiGe island side facets, crystal truncation rods of different orientations were independently excited and thus became distinguishable in the scattering patterns, as shown in Fig. 16(c). An analog experiment was reported by Diaz et al. (2009), who implemented a method that does not require the collection of the whole 3D reciprocal space at each position in real space, thus limiting beam instability problems during the

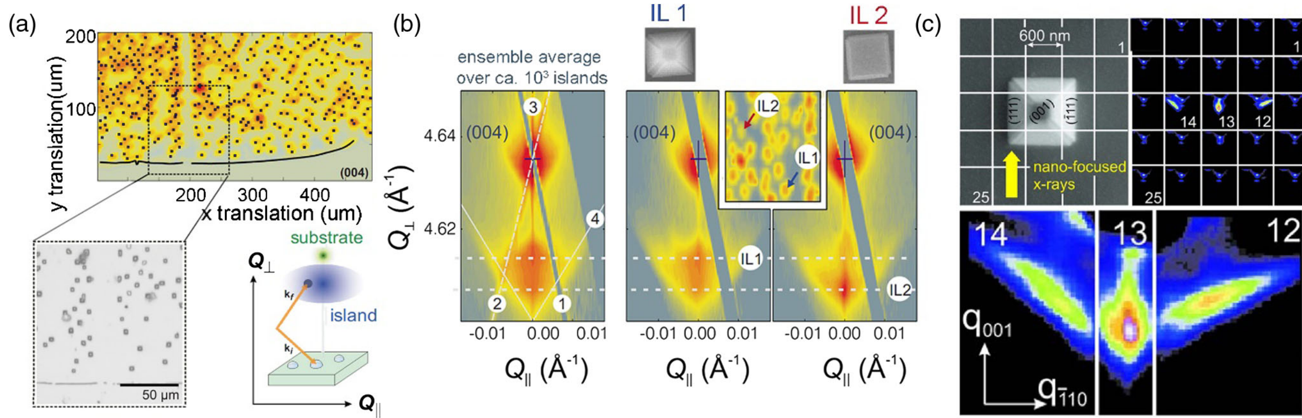

FIG. 16. (a) Top: SXD map showing the diffracted intensity at the **Q** value of (004) Bragg reflection for relaxed SiGe/Si(001). Bottom left: Optical microscopy image showing a portion of the SXD map. Bottom right: Cartoon schematizing the method. When the μm-focused x-ray spot illuminates a single SiGe island a diffused peak is observed, due to lattice spacing distribution inside the SiGe islands (blue halo) together with the sharp (004) peak of the Si substrate (green peak), appearing at a different **Q** value. (b) RSM of SiGe islands around (004) reflection. The left panel was obtained with a defocused beam averaging the scattering from about 10^3 islands. 1: linear detector saturation streak, 2: monochromator streak, 3: Si surface crystal truncation rod, and 4: facet streaks originating from the (111) island side facets. Right panels: RSM from two individual islands IL1 (fully developed truncated pyramid) and IL2 (flat island). The top insets report the corresponding SEM micrographs. Adapted from Mocuta et al., 2008. (c) Top panels: 3×3 μm^2 SEM micrograph of a single SiGe island and corresponding SXD map obtained using the diffusely scattered x-ray intensity in proximity of the symmetric Si(004) reflection. Bottom panel: Reassembled diffraction pattern of a single island, obtained using frames 12–14 of the SXD map. Adapted from Hanke et al., 2008.

measurements. Several advanced studies on the SiGe/Si(001) and analogous systems have been successively carried out (Dubslaff et al., 2010). Of interest are the combined atomic force microscopy (AFM) and micro-XRD *in situ* studies investigating the elastic properties of individual SiGe islands (Rodrigues et al., 2009; Scheler et al., 2009). Successively, the strain fields inside and around a single SiGe island (which serves as a stressor for the Si channel in a MOSFET was mapped using the x-ray nanobeam of ID01 (ESRF) (Hrauda et al., 2011). Tensile strain up to 1% along the source-drain direction in the MOSFET Si channel above the SiGe stressor dot was evidenced using RSM and FEM-based simulations; see Fig. 17 for additional details.

An example of a SiC/Si MOSFET device was reported in Sec. IV.D.4.

2. III-V semiconductors

For more than four decades, the field of optoelectronic devices has been dominated by III-V heterostructures (Esaki, 1986; Cingolani and Ploog, 1991; Chang and Esaki, 1992; Alferov, 2001; Vurgaftman, Meyer, and Ram-Mohan, 2001; Mokkapati and Jagadish, 2009) because of their direct band gap. More recently, applications in high-efficiency solar cells have been realized (Cotal et al., 2009; Gai et al., 2017), while the possibility to realize CMOS devices with

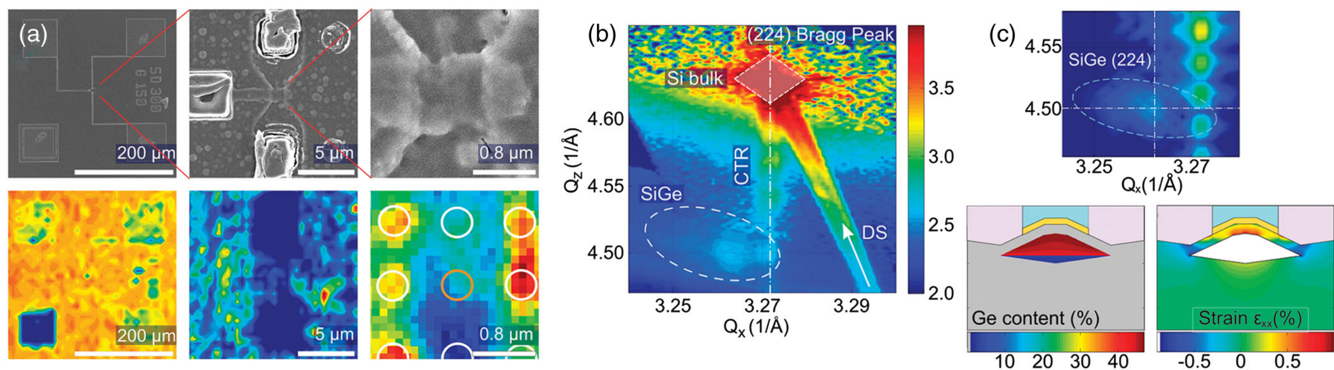

FIG. 17. (a) Top panels: SEM images of the SiGe/Si MOSFET device at increasing magnifications. Bottom panels: SDX maps collected at similar scales; left panel: SDX map monitoring diffracted intensities around the Si(004) reflection for finding the transistor junction; middle and right panels: SDX map monitoring diffracted intensities around the SiGe(224) reflection for locating the dot islands. (b) RSM map around the (224) reflection measured on the SiGe dot buried under the transistor gate; the map includes the Si (224) bulk peak and the SiGe(224) dot signal in its lower left section (highlighted by the dashed circle). (c) Top: FEM-based simulated data, calculated for the region around the diffuse SiGe(224) signal, defined with the orange rectangular box in (b); bottom panels: resulting 2D maps of the Ge concentration and the in-plane strain ε_{xx}. Adapted from Hrauda et al., 2011.

III-V semiconductors (del Alamo, 2011) has attracted interest because of the extraordinary high electron mobility in some III-V compounds, up to 1 order of magnitude higher than in silicon at a comparable sheet density.

In particular, III-V semiconductor nanowires are relevant for optoelectronic device applications (Joyce *et al.*, 2011). Among them, GaAs/InGaAs rolled-up nanotubes (microtubes) [RUN(M)Ts] (Prinz *et al.*, 2000; Schmidt and Eberl, 2001) are peculiar structures, constituted by a crystalline layer which is oriented in all azimuthal directions, thus exhibiting a nearly perfect cylindrical symmetry. These objects can be obtained by rolling up a highly strained single-crystalline multilayer. After a partial release from a substrate by selective underetching, the free multilayer relaxes the strain elastically by rolling up into a well-positioned microtube or nanotube, whose radius is influenced by elastic properties and multilayer thickness (Deneke *et al.*, 2002). Semiconductor RUNTs (Prinz *et al.*, 2000; Schmidt and Eberl, 2001; Schmidt *et al.*, 2002; Huang *et al.*, 2005; Mendach *et al.*, 2006), having a wall thickness of several monolayers, possess an excellent crystalline quality and exhibit several correspondences with their carbon-based equivalents. They find application as integrative components such as 2D confined channels for fluid filling and transport (Deneke and Schmidt, 2004), coils, transformers, capacitors (Schmidt *et al.*, 2002), or optical waveguides (Mendach *et al.*, 2006). Moreover, RUMTs containing light emitters are used as optical ring resonators (Kipp *et al.*, 2006; Mendach *et al.*, 2008; Strelow *et al.*, 2008) for optoelectronics (Li and Mi, 2009), where the emission energy is tuned by the tube local curvature and the strain of both the integrated emitter and the RUMT (Hosoda *et al.*, 2003).

An in-depth characterization of local strain distribution in RUNTs is required to understand the growth process and to optimize the resulting mechanical and electronic properties toward technological applications such as band-gap engineering for optoelectronic devices (Lamberti, 1996a, 1996b). It was demonstrated, combining micro-Raman (Deneke *et al.*, 2004; Songmuang *et al.*, 2006) and TEM (Prinz *et al.*, 2002; Deneke *et al.*, 2004; Songmuang *et al.*, 2006), that RUNTs are formed by an alternation of crystalline and noncrystalline layers representing a radial superlattice (Deneke *et al.*, 2004). Nevertheless, a nondestructive structural characterization of superlattice interfaces, without removal of the RUNTs from the substrate, required the use of XRD (Pietsch, Holý, and Baumbach, 2004). Conventional laboratory diffraction, using x-ray beams with a size between 0.1 and 1 mm, provides structural information statistically averaged over the whole illuminated sample, i.e., over 10^4–10^7 individual RUNTs (Stangl *et al.*, 2009).

The local structure, the lattice parameter, and the strain distributions of individual GaAs/InGaAs RUNTs connected to a GaAs(001) substrate were investigated using the microprobe setup available at the beam line ID01 of the ESRF (Krause *et al.*, 2006), providing a $6 \times 6\ \mu\mathrm{m}^2$ spot at 10 keV (intensity 10^9 photons/s, divergence 2×10^{-2} deg) with a circular Fresnel zone plate [see Sec. S-III.A of the Supplemental Material (729)]. Three pseudomorphic GaAs/InGaAs bilayers have been grown with different GaAs thickness [Fig. 18(a) reports the SEM micrographs for the corresponding RUNTs].

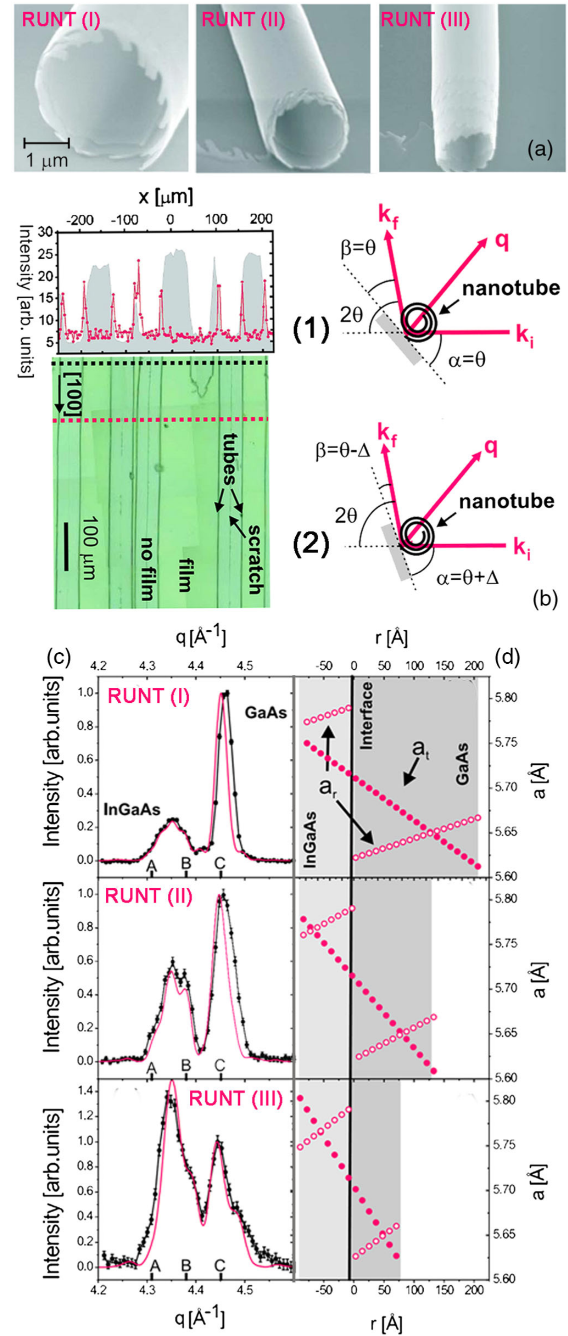

FIG. 18. (a) SEM micrographs of the three pseudomorphic GaAs/InGaAs RUNTs exhibiting different GaAs thickness: (I), (II), and (III). (b) Correlation between the optical microscopy image and the x-ray measurements determining the RUNT position: the selected tube is optically prealigned with its axis perpendicular to the incoming x-ray beam. Because of the rolling up, the crystalline lattice of the RUNT is oriented isotropically perpendicular to the tube axis, and the isotropic scattering intensity in the azimuthal direction is independent of α, geometry (1) By detuning the incident angle, geometry (2), the thermal diffuse background scattering of the substrate is significantly reduced, allowing the scattering of the RUNTs to be discriminated from the background signal. (c) Experimental intensity distribution, normalized to the GaAs (004) reflection for RUNTs (I)–(III) (black dots) and corresponding simulations (pink curves). (d) Lattice parameter distribution in tangential and radial directions (a_t, full dots, and a_r, empty dots, respectively) as used for the simulations. Adapted from Krause *et al.*, 2006.

The alternate use of optical alignment and XRD scans allowed the identification of the individual RUNT for structural characterization; see Fig. 18(b). RUNTs (I)–(III) exhibit a diffraction pattern [Fig. 18(c)] with two well-defined Bragg peaks at $q \approx 4.45$ and at 4.35 Å^{-1}. The former corresponds to the (004) bulk GaAs position [$a_{\text{GaAs}} = 5.653$ Å, $d(004) = 1.413$ Å, and $q = 4.446$ Å^{-1}, see marker C in Fig. 18(c)], while the latter is intermediate between the fully strained (marker A, measured in the as-grown film along the growth direction) and the fully relaxed InGaAs (marker B) from Vegard's law (Vegard, 1921).

This observation indicates that the crystalline bilayer is also maintained in the RUNTs, while the intermediate position of the InGaAs reflection demonstrates a partial strain release in the individual layers, due to a mutual torsional moment. The lattice parameter distributions of the RUNTs have been obtained minimizing the total elastic energy within the continuum strain theory (Grundmann, 2003) [see Fig. 18(d)]. This distribution allows one to simulate the XRD patterns within the kinematic approximation [pink curves in Fig. 18(c)], resulting in an excellent agreement with experimental ones (black dots).

Successively, the same experimental or simulation approach yielded a comprehensive study on the strain state in different semiconductor RUNTs (bilayers, multilayers, and layers with dislocations), evidencing the influence of different layer composition and configuration on lattice relaxation (Malachias et al., 2009). The same group correlated the local strain with the shift in optical response of an AlGaAs/GaAs quantum well integrated in the wall of RUMT along the tube axis, combining micro-XRD (6×5 μm^2 spot) with micro-PL (photoluminescence) (1×1 μm^2 spot) at 10 K demonstrating that the AlGaAs/GaAs RUMTs exhibit different strain states on different windings at the same lateral position (Deneke et al., 2010).

In summary, the discussed studies highlight the potential of micro-XRD as a nondestructive probe to study the local structure of individual semiconductor RUN(M)Ts of various compositions, thicknesses, and sizes, overcoming the limits of incoherent statistical averaging affecting standard diffraction analysis, and providing fundamental understanding in the structure and properties relationship needed to design future integrated devices.

Semiconductor nanowires are considered as promising candidates to realize high-sensitivity and high-selectivity nanosensors, mostly due to their large surface-to-volume ratio and their ability to simultaneously provide optical guiding and electrical driving. The application-driven development of such nanodevices unavoidably relies on the possibility not only to grow, but to also characterize individual nanowires with high space and time resolution. Figure 19(a) reports a scheme of the multimodal characterization setup installed at the ID22 (now ID16B) nanoprobe beam line of the ESRF, which perfectly matches such a challenging necessity. By exploiting this setup, structural, compositional, and optical information can be simultaneously accessed with high temporal and spatial resolution. In particular, during a raster scan of the sample, it is possible to simultaneously collect (i) the XRF signal, using a Si drift detector, (ii) XRD patterns, using a fast readout low noise (FReLoN) camera (Labiche et al., 2007), and (iii) optical

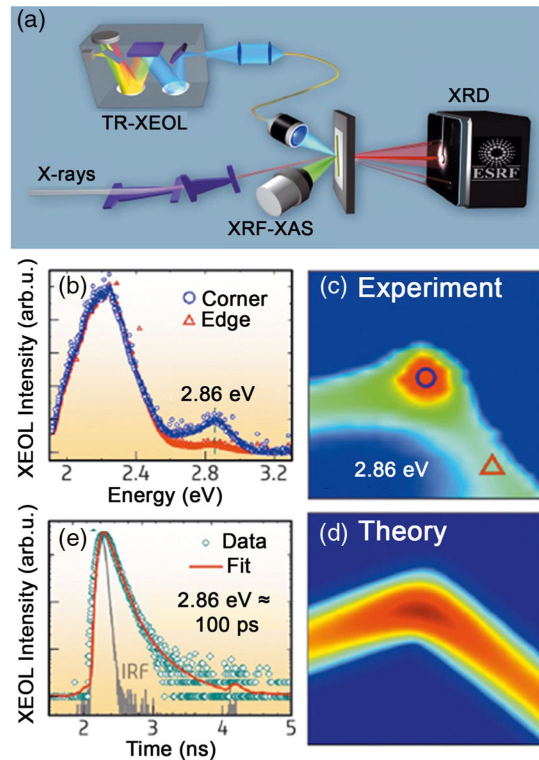

FIG. 19. (a) Scheme of the multimodal nanocharacterization setup available at the ID22 (successively implemented and moved to ID16B) beam line of the ESRF. (b) XEOL spectra collected on the corner (blue circles) and edge (red triangles) points evidenced in (c) with the same symbols. (c) $800 \times 800\,\text{nm}^2$ XEOL intensity map (acquired at the MQW emission energy of 2.86 eV) of a hexagonal core-shell MQW structure. (d) Electron probability density calculated for the same structure. (e) Decay of the time-resolved XEOL signal collected for the MQW emission at the hexagon corner. Adapted from Martinez-Criado, Segura-Ruiz, Alen et al., 2014.

photons emitted upon x-ray excitation (XEOL signal) by employing a far-field optical system.

The nanobeam setup described recently allowed one to probe at the nanoscale the effect of the geometrical quantum confinement in an individual coaxial $\text{GaN}/\text{In}_x\text{Ga}_{1-x}\text{N}/n\text{-GaN}$ nanowire-based light emitting diode (LED) (Martinez-Criado, Segura-Ruiz, Alen et al., 2014). In particular, by exploiting the XEOL technique, it was possible to optically image the nanosized-dependent dynamics in the investigated nanowire.

Nano-XRF analysis confirmed that the nanowire radial composition is consistent with the heterostructure design, whereas the most insightful results were obtained by XEOL. After photoexcitation, both the excited electron and the hole carriers relax by emitting XRF photons, electrons, and lower energy phonons until they reach their respective band minima in proximity of the semiconductor band-gap energy (typically 0.5–3 eV). The radiative recombination of these thermalized electron-hole pairs yields the XEOL signal (see also Sec. III.D), which shows a characteristic decay time in the few tens of ps–few tens of ns range, depending on the spatial overlap of the carriers.

Figures 19(b)–19(d) report an overview on the results obtained by scanning the $\text{In}_x\text{Ga}_{1-x}\text{N}/\text{GaN}$ core-multishell

nanowire with a $60 \times 60\ \mathrm{nm}^2$ nanobeam across its radial direction. The XEOL spectra reported in Fig. 19(b) were collected in the corner and edge regions of the hexagonal cross section of the nanowire. Two emission bands were observed in both positions, including a broad peak at 2.21 eV, assigned to the common yellow band, and a narrower band at 2.86 eV, ascribed to the transitions from the InGaN/GaN MQWs. The spatial projection of the XEOL intensity at 2.86 eV is shown in Fig. 19(c), evidencing that the MQW signal is maximized at the hexagon corners. Based on theoretical calculations, they suggested that such an effect might be due to geometrical quantum confinement. In particular, Fig. 19(d) reports the calculated squared electron wave function for the ground state, showing a clear localization at the corner and a progressive decaying toward the hexagon edges. Operating in the 16-bunch filling mode of the source (50-ps pulses, 5.68 MHz repetition frequency), time-resolved-XEOL data could be simultaneously acquired while scanning the nanowire with the x-ray nanobeam. The decay time of 100 ps found for the time-resolved XEOL signal collected for the MQW emission at the hexagon corner [Fig. 19(e)] supported the occurrence of ultrafast recombination phenomena, likely connected with quantum confinement size effects in the nanowire.

The last example of this section devoted to III-V semiconductors concerns GaAs-based homojunctions that are widely used in the device technology for high-speed high-power applications (Farag, Fadel, and Yahia, 2012). They are realized using epitaxial techniques alternating p- and n-doped GaAs layers of desired thickness grown on a GaAs substrate. Such semiconductor heterostructures are of difficult characterization as no topographical or chemical heterogeneities are present. Figure 20 shows an early example of the applications of PES spectromicroscopy to semiconductor interface research (Barbo *et al.*, 2000), reporting cross-sectional pictures of a sequence of GaAs p-n homojunctions of different thickness grown by molecular beam epitaxy. The experiment was performed at the spectromicroscopy beam line of the ELETTRA synchrotron (Casalis *et al.*, 1995; Marsi *et al.*, 1997) using the photon focusing and scanning approach with a Schwarzschild objective (Margaritondo, 2013). The contrast of the image is based on the shift in energy between the Ga$(3d)$ level in p-type and n-type GaAs: Fig. 20(a) was obtained with photoelectrons corresponding to the Ga$(3d)$ core-level energy in n-type GaAs and Fig. 20(b) for the same

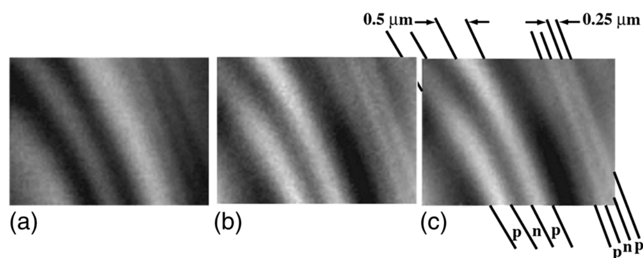

FIG. 20. PES intensity maps for the Ga$(3d)$ peak in a sequence of p-n GaAs homojunctions. (a) Map for the Ga$(3d)$ peak in n-GaAs; (b) map for the Ga$(3d)$ peak in p-GaAs; (c) digit-by-digit subtraction image of (b) from (a). Note the reversed contrast between (a) and (b), further enhanced in the subtraction image. From Barbo *et al.*, 2000.

core level in p-type GaAs. Therefore, bright areas correspond to n-type zones in Fig. 20(a) and vice versa in Fig. 20(b). The n-p contrast is further enhanced in Fig. 20(c) that corresponds to the digit-by-digit subtraction of Fig. 20(b) from Fig. 20(a).

3. II-VI semiconductors

II-VI semiconductors play a relevant role in mid-IR lasers (Deloach *et al.*, 1996; Mirov *et al.*, 2007, 2015) and in LEDs characterized by a large energy emission tunability with a narrow emission spectrum (Haase *et al.*, 2010). Among all possible examples, we selected a characterization of luminescent CdSe/CdS nanocrystals (Li *et al.*, 2003; Carbone *et al.*, 2007; Chen *et al.*, 2013), with the innovative ptychographic coherent x-ray diffractive imaging (PCDI).

PCDI (Thibault *et al.*, 2008; Dierolf *et al.*, 2010) is the scanning-mode version of CDI and was originally proposed by Hoppe (1969) in the field of electron microscopy. In a PCDI experiment, the sample is translated across a finite-size illumination function (probe) and a series of diffraction patterns is registered, while laterally shifting the localized probe across the object (Rodenburg *et al.*, 2007; Thibault *et al.*, 2008). In the data collection scheme, each pattern overlaps with the adjacent ones [see Fig. 21(a)], to fulfill specific overlapping conditions and ensure a large degree of redundancy in the data. In this way, a ptychographical iterative engine (PIE) (Faulkner and Rodenburg, 2004; Maiden and Rodenburg, 2009) can be used combining data redundancy and iterative phase retrieval algorithms to phase at the same time the probe and the object complex transmission function. Mathematically speaking, each diffraction pattern is folded (*ptycho*) into another by convolution, giving the name to the technique. The PIE algorithm employs an on-going estimate of the object function, which is continually updated. It is an iterative method: the calculated exit wave (a product of the complex illumination function of the probe and the transmission function of the object) is propagated to the Fraunhofer plane where the modulus is replaced by the recorded data and phase preserved. Upon back propagation, the resulting exit wave differs from the previously calculated exit wave. The difference between these is used to update the current estimate of the object function, weighted according to the modulus and phase of the probe at each point over the object. PCDI has no limitation on the sample extension and therefore it has been largely applied: it was adopted for label-free cell tomography (Nam *et al.*, 2013) to inspect local strain fields or lattice defects and plastic deformation with nanoscale probes (Godard *et al.*, 2011; Takahashi *et al.*, 2013), and for *in situ* and *operando* studies on planar devices (Hruszkewycz *et al.*, 2013). Figure 21 reports on the PCDI imaging of composite materials, made of 25 μm thick polystyrene (PS) films embedding CdSe/CdS octapod-shaped nanocrystals (De Caro *et al.*, 2016). The question here is to image the exact architecture of the nanocrystals, i.e., to discriminate between linear chains, such as those found for the as-deposited nanocrystals [Fig. 21(b)] and other types of packing. More likely, aggregated clusters due to pod-to-pod contact among the octapod's arms are expected. SEM or TEM direct microscopy cannot be applied in this case, due to the large thickness of the films. Additionally, in order to visualize the nanocrystals, not even individually, a spatial resolution

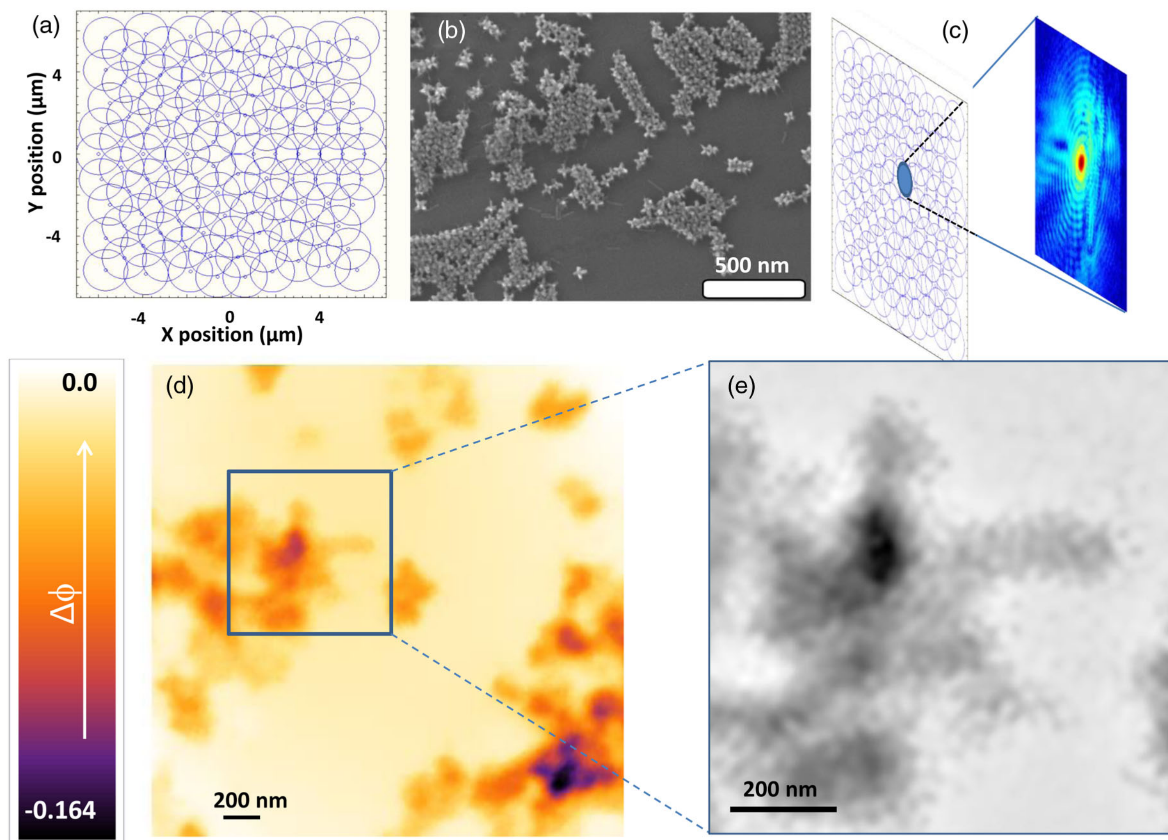

FIG. 21. (a) Data collection scheme of a PCDI experiment realized at the cSAXS PSI beam line. (b) SEM image of CdSe/CdS octapod-shaped nanocrystals grouped in linear chains. (c) Typical speckled diffraction pattern as collected for each of the overlapping area of the explored region. (d) Reconstructed $2.5 \times 2.5\ \mu m^2$ image. (e) Detail of (d). (a), (c) Previously unpublished. (b), (d), and (e) Adapted from De Caro *et al.*, 2016.

better than their size (~100 nm) is needed. The entire area to explore is several μm^2. All these requirements (large penetration depth of the probe, high spatial resolution, large field of view to explore) automatically select PCDI as the only technique which can solve the problem. Experiments were performed at the coherent SAXS (cSAXS) beam line of the Paul Scherrer Institute (PSI) with a 450 nm focused beam, collecting speckled diffraction patterns in cSAXS mode for each of the overlapping areas of the explored region, as schematically depicted in Fig. 21(c). Figure 21(d) shows the reconstructed $2.5 \times 2.5\ \mu m^2$ image, as obtained by phasing the raw cSAXS speckled data set (Dierolf *et al.*, 2010). A smaller area $870 \times 870\ nm^2$ is zoomed in Fig. 21(e). The phased image is obtained at a spatial resolution of 27 nm and allows visualizing the octapods forming interconnected structures.

4. Oxide semiconductors

For this important class of materials, we selected two examples where the oxidic phase has been grown in the form of nanowires: Co-doped nanowires and a system based on a Ga-doped SnO_2/Cr-doped Ga_2O_3 junction. More generally, nanowires have been suggested as ideal systems for the assembly of devices employed in a wide range of applications such as memory, sensing, logic, light emission, and waveguide devices. Large-scale integration of nanowires into functional circuits requires practical interconnections for nanoscale devices. Significant effort has been done toward the development of crossed semiconducting nanowires (Wu *et al.*, 2004), but the formation of individual structures is still challenging and it requires a systematic study of the structural and chemical properties of contact points between different nanowires. In this context, several aspects need to be investigated in detail, including the role of impurities during coupling formation, the local atomic site configuration, the preferable way to tune in a controlled way local composition, diffusion paths, and/or structural modifications, and to avoid phase separation (Chou *et al.*, 2014).

Recently, by using the hard-x-ray nanoprobe obtained with multilayer-coated Kirkpatrick-Baez (KB) mirrors [Sec. S-II.B of the Supplemental Material (729)] at the beam line ID22NI (today ID16B) of the ESRF, such issues have been addressed by investigating a nanowire junction given by Ga-doped SnO_2 nanowires lying across a Cr-doped Ga_2O_3 nanowire obtained in a one-step thermal evaporation method (Martinez-Criado, Segura-Ruiz, Chu *et al.*, 2014). Five polymorphs of Ga_2O_3 (α, β, γ, δ, and ε) are known from the literature, where only the α and β phases exhibit a known crystallographic structure. The monoclinic β-Ga_2O_3 phase is the thermodynamically stable one and shows Ga ions in both tetrahedral and octahedral sites in a 1:1 ratio. Conversely, the α-Ga_2O_3 phase is trigonal and hosts Ga ions in octahedral coordination only. The γ-Ga_2O_3 phase has a spinel structure, hosting Ga cations in both tetrahedral and octahedral sites but with different ratios

compared to β-Ga_2O_3. Finally, SnO_2 exhibits a rutilelike structure, where Sn occupies octahedral sites.

Figure 22 summarizes the x-ray nanoimaging (obtained using a 12-keV $100 \times 100\,nm^2$ spot nanobeam with 5×10^{10} photons/s) and SEM characterization of the individual multiwire structure. From XRF maps, Sn and Ga are efficiently contrasted, and Cr (the dopant present in the Ga_2O_3 wire) is clearly localized. In correspondence to the morphological heterogeneities highlighted by SEM, small features were observed. The junction region [dashed circle in Fig. 22(c)] is magnified in Figs. 22(d)–22(f), using SEM, and both x-ray transmission and XRF nanoimaging. The concentrations of the dopants were estimated as (0.72 ± 0.01) at. % Ga in SnO_2, (6.07 ± 0.01) at. % Sn, and (0.014 ± 0.004) at. % Cr in Ga_2O_3. Previous studies suggested that the physical properties of the multiwire nanostructure, e.g., its magnetic response, are strongly influenced by interdiffusion phenomena occurring though the formation of mixed spinel structures at the heterointerfaces (Nagashima *et al.*, 2012). However, for the studied nanostructure, nano-XRF revealed a compositionally uniform junction region, without any evidence of elemental diffusion, junction-induced defects, and/or agglomeration processes.

The use of Ga K-edge nano-XANES allowed access to deeper information on the partial DOS in the conduction band, in both the junction region and outside [Fig. 22(h)]. Nano-XANES demonstrated that the nanowire junction does not induce any significant structural disorder. Indeed, in both the junction region and outside the XANES were equivalent, showing in both cases peaks ascribed to the Ga sites of β-Ga_2O_3 and α-Ga_2O_3 phases in tetrahedral and octahedral coordination geometry, based on the comparison with reference polymorphs. Nano-EXAFS [Fig. 22(i)] also provided information on the local coordination environment of Ga sites at the junction region. Experimental spectra were fitted using model clusters with a mixed environment of α-Ga_2O_3 and monoclinic β-Ga_2O_3, by fixing the coordination number of first-shell O and second-shell Ga for both α- and β-Ga_2O_3 polymorphs. EXAFS fitting in the nanowire, outside the intersection area, resulted in a Ga-O distance of 1.83 Å, in good agreement with the values reported for tetrahedral Ga sites in β-Ga_2O_3. However, in the junction region, the EXAFS analysis revealed a significantly longer Ga-O distance of 1.86 Å, hence suggesting that a different phase could be formed at the nanowires' crossing point.

Transition-metal ions have been widely used as dopants in semiconductor nanowires because of their interesting magnetic properties and potential use in spintronic applications (Dietl *et al.*, 2000, 2015; Ohno *et al.*, 2000; Heo *et al.*, 2004; Macdonald, Schiffer, and Samarth, 2005; Dietl, 2010; Mino, Gianolio *et al.*, 2013). However, it is difficult to dope these nanostructures by standard growth techniques. An alternative option is ion implantation that allows the control of the concentration with micrometric precision of the dopant atoms using different ion energies and doses and subsequent thermal annealing (see Sec. I.B.3). For these materials, an in-depth, spatially resolved, characterization of the distribution of the dopants and of their local structural and electronic configuration is important to better understand and optimize the implantation and annealing processes. Several studies have employed XANES and EXAFS averaged over an ensemble of nanowires to characterize average local atomic structure and

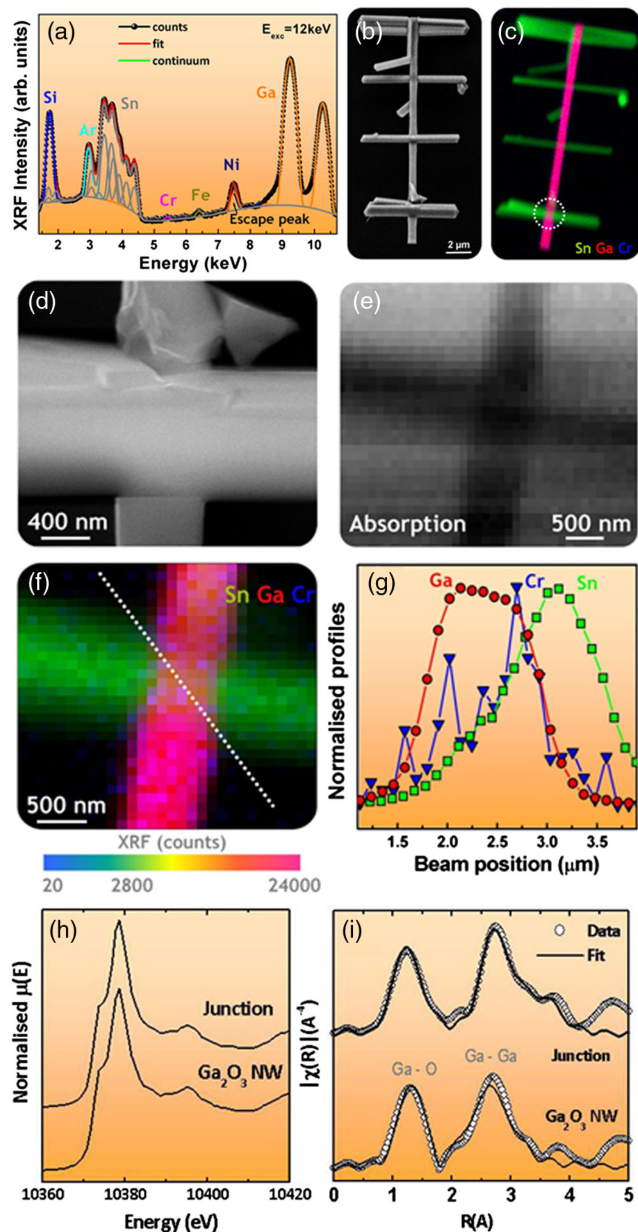

FIG. 22. (a) Average XRF spectrum (collected exciting at 12 keV) of the crossed multiwire structure. (b) SEM micrograph of the structure. (c) Color map of XRF intensities for Ga, Sn, and Cr [red, green, and blue, respectively(light gray, white, and dark gray)], reported using a brightness scale (dark: low counts; light: high counts). A SEM magnification of the region marked with the white circle is reported in (d). (d) SEM micrograph of the nanowire junction. (e) 12-keV x-ray transmission map of the junction region. (f) Detail of the RGB XRF map in the junction region, same color code as in (c). (g) Normalized XRF profiles for Ga (red circles), Sn (green squares), and Cr (blue triangles), acquired along the white dotted line visible in (f). (h) Ga K-edge XANES spectra (vertically shifted for clarity) collected in the junction region and outside. (i) Experimental (white circles) Ga K-edge FT of the EXAFS spectra and respective best fits (solid lines) collected at the junction and outside. Adapted from Martinez-Criado, Segura-Ruiz, Chu *et al.*, 2014.

secondary phases (Yuhas *et al.*, 2007). For several years, it has been hard to provide a stable x-ray nanobeam along the energy scan needed to collect a XANES or, even more, an EXAFS

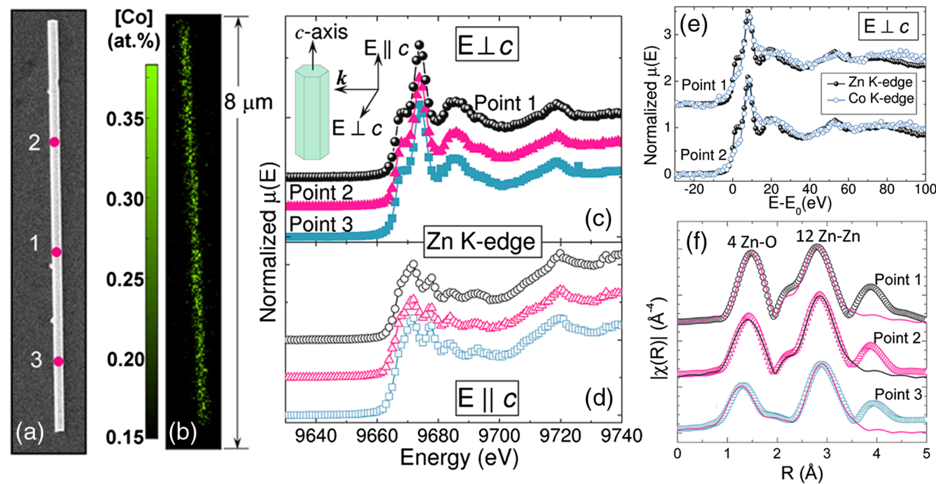

FIG. 23. (a) SEM micrograph of a single ZnO nanowire implanted with Co. (b) Map showing the Co $K\alpha$ and $K\beta$ fluorescence collected using a 12 keV beam. The Co content was determined from the XRF quantification. (c), (d) Zn K-edge XANES spectra, collected at points 1–3 of (a), with the c axis oriented perpendicular (c), or parallel (d), to the electric field vector of the x-ray beam. (e) Zn (black dots) and Co (blue dots) K-edge XANES spectra collected at points 1 and 2. For both edges, the abscissa axis has been obtained rescaling the photon energy with respect to the ionization energy, allowing a direct comparison. (f) Magnitude of the experimental Zn K-edge FT of the EXAFS functions collected at points 1–3 of (a) (scattered dots) and corresponding best fits (solid lines). Adapted from Segura-Ruiz *et al.*, 2011.

spectrum. At the ESRF, using a pair of KB silicon mirrors it was possible to obtain an intense (10^{11} photons/s), monochromatic x-ray spot of $0.1 \times 0.1\ \mu m^2$, stable along a whole EXAFS scan across the Zn K edge (Segura-Ruiz *et al.*, 2011) for studying the short-range order in a single Co-implanted ZnO nanowire. Moreover, the linear polarization of the synchrotron light (Lamberti, Groppo *et al.*, 2003; Lamberti, 2004; Luches *et al.*, 2004) was used to detect preferentially oriented defects created during the ion implantation process.

The regions where the XAS spectra have been collected are indicated in the SEM image reported in Fig. 23(a) (1, 2, and 3 labels). Figure 23(b) reports a Co x-ray fluorescence map allowing the quantitative estimation of the dopant content. This study indicates a homogeneous cobalt distribution along the ZnO nanowire, discarding clustering effects. The effect of beam polarization on the Zn K-edge XANES spectra collected at points 1–3 can be appreciated comparing Figs. 23(c) and 23(d). The spectral features reflect the hexagonal structure, with no evidence of lattice damage at the three points of the ZnO nanowire.

Space-resolved Co K-edge XANES was used to determine the structural and electronic states of implanted cobalt ions along the Zn nanowire [Fig. 23(e)]. The Co K-edge XANES features (blue dots) fully reproduces the Zn K-edge ones (black dots), proving that Co ions are isomorphically incorporated into the wurtzite host lattice at the Zn sites. The oxidation state of implanted Co ions was determined to be +2 after comparison with literature XANES spectra of a high-quality wurtzite $Zn_{0.9}Co_{0.1}O$ epitaxial film (Ney *et al.*, 2008). Zn K-edge nano-EXAFS measurements provide insight on the local order of the host lattice; see Fig. 23(f). The EXAFS study revealed that, along the nanowire, the Zn-O and Zn-Zn distances match those of pure ZnO (1.98 and 3.25 Å) discarding amorphization phenomena and confirming the effectiveness of the thermal annealing in recovering of the ZnO lattice damage induced by the ion implantation process (Segura-Ruiz *et al.*, 2011).

5. Other (nonoxide) magnetic semiconductors

The relevance that magnetic semiconductors had in the last two decades in solid-state and applied physics (Gardelis *et al.*, 1999; Dietl *et al.*, 2000, 2015; Gould *et al.*, 2007; Dietl, 2010; Hirohata and Takanashi, 2014) makes this category of materials worth having an *ad hoc* section in this review in addition to the examples already discussed in Sec. IV.A.4. Selected examples are two XAS studies on Mn-doped GaN and on Si-doped AlGaN and a coherent x-ray diffraction study on Fe_2P nanorods.

The formation of clusters in semiconductors is extremely interesting from both a fundamental and a technological point of view since their presence can strongly modify several physical properties of the material. For example, the distribution and dimension of magnetic inclusions are of primary importance in dilute magnetic semiconductors (Dietl, 2010), which are promising candidates for innovative multifunctional spintronics devices (Cui *et al.*, 2005) and LEDs (Amano, 2015). In this respect, an interesting material is GaN doped with ~5 at. % of Mn which was predicted to show a Curie temperature higher than room temperature (Dietl *et al.*, 2000). The cluster formation in GaN:Mn and the theory of ferromagnetism in these spin-based systems have been widely studied. A crucial issue has been whether the material is an alloy of GaN:Mn or if it is GaN with precipitates or secondary phases which generate the magnetic responses. However, a general problem of cluster-related studies is that the important physical parameters are often not measurable using conventional laboratory techniques.

In this context, the intense x-ray microbeam ($1 \times 1\ \mu m^2$ with photon flux $\sim 5 \times 10^{10}$ photons/s at the Mn K edge) available at the ESRF ID22 beam line (successively implemented and moved

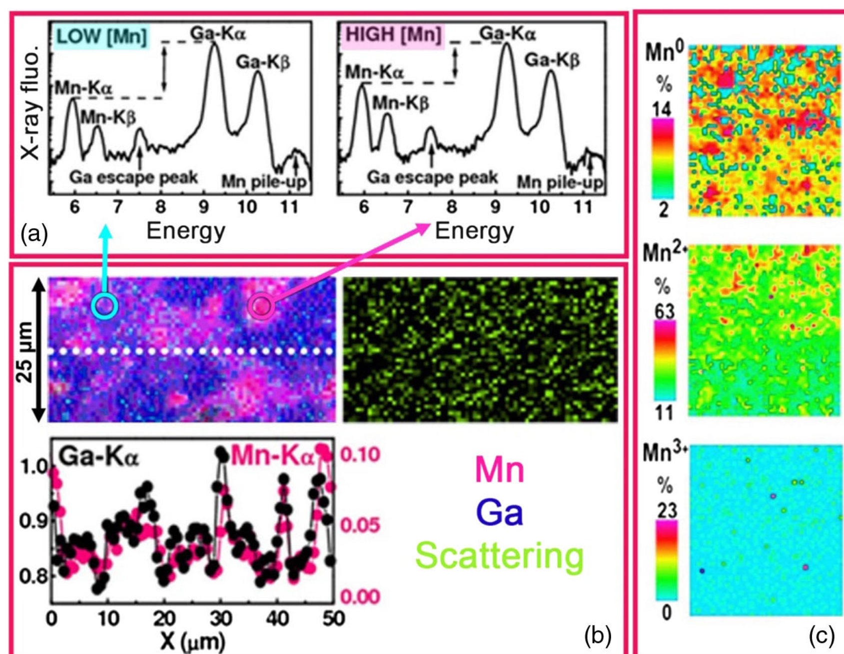

FIG. 24. (a) Average XRF spectra acquired in different areas of a GaN:Mn sample. (b) Color map: pink, blue, and green (dark gray, black, and light gray) correspond to the Mn $K\alpha$, Ga $K\alpha$ fluorescence lines, and Compton scattering signal, respectively. Ga (black) and Mn (pink) fluorescence profiles along the white scan line are also shown. (c) Mn oxidation state maps showing Mn^0, Mn^{2+}, and Mn^{3+} centers. (a), (b) Adapted from Martinez-Criado, Somogyi, Ramos et al., 2005. (c) Previously unpublished figure, reporting data published in Martinez-Criado, Somogyi, Homs et al. (2005).

to ID16B) was a powerful tool to study GaN:Mn layers with Mn contents ranging from 10^{18} up to 10^{21} atoms cm^{-3}. Uniform maps without intensity changes were observed for most of the samples, highlighting a homogeneous distribution of both Ga and Mn at the length scale of the beam size. However, for the highest Mn concentration (5.4×10^{21} atoms cm^{-3}), the data showed a clear correlation between the Ga and Mn locations (see Fig. 24), suggesting a partial substitution of Ga by Mn (Sato et al., 2002). Since the diffusion length of the surface atoms and the local strain field are both finite, Mn clustering becomes more likely in heavily doped samples.

XANES spectra were also acquired at the Mn K edge showing the dipole-allowed transitions from Mn $1s$ states to unoccupied $4p$-like states. At very high Mn doping, the reduced amplitude of all oscillations reflected a modification in the local chemical and crystallographic environments around Mn, confirming the presence of doping-induced disorder effects (Martinez-Criado, Somogyi, Ramos et al., 2005). Successively, the same group investigated in detail the system GaN:Gd. (Martinez-Criado et al., 2008).

With a similar approach, Somogyi et al. (2007) investigated Si impurities in AlGaN, grown by molecular beam epitaxy, using a 2×1 μm^2 beam at the LUCIA station (Flank et al., 2006) of the Swiss Light Source (SLS). Lucia was then moved to SOLEIL synchrotron and replaced at SLS by the Phoenix beam line. They observed by scanning micro-XRF the formation of Si clusters with compositional modulation (higher Al and lower Ga concentrations) within Si-rich precipitates (Fig. 25). By micro-XANES it was highlighted that the static disorder around the Si atoms increases with the Si content, while the hexagonal crystal structure is maintained. These results show that phase separation occurs in AlGaN, although it was believed to be unlikely owing to the small lattice mismatch between GaN and AlN.

Fe_2P magnetic nanorods have been chosen as a representative material to show the potentialities of x-ray CDI (see Sec. III.B). Different types of x-ray CDI experiments have been conducted so far (Chapman and Nugent, 2010): in Bragg

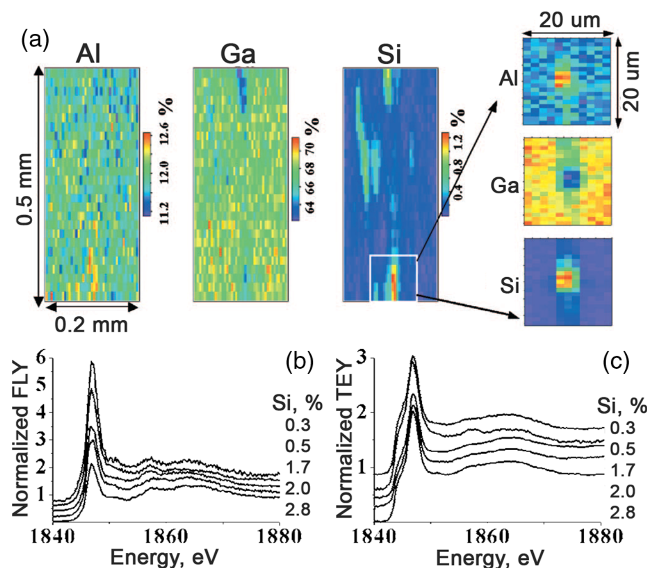

FIG. 25. (a) XRF maps obtained on AlGaN:Si selecting the Al-$K\alpha$, Si-$K\alpha$ and Ga-$L\alpha$ fluorescence lines. The pixel size is 5×20 μm^2 ($H \times V$) in the larger and 2×1 μm^2 in the smaller maps. (b), (c) Si K-edge XANES spectra acquired at points with different Si concentrations in both (b) fluorescence yield (FLY) and (c) TEY modes. Adapted from Somogyi et al., 2007.

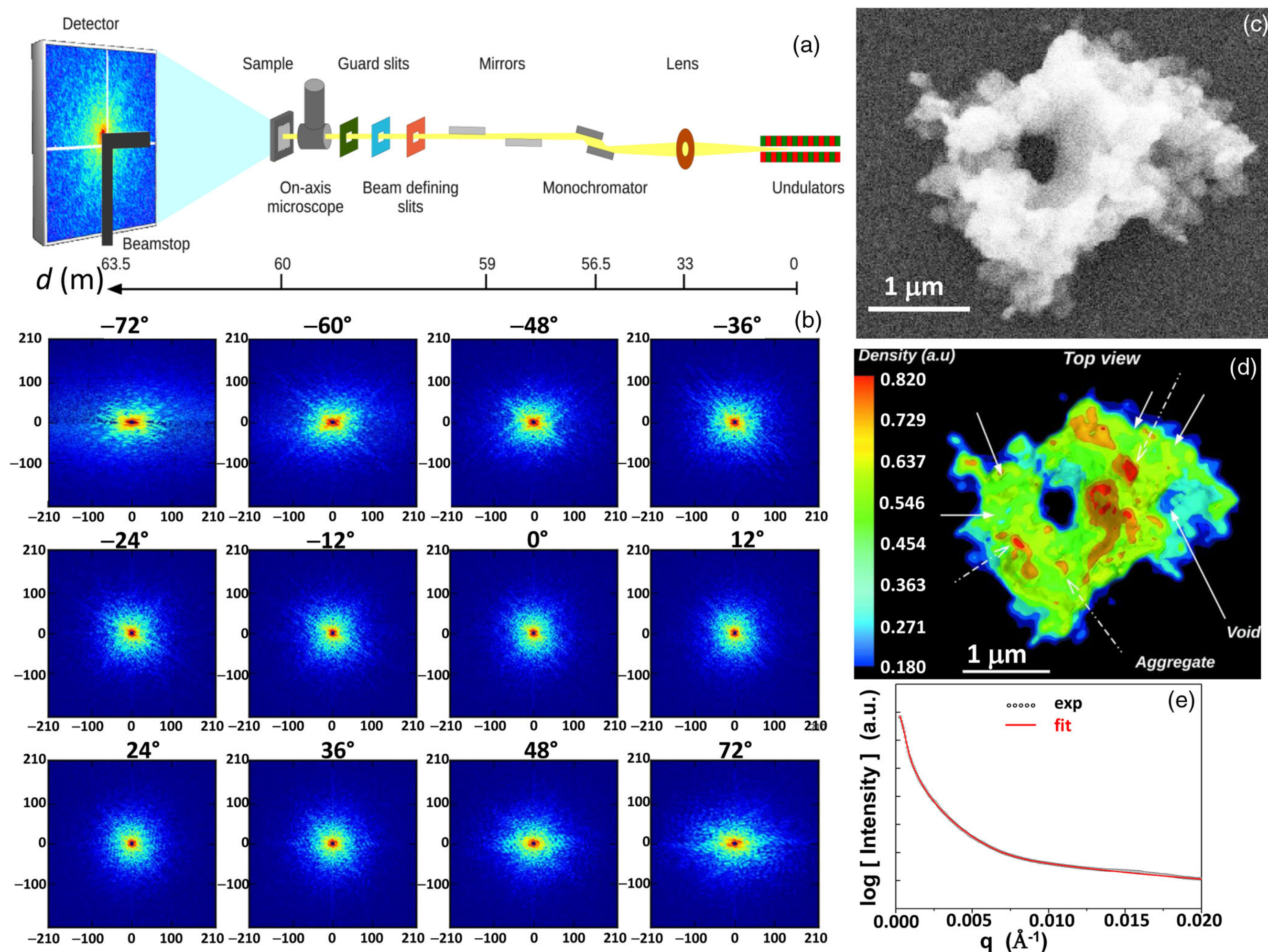

FIG. 26. (a) Sketch of the experimental setup at the ID10 beam line of the ESRF reporting the distance d from the x-ray source of the different elements. (b) Example of some CDI diffraction patterns among the 73 frames taken for sample tilts between −72° and +72° with a step of 2°. (c) SEM image of the investigated Fe_2P cluster. (d) Reconstructed 3D image of the sample (resolution of 59 nm). Continuous arrows show several voids; dashed arrows point to the high-density aggregates. (e) Averaged SAXS profile (experimental, black circles) and computed profile (red line). (a)–(d) From Chushkin et al., 2014. (e) From Dr. Chushkin (ESRF).

geometry (Bragg CDI) (Pfeifer et al., 2006; Clark et al., 2013) or working in the forward direction in SAXS-like geometry, namely, plane wave CDI (Miao, Ishikawa et al., 2002; Chapman et al., 2006) and Fresnel or keyhole CDI (Williams et al., 2006). Dedicated beam lines to perform CDI experiments are today available at most of the synchrotron sources around the world and at FELs. At FELs, having overcome dose-related problems (Howells et al., 2009), see Sec. III.I, interesting crystallographic results have been achieved so far with respect to the structure solution of protein nanocrystals (Ginn et al., 2015). The same concepts have been extended to electrons, realizing electron diffractive imaging experiments (Miao, Ohsuna et al., 2002; De Caro et al., 2010).

Figure 26 shows the CDI data collected at the ESRF ID10 beam line (Chushkin et al., 2014) in transmission geometry, which we call “a coherent SAXS experiment.” A micrometric cluster of Fe_2P magnetic nanorods (length $= 38 \pm 12$ nm, diameter $= 4 \pm 1$ nm) was coherently illuminated [see Fig. 26(b)]. A transmission geometry was adopted with a 10 μm beam, selected by a pinhole, as sketched in Fig. 26(a). The diffraction patterns and the background were measured for 300 s each; the collection of 73 2D diffraction patterns taken for sample tilts between −72° and +72° with a step of 2° required 24 h [Fig. 26(b)]. The SEM micrograph and a projection of the 3D image of the sample, as obtained by phasing the CDI data set in Fig. 26(b), are reported in Figs. 26(c) and 26(d), respectively. The 3D image resolution of the CDI phase-retrieved data is 59 nm, which is insufficient to resolve the individual nanorods but allows one to identify dense aggregates and voids and therefore to speculate on the aggregation process. The 3D speckled SAXS patterns in Fig. 26(b) were radially averaged to obtain the SAXS curve reported in Fig. 26(e) (black circles). The featureless curve was fitted taking into account two structural levels. From the fit [red line in Fig. 26(e)], the authors gained information on the existence of two scattering length scales in the sample, characterized by a gyration radii of $Rg1 = 431.6 \pm 4.1$ nm or $Rg2 = 39.8 \pm 5.5$ nm and power law exponent of $P1 = 3.44 \pm 0.06$ (mass fractal) or $P2 = 1.9 \pm 0.12$ (surface fractal), respectively. The mass fractal component ($Rg1$, $P1$) scales quite nicely with the size of the 3D network of nanoparticles; the surface one ($Rg2$, $P2$) with the length of the nanorods. This example shows that a featureless SAXS

pattern can provide average information of the scattering length scales [Fig. 26(e)], while the speckled cSAXS data set permits one to arrive at a complete 3D structural reconstruction of the electron density [Fig. 26(d)].

B. Metals

Besides their size- and shape-dependent optical properties (Kelly *et al.*, 2003; Sau *et al.*, 2010), metal nanoparticles play a relevant role in different fields, including electrochemistry (Murray, 2008), biomedicine (Liao, Nehl, and Hafner, 2006; Biju *et al.*, 2008; Arvizo *et al.*, 2012), photophysics (Noguez and Garzon, 2009; Linic *et al.*, 2015), surface-enhanced Raman scattering (SERS) (Gopinath *et al.*, 2009; Sanles-Sobrido *et al.*, 2009; Budnyk *et al.*, 2010) water purification (Pradeep, 2009), photocatalysis (Kamat, 2002; Linic *et al.*, 2013), and catalysis (Agostini *et al.*, 2009; Groppo *et al.*, 2010; Dhakshinamoorthy and Garcia, 2012; Campbell, 2013; Zhao *et al.*, 2015; Navalon *et al.*, 2016; Braglia *et al.*, 2017a, 2017b; Bugaev *et al.*, 2017a, 2017b; Manzoli *et al.*, 2017). In this section, examples are chosen among metal nanoparticles relevant in catalysis (Coppens *et al.*, 1992).

In this regard, it is worth underlining that catalysis is the branch of science aimed at (i) increasing the rate of a chemical reaction (e.g., $A + B \to C$, typically finding a new path concerning new intermediates characterized by a lower activation energy) and (ii) improving the selectivity toward the desired product C (usually $A + B$ yields different $C, D, E, \ldots$ products, with different branching ratios) (Chorkendorff and Niemantsverdriet, 2007; Norskov *et al.*, 2014). This goal is achieved by inserting into the reacting medium a substance called a "catalyst." Usually the catalyst undergoes multiple chemical transformations, but at the end of the cycle unlike other reactants (A, B) it remains unchanged, so that it is not consumed and can start the conversion of a couple of new molecules $A + B$ into C, and so on, indefinitely. The main goal of a physical approach in catalysis is the understanding, at the atomic and electronic levels, of the changes undergone by the active phase of the catalyst along the catalytic cycle (Lamberti *et al.*, 1997; Agostini *et al.*, 2007; Janssens *et al.*, 2015; Pappas *et al.*, 2017).

The great benefit of hard-x-ray spectroscopy techniques such as XAS (Prins and Koningsberger, 1988; Evans, 1997; Newton, 2008; Bordiga *et al.*, 2010, 2013; Frenkel *et al.*, 2011; Frenkel, 2012; Bonino *et al.*, 2015; Tromp, 2015; Lamberti and van Bokhoven, 2016; Borfecchia *et al.*, 2018), XANES (Fernandez-Garcia, 2002; Regli *et al.*, 2007; van Bokhoven and Lamberti, 2014; Guda *et al.*, 2015), XES (Glatzel and Bergmann, 2005; Singh, Lamberti, and van Bokhoven, 2010; Seenivasan *et al.*, 2013; Gallo and Glatzel, 2014; Garino *et al.*, 2014; Borfecchia *et al.*, 2015; Groppo *et al.*, 2015; Lomachenko *et al.*, 2016; Tyrsted *et al.*, 2016; Barzan *et al.*, 2017; Martini *et al.*, 2017; Tulchinsky *et al.*, 2017; Stubbs *et al.*, 2018), and hard-x-ray scattering techniques such as XRD (Clausen, Topsoe, and Frahm, 1998; Bazin, Guczi, and Lynch, 2002; Milanesio *et al.*, 2003; Agostini *et al.*, 2010; Ingham, 2015; Andersen *et al.*, 2017), SAXS (Groppo *et al.*, 2012; Agostini *et al.*, 2014; Groppo, Agostini *et al.*, 2015; Ingham, 2015; Li, Senesi, and Lee, 2016), and total scattering (Neilson *et al.*, 2010; Newton *et al.*, 2012; Bozin, Juhás, and Billinge, 2013; Tyrsted *et al.*, 2014; Prasai, Ren *et al.*, 2015; Prasai, Wilson *et al.*, 2015) applied to catalyst investigation is due to the high penetration depth of hard x rays, allowing one to measure catalysts under *operando* conditions, i.e., in the presence of reactants and products from the gas or liquid phases. This requires specific experimental setups, including *ad hoc* conceived reaction cells (Lamberti *et al.*, 2003; Grunwaldt *et al.*, 2004; Meunier, 2010; Bordiga *et al.*, 2013; Doronkin, Lichtenberg, and Grunwaldt, 2017; Agostini, Gianolio, and Lamberti, 2018), where temperature and gas feed composition can be remotely controlled in order to understand structural and electronic changes of the active phase under *in situ* or *operando* conditions.

Most of the heterogeneous catalysts consist of a diluted active phase highly dispersed on a high-surface area support. Standard characterization techniques average the analysis over a wide volume (typically some mm^3); in some cases such an averaging process implies a loss of relevant information and space-resolved experiments become mandatory (de Smit and Weckhuysen, 2008; de Smit *et al.*, 2008; Grunwaldt and Schroer, 2010; Buurmans and Weckhuysen, 2012; Andrews and Weckhuysen, 2013; Grunwaldt, Wagner, and Dunin-Borkowski, 2013; Han *et al.*, 2015; Meirer, Kalirai, Morris *et al.*, 2015; Price, Geraki *et al.*, 2015; Price, Ignatyev *et al.*, 2015; Cats *et al.*, 2016). The recent developments in synchrotron source brightness, x-ray optics, and detector technology previously discussed (Sec. II) have enabled the development of structural and chemical imaging in which 2D or 3D images of the sample are obtained with resolution in the submicrometer, down to some nanometer scale. Here each point of the 2D (3D) matrix contains either a full x-ray scattering pattern (Budai *et al.*, 2008), a full XAS spectrum (Gonzalez-Jimenez *et al.*, 2012; Aramburo *et al.*, 2013; Cats *et al.*, 2013), or a full XRF spectrum, allowing chemical speciation by differential absorption contrast imaging (Meirer, Kalirai, Weker *et al.*, 2015; Meirer, Morris *et al.*, 2015). *A posteriori* the extraction of more detailed, spatially resolved information on the sample will be achieved by *ad hoc* conceived 3D reconstruction analysis codes (Liu *et al.*, 2012, 2013).

1. Chemical imaging of a single catalyst metal nanoparticle

Heterogeneous catalysts consist of an agglomeration of particles having dimension in the μm to some nm range. Several breakthrough experiments have been performed in the last years exploiting x-ray microbeams and nanobeams to investigate the behavior of a single catalyst particle under reaction conditions (Liu *et al.*, 2016). Hereafter, we provide a selection of relevant highlights in this field.

The oxidation state and the local coordination structure of a nickel oxide deposited on a ceria-zirconia support catalyst was characterized by Ni K-edge micro-XAS, discriminating the catalytically active and inactive phases of a single catalyst particle during the CH_4 steam reforming reaction to produce syngas ($CH_4 + H_2O \to 3H_2 + CO$) (Tada *et al.*, 2011).

XRF tomography was used to investigate the 3D deposition of poisoning metals (Fe, Ni, V, Ca, and Ti) within an individual particle of ultrastable Y (USY) zeolite at different catalytic life stages of the fluid catalytic cracking (FCC) reaction (Kalirai *et al.*, 2015). This is a relevant study, as the FCC is a key reaction in petrochemistry to convert the

high-boiling hydrocarbon fraction of petroleum crude oil into more valuable gasoline, olefinic gases, and other products (Vogt and Weckhuysen, 2015). They found that Fe, Ni, and Ca exhibit an important concentration at the exterior part of the USY particle, being significantly colocalized. Their concentrations increase as a function of time during the catalytic life stage, but the deposition profiles remain invariant. Conversely, V penetrates deeper inside the particle with increasing reaction time.

Hard-x-ray nanotomography was used to investigate an individual iron-based Fischer-Tropsch-to-Olefins (FTO) (Van der Laan and Beenackers, 1999; de Smit and Weckhuysen, 2008) catalyst particle at elevated temperatures (1000 K) and pressures (30 bar). 3D and 2D maps with 30 nm resolution have been reconstructed, showing heterogeneities in the chemical composition and pore structure of a single 20 μm catalyst particle (Gonzalez-Jimenez et al., 2012).

A nanoreactor originally designed for high-resolution environmental TEM (Creemer et al., 2008) was adapted for STXM at the beam line 11.0.2 (Kilcoyne et al., 2003) of the ALS synchrotron of the Berkeley National Laboratory (BNL), operating in the soft-x-ray region. The researchers investigated in working conditions at atmospheric pressure up to 350 °C a complex iron-based FTO catalyst, where a mixture of CO and H_2 reactants is converted into hydrocarbon chains through a polymerization reaction. Collecting Fe L_2- and L_3-, C K- and O K-edge NEXAFS spectra with a 35×35 nm^2 sampling mesh, they were able to follow *in situ* both the phase changes of the active phase and the nature of carbon species produced in the reaction.

The last example concerns an environmental scanning photoemission microscopy (SPEM) study performed at the ESCA microscopy beam line (Casalis et al., 1995; Marsi et al., 1997) of the Elettra synchrotron on a PtRh single catalyst particle (Sezen et al., 2015). The beam line is equipped with a dynamic high-pressure setup, based on the control of the μ moles of gas injected into the SPEM chamber to maximize the pressure at the sample surface without exceeding the global pressure limits required for the SPEM operation (Amati, Abyaneh, and Gregoratti, 2013); see Figs. 27(a) and 27(b). Figures 27(c) and 27(d) compared a standard SEM image of a PtRh NP with the SPEM one obtained using the $\mathrm{Rh}(3d_{5/2})$ core level on a similar NP. The identical shape, size, and morphology information encoded in both the $\mathrm{Rh}(3d_{5/2})$ and $\mathrm{Pt}(4f_{7/2})$ SPEM maps (the latter is not reported) indicated a stoichiometric homogeneity of the probed NP. Figure 27(e) reports the $\mathrm{Rh}(3d_{5/2})$ spectra acquired from selected points [labeled as A and B in Fig. 27(d)] of the reduced PtRh particle, compared with that of the reference spectrum acquired on a clean Rh(100) surface. The Rh spectra acquired at points A and B of the reduced particle are equivalent, resulting in two components at

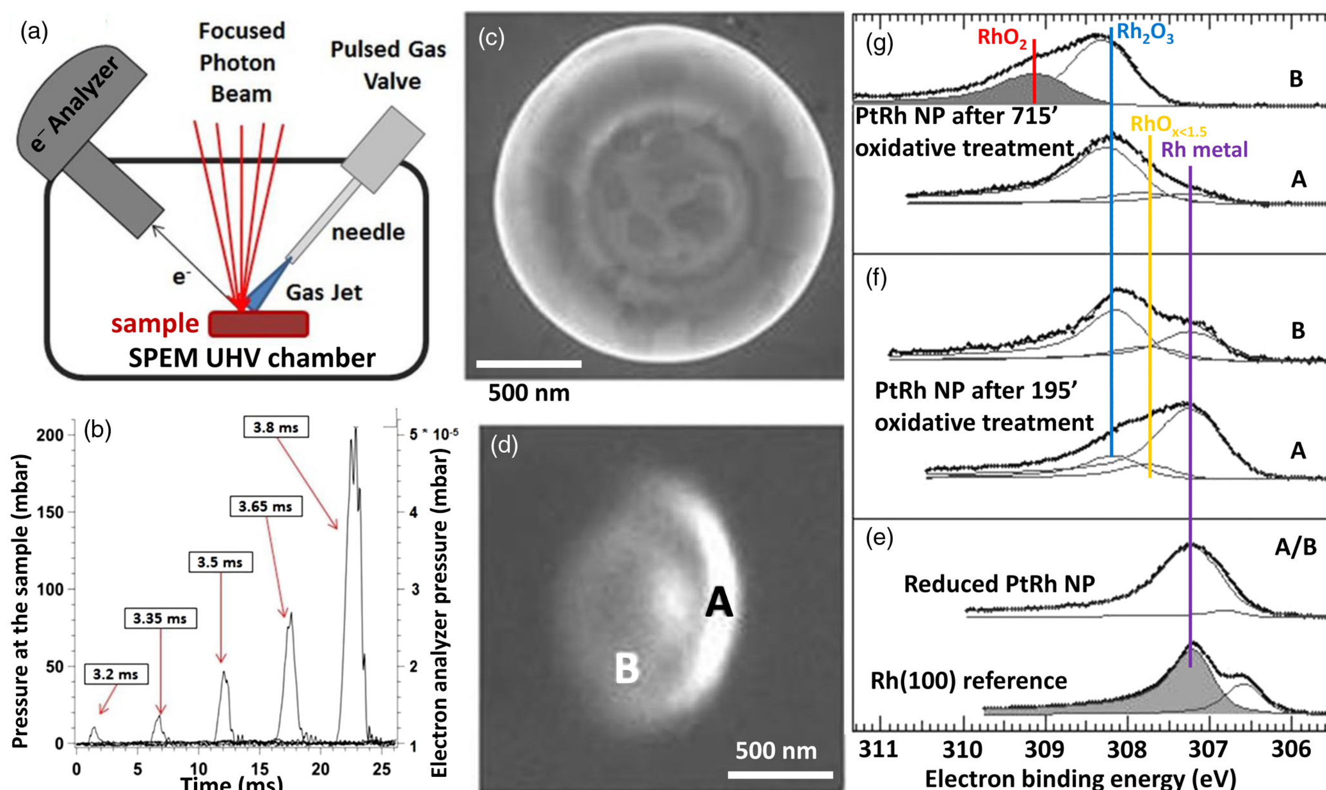

FIG. 27. (a) Sketch of the dynamic high-pressure setup available at the ESCA microscopy beam line at Elettra. (b) Time profiles of the pressure values at the sample (left axis) and inside the electron analyzer (right axis) as a function of pulse duration of a pulsed valve fed by an O_2 gas pressure of 3.5 bar. (c) Standard SEM micrograph of a polycrystalline PtRh particle. (d) SPEM $\mathrm{Rh}(3d_{5/2})$ map of a PtRh particle with a similar shape. (e) $\mathrm{Rh}(3d_{5/2})$ spectra acquired on a metal Rh(100) reference sample and on the reduced PtRh particle. (f), (g) $\mathrm{Rh}(3d_{5/2})$ spectra acquired from the two points of the PtRh particle, labeled as A and B in (d), after an oxidation treatment of increasing duration (195 and 715 min, respectively). All XPS spectra were acquired with a photon energy of 650 eV. Adapted from Sezen et al., 2015.

binding energies (BEs) of 307.2 (strong) and 306.8 eV (weak), which are assigned to bulk and surface components, respectively (Baraldi *et al.*, 2005). The comparison of the Rh bulk component measured on the particle with that of the Rh(100) single crystals shows a marked peak broadening, due to a poor long-range order of the NP and to an effect of the alloying process with Pt atoms. The Rh($3d_{5/2}$) spectra obtained after oxidation at 473 K for 195 and 715 min are shown in Figs. 27(f) and 27(g), respectively. The spatially resolved study reveals a different local oxidation at points A and B of the PtRh NP. The deconvolution of the spectra after 195 min exposure needs three components located at binding energies of 307.2, 307.7, and 308.2 eV due to Rh_2O_3, $RhO_{x<1.5}$, and Rh metal phases, respectively. The different local activity toward oxidation is more evident after the longer exposure [Fig. 27(g)]. The metallic component is extremely weak at A and completely absent at B. The deconvolution of the spectrum acquired at B needs an additional component at BE $= 309.0$ eV, assigned to a RhO_2 phase, and the Rh_2O_3 component becomes dominant in both spectra. The analysis of the Pt($4f_{7/2}$) peak (not reported) resulted in an analogous behavior for Pt with the only major difference of a lower oxidation rate with respect to Rh. The observed compositional complexity of the PtRh particles confirms that in catalytic reactions only fractions of the particle surface behave as an active catalyst (Sezen *et al.*, 2015).

In addition to the discussed soft- and hard-x-ray methods, it is worth mentioning that also UV-vis, synchrotron-based IR, and confocal fluorescence microspectroscopy can be used to shed light on working catalysts at the single particle level (Qian *et al.*, 2014; Kerssens *et al.*, 2016).

2. Catalytic beds

In a fixed-bed catalytic industrial reactor, typically a cylinder from a few to some meters in diameter with a length ranging from some to several meters, the reactants (in the gas or a liquid phase) flow through the reactor length (technically defined as a catalytic bed) interacting with the catalyst and giving rise to the desired products. This industrial setup implies that the atmosphere surrounding the catalyst is progressively different while moving from the beginning (where it is rich in reactants and poor in products) to the end of the catalytic bed (where it is poor in reactants and rich in products). This also implies that the average composition of the active phase may be different, as it is subjected to different reaction conditions. The optimization of the chemical composition and of the operation temperature of a fixed bed catalytic reactor requires two-dimensional space and time-resolved *operando* experiments, where the nature of the active phase can be probed along the catalytic bed (space resolution) and along the response of the catalyst to external stimuli such as temperature or gas composition changes (time resolution).

At the laboratory scale, a fixed bed catalytic reactor is easily simulated with a capillary of defined diameter (to optimize x-ray absorption). Figure 28(a) schematizes such an experimental setup optimized to follow with time and space resolution the partial oxidation of hydrocarbons to CO and H_2, which is an important alternative to presently utilized processes in natural gas and biomass conversion such as steam and autothermal reforming (Plass and Reimelt, 2007). The investigated catalyst was a 2.5 wt. % Rh-2.5 wt. % Pt/Al_2O_3 system prepared by flame spray pyrolysis. The authors monitored Pt L_3-XAS and online mass spectrometry of the gas outlet during heat-up in the reaction gas mixture ($CH_4/O_2 = 2/1$ in He carrier) (Kimmerle *et al.*, 2009). Pt L_3-edge XANES is a technique of choice to monitor the oxidation state of platinum as it mainly promotes core $2p_{3/2}$ electrons into empty $5d_{3/2}$, $5d_{5/2}$, and $6s$ valence states, so mainly probing the unoccupied density of $5d$ and $6s$ states. As the electronic configuration of platinum is Pt^0 ($6s^1 5d^9$) and Pt^{II} ($6s^0 5d^8$), an increase of the Pt oxidation states results in a higher density of unoccupied $5d$ and $6s$ states that results in an increased Pt L_3-edge white line intensity (Hall *et al.*, 2003; Yoshida *et al.*, 2005; Oien *et al.*, 2015), the absorption resonance at 11 596 eV in Fig. 28(b). This means that, without collecting a whole XANES spectrum, fixing the monochromator at that specific energy, it will be possible to follow with a high time resolution the change in oxidation state of the active platinum phase. A full-field x-ray absorption spectroscopic microscopy setup (Sec. III.G.1), realized locating a FReLoN camera (Labiche *et al.*, 2007), provides the simultaneous space resolution.

Below the ignition temperature (330 °C oven temperature) only CO_2 and H_2O were detected as products by mass spectrometry, and XAS revealed that the whole catalyst bed stays in the oxidized phase. At temperatures higher than ignition, XAS showed that the Pt oxidation state decreases from $+2$ to 0, while moving from the inlet to the outlet of the catalytic bed as schematically represented in Fig. 28(a).

Monitoring the central part of the catalytic bed, a change in the XAS spectra was observed in the s-time scale, as shown in Figs. 28(c)–28(g). In this sequence, the working catalyst was heated up to and above the ignition temperature (reached at $t_1 = 0$) with a ramp rate of 5 °C/ min. The x-ray camera collected frames at a frequency of 4 Hz, monitoring the changes in the oxidation state of the active Pt phase each 1.25 °C. The darker color progressively appearing in Figs. 28(c)–28(g) indicates a decrease in the x-ray absorption at 11 596 eV, testifying the $Pt^{II} \rightarrow Pt^0$ reduction, which progresses from the outlet of the catalytic bed upstream toward its inlet (Kimmerle *et al.*, 2009). In the same study, they were able to closely investigate single catalyst particles. The authors observed that reduction does not occur at once over the whole particle, but progresses from its inside outward [Figs. 28(h)–28(l)] within a time scale of less than 2 s.

The same group investigated the structure of Fe and Cu sites along the selective catalytic reduction (SCR) of NO_x by NH_3 and related reactions (NH_3 adsorption or oxidation, NO oxidation) using space- and time-resolved XAS along the catalyst bed over Fe-β, FeZSM-5 zeolites and Cu-SAPO-34 catalysts (Doronkin *et al.*, 2014). They found important oxidation state gradients for both Fe and Cu along the catalytic bed for the reactions involving NH_3 and NO_x SCR. For the NH_3 oxidation reaction, a less pronounced gradient was observed. The oxidation state gradient was correlated with the NH_3 concentration and was more relevant in the presence of NO_x. Above 250 °C the Fe and Cu sites at the beginning of the catalyst bed were found in a partially reduced state, whereas they were more oxidized in the subsequent zones where NH_3 and NO concentrations decrease. Again above

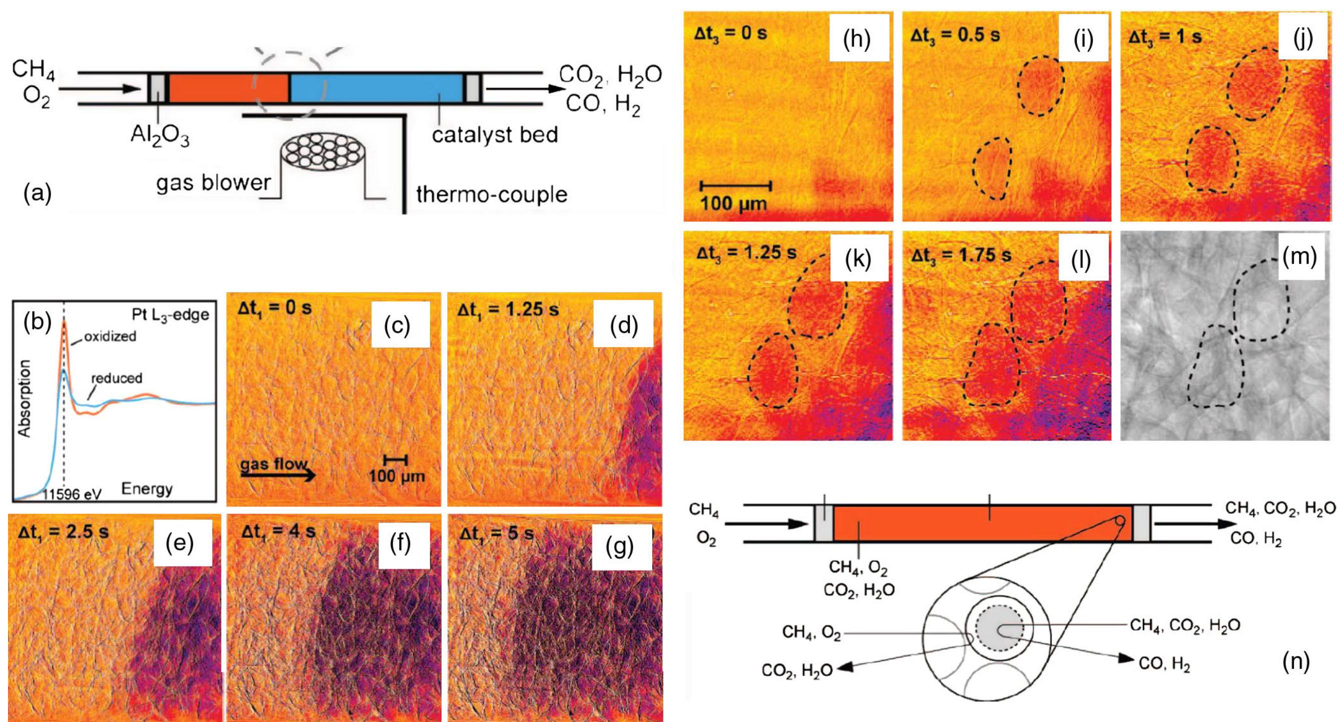

FIG. 28. (a) General scheme of a typical fixed-bed quartz capillary setup with reactor, gas blower, and thermocouple. The red and blue (dark and light gray) represent the parts of the catalytic bed where Pt particles are in the oxidized and reduced phases, respectively. (b) Pt L_3-edge XANES spectra of oxidized and reduced Pt phases (measured at the inlet and the end zone of the catalytic bed, respectively). The highest contrast between the spectra of the two species occurs at 11 596 eV. (c)–(g) Time evolution of the front of reduction of the catalyst moving through the middle part of the fixed bed monitored by measuring the absorption coefficient at 11 596 eV. The size of the reported region is $1 \times 1\ \mathrm{mm}^2$: reduced species (red-violet, dark gray); oxidized species (yellow-orange, light gray). (h)–(l) Similar to (c)–(g) for the reduction (ignition) of single particles. (m) Pure x-ray absorption image of the region monitored in (h)–(l). (n) Model for the reduction of single particles at the end of the catalyst bed during ignition of the catalytic partial oxidation of methane. O_2 is fully consumed in an outer layer and reforming reactions occur on the inside, which causes the noble metals to be reduced. Adapted from Kimmerle *et al.*, 2009.

250 °C, Fe zeolites exhibit a reverse effect with the Fe oxidation state that decreases from inlet to outlet. This was explained in terms of ammonia inhibition. The obtained data allowed them to conclude that both NH_3 and NO_x are involved in a reaction over the corresponding transition-metal site, and the metal site reoxidation is a rate-limiting step of the NH_3-SCR for these catalysts. In a successive work, they extended this study using valence-to-core XES spectroscopy (Gunter *et al.*, 2016).

C. Superconductors

Since its discovery in the mid-1980s (Bednorz and Muller, 1986, 1988; Muller, Takashige, and Bednorz, 1987), high-temperature superconductivity is still a complex field puzzling solid-state physicists (Fradkin, Kivelson, and Tranquada, 2015; Gor'kov and Kresin, 2018). High-transition-temperature (high-T_c) oxide superconductors are characterized by complex structures in which oxygen interstitials or vacancies can influence the bulk properties. For instance, the oxygen interstitials in the spacer layers separating the superconducting CuO_2 planes can undergo ordering phenomena in $Sr_2O_{1+y}CuO_2$ (Liu *et al.*, 2006), $YBa_2Cu_3O_{6+y}$ (Frello *et al.*, 1997), and La_2CuO_{4+y} (Fratini *et al.*, 2010), which induce enhancements in the transition temperatures with no changes in hole concentrations.

Bianconi and co-workers (Fratini *et al.*, 2010) employed the 1 μm^2 beam available at the ESRF ID13 beam line to show by scanning x-ray microdiffraction that the ordering of oxygen interstitials in the La_2O_{2+y} spacer layers of La_2CuO_{4+y} is characterized by a fractal distribution up to a maximum limiting size of 400 μm. Interestingly, these fractal distributions of dopants seem to enhance superconductivity at high temperature.

Using the same setup they also performed a mixed real- and reciprocal-space study of the spatial heterogeneity of the lattice incommensurate supermodulation in a single crystal of $Bi_2Sr_2CaCu_2O_{8+y}$ with $T_c = 84$ K, highlighting an amplitude distribution of the supermodulation with large lattice fluctuations at the microscale (Poccia, Campi *et al.*, 2011).

The same approach was also employed to image the spatial distribution of both short-range charge-density-wave "puddles" (domains with only a few wavelengths) and quenched disorder in $HgBa_2CuO_{4+y}$ (Campi *et al.*, 2015), the single-layer cuprate with the highest critical temperature (Karpinski *et al.*, 1999). They highlighted the fact that even in this "ideal" single-layer system at optimum doping ($T_c = 95$ K), the charge-density-wave order self-organizes

into puddles, forming an inhomogeneous landscape with an emergent complex network geometry. These results confirm the universality of mesoscale phase separation even in the most optimized superconducting cuprates, suggesting that the superconductivity will be nonuniform throughout what is a granular medium.

The two examples which will be discussed in more detail in this section are the scanning micro-XRD study of $K_xFe_{2-y}Se_2$ as a function of temperature and the use of an x-ray nanobeam to modify the conducting properties of $Bi_2Sr_2CaCu_2O_{8+\delta}$ single crystal, realizing an intrinsic Josephson junction device.

1. Structural investigations of high-temperature superconductors

Recently Bianconi and co-workers (Ricci *et al.*, 2015) employed the $2 \times 2\ \mu m^2$ beam available at the coherence beam line P10 of PETRA III synchrotron in Hamburg to investigate by scanning micro-XRD the different phases in superconducting $K_xFe_{2-y}Se_2$ as a function of temperature. In an early study (Ricci *et al.*, 2011) they highlighted an intrinsic nanoscale phase separation in $K_xFe_{2-y}Se_2$ reporting the coexistence of a magnetic phase, showing an expanded lattice with superstructures ascribed to Fe vacancy ordering and a nonmagnetic phase with an in-plane compressed lattice. In their last study Ricci *et al.* (2015) monitored the thermal evolution across the superconducting transition temperature ($T_c \sim 32$ K), phase separation temperature ($T_{ps} \sim 520$ K), and iron-vacancy order temperature ($T_{vo} \sim 580$ K). They detected an iron-vacancy ordered tetragonal magnetic phase (AFM phase), a minority orthorhombic metallic filamentary phase, and an interface phase with tetragonal symmetry. The metallic phase is surrounded by this interface phase below ~300 K, and it is embedded in the insulating texture. The spatial distribution of coexisting phases at different temperatures, reported in Fig. 29, highlights the formation of protected metallic percolative paths in the majority texture with large magnetic moment, required for the electronic coherence for the superconductivity. In addition, they reported a clear reorganization of iron-vacancy order around the T_c and T_{ps} and they highlighted that the interface phase, mostly associated with a different iron-vacancy configuration, may be important for protecting the percolative superconductivity in $K_xFe_{2-y}Se_2$.

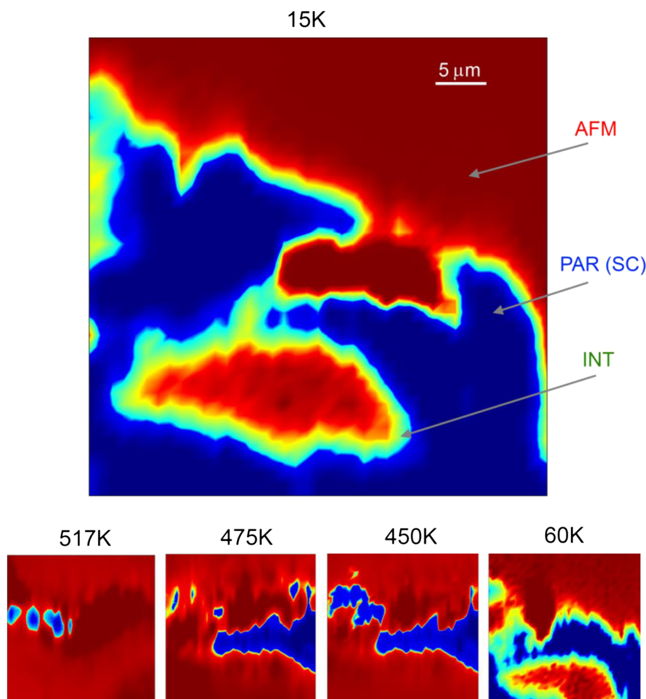

FIG. 29. Spatial distribution of different $K_xFe_{2-y}Se_2$ phases at 15 K. The intensity distribution is obtained by integrating intensities of (004) diffraction peaks corresponding to different phases. The interface phase (green, white) is clearly visible between the majority AFM phase (red, dark gray) and the minority metallic filamentary phase (blue, black). The lower panels show the spatial distributions of different phases at several temperatures, revealing the evolution of percolative paths (blue) below the phase separation temperature, getting protection of the interface phase (green) at low temperature. Adapted from Ricci et al., 2015.

Another interesting example of the application of space-resolved XRD to superconductor oxides is the study of the growth mechanism of nonlinearly shaped $YBa_2Cu_3O_x$ microcrystals (Cagliero *et al.*, 2012). The researchers performed nano-XRD using the $152 \times 107\ nm^2$ beam of the former ESRF ID22 beam line (presently ID16B) and they demonstrated that the crystals show a structural arrangement with the cell oriented along the starting growth direction, laterally shifting in its stacking while the growth proceeds, thus giving rise to a macroscopic curvature without generating twinned domains.

2. Direct-write x-ray nanopatterning of cuprate superconductors

This section is devoted to the discussion of a new emerging research line which exploits the x-ray microbeams and nanobeams not to characterize, but to modify the materials' properties in a controlled way, exploiting an effect that normally is considered unwanted radiation damage as discussed in Sec. III.I. In the past, conventional x-ray lithography already showed the potential to achieve definitions down to 20 nm, based on the traditional process using the x rays to induce some difference in the chemical resistance of the photoresist to the developing solution employed in the etching step. However, further developments exploiting radiation with shorter wavelengths have been hindered by problems related to the fabrication of suitable masks with both high contrast in their absorbing power and small enough features (Marmiroli and Amenitsch, 2012).

One-step direct-write techniques could overcome the inherent limitations of the traditional approach based on photoresist impression and subsequent etching. Actually, some direct-write techniques have been developed to modify the substrate properties without any photoresist. Among them, the focused-electron beam and the focused-ion-beam-induced deposition and etching (Tseng, 2005; Randolph, Fowlkes, and Rack, 2006), along with the scanning-probe lithography (Tseng, Notargiacomo, and Chen, 2005), are the most common. Also some studies employing x rays have been reported, mainly devoted to the patterning of organic or organometallic materials (Katoh *et al.*, 2001; Costacurta *et al.*, 2010; Leontowich and Hitchcock, 2011; Leontowich *et al.*, 2013).

Concerning inorganic materials, a few experiments have shown that SR can directly modify their properties by photon-induced displacement of light atoms in their crystal structure. For instance, Larciprete *et al.* (2002) created clusters of color centers in LiF with typical sizes of about 500 nm by inducing fluorine vacancies employing the 100 nm beam at 640 eV of the ESCA microscopy beam line at Elettra. Another experiment succeeded in modifying the transition temperature T_c of a La_2CuO_{4+y} cuprate superconductor using a 100 μm beam at 12.4 keV (Poccia, Fratini *et al.*, 2011).

Recently Pagliero *et al.* (2014) showed that irradiation with a $117 \times 116\,nm^2$ beam at 17 keV can affect both structural and electronic properties of $Bi_2Sr_2CaCu_2O_{8+\delta}$ (Bi-2212) microcrystals, which have a typical $T_c \approx 80$–90 K. In this material the oxygen nonstoichiometry plays a key role since oxygen content is directly related to the structural and electronic properties, being able to tune the material T_c and even to drive it into a nonsuperconducting state (Inomata *et al.*, 2003; Cagliero *et al.*, 2009; Mino, Bonino *et al.*, 2017; Mino, Borfecchia *et al.*, 2017). The study highlighted the fact that the nanobeam induces a progressive oxygen depletion in the microcrystals resulting in c-axis elongation and increase of electrical resistance.

These results paved the way for the realization of the first electrical device by direct-write hard-x-ray nanopatterning (Truccato *et al.*, 2016). Indeed, the Bi-2212 structure can be described as a stack of superconducting crystal planes containing Cu ions, intercalated by insulating planes containing Bi ions. This special crystal structure has a twofold consequence: (i) the current senses much less resistance when flowing along the Cu planes (ab plane) compared to the normal direction (c axis), and (ii) in the superconducting state all the Cu planes are coupled via the Josephson effect because of the thinness of the Bi insulating layers (Kleiner *et al.*, 1992). This intrinsic Josephson junction (IJJ) structure can be exploited to obtain radiation emission in the THz range. In order to exploit the IJJ effect the current has to be forced to flow along the c axis by patterning the crystal by photolithographic processes or by FIB etching (Latyshev *et al.*, 1999), thus introducing vacuum/oxide interfaces at some stage of the process to define the device geometry. However, the observation that a high enough x-ray dose could drive the material into a nonsuperconducting state suggested the possibility to pattern it into the desired geometry using a hard-x-ray nanobeam without intermediate photoresist-related and etching stages.

Figure 30(a) shows the typical chip used for x-ray nanopatterning, allowing *in situ* electrical characterization. The Bi-2212 crystals were irradiated with a $57 \times 45\ nm^2$ probe at the ESRF ID16B beam line in order to pattern two "trench" regions by locally inducing nonsuperconducting properties [Figs. 30(b) and 30(c)]. By displacing the trenches along the direction of the crystal thickness (trench 1: up, trench 2: down), the current can be forced to flow along the c axis, i.e., normally to the Cu planes, obtaining a zigzag path for the current.

Experimental evidence of successful patterning is provided by Fig. 30(d) since the typical Josephson behavior of these I-V curves can be observed only if the current flows along the direction normal to the superconducting Cu planes. Direct SEM observation revealed that the material was not removed from the trench regions and only some local crystal expansion occurred. Nano-XRD patterns acquired in the trench regions confirmed that the Bi-2212 crystal structure was preserved, with the appearance of some Bi_2O_3 that could be compatible with oxygen loss from the crystals.

More recently, the same group reported the fabrication of a Josephson device on a Bi-2212 microcrystal by drawing two single lines of only 50 nm width using a 17.4 keV synchrotron nanobeam (Mino, Bonino *et al.*, 2017). A precise control of the fabrication process was achieved by monitoring *in situ* the variations of the device electrical resistance during x-ray irradiation [see Fig. 31(a)], allowing one to stop the irradiation as soon as the desired electrical effect is obtained, without significant distortion of the crystal structure.

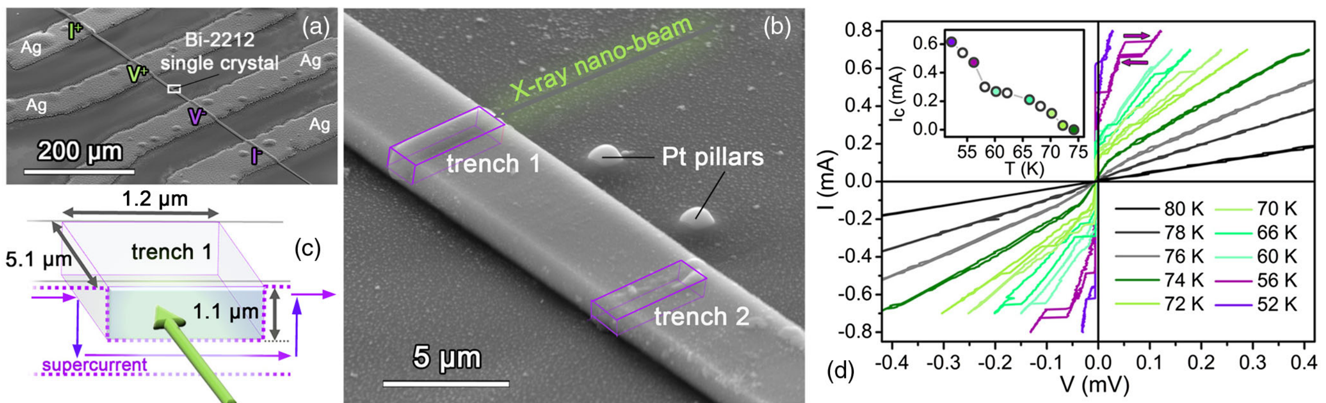

FIG. 30. (a) Typical layout of the chip used for device writing. Current and voltage electrodes are labeled as I^+, I^-, V^+, and V^-. (b) Irradiation geometry used at the ESRF ID16B beam line to pattern the device in the central part of the chip. Pt pillars are used for alignment purposes only. Superconducting Cu planes are parallel to the substrate. (c) Sketch of trench 1, along with the supercurrent path induced by the trench. The green arrow represents the x-ray nanobeam. (d) I-V characteristics of a patterned device measured at constant temperatures between 52 and 80 K. The purple arrows exemplify the typical hysteretic pattern in the case of $T = 56$ K. The inset shows the temperature behavior of the corresponding critical current values I_c. Void circles refer to curves that have not been shown in the main panel for clarity. Unpublished figure reporting data published in Truccato *et al.* (2016).

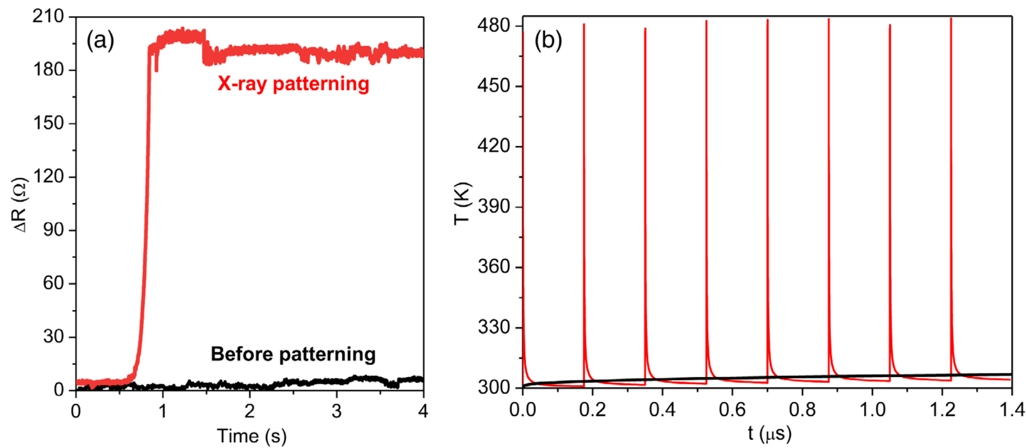

FIG. 31. (a) Variation of the electrical resistance of the Bi-2212 sample measured online during the x-ray exposure to write the first trench (red curve, dark gray). The black curve represents the initial sample resistance immediately before the x-ray nanopatterning procedure. (b) Temporal evolution of the sample temperature calculated with the finite-element method at the point of maximum temperature considering the average continuous photon flux (black curve) and the pulsed nature of SR (red curve, dark gray). The initial temperature of the system was set to 300 K. Previously unpublished figure reporting data published in Mino, Bonino *et al.* (2017).

To clarify the microscopic origin of the observations, the authors performed time-dependent finite-element model simulations to model the heating effect of the x-ray nanobeam, taking into account the intrinsically pulsed nature of synchrotron radiation [see Fig. 31(b)]. They showed that, considering the average heating power density over macroscopic time scales, the sample temperature increases by only 23 K, reaching the steady state after a few milliseconds. Conversely, considering the instantaneous heating power density (the experiment was performed in 16-bunch filling mode), peak temperature increases up to 180 K, which can be sufficient to significantly modify the oxygen content (Cagliero *et al.*, 2009; Mino, Borfecchia *et al.*, 2017).

These results highlight the fact that a conceptually new mask-free patterning method for oxide electrical devices based on x rays is really possible, with potential advantages in terms of heat dissipation, chemical contamination, and high aspect ratio of the devices.

D. Devices

The spatial resolution of x-ray nanobeams can also be exploited for investigating a working device. The last example of the previous section already represents a study in this direction, while a GeSi/Si MOSFET device was discussed in Sec. IV.A.1. Selected examples for this section are a III-V multi-quantum-well laser for optoelectronic (Sec. IV.D.1), memristive devices (Sec. IV.D.2), the investigation of impurities in Si solar cells (Sec. IV.D.3), and a SiC/Si MOSFET (Sec. IV.D.4).

1. MQWs for optoelectronic applications

Multi-quantum-well structures realized by quaternary III-V semiconductor alloys are key components in optical communication systems. Optoelectronic devices often require the integration of two different functions in the same chip. Selective area growth (SAG) (Coltrin and Mitchell, 2003) is a powerful technique to achieve monolithic integration of multifunctional structures with complementary electronic and optical properties. SAG is based on the perturbation of the precursor fluxes caused by a suitable mask (usually SiO_2). When the metalorganic compounds impinge on the dielectric mask, they are deflected and migrate through the unmasked regions of the substrate where the growth takes place. In this way, the precursors coming from the gas phase are enriched by the flux deflected by the mask resulting in a variation in composition and thickness of the material grown near (SAG region) and far (FIELD region) from the mask [Fig. 32(a)].

The gradient of the layer thickness and the chemical composition in the growth plane, obtained with the SAG technique, requires highly focused beams to properly determine the multi-quantum-well period and the barrier and well composition in a space-resolved way. Sirenko and co-workers successfully performed high-resolution XRD measurements on SAG InGaAlAs and InGaAsP MQW structures using the microbeams available at the CHESS A2 beam line (Sirenko *et al.*, 2005) and at the APS 2-ID-D microscope beam line (Sirenko *et al.*, 2006). In the first study Sirenko *et al.* (2005) investigated the thickness and the strain variations as a function of the oxide mask width. Important structural changes were observed from the perfect quality MQWs in the SAG structures with the narrow oxide masks (less than 45 μm) to the strain-relaxed MQWs in the SAG regime with the wide oxide masks (more than 50 μm). In the second study, the cross-sectional thickness and strain variations in SAG ridge waveguides were measured by nano-XRD with a beam size of $240 \times 350\,\mathrm{nm}^2$. More recently Bonanno *et al.* (2013) were able to determine at the nanoscale the chemical composition and planar orientation of group III-nitride nanowires grown by nano-SAG using a nanobeam of 240 nm available at the 2-ID-D beam line (Libera *et al.*, 2002) of the APS at Argonne National Labs.

Another interesting device realized by the SAG technique is the electroabsorption modulated laser, realized by monolithic integration of a distributed feedback (DFB) laser with an electroabsorption modulator (EAM). The EAM and DFB laser are located, respectively, in the FIELD and SAG regions in

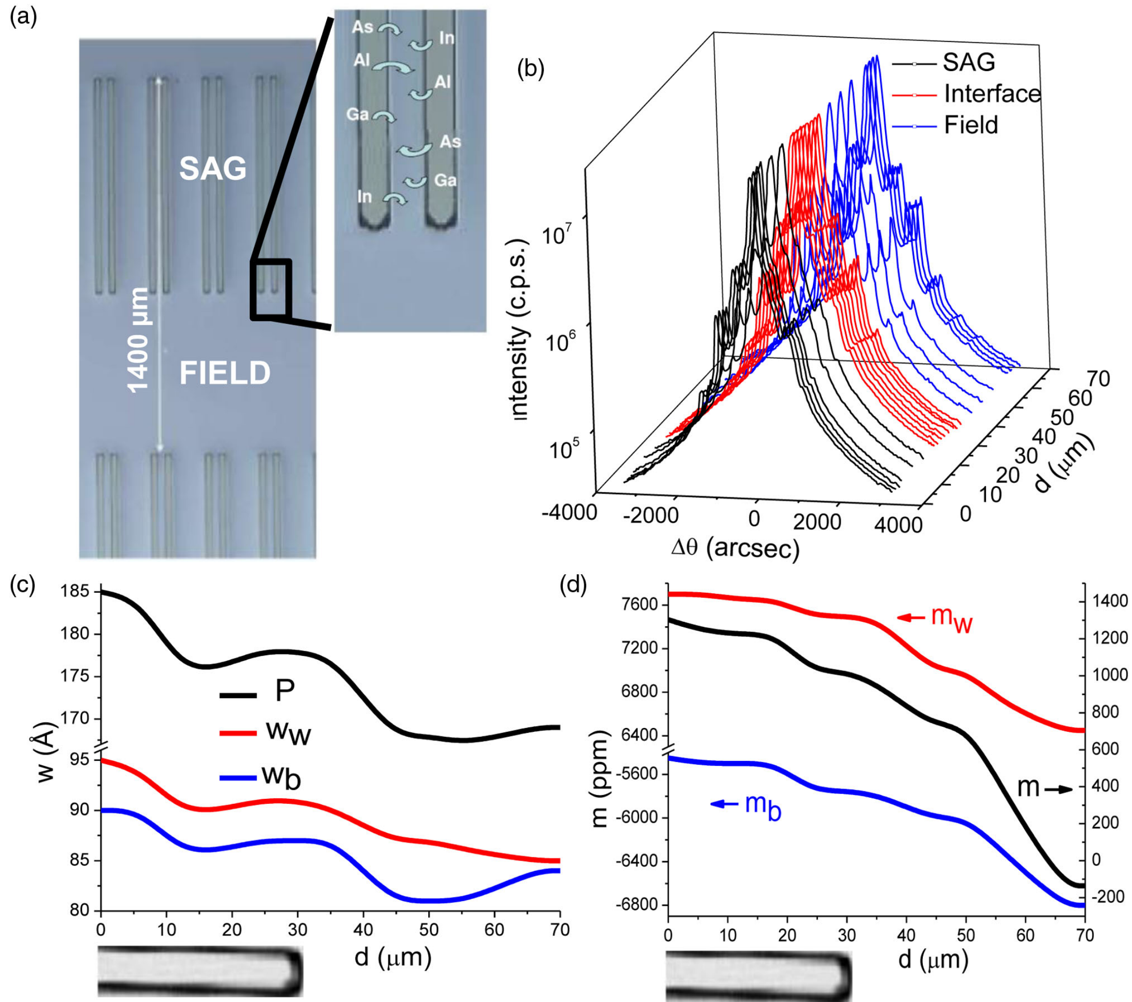

FIG. 32. (a) Optical micrograph of the InP substrate patterned with SiO_2 stripes used for the SAG technique. In the inset a magnification of the interface between SAG and FIELD regions clarifying the growth mechanism is shown. All the measurements have been performed along the white line parallel to the SiO_2 stripes and equidistant from them. This mask had 20 μm wide SiO_2 stripes with a 30 μm gap between them. (b) XRD patterns acquired along the line reported in (a), starting 30 μm before the end of the stripes in the SAG region. (c) Barrier and well widths and period as a function of the position, obtained by simulation of the experimental XRD patterns reported in (b). (d) Similar to (c) for the well, barrier, and overall mismatches. Adapted from Mino, Gianolio et al., 2010.

Fig. 32(a). This device exploits the Stark effect to switch the EAM between an opaque and a transparent state by applying a variable voltage to modulate the DFB laser emission, enabling long-distance communication at high frequency. Mino et al. performed a complete characterization of a SAG electroabsorption modulated laser device of industrial interest based on an $Al_{xw}Ga_{yw}In_{1-xw-yw}As/Al_{xb}Ga_{yb}In_{1-xb-yb}As$ (compressive-strained well–tensile-strained barrier) MQW structure grown on InP by metalorganic chemical vapor deposition (Mino, Gianolio et al., 2010; Mino et al., 2011).

The structural parameters of the sample were investigated by micro-XRD and a simulation of the XRD patterns allowed the authors to obtain the widths [w_b, w_w, Fig. 32(c)] and the mismatches [m_b, m_w, Fig. 32(d)] of the barrier and the well by fitting the experimental patterns [Fig. 32(b)] (Mino, Gianolio et al., 2010). Both w_b and w_w show a gradual increase moving from the FIELD to the SAG region, ascribed to the material enrichment induced by the mask in the SAG region. Also m_b and m_w increase moving from the FIELD to the SAG reflecting the expected modulation of the $Al_xGa_yIn_{1-x-y}As$ composition of the barrier and well layers. Also on a similar device, the variation of the bond distances moving from the SAG to the FIELD region was investigated using micro-EXAFS (Mino et al., 2011).

In a later study (Mino, Agostino et al., 2012) the same group combined laboratory micro-PL and synchrotron micro-XRF to correlate the variation in the energy gap measured for the different masks with the corresponding change in chemical composition of the MQW structures. As visible in Fig. 33(a), the micro-PL spectra highlight that, as expected, the difference in the energy gap between the SAG and FIELD regions becomes smaller by decreasing the stripes' width. The modulation in the chemical composition of the heterostructure is highlighted by the maps showing the ratio between the Ga and As XRF signals, which prove that a gradient in the average well or barrier chemical composition is present [Fig. 33(b)]. In detail, although a complete quantitative XRF analysis was not possible, the maps pointed out that the average Ga content of the alloy progressively increases by moving from the SAG to the FIELD. A complete quantitative XRF study was performed

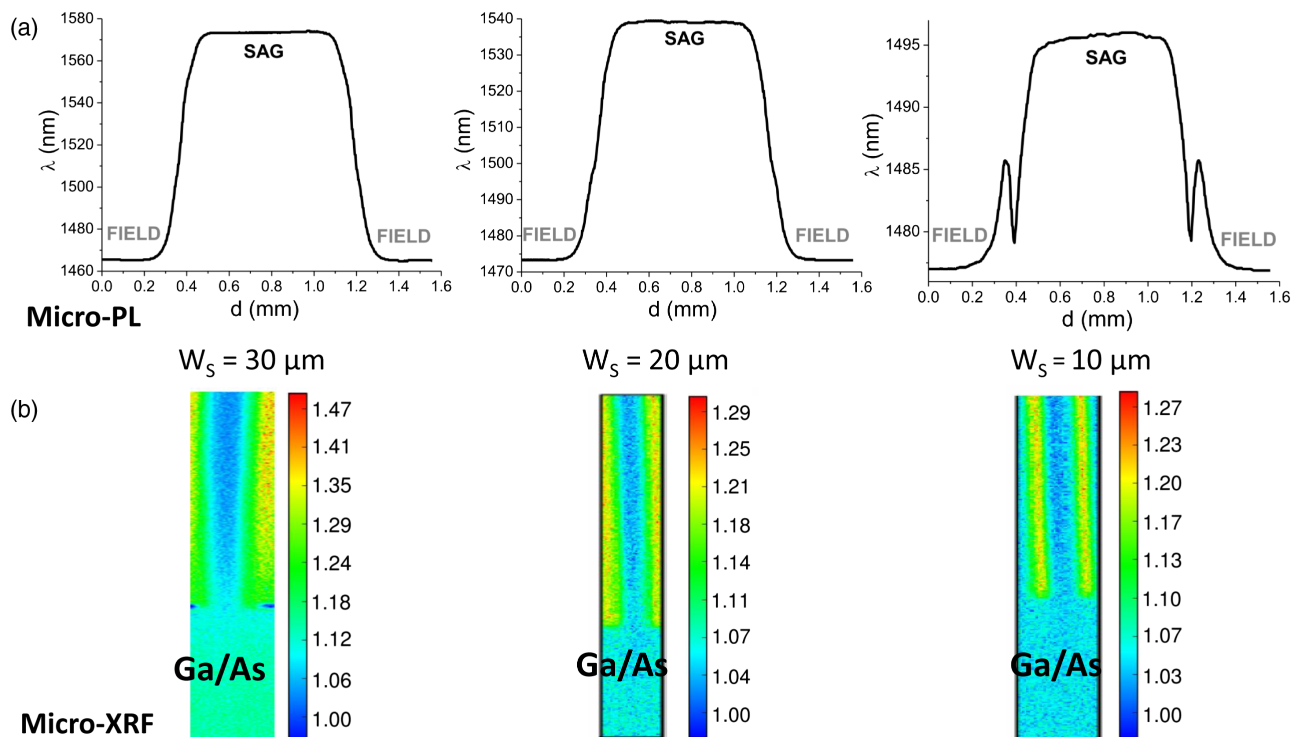

FIG. 33. (a) Wavelength corresponding to the maximum of emission for each PL spectrum acquired on samples with different SiO_2 stripes' width (W_S) along the white line shown in Fig. 32(a). (b) Spatial maps of the ratio between Ga ($K\alpha$) and As ($K\beta$) fluorescence counts which point out the variation in the average (between well and barrier) $Al_xGa_yIn_{1-x-y}As$ alloy composition between SAG and FIELD regions for the different masks. The horizontal × vertical dimensions of the maps are 55 × 230, 50 × 290, and 50 × 205 μm^2 for the samples with W_S = 30, 20 and 10 µm, respectively. Adapted from Mino, Agostino *et al.*, 2012.

for a SAG $In_{1-x}Ga_xAs$ film using a theoretical influence coefficients algorithm (Mino, Agostino *et al.*, 2010).

2. Switching mechanism in memristive devices

Memristive devices for redox-based resistive switching random access memory (ReRAM), owing to their promising properties with respect to scaling, power consumption, and switching speed, are nowadays intensively investigated to develop new solutions to meet the increasing demand for high-density and low-cost data storage devices (Jeong *et al.*, 2012; Pan *et al.*, 2014). The operation principle of these devices is based on a reversible resistance change of the dielectric layer in a simple capacitor structure (Waser *et al.*, 2009). This resistance change is the result of voltage-driven migration of oxygen vacancies, which act as mobile donors. After a so-called electroforming step, which creates oxygen vacancy channels (the "filaments") in an insulating matrix within the dielectric, the device resistance can be switched between a high resistance state (HRS) and a low resistance state (LRS). In the HRS, the filament consists of a so-called plug, which is a highly *n*-conductive region of the oxide film and a potential barrier (called a disk) between the active electrode and the plug. Upon application of a negative voltage, oxygen vacancies from the plug are attracted into the barrier, which turns the cell into the LRS. For the reset, a positive voltage repels the oxygen vacancies, leading to a local reoxidation, and turns the cell into the HRS again.

Nowadays large research efforts are devoted to investigate the underlying nanoscale physicochemical processes taking place during switching, which for the moment remain elusive and controversial. In this respect, soft-x-ray spectromicroscopy has provided useful insight into this issue, helping also to develop predictive models (Baeumer *et al.*, 2015). Scanning transmission x-ray spectromicroscopy at the O K edge was used to study *in situ* the switching of HfO_2 memristors (Kumar *et al.*, 2016). They highlighted the formation of a localized oxygen-deficient conductive channel surrounded by a low-conductivity ring of excess oxygen. The as-grown resistance state could be restored by thermal annealing which homogenized the segregated oxygen. Moreover, the formation and dissolution of the conduction channel were successfully modeled by radial thermophoresis and Fick diffusion of oxygen atoms driven by Joule heating.

Operando spectromicroscopy on $SrTiO_3$-based memristive devices using graphene electrodes was performed at the beam line UE56/1-SGM at BESSY II (Baeumer *et al.*, 2016). The research group investigated a complete switching cycle LRS-HRS-LRS-HRS by acquiring O K-edge image stacks after each switching event. Considering the entire device area, they found a ROI exhibiting reduced intensity in the LRS [red (dark gray) spot in Fig. 34(a)]. Extracting the entire O K-edge spectrum for this ROI and the surrounding area, they highlighted the fingerprint of reduced $SrTiO_3$ for the ROI [Fig. 34(b)]. The same ROI shows much weaker intensity reduction with respect to the surrounding device area in the HRS [Fig. 34(c)], suggesting that this region is a switching filament. The change in normalized intensity of the ROI for this filament in each resistance state exhibited a direct correlation with the device

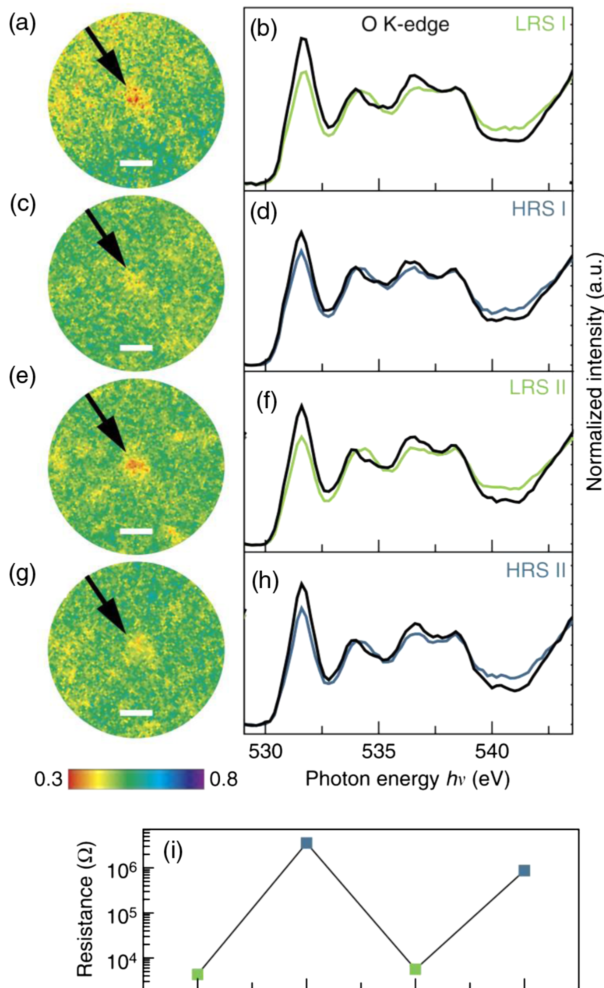

FIG. 34. (a), (c), (e), (g) Photoelectron emission microscopy images of the switching filament in the LRS, HRS, LRS II, and HRS II, respectively (indicated by the black arrow) for a photon energy of 531.6 eV. Scale bars, 1 μm. (b), (d), (f), (h) O *K*-edge spectra for the switching filament in (a), (c), (e), (g) [green and blue lines for the LRS and HRS, respectively (light and dark gray)] and the surrounding device area (black lines). (i) Device resistance as a function of the device state. Adapted from Baeumer *et al.*, 2016.

resistance [Fig. 34(i)]. They concluded that the resistance change in $SrTiO_3$-based memristors is due to a spatially confined redox reaction. This reaction, in turn, leads to a measurable and quantifiable valence change between the HRS and the LRS, confirming the so-called valence change mechanism for resistive switching in transition-metal oxides.

Another study in which soft-x-ray spectromicroscopy played a key role was the space-resolved investigation of TiO_x phases in TiO_2-based memristive devices (Carta *et al.*, 2016). Indeed, the localized reduction of the metal-oxide thin film is considered to be the key mechanism responsible for forming conductive phases in ReRAM devices, enabling their resistive switching capacity. However, the quantitative spatial identification of such conductive regions is a difficult task, especially for metal oxides capable of exhibiting multiple phases as in the case of TiO_x (Liborio and Harrison, 2008; Mino, Spoto *et al.*, 2012, 2013). By acquiring a sequence of x-ray images of the cross section of the TiO_x thin film at closely spaced photon energies, the researchers visualized the location of the reduced area and demonstrated that the conductive localized region is composed of a reduced TiO_x phase with a O/Ti ratio close to 1.37. They also identified crystalline rutile and orthorhombiclike TiO_2 phases in the proximity of the main reduced area, suggesting that the temperature increases locally up to 1000 K owing to Joule heating during resistive switching (Menzel *et al.*, 2015).

3. Impurities in Si for solar cells

The demand for high purity silicon is continuously increasing; therefore, nowadays new alternative sources have been sought, which often supply Si containing higher concentrations of transition-metal impurities. Since these impurities limit the charge carrier diffusion lengths and thus the efficiency of the solar cells, it is highly desirable to find suitable strategies to minimize these unwanted effects.

In this context, the use of synchrotron x-ray microbeams can provide crucial information to minimize the adverse effects of metal impurities. For instance, Buonassisi *et al.* (2005) exploited the x-ray microprobes available at APS and at the ALS to perform XRF mapping, XBIC and XAS with a high spatial resolution. They determined the spatial distribution of two kinds of metal defects in commercial solar grade Si: nanometric densely packed Fe silicide precipitates and micrometric sparsely distributed Fe oxide particles. The relative abundance of these precipitates depends on the cooling rate adopted during the crystallization: at slow rates, bigger and sparsely distributed oxide particles are formed. In this case the carrier diffusion length is 4 times higher than for crystals with nanometric densely packed precipitates. The micro-XAS measurements were crucial to provide a structural and chemical foundation for the crystallization procedure which ensures the best transport properties.

Other investigations have been devoted to the problem of diode breakdown in multicrystalline silicon solar cells and three main different mechanisms have been identified (Gundel *et al.*, 2009; Kwapil, Kasemann *et al.*, 2009). One of them involves recombination centers in the silicon crystal, usually associated with dislocations and grain boundaries. The breakdown voltage resulted to be lower at higher impurity concentration in the Si wafer. Thus, a crucial question is if the transition metals directly lead to prebreakdown or if secondary effects, such as dislocation multiplication owing to strain fields in the Si crystal, lead to a decrease in the breakdown voltage. Micro-XRF is the perfect technique to clarify this issue since no sample preparation (which would be necessary for instance for TEM analysis), which could alter the sample properties, is required.

Kwapil, Gundel *et al.* (2009) examined a solar cell from the bottom of the ingot using a nano-x-ray beam. The local prebreakdown behavior was investigated by bias-dependent electroluminescence intensity measurements. A sample of $10 \times 20\ mm^2$ showing a high density of prebreakdown sites, which were associated with recombination-active defects, was prepared. Then, electroluminescence and photoluminescence maps were acquired with a spatial resolution of 1 μm. By applying 10 V to the material, breakdown light emission was detected at the points marked with white circles in the SEM micrograph in Fig. 35. Both sites emit light in an area of around 5 to 10 μm in

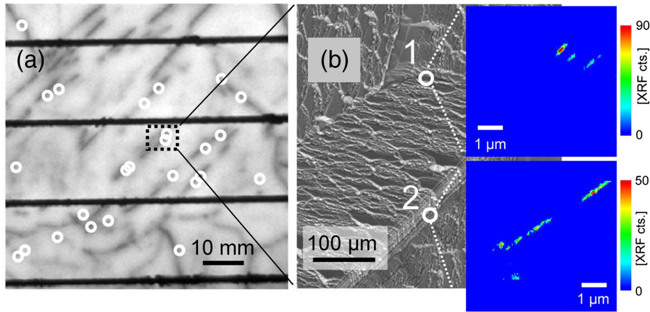

FIG. 35. (a) Forward bias electroluminescence image of part of the solar cell showing recombination-active defects. Breakdown light emission was observed at the sites marked by the white circles. (b) SEM image of the part of the solar cell marked by the dotted rectangle in (a); the micro-XRF maps of metal Fe precipitates, labeled as 1 and 2 in the SEM micrograph and highlighted by white circles, are also reported. Adapted from Kwapil, Gundel *et al.*, 2009.

diameter and are localized along grain boundaries. Using the markers determined in the luminescence maps, the micro-XRF maps were acquired in an area of $20 \times 20\ \mu m^2$ centered at the prebreakdown spots. Employing an intense x-ray beam of $100 \times 100\ nm^2$ and 10^{12} photons/s, transition-metal precipitates with a diameter of some tens of nanometers were highlighted (see Fig. 35). Iron precipitate colonies were found at both prebreakdown sites. They are distributed along single lines which correspond to the grain boundaries. In one case, a copper precipitate was also detected (Kwapil, Gundel *et al.*, 2009). The next step would be to clarify the physical mechanism at the basis of the observed breakdown behavior: a possible explanation is that the presence of an electrical charge near metal precipitates can increase the local electric field and induce the local prebreakdown.

In a similar study, combining XBIC, XRF, and XAS, Trushin *et al.* (2010) highlighted the fact that Si_3N_4/SiC particles, which are often detected at the (sub)micrometer scale in polycrystalline-Si blocks, are effective sinks for Fe and Cu impurities (Fig. 36). The concentration of copper precipitates, present as copper-rich silicide Cu_3Si, at the SiC inclusions was significantly larger than that at Si_3N_4 rods. The annealing at 950 °C, which is known to facilitate oxygen precipitation in Si, was found to lead to increased precipitation of nanoscale iron disilicide particles both inside the grains and at grain boundaries.

4. Quantum dots in field effect transistors

The microelectronic industry is constantly looking for new technological solutions to further improve performances and speed of Si-based integrated devices such as MOSFETs and CMOS transistors. An interesting method, representing a promising alternative to the traditional downscaling of device dimensions, is based on the realization of strain distribution in the current-carrying regions of the transistor in order to enhance the carrier mobility. Indeed, as initially illustrated by Bardeen and Shockley (1950) and subsequently quantified by Smith (1954), the local strain applied to semiconductor crystals directly influences the material resistivity and the carrier mobility.

Different strategies have then been proposed to induce such local strain in the channel of MOS-based devices. A common method is based on the deposition of embedded heteroepitaxial structures into Si trenches (Thompson *et al.*, 2004; Chui *et al.*, 2007). The most common compound employed for stressor structures is SiGe (Rim, Hoyt, and Gibbons, 2000), with lattice spacing larger than silicon to induce a compressive strain on the channel, and SiC, which conversely causes an in-plane tensile strain, due to its shorter lattice parameter. An alternative approach is the growth of stressed thin layers (e.g., Si_3N_4) overlying the transistor. In this case, the edges of the gate region generate local stress concentrations on the source-drain Si channel, leading to an in-plane strain distribution with the same sign of the overlaying layer (Ito *et al.*, 2002).

The two approaches described before both induce a heterogeneous strain distribution within the current-carrying channel. Simplified models based only on electrical parameters and assuming a uniform stress along the channel are not adequate to reliably predict device performances. Direct measurements of the local strain state across the current-carrying paths within the device are thus crucial, although challenging in several aspects.

The techniques based on electron microscopes (e.g., convergent beam electron diffraction) have an outstanding spatial resolution (Ang *et al.*, 2005; Hue *et al.*, 2008), but the sample preparation can significantly modify the original strain state of the material. Micro-Raman spectroscopy can provide information on the local strain at the submicrometric scale (Dewolf, Norstrom, and Maes, 1993; Wolverson, 2013), but the strain tensor dimensionality has to be assumed *a priori*, and a calibration procedure is required. In addition, the laser-induced heating of the material can influence the results, as reported, for instance, for silicon-on-insulator (SOI) layers (Georgi, Hecker, and Zschech, 2007).

Direct measurements of the local strain distribution can be performed nondestructively with submicrometric spatial resolution by XRD employing synchrotron microprobes or nanoprobes. This research line has been extensively developed at the microdiffraction beam line 2-ID-D (Libera *et al.*, 2002) of APS

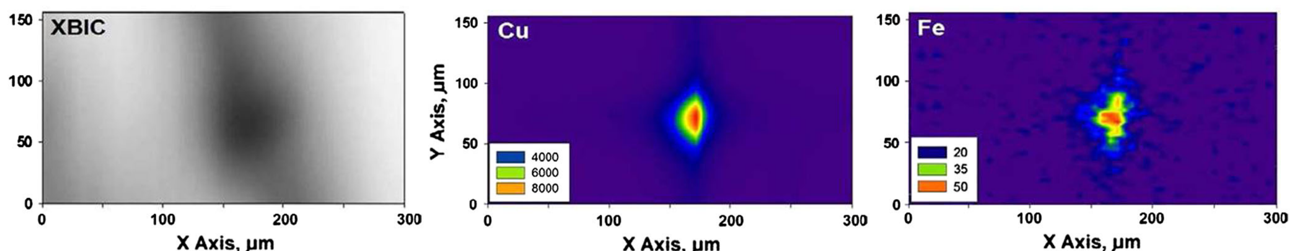

FIG. 36. XBIC image and XRF maps for Cu-$K\alpha$ and Fe-$K\alpha$ in the polycrystalline-Si solar cell. Adapted from Trushin *et al.*, 2010.

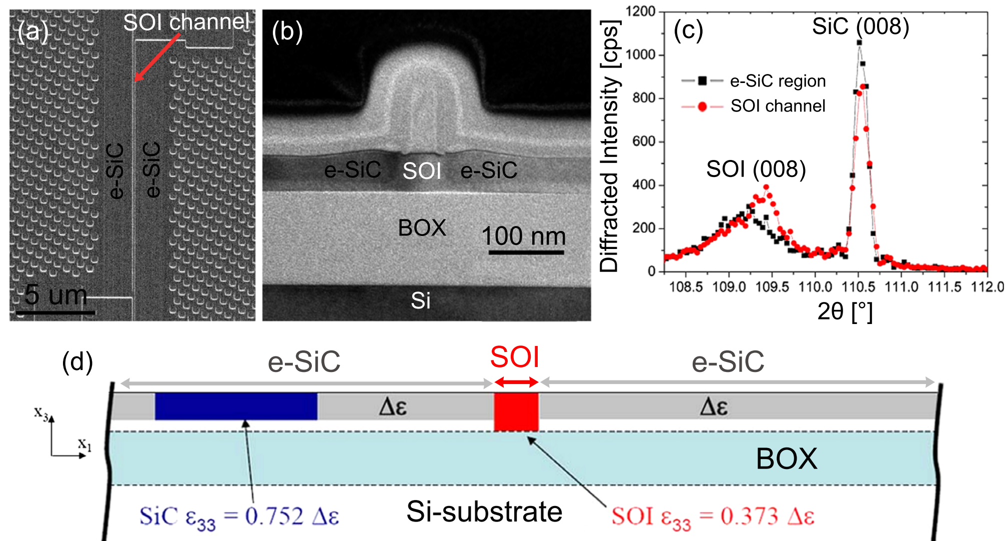

FIG. 37. (a) Plan-view SEM image of the *e*-SiC/SOI channel device. (b) Cross-sectional TEM image of the *e*-SiC/SOI channel. (c) Micro-XRD patterns acquired in the SOI channel (red dots) and 0.8 μm away from the channel (black squares). (d) Schematic cross-sectional geometry of the device, indicating the out-of-plane strain ε_{33} calculated using the Eshelby inclusion model in the SOI channel (red region, dark gray) and in the *e*-SiC feature 0.8 μm away from the channel (blue region, black) corresponding to the XRD measurement locations. Adapted from Murray *et al.*, 2009.

(Eastman *et al.*, 2002; Murray *et al.*, 2003, 2009; Parikh *et al.*, 2007; Polvino *et al.*, 2008) and at the X20A beam line (Noyan *et al.*, 2000) of Brookhaven National Laboratory's National Synchrotron Light Source (Mooney *et al.*, 1999; Yan, Murray, and Noyan, 2007).

The earlier studies performed by Mooney *et al.* (1999) and later by Eastman *et al.* (2002) were devoted to the microstructural features in $Si_{1-x}Ge_x/Si(001)$ epitaxial layers, with application in high-speed field-effect transistors (FETs) as a buffer layer on which strained Si or $Si_{1-x}Ge_x$ carrier channels can be pseudomorphically grown (Meyerson, 1992; Arafa *et al.*, 1996; Mooney, 1996; Koester *et al.*, 2001). For example, high angular-resolution rocking curves measured in different spatial positions on the layer using a 8.05 keV microbeam highlighted the presence of individual tilted rectangular columnar micrograins in step-graded $Si_{1-x}Ge_x/Si$ epilayers (Eastman *et al.*, 2002).

In the following years many researchers investigated the local strain distribution by micro-XRD *in situ* within the final device in its fully operational state. The effect of both overlying thin film features (Murray *et al.*, 2003, 2010, 2011; Yan, Murray, and Noyan, 2007) and embedded stressor structures (Parikh *et al.*, 2007; Murray *et al.*, 2009, 2010) on the resulting FET channel strain was studied. Murray *et al.* (2010) employed the 0.25×0.3 μm^2 beam available at the 2-ID-D beam line of the APS to characterize the local strain induced in a SOI-CMOS device channel by embedded silicon-carbon source or drain regions. The devices had 60 nm long SOI channels, with *e*-SiC embedded structures of around 1.85 μm in length adjacent to source and drain regions [see Fig. 37(a)]. The TEM cross section reported in Fig. 37(b) shows the SOI current-carrying channel surrounded by the *e*-SiC features (around 40 nm in thickness), and the underlying buried oxide (BOX) layer isolating the SOI from the silicon substrate.

Figure 37(c) shows the XRD patterns acquired in the SOI channel (red circles) and 0.8 μm away in the *e*-SiC region (black squares). Si (008) and *e*-SiC (008) diffraction peaks were detected during the same $\theta/2\theta$ scan, with the x-ray beam intercepting both types of layers. The measured out-of-plane strains in the *e*-SiC region, calculated from the diffraction data reported in Fig. 37(c), are 0.355% in the proximity of the channel and 0.350% 0.8 μm away from the channel, in accordance with the values calculated using the Eshelby inclusion model [see Fig. 37(d)]. The researchers were also able to determine the depth-averaged strain information from the current-carrying path, resulting in an out-of-plane compressive strain of -0.167 %, which is 95% of the theoretical value.

V. CONCLUSIONS AND PERSPECTIVES

In summary, synchrotron x-ray microprobe and nanoprobe beam lines [Sec. S-IV of the Supplemental Material (729)] have been built during the past years in highly sophisticated and reliable schemes to meet the important characterization challenges in several scientific fields. The richness of x-ray radiation-matter interactions (Sec. I.C and III.A) has enabled great improvements and major impacts from medicine to biology, cosmetics and food, from chemistry to physics (both solid-state and applied), from information to communication, from the automotive industry to aerospace, from clean energy sources to environmental, geological, and climate change issues, from high pressure to cultural heritage (Sec. I.A). In materials science, analytical approaches and concepts at the micrometer and nanometer length scales were demanded to get deeper insight into the composition, structure, size, shape, function, and performance of materials.

Progress in x-ray microscopes is rapid [Sec. II and Sec. S-I–S-III of the Supplemental Material (729)] and yields new information that cannot be gained using alternative tools.

Despite their strengths, other available probes (e.g., electrons, neutrons, ions, see Secs. I.B.2, I.B.3, and I.B.4, respectively) impose severe limitations in terms of *in situ* conditions, energy tunability, wavelength range, flux, penetration depth, source brightness, as well as the need for high-vacuum conditions and demanding sample preparation, which have been overcome using SR sources. The development of more brilliant, coherent, and more powerful x-ray facilities, such as XFELs and DLSRs (Sec. I.C), has allowed foreseeing, for the next ten years of x-ray science, revolutionary developments (e.g., single molecule imaging and femtosecond protein nanocrystallography) (Yabashi and Tanaka, 2017). In parallel, colossal advances in nanofabrication and metrology have been achieved to develop nanofocusing devices for both soft- and hard-x-ray regimes. Several routes and combinatorial strategies are today explored based on refractive, diffractive, and reflective optics [Secs. II.B, II.C, and II.D (and, more in detail, Secs. S-I, S-II, and S-III of the Supplemental Material (729), respectively)]. As a result, scanning and full-field x-ray microscopes (Secs. III.G.2 and III.G.3, respectively) can be found installed all over (mostly in long beam lines) at synchrotron light sources. Exploiting these setups, a large number of spatially resolved properties are concurrently investigated in 2D or 3D by combining multiple modalities and contrast mechanisms.

So far, most of the current reports are focused on methodological development (e.g., *in situ* and *operando* instruments, phase-contrast imaging, tomography, ptychography, etc.), focusing optics (x-ray lenses and novel schemes), applications (biological imaging, magnetic, and elemental contrast), and new facilities (compact light sources, XFELs, and DLSRs). However, there are still relevant challenges in terms of new sources, sample preservation, high throughput and screenings, time- and space-resolved (4D) studies under extreme thermodynamic conditions (temperature, pressure, magnetic, and electric fields). For example, to mitigate the effects of possible radiation damage (Sec. III.I), which is critical in life science, cryocooling and subpicosecond pulses with 2D and 3D nanometric resolution capabilities are under development. In parallel, more and more x-ray microscopes are also becoming commercially available for home-laboratory use (Altamura *et al.*, 2012; Dudchik *et al.*, 2016). The exploitation of DLSRs will soon stimulate an increased use of coherence-based imaging methods (e.g., ptychography, CDI) with a significantly shorter data collection time. Moreover, the reduced emittance will produce a drastic gain in photon flux improving the detection limits close to single atoms. The major drawback of such brilliant x-ray sources concerns the radiation damage effects that have been discussed in Sec. III.I. The high spectral brilliance provided by XFELs (Sec. I.C.2) will give rise to new disciplines such as nonlinear x-ray optics, or the generation of exotic matter states under extremely high-energy densities.

Within the same perspectives, future x-ray microprobes and nanoprobes will include focusing devices with resolution better than 1 nm (depending on the dose tolerance of the sample), superior efficiency, and achromaticity in an extended x-ray energy range. The achievable resolution of hard-x-ray lenses is following a Moore's law trajectory; see Fig. 7. Furthermore, coming x-ray nanoprobes will present more integration of complementary tools and probes for static and dynamic multiscale studies (e.g., attosecond experiments, pump-probe x-ray imaging). New approaches will emerge, such as light-sheet Compton microscopy, x-ray resonant saturated structured illumination microscopy, synchrotron x-ray scanning tunneling microscopy, providing isotropic 1 nm resolution in 3D even for biological specimens in their natural state. As a consequence, cutting-edge technologies will be crucial for the development of the necessary instrumentation, including nanomechanics (nanopositioning devices, mechanical-testing equipment), advanced detection systems (e.g., integrating energy-dispersive pixelated detectors) with improved spatial resolution, sensitivity and dynamic range, ultrafast readout electronics for detectors, controlled fast heating and cooling devices, control software for big data handling and fast transfer, online data processing strategies, new reconstruction algorithms, and machine learning schemes.

LIST OF SYMBOLS AND ABBREVIATIONS

1D	one dimensional
2D	two dimensional
3D	three dimensional
AFM	atomic force microscopy
ALS	Advanced Light Source
APS	Advanced Photon Source
ARPES	angle-resolved photoemission spectroscopy
AXS	anomalous x-ray scattering
BE	binding energy
BNL	Brookhaven National Laboratory
CCD	charge-coupled device
CL	cathodoluminescence
CLS	Canadian Light Source
CDI	coherent diffractive imaging
COLTRIMS	target recoil ion momentum spectroscopy
CMOS	complementary metal-oxide semiconductor
cSAXS	coherent SAXS
DESY	Deutsches Elektronen-Synchrotron
DFB	distributed feedback (laser)
DoF	depth of field
DOS	density of states
EAM	electroabsorption modulator
EDS	energy-dispersive spectrometry
EDX	energy-dispersive x-ray (spectrometry)
EPMA	electron probe microanalysis
ESCA	electron spectroscopy for chemical analysis
DLSR(s)	diffraction-limited storage ring(s)
ERDA	elastic recoil detection analysis
ESRF	European Synchrotron Radiation Facility
EXAFS	extended x-ray absorption fine structure
FCC	fluid catalytic cracking
FEL	free-electron laser
FEM	finite-element method (simulations)
FIB	focused ion beam

FLY fluorescence yield
FReLoN fast readout low noise (2D x-ray camera)
FT Fourier transform
FTO Fischer-Tropsch to olefins
FWHM full width at half maximum
HRS high resistance state
HEIS high-energy ion scattering
IBA ion-beam analysis
IJJ intrinsic Josephson junction
IMFP inelastic mean free path
IR infrared
KB Kirkpatrick-Baez (mirrors)
LED light emitting diode
LEIS low-energy ion scattering
LRS low resistance state
MC Monte Carlo
MEIS medium-energy ion scattering
MLL multilayer Laue lens
MOS metal-oxide semiconductor
MOSFET metal-oxide-semiconductor field-effect transistor
MQW multiquantum well
NEXAFS near-edge x-ray absorption fine structure
NP nanoparticle
NRA nuclear reaction analysis
NW nanowire
PCDI ptychographic coherent x-ray diffractive imaging
PDF pair distribution function
PES photoelectron spectroscopy
PIE ptychographical iterative engine
PIGE proton-induced or particle-induced γ-ray emission (spectroscopy)
PIXE proton-induced or particle-induced x-ray emission (spectroscopy)
PL photoluminescence
RBS Rutherford backscattering spectroscopy
RD radiation damage
ReRAM redox-based resistive switching random access memory
RIXS resonant inelastic x-ray scattering
RSM (x-ray) reciprocal-space mapping
ROI region(s) of interest
RT room temperature
RUMT rolled-up microtubes
RUNT rolled-up nanotubes
SAG selective area growth
SAXD small-angle x-ray diffraction
SAXS small-angle x-ray scattering
SCR selective catalytic reduction
SEM scanning electron microscopy
SIMS secondary ion mass spectrometry
SOI silicon on insulator
SPEM scanning photoemission microscopy
SR synchrotron radiation
STXM scanning transmission x-ray microscope
SXD scanning x-ray diffraction
TEM transmission electron microscopy
TEY total electron yield
TR time resolved
TTF Tesla Test Facility
TXRF total reflection x-ray fluorescence
TXM transmission x-ray microscopy
UPS ultraviolet photoelectron spectroscopy
uSAXD ultrasmall-angle x-ray diffraction
uSAXS ultrasmall-angle x-ray scattering
USY ultrastable Y (zeolite)
WAXD wide-angle x-ray diffraction
WAXS wide-angle x-ray scattering
WDXRF wavelength-dispersive x-ray fluorescence
XAFS x-ray absorption fine structure
XANES x-ray absorption near-edge structure
XAS x-ray absorption spectroscopy
XBIC x-ray-beam-induced current
XEOL x-ray-excited optical luminescence
XES x-ray emission spectroscopy
XFEL x-ray free-electron laser
XPEEM x-ray photoemission electron microscope
XPS x-ray photoelectron spectroscopy
XRD x-ray diffraction
XRF x-ray fluorescence
XRM x-ray microscope (or microscopy)
XRS x-ray Raman scattering
ZP zone plate

ACKNOWLEDGMENTS

We are indebted to Professor P. Olivero (Department of Physics, Turin University) for a critical reading of Sec. I.B.3 and for stimulating discussion on ion beams. G. M.-C. was partially supported by the European Synchrotron Radiation Facility (ESRF), Consejo Superior de Investigaciones Científicas (CSIC), and Ministerio de Economía y Competitividad (MINECO) through Projects No. 201660I001 and EUIN-2017-88844. C. L. thanks the Russian Ministry of Education and Science for support (megagrant of the Russian Federation Government No. 14.Y26.31.0001).

REFERENCES

Adam, J. F., J. P. Moy, and J. Susini, 2005, Rev. Sci. Instrum. **76**, 091301.
Adams, F., K. Janssens, and A. Snigirev, 1998, J. Anal. At. Spectrom. **13**, 319.
Ade, H., and H. Stoll, 2009, Nat. Mater. **8**, 281.
Agostini, G., D. Gianolio, and C. Lamberti, 2018, in International Tables Volume I, 3.38, edited by C. T. Chantler, B. Bunker, and F. Boscherini (IUCr), p. invited contribution (in press).

Agostini, G., E. Groppo, S. Bordiga, A. Zecchina, C. Prestipino, F. D'Acapito, E. van Kimmenade, P. C. Thune, J. W. Niemantsverdriet, and C. Lamberti, 2007, J. Phys. Chem. C **111**, 16437.
Agostini, G., C. Lamberti, L. Palin, M. Milanesio, N. Danilina, B. Xu, M. Janousch, and J. A. van Bokhoven, 2010, J. Am. Chem. Soc. **132**, 667.
Agostini, G., C. Lamberti, R. Pellegrini, G. Leofanti, F. Giannici, A. Longo, and E. Groppo, 2014, ACS Catal. **4**, 187.
Agostini, G., R. Pellegrini, G. Leofanti, L. Bertinetti, S. Bertarione, E. Groppo, A. Zecchina, and C. Lamberti, 2009, J. Phys. Chem. C **113**, 10485.
Aldica, G., S. Cagliero, A. Agostino, C. Lamberti, and M. Truccato, 2011, Supercond. Sci. Technol. **24**, 035009.
Alferov, Z. I., 2001, Rev. Mod. Phys. **73**, 767.
Allaria, E., *et al.*, 2016, AIP Conf. Proc. **1741**, 020006.
Alonso, J. A., M. J. Martinez-Lope, A. Aguadero, and L. Daza, 2008, Prog. Solid State Chem. **36**, 134.
Alonso-Mori, R., *et al.*, 2012, Proc. Natl. Acad. Sci. U.S.A. **109**, 19103.
Als-Nielsen, J., and D. McMorrow, 2001, *Elements of Modern X-Ray Physics* (JohnWiley & Sons, London, UK).
Altamura, D., R. Lassandro, F. A. Vittoria, L. De Caro, D. Siliqi, M. Ladisa, and C. Giannini, 2012, J. Appl. Crystallogr. **45**, 869.
Altarelli, M., 2011, Nucl. Instrum. Methods Phys. Res., Sect. B **269**, 2845.
Altarelli, M., and A. P. Mancuso, 2014, Phil. Trans. R. Soc. B **369**, 20130311.
Amano, H., 2015, Rev. Mod. Phys. **87**, 1133.
Amati, M., M. K. Abyaneh, and L. Gregoratti, 2013, J. Instrum. **8**, T05001.
Andersen, C. W., E. Borfecchia, M. Bremholm, M. R. V. Jorgensen, P. N. R. Vennestrom, C. Lamberti, L. F. Lundegaard, and B. B. Iversen, 2017, Angew. Chem., Int. Ed. **56**, 10367.
Andrews, J. C., and B. M. Weckhuysen, 2013, ChemPhysChem **14**, 3655.
Ang, K. W., K. J. Chui, V. Bliznetsov, C. H. Tung, A. Du, N. Balasubramanian, G. Samudra, M. F. Li, and Y. C. Yeo, 2005, Appl. Phys. Lett. **86**, 093102.
Arafa, M., K. Ismail, J. O. Chu, B. S. Meyerson, and I. Adesida, 1996, IEEE Electron Device Lett. **17**, 586.
Aramburo, L. R., Y. J. Liu, T. Tyliszczak, F. M. F. de Groot, J. C. Andrews, and B. M. Weckhuysen, 2013, ChemPhysChem **14**, 496.
Ariga, K., M. Li, G. J. Richards, and J. P. Hill, 2011, J. Nanosci. Nanotechnol. **11**, 1.
Arion, T., and U. Hergenhahn, 2015, J. Electron Spectrosc. Relat. Phenom. **200**, 222.
Arrighi, V., and J. S. Higgins, 2004, Plast. Rubber Compos. **33**, 313.
Arvizo, R. R., S. Bhattacharyya, R. A. Kudgus, K. Giri, R. Bhattacharya, and P. Mukherjee, 2012, Chem. Soc. Rev. **41**, 2943.
Assmann, W., H. Huber, C. Steinhausen, M. Dobler, H. Gluckler, and A. Weidinger, 1994, Nucl. Instrum. Methods Phys. Res., Sect. B **89**, 131.
Avasthi, D. K., and G. K. Mehta, 2011, *Swift Heavy Ions for Materials Engineering and Nanostructuring*, Springer Series in Materials Science Vol. 145 (Springer-Verlag, Berlin).
Baer, D. R., *et al.*, 2013, J. Vac. Sci. Technol. A **31**, 050820.
Baer, T., and R. P. Tuckett, 2017, Phys. Chem. Chem. Phys. **19**, 9698.
Baeumer, C., *et al.*, 2015, Nat. Commun. **6**, 8610.
Baeumer, C., *et al.*, 2016, Nat. Commun. **7**, 12398.
Baez, A. V., 1961, J. Opt. Soc. Am. **51**, 405.
Bagus, P. S., E. S. Ilton, and C. J. Nelin, 2013, Surf. Sci. Rep. **68**, 273.
Bajt, S., *et al.*, 2018, Light Sci. Appl. **7**, 17162.
Baraldi, A., *et al.*, 2005, J. Am. Chem. Soc. **127**, 5671.
Barbo, F., M. Bertolo, A. Bianco, G. Cautero, S. Fontana, T. K. Johal, S. La Rosa, G. Margaritondo, and K. Kaznacheyev, 2000, Rev. Sci. Instrum. **71**, 5.
Bardeen, J., and W. Shockley, 1950, Phys. Rev. **80**, 72.
Barzan, C., A. Piovano, L. Braglia, G. A. Martino, C. Lamberti, S. Bordiga, and E. Groppo, 2017, J. Am. Chem. Soc. **139**, 17064.
Batyuk, A., *et al.*, 2016, Sci. Adv. **2**, e1600292.
Bazin, D., L. Guczi, and J. Lynch, 2002, Appl. Catal., A **226**, 87.
Beaumont, S. K., S. Alayoglu, V. V. Pushkarev, Z. Liu, N. Kruse, and G. A. Somorjai, 2013, Faraday Discuss. **162**, 31.
Bednorz, J. G., and K. A. Muller, 1986, Z. Phys. B **64**, 189.
Bednorz, J. G., and K. A. Muller, 1988, Rev. Mod. Phys. **60**, 585.
Beer, A., 1852, Ann. Phys. (Berlin) **162**, 78.
Beguiristain, H. R., I. S. Anderson, C. D. Dewhurst, M. A. Piestrup, J. T. Cremer, and R. H. Pantell, 2002, Appl. Phys. Lett. **81**, 4290.
Bencivenga, F., F. Capotondi, E. Principi, M. Kiskinova, and C. Masciovecchio, 2015, Adv. Phys. **63**, 327.
Benninghoven, A., 1994, Angew. Chem., Int. Ed. Engl. **33**, 1023.
Bergh, M., N. Timneanu, and D. van der Spoel, 2004, Phys. Rev. E **70**, 051904.
Bergmann, U., and P. Glatzel, 2009, Photosynth. Res. **102**, 255.
Bertilson, M., O. von Hofsten, U. Vogt, A. Holmberg, and H. M. Hertz, 2009, Opt. Express **17**, 11057.
Bertrand, L., S. Schoder, D. Anglos, M. B. H. Breese, K. Janssens, M. Moini, and A. Simon, 2015, Trac. Trends Anal. Chem. **66**, 128.
Bianconi, A., D. Jackson, and K. Monahan, 1978, Phys. Rev. B **17**, 2021.
Biesinger, M. C., L. W. M. Lau, A. R. Gerson, and R. S. C. Smart, 2010, Appl. Surf. Sci. **257**, 887.
Biju, V., T. Itoh, A. Anas, A. Sujith, and M. Ishikawa, 2008, Anal. Bioanal. Chem. **391**, 2469.
Bilderback, D. H., 2003, X-Ray Spectrom. **32**, 195.
Bilderback, D. H., P. Elleaume, and E. Weckert, 2005, J. Phys. B **38**, S773.
Bilderback, D. H., and E. Fontes, 1997, AIP Conf. Proc. **417**, 147.
Bleuet, P., L. Lemelle, R. Tucoulou, P. Gergaud, G. Delette, P. Cloetens, J. Susini, and A. Simionovici, 2010, Trac Trends in Analytical Chemistry **29**, 518.
Bonanno, P. L., *et al.*, 2013, Thin Solid Films **541**, 46.
Bonino, F., E. Groppo, C. Prestipino, G. Agostini, A. Piovano, D. Gianolio, L. Mino, E. Gallo, and C. Lamberti, 2015, in *Synchrotron Radiation: Basics, Methods and Applications*, edited by S. Mobilio, F. Boscherini, and C. Meneghini (Springer, Berlin/Heidelberg), p. 717.
Bordiga, S., F. Bonino, K. P. Lillerud, and C. Lamberti, 2010, Chem. Soc. Rev. **39**, 4885.
Bordiga, S., A. Damin, F. Bonino, G. Ricchiardi, A. Zecchina, R. Tagliapietra, and C. Lamberti, 2003, Phys. Chem. Chem. Phys. **5**, 4390.
Bordiga, S., E. Groppo, G. Agostini, J. A. van Bokhoven, and C. Lamberti, 2013, Chem. Rev. **113**, 1736.
Borfecchia, E., E. Groppo, S. Bordiga, and C. Lamberti, 2018, in International Tables Volume I, 8.10, edited by C. T. Chantler, B. Bunker, and F. Boscherini (IUCr), p. invited contribution (in press).
Borfecchia, E., K. A. Lomachenko, F. Giordanino, H. Falsig, P. Beato, A. V. Soldatov, S. Bordiga, and C. Lamberti, 2015, Chem. Sci. **6**, 548.
Borfecchia, E., L. Mino, D. Gianolio, C. Groppo, N. Malaspina, G. Martinez-Criado, J. A. Sans, S. Poli, D. Castelli, and C. Lamberti, 2012, J. Anal. At. Spectrom. **27**, 1725.
Borfecchia, E., *et al.*, 2013, in *Synthesis and characterization of inorganic micro and nano-materials*, edited by A. Di Benedetto and M. Aresta (De Gruyter, Berlin/Boston), p. 93.

Born, M., and E. Wolf, 1999, *Principles of Optics: Electromagnetic Theory of Propagation, Interference and Diffraction of Light* (Cambridge University Press, Cambridge, England), 7th ed.

Boscherini, F., 2013, in *Characterization of Semiconductor Heterostructures and Nanostructures*, edited by C. Lamberti and G. Agostini (Elsevier, Amsterdam), p. 259, 2nd ed.

Bostedt, C., S. Boutet, D. M. Fritz, Z. R. Huang, H. J. Lee, H. T. Lemke, A. Robert, W. F. Schlotter, J. J. Turner, and G. J. Williams, 2016, Rev. Mod. Phys. **88**, 015007.

Boutet, S., *et al.*, 2012, Science **337**, 362.

Bozin, E. S., P. Juhás, and S. J. L. Billinge, 2013, in *Characterization of Semiconductor Heterostructures and Nanostructures*, edited by C. Lamberti and G. Agostini (Elsevier, Amsterdam), p. 229, 2nd ed.

Bragg, W. H., and W. L. Bragg, 1913, Proc. R. Soc. A **88**, 428.

Braglia, L., *et al.*, 2017a, Faraday Discuss. **201**, 277.

Braglia, L., *et al.*, 2017b, Phys. Chem. Chem. Phys. **19**, 27489.

Bras, W., I. P. Dolbnya, D. Detollenaere, R. van Tol, M. Malfois, G. N. Greaves, A. J. Ryan, and E. Heeley, 2003, J. Appl. Crystallogr. **36**, 791.

Breese, M. B. H., D. N. Jamieson, and P. J. C. King, 1996, *Material Analysis Using a Nuclear Microprobe* (John Wiley and Sons Inc., New York).

Brongersma, H. H., M. Draxler, M. de Ridder, and P. Bauer, 2007, Surf. Sci. Rep. **62**, 63.

Brown, G. E., G. Calas, G. A. Waychunas, and J. Petiau, 1988, Rev. Mineral. **18**, 431 [http://www.minsocam.org/MSA/RIM/rim18.html].

Budai, J. D., W. Liu, J. Z. Tischler, Z. W. Pan, D. P. Norton, B. C. Larson, W. Yang, and G. E. Ice, 2008, Thin Solid Films **516**, 8013.

Budnyk, A. P., A. Damin, G. Agostini, and A. Zecchina, 2010, J. Phys. Chem. C **114**, 3857.

Bugaev, A. L., *et al.*, 2017a, Catal. Today **283**, 119.

Bugaev, A. L., *et al.*, 2017b, J. Phys. Chem. C **121**, 18202.

Buonassisi, T., A. A. Istratov, M. A. Marcus, B. Lai, Z. H. Cai, S. M. Heald, and E. R. Weber, 2005, Nat. Mater. **4**, 676.

Buurmans, I. L. C., and B. M. Weckhuysen, 2012, Nat. Chem. **4**, 873.

Cagliero, S., *et al.*, 2009, J. Synchrotron Radiat. **16**, 813.

Cagliero, S., *et al.*, 2012, Supercond. Sci. Technol. **25**, 125002.

Calas, G., A. Manceau, J. M. Combes, and F. Farges, 2002, in *Absorption Spectroscopy in Mineralogy*, edited by A. Mottana and F. Burragato (Elsevier, Amsterdam), p. 171.

Cammarata, M., M. Levantino, F. Schotte, P. A. Anfinrud, F. Ewald, J. Choi, A. Cupane, M. Wulff, and H. Ihee, 2008, Nat. Methods **5**, 881.

Campbell, C. T., 2013, Acc. Chem. Res. **46**, 1712.

Campi, G., *et al.*, 2015, Nature (London) **525**, 359.

Carbone, L., *et al.*, 2007, Nano Lett. **7**, 2942.

Carnis, J., *et al.*, 2014, Sci. Rep. **4**, 6017.

Carta, D., A. P. Hitchcock, P. Guttmann, A. Regoutz, A. Khiat, A. Serb, I. Gupta, and T. Prodromakis, 2016, Sci. Rep. **6**, 21525.

Carter, S., A. S. Fisher, M. W. Hinds, S. Lancaster, and J. Marshall, 2013, J. Anal. At. Spectrom. **28**, 1814.

Casalis, L., *et al.*, 1995, Rev. Sci. Instrum. **66**, 4870.

Cats, K. H., J. C. Andrews, O. Stephan, K. March, C. Karunakaran, F. Meirer, F. M. F. de Groot, and B. M. Weckhuysen, 2016, Catal. Sci. Technol. **6**, 4438.

Cats, K. H., I. D. Gonzalez-Jimenez, Y. J. Liu, J. Nelson, D. van Campen, F. Meirer, A. M. J. van der Eerden, F. M. F. de Groot, J. C. Andrews, and B. M. Weckhuysen, 2013, Chem. Commun. (Cambridge) **49**, 4622.

Ceolin, D., *et al.*, 2013, J. Electron Spectrosc. Relat. Phenom. **190**, 188.

Chaboy Nalda, J., 2008, in *Instrumental Techniques Applied to Mineralogy and Geochemistry*, edited by I. Subias and B. Bauluz (Sociedad Española de Mineralogía, Zaragoza, Spain), p. 43.

Chang, L. L., and L. Esaki, 1992, Phys. Today **45**, 36.

Chaparro, S. A., J. Drucker, Y. Zhang, D. Chandrasekhar, M. R. McCartney, and D. J. Smith, 1999, Phys. Rev. Lett. **83**, 1199.

Chapman, H. N., and K. A. Nugent, 2010, Nat. Photonics **4**, 833.

Chapman, H. N., *et al.*, 2006, Nat. Phys. **2**, 839.

Chapman, H. N., *et al.*, 2011, Nature (London) **470**, 73.

Cheetham, A. K., and A. P. Wilkinson, 1992, Angew. Chem., Int. Ed. Engl. **31**, 1557.

Chen, H., R. G. Downing, D. F. R. Mildner, W. M. Gibson, M. A. Kumakhov, I. Y. Ponomarev, and M. V. Gubarev, 1992, Nature (London) **357**, 391.

Chen, O., *et al.*, 2013, Nat. Mater. **12**, 445.

Chen, S., *et al.*, 2014, J. Synchrotron Radiat. **21**, 66.

Cheng, X. M., and D. J. Keavney, 2012, Rep. Prog. Phys. **75**, 026501.

Chorkendorff, I., and J. W. Niemantsverdriet, 2007, *Concepts of modern catalysis and kinetics* (Wiley, Berlin), 2nd ed.

Chou, Y. C., K. Hillerich, J. Tersoff, M. C. Reuter, K. A. Dick, and F. M. Ross, 2014, Science **343**, 281.

Chui, K. J., K. W. Ang, N. Balasubramanian, M. F. Li, G. S. Samudra, and Y. C. Yeo, 2007, IEEE Trans. Electron Devices **54**, 249.

Chushkin, Y., F. Zontone, E. Lima, L. De Caro, P. Guardia, L. Manna, and C. Giannini, 2014, J. Synchrotron Radiat. **21**, 594.

Chwiej, J., D. Adamek, M. Szczerbowska-Boruchowska, A. Krygowska-Wajs, S. Bohic, and M. Lankosz, 2008, J. Trace Elem. Med. Biol. **22**, 183.

Cingolani, R., and K. Ploog, 1991, Adv. Phys. **40**, 535.

Clark, J. N., *et al.*, 2013, Science **341**, 56.

Clausen, B. S., H. Topsoe, and R. Frahm, 1998, Adv. Catal. **42**, 315.

Cloetens, P., W. Ludwig, J. Baruchel, D. Van Dyck, J. Van Landuyt, J. P. Guigay, and M. Schlenker, 1999, Appl. Phys. Lett. **75**, 2912.

Collingwood, J. F., A. Mikhaylova, M. Davidson, C. Batich, W. J. Streit, J. Terry, and J. Dobson, 2005, J. Alzheimers Dis. **7**, 267.

Coltrin, M. E., and C. C. Mitchell, 2003, J. Cryst. Growth **254**, 35.

Coppens, P., D. E. Cox, E. Vlieg, and I. K. Robinson, 1992, *Synchrotron Radiation Crystallography* (Academic Press, London).

Costacurta, S., L. Malfatti, A. Patelli, P. Falcaro, H. Amenitsch, B. Marmiroli, G. Grenci, M. Piccinini, and P. Innocenzi, 2010, Plasma Process. Polym. **7**, 459.

Cotal, H., C. Fetzer, J. Boisvert, G. Kinsey, R. King, P. Hebert, H. Yoon, and N. Karam, 2009, Energy Environ. Sci. **2**, 174.

Cotte, M., J. Szlachetko, S. Lahlil, M. Salome, V. A. Sole, I. Biron, and J. Susini, 2011, J. Anal. At. Spectrom. **26**, 1051.

Cotte, M., E. Welcomme, V. A. Sole, M. Salome, M. Menu, P. Walter, and J. Susini, 2007, Anal. Chem. **79**, 6988.

Creemer, J. F., S. Helveg, G. H. Hoveling, S. Ullmann, A. M. Molenbroek, P. M. Sarro, and H. W. Zandbergen, 2008, Ultramicroscopy **108**, 993.

Cubukcu, H. E., O. Ersoy, E. Aydar, and U. Cakir, 2008, Micron **39**, 88.

Cui, X. Y., J. E. Medvedeva, B. Delley, A. J. Freeman, N. Newman, and C. Stampfl, 2005, Phys. Rev. Lett. **95**, 256404.

Cushman, C. V., P. Bruner, J. Zakel, G. H. Major, B. M. Lunt, N. J. Smith, T. Grehl, and M. R. Linford, 2016, Anal. Methods **8**, 3419.

Damascelli, A., Z. Hussain, and Z. X. Shen, 2003, Rev. Mod. Phys. **75**, 473.

Da Silva, J. C., A. Pacureanu, Y. Yang, S. Bohic, C. Morawe, R. Barrett, and P. Cloetens, 2017, Optica **4**, 492.

David, C., *et al.*, 2011, Sci. Rep. **1**, 57.

David, D., 1992, Surf. Sci. Rep. **16**, 333.

de Abajo, F. J. G., 2010, Rev. Mod. Phys. **82**, 209.

De Caro, L., D. Altamura, M. Arciniegas, D. Siliqi, M. R. Kim, T. Sibillano, L. Manna, and C. Giannini, 2016, Sci. Rep. **6**, 19397.

De Caro, L., E. Carlino, G. Caputo, P. D. Cozzoli, and C. Giannini, 2010, Nat. Nanotechnol. **5**, 360.

de Jonge, M. D., C. G. Ryan, and C. J. Jacobsen, 2014, J. Synchrotron Radiat. **21**, 1031.

del Alamo, J. A., 2011, Nature (London) **479**, 317.

Deloach, L. D., R. H. Page, G. D. Wilke, S. A. Payne, and W. F. Krupke, 1996, IEEE J. Quantum Electron. **32**, 885.

Denecke, M. A., 2016, in *X-Ray Absorption and X-Ray Emission Spectroscopy: Theory and Applications*, edited by J. A. van Bokhoven and C. Lamberti (John Wiley & Sons, Chichester, UK), p. 523.

Denecke, R., 2005, Appl. Phys. A **80**, 977.

Deneke, C., N. Y. Jin-Phillipp, I. Loa, and O. G. Schmidt, 2004, Appl. Phys. Lett. **84**, 4475.

Deneke, C., A. Malachias, S. Kiravittaya, M. Benyoucef, T. H. Metzger, and O. G. Schmidt, 2010, Appl. Phys. Lett. **96**, 143101.

Deneke, C., C. Muller, N. Y. Jin-Phillipp, and O. G. Schmidt, 2002, Semicond. Sci. Technol. **17**, 1278.

Deneke, C., and O. G. Schmidt, 2004, Appl. Phys. Lett. **85**, 2914.

Deng, J. J., D. J. Vine, S. Chen, Y. S. G. Nashed, Q. L. Jin, N. W. Phillips, T. Peterka, R. Rossc, S. Vogt, and C. J. Jacobsen, 2015, Proc. Natl. Acad. Sci. U.S.A. **112**, 2314.

Dera, P., 2010, in *High-Pressure Crystallography: from fundamental phenomena to technological applications*, edited by E. Boldyreva and P. Dera (Springer Sciences, Dordrecht), p. 11.

Deslattes, R. D., E. G. Kessler, P. Indelicato, L. de Billy, E. Lindroth, and J. Anton, 2003, Rev. Mod. Phys. **75**, 35.

de Smit, E., and B. M. Weckhuysen, 2008, Chem. Soc. Rev. **37**, 2758.

de Smit, E., *et al.*, 2008, Nature (London) **456**, 222.

De Stasio, G., G. F. Lorusso, T. Droubay, M. Kohli, P. Muralt, P. Perfetti, G. Margaritondo, T. F. Kelly, and B. P. Tonner, 1996, Rev. Sci. Instrum. **67**, 737.

Dettmar, C. M., J. A. Newman, S. J. Toth, M. Becker, R. F. Fischetti, and G. J. Simpson, 2015, Proc. Natl. Acad. Sci. U.S.A. **112**, 696.

Dewolf, I., H. Norstrom, and H. E. Maes, 1993, J. Appl. Phys. **74**, 4490.

Dhakshinamoorthy, A., and H. Garcia, 2012, Chem. Soc. Rev. **41**, 5262.

Diaferia, C., F. A. Mercurio, C. Giannini, T. Sibillano, G. Morelli, M. Leone, and A. Accardo, 2016, Sci. Rep. **6**, 26638.

Diaz, A., C. Mocuta, J. Stangl, J. Vila-Comamala, C. David, T. H. Metzger, and G. Bauer, 2009, Phys. Status Solidi A **206**, 1829.

Di Cicco, A., F. D'Amico, G. Zgrablic, E. Principi, R. Gunnella, F. Bencivenga, C. Svetina, C. Masciovecchio, F. Parmigiani, and A. Filipponi, 2011, J. Non-Cryst. Solids **357**, 2641.

Dierolf, M., A. Menzel, P. Thibault, P. Schneider, C. M. Kewish, R. Wepf, O. Bunk, and F. Pfeiffer, 2010, Nature (London) **467**, 436.

Dietl, T., 2010, Nat. Mater. **9**, 965.

Dietl, T., H. Ohno, F. Matsukura, J. Cibert, and D. Ferrand, 2000, Science **287**, 1019.

Dietl, T., K. Sato, T. Fukushima, A. Bonanni, M. Jamet, A. Barski, S. Kuroda, M. Tanaka, P. N. Hai, and H. Katayama-Yoshida, 2015, Rev. Mod. Phys. **87**, 1311.

Ditchburn, R. W., 1991, *Light*, Dover Books on Physics (Dover Publications Inc., New York).

Doring, F., *et al.*, 2013, Opt. Express **21**, 19311.

Dorner, R., V. Mergel, O. Jagutzki, L. Spielberger, J. Ullrich, R. Moshammer, and H. Schmidt-Bocking, 2000, Phys. Rep. **330**, 95.

Doronkin, D. E., M. Casapu, T. Gunter, O. Muller, R. Frahm, and J. D. Grunwaldt, 2014, J. Phys. Chem. C **118**, 10204.

Doronkin, D. E., H. Lichtenberg, and J.-D. Grunwaldt, 2017, in *XAFS Techniques for Catalysts, Nanomaterials, and Surfaces*, edited by Y. Iwasawa, K. Asakura, and M. Tada (Springer, New York), p. 75.

Dorsch, W., B. Steiner, M. Albrecht, H. P. Strunk, H. Wawra, and G. Wagner, 1998, J. Cryst. Growth **183**, 305.

Dubslaff, M., M. Hanke, S. Schoder, M. Burghammer, T. Boeck, and J. Patommel, 2010, Appl. Phys. Lett. **96**, 133107.

Dudchik, Y. I., P. A. Ershov, M. V. Polikarpov, A. Y. Goikhman, I. I. Snigireva, and A. A. Snigirev, 2016, J. Surf. Invest.: X-Ray, Synchrotron Neutron Tech. **10**, 1011.

Duffort, V., V. Caignaert, V. Pralong, B. Raveau, M. R. Suchomel, and J. F. Mitchell, 2014, Solid State Commun. **182**, 22.

Eastman, D. E., C. B. Stagarescu, G. Xu, P. M. Mooney, J. L. Jordan-Sweet, B. Lai, and Z. Cai, 2002, Phys. Rev. Lett. **88**, 156101.

Edwards, G. S., S. J. Allen, R. F. Haglund, R. J. Nemanich, B. Redlich, J. D. Simon, and W. C. Yang, 2005, Photochem. Photobiol. **81**, 711.

Egelhoff, W. F., 1987, Surf. Sci. Rep. **6**, 253.

Eggl, E., M. Dierolf, K. Achterhold, C. Jud, B. Gunther, E. Braig, B. Gleich, and F. Pfeiffer, 2016, J. Synchrotron Radiat. **23**, 1137.

Eisebitt, S., J. Luning, W. F. Schlotter, M. Lorgen, O. Hellwig, W. Eberhardt, and J. Stohr, 2004, Nature (London) **432**, 885.

Eland, J. H. D., P. Linusson, L. Hedin, E. Andersson, J. E. Rubensson, and R. Feifel, 2008, Phys. Rev. A **78**, 063423.

Eland, J. H. D., O. Vieuxmaire, T. Kinugawa, P. Lablanquie, R. I. Hall, and F. Penent, 2003, Phys. Rev. Lett. **90**, 053003.

Emma, P., *et al.*, 2010, Nat. Photonics **4**, 641.

Emura, S., T. Moriga, J. Takizawa, M. Nomura, K. R. Bauchspiess, T. Murata, K. Harada, and H. Maeda, 1993, Phys. Rev. B **47**, 6918.

Endo, K., P. Badica, G. Uehara, and H. Kado, 2011, IEEE Trans. Appl. Supercond. **21**, 2771.

Eriksson, M., J. F. van der Veen, and C. Quitmann, 2014, J. Synchrotron Radiat. **21**, 837.

Erko, A. I., V. V. Aristov, and B. Vidal, 1996, *Diffraction X-ray optics* (Institute of Physics Publishing, Bristol/Philadelphia).

Erko, I., M. Idir, T. Krist, and A. G. Michette, 2008, Eds., *Modern Developments in X-Ray and Neutron Optics* (Springer, Berlin).

Erni, R., M. D. Rossell, C. Kisielowski, and U. Dahmen, 2009, Phys. Rev. Lett. **102**, 096101.

Esaki, L., 1986, IEEE J. Quantum Electron. **22**, 1611.

Escher, M., *et al.*, 2005, J. Electron Spectrosc. Relat. Phenom. **144–147**, 1179.

Eschrig, M., 2006, Adv. Phys. **55**, 47.

Eskildsen, M. R., P. L. Gammel, E. D. Isaacs, C. Detlefs, K. Mortensen, and D. J. Bishop, 1998, Nature (London) **391**, 563.

Evans, J., 1997, Chem. Soc. Rev. **26**, 11.

Evans-Lutterodt, K., A. Stein, J. M. Ablett, N. Bozovic, A. Taylor, and D. M. Tennant, 2007, Phys. Rev. Lett. **99**, 134801.

Fahrni, C. J., 2007, Curr. Opin. Chem. Biol. **11**, 121.

Falcone, R., C. Jacobsen, J. Kirz, S. Marchesini, D. Shapiro, and J. Spence, 2011, Contemp. Phys. **52**, 293.

Fan, W., M. A. Snyder, S. Kumar, P. S. Lee, W. C. Yoo, A. V. McCormick, R. L. Penn, A. Stein, and M. Tsapatsis, 2008, Nat. Mater. **7**, 984.

Fang, B., J. H. Kim, M. S. Kim, and J. S. Yu, 2013, Acc. Chem. Res. **46**, 1397.

Farag, A. A. M., M. Fadel, and I. S. Yahia, 2012, Curr. Appl. Phys. **12**, 1436.

Farges, F., and M. Cotte, 2016, in *X-Ray Absorption and X-Ray Emission Spectroscopy: Theory and Applications*, edited by J. A. van Bokhoven and C. Lamberti (John Wiley & Sons, Chichester, UK), p. 609.

Faulkner, H. M. L., and J. M. Rodenburg, 2004, Phys. Rev. Lett. **93**, 023903.

Fayard, B., M. Salome, K. Takemoto, H. Kihara, and J. Susini, 2009, J. Electron Spectrosc. Relat. Phenom. **170**, 19.

Fernandez-Garcia, M., 2002, Catal. Rev. Sci. Eng. **44**, 59.

Fienup, J. R., 2013, Appl. Opt. **52**, 45.

Fitzsimmons, M. R., *et al.*, 2004, J. Magn. Magn. Mater. **271**, 103.

Flank, A. M., *et al.*, 2006, Nucl. Instrum. Methods Phys. Res., Sect. B **246**, 269.
Fletcher, L. B., *et al.*, 2015, Nat. Photonics **9**, 274.
Fournier, C., C. Merlet, O. Dugne, and M. Fialin, 1999, J. Anal. At. Spectrom. **14**, 381.
Fradkin, E., S. A. Kivelson, and J. M. Tranquada, 2015, Rev. Mod. Phys. **87**, 457.
Frank, M., *et al.*, 2014, IUCrJ **1**, 95.
Frasinski, L. J., *et al.*, 2013, Phys. Rev. Lett. **111**, 073002.
Fratini, M., N. Poccia, A. Ricci, G. Campi, M. Burghammer, G. Aeppli, and A. Bianconi, 2010, Nature (London) **466**, 841.
Frello, T., N. H. Andersen, J. Madsen, M. Kali, M. vonZimmermann, O. Schmidt, H. F. Poulsen, J. R. Schneider, and T. Wolf, 1997, Physica C (Amsterdam) **282–287**, 1089.
Frenkel, A. I., 2012, Chem. Soc. Rev. **41**, 8163.
Frenkel, A. I., A. Yevick, C. Cooper, and R. Vasic, 2011, Annu. Rev. Anal. Chem. **4**, 23.
Froideval, A., A. Badillo, J. Bertsch, S. Churakov, R. Dahn, C. Degueldre, T. Lind, D. Paladino, and B. D. Patterson, 2011, J. Nucl. Mater. **416**, 242.
Fuhrmann, T., M. Kinne, B. Trankenschuh, C. Papp, J. F. Zhu, R. Denecke, and H. P. Steinruck, 2005, New J. Phys. **7**, 107.
Fuhrmann, T., M. Kinne, C. M. Whelan, J. F. Zhu, R. Denecke, and H. P. Steinruck, 2004, Chem. Phys. Lett. **390**, 208.
Fujita, N., K. Ishii, and H. Ogawa, 2011, Nucl. Instrum. Methods Phys. Res., Sect. B **269**, 1023.
Fukutani, K., 2002, Curr. Opin. Solid State Mater. Sci. **6**, 153.
Gai, B. J., Y. K. Sun, H. Lim, H. D. Chen, J. Faucher, M. L. Lee, and J. Yoon, 2017, ACS Nano **11**, 992.
Galindo, R. E., R. Gago, D. Duday, and C. Palacio, 2010, Anal. Bioanal. Chem. **396**, 2725.
Gallo, E., and P. Glatzel, 2014, Adv. Mater. **26**, 7730.
Gallo, E., A. Piovano, C. Marini, O. Mathon, S. Pascarelli, P. Glatzel, C. Lamberti, and G. Berlier, 2014, J. Phys. Chem. C **118**, 11745.
Gambirasio, A., M. Bernasconi, and L. Colombo, 2000, Phys. Rev. B **61**, 8233.
Gardelis, S., C. G. Smith, C. H. W. Barnes, E. H. Linfield, and D. A. Ritchie, 1999, Phys. Rev. B **60**, 7764.
Garino, C., E. Borfecchia, R. Gobetto, J. A. van Bokhoven, and C. Lamberti, 2014, Coord. Chem. Rev. **277–278**, 130.
Garman, E. F., 2010, Acta Crystallogr. Sect. D **66**, 339.
Garman, E. F., and M. Weik, 2017, J. Synchrotron Radiat. **24**, 1.
Gauvin, R., 2012, Microsc. Microanal. **18**, 915.
Georgi, C., M. Hecker, and E. Zschech, 2007, J. Appl. Phys. **101**, 123104.
Giannini, C., D. Altamura, B. M. Aresta, T. Sibillano, D. Siliqi, and L. De Caro, 2013, in *Synthesis and characterization of inorganic micro and nano-materials*, edited by A. Di Benedetto and M. Aresta (De Gruyter, Berlin/Boston), p. 137.
Giannini, C., M. Ladisa, D. Altamura, D. Siliqi, T. Sibillano, and L. De Caro, 2016, Crystals **6**, 87.
Gilmore, I. S., 2013, J. Vac. Sci. Technol. A **31**, 050819.
Gilow, C., E. Zolotoyabko, O. Paris, P. Fratzl, and B. Aichmayer, 2011, Cryst. Growth Des. **11**, 2054.
Ginn, H. M., *et al.*, 2015, Nat. Commun. **6**, 6435.
Glatter, O., 1979, J. Appl. Crystallogr. **12**, 166.
Glatzel, P., and U. Bergmann, 2005, Coord. Chem. Rev. **249**, 65.
Gnodtke, C., U. Saalmann, and J. M. Rost, 2009, Phys. Rev. A **79**, 041201.
Godard, P., G. Carbone, M. Allain, F. Mastropietro, G. Chen, L. Capello, A. Diaz, T. H. Metzger, J. Stangl, and V. Chamard, 2011, Nat. Commun. **2**, 568.
Gonzalez-Jimenez, I. D., *et al.*, 2012, Angew. Chem., Int. Ed. Engl. **51**, 11986.
Gopinath, A., S. V. Boriskina, B. M. Reinhard, and L. Dal Negro, 2009, Opt. Express **17**, 3741.
Gordillo, N., C. Habchi, L. Daudin, A. Sakellariou, F. Delalee, P. Barberet, S. Incerti, H. Seznec, and P. Moretto, 2011, Nucl. Instrum. Methods Phys. Res., Sect. B **269**, 2206.
Gor'kov, L. P., and V. Z. Kresin, 2018, Rev. Mod. Phys. **90**, 011001.
Gould, C., K. Pappert, G. Schmidt, and L. W. Molenkamp, 2007, Adv. Mater. **19**, 323.
Goulon, J., P. Tola, M. Lemonnier, and J. Dexper-Ghys, 1983, Chem. Phys. **78**, 347.
Graewert, M. A., and D. I. Svergun, 2013, Curr. Opin. Struct. Biol. **23**, 748.
Greivenkamp, J. E., 2004, *Field Guide to Geometrical Optics* (SPIE Press, Bellingham, WA).
Groppo, E., G. Agostini, E. Borfecchia, A. Lazzarini, W. Liu, C. Lamberti, F. Giannici, G. Portale, and A. Longo, 2015, ChemCatChem **7**, 2188.
Groppo, E., G. Agostini, A. Piovano, N. B. Muddada, G. Leofanti, R. Pellegrini, G. Portale, A. Longo, and C. Lamberti, 2012, J. Catal. **287**, 44.
Groppo, E., W. Liu, O. Zavorotynska, G. Agostini, G. Spoto, S. Bordiga, C. Lamberti, and A. Zecchina, 2010, Chem. Mater. **22**, 2297.
Groppo, E., *et al.*, 2015, ChemCatChem **7**, 1432.
Grundmann, M., 2003, Appl. Phys. Lett. **83**, 2444.
Gruner, S. M., 2010, AIP Conf. Proc. **1234**, 69.
Grunwaldt, J. D., M. Caravati, S. Hannemann, and A. Baiker, 2004, Phys. Chem. Chem. Phys. **6**, 3037.
Grunwaldt, J. D., and C. G. Schroer, 2010, Chem. Soc. Rev. **39**, 4741.
Grunwaldt, J. D., J. B. Wagner, and R. E. Dunin-Borkowski, 2013, ChemCatChem **5**, 62.
Grutzmacher, D., *et al.*, 2007, Nano Lett. **7**, 3150.
Guda, S. A., *et al.*, 2015, J. Chem. Theory Comput. **11**, 4512.
Gundel, P., G. Martinez-Criado, M. C. Schubert, J. A. Sans, W. Kwapil, W. Warta, and E. R. Weber, 2009, Phys. Status Solidi RRL **3**, 275.
Gunter, T., D. E. Doronkin, A. Boubnov, H. W. P. Carvalho, M. Casapu, and J. D. Grunwaldt, 2016, Top. Catal. **59**, 866.
Gunther, S., B. Kaulich, L. Gregoratti, and M. Kiskinova, 2002, Prog. Surf. Sci. **70**, 187.
Guthrie, M., 2015, J. Phys. Condens. Matter **27**, 153201.
Guttmann, P., C. Bittencourt, S. Rehbein, P. Umek, X. X. Ke, G. Van Tendeloo, C. P. Ewels, and G. Schneider, 2012, Nat. Photonics **6**, 25.
Guttmann, P., X. Zeng, M. Feser, S. Heim, W. Yun, and G. Schneider, 2009, J. Phys. Conf. Ser. **186**, 012064.
Haase, M. A., J. Xie, T. A. Ballen, J. Zhang, B. Hao, Z. H. Yang, T. J. Miller, X. Sun, T. L. Smith, and C. A. Leatherdale, 2010, Appl. Phys. Lett. **96**, 231116.
Hall, M. D., G. J. Foran, M. Zhang, P. J. Beale, and T. W. Hambley, 2003, J. Am. Chem. Soc. **125**, 7524.
Han, H. L., G. Melaet, S. Alayoglu, and G. A. Somorjai, 2015, ChemCatChem **7**, 3625.
Hanke, M., M. Dubslaff, M. Schmidbauer, T. Boeck, S. Schoder, M. Burghammer, C. Riekel, J. Patommel, and C. G. Schroer, 2008, Appl. Phys. Lett. **92**, 193109.
Hanke, M., M. Schmidbauer, R. Kohler, F. Syrowatka, A. K. Gerlitzke, and T. Boeck, 2004, Appl. Phys. Lett. **84**, 5228.
Harks, P., F. M. Mulder, and P. H. L. Notten, 2015, J. Power Sources **288**, 92.
Hasan, M. Z., and J. E. Moore, 2011, "Three-Dimensional Topological Insulators," in *Annual Review of Condensed Matter Physics*, Vol. 2, edited by J. S. Langer (Annual Reviews, Palo Alto), p. 55.

Hau-Riege, S. P., 2011, *High-Intensity X-Rays Interaction with Matter* (Wiley-VCH, Weinheim).
Hedman, B., K. O. Hodgson, J. R. Helliwell, R. Liddington, and M. Z. Papiz, 1985, Proc. Natl. Acad. Sci. U.S.A. **82**, 7604.
Hehre, W. J., L. Radom, P. V. R. Schleyer, and J. A. Pople, 1986, *Ab initio molecular orbital theory* (Wiley-Interscience, New York).
Helfen, L., T. Baumbach, P. Mikulik, D. Kiel, P. Pernot, P. Cloetens, and J. Baruchel, 2005, Appl. Phys. Lett. **86**, 071915.
Helfen, L., A. Myagotin, P. Pernot, M. DiMichiel, P. Mikulik, A. Berthold, and T. Baumbach, 2006, Nucl. Instrum. Methods Phys. Res., Sect. A **563**, 163.
Hellman, F., *et al.*, 2017, Rev. Mod. Phys. **89**, 025006.
Hemonnot, C. Y. J., J. Reinhardt, O. Saldanha, J. Patommel, R. Graceffa, B. Weinhausen, M. Burghammer, C. G. Schroer, and S. Koster, 2016, ACS Nano **10**, 3553.
Henderson, R., 1995, Q. Rev. Biophys. **28**, 171.
Henke, B. L., E. M. Gullikson, and J. C. Davis, 1993, At. Data Nucl. Data Tables **54**, 181.
Heo, Y. W., D. P. Norton, L. C. Tien, Y. Kwon, B. S. Kang, F. Ren, S. J. Pearton, and J. R. LaRoche, 2004, Mater. Sci. Eng. R-Rep. **47**, 1.
Hirohata, A., and K. Takanashi, 2014, J. Phys. D **47**, 193001.
Holton, J. M., 2009, J. Synchrotron Radiat. **16**, 133.
Holton, J. M., and K. A. Frankel, 2010, Acta Crystallogr. Sect. D **66**, 393.
Honkavaara, K., 2017, "Status of the FLASH FEL user facility at DESY," in *Proceedings of the 38th International Free Electron Laser Conference, FEL2017*, edited by K. Bishopsberger and V. R. W. Schaa (Joint Accelerator Conferences, CERN, Geneva), p. 14.
Honnicke, M. G., J. W. Keister, R. Conley, K. Kaznatcheev, P. Z. Takacs, D. S. Coburn, L. Reffi, and Y. Q. Cai, 2011, J. Synchrotron Radiat. **18**, 862.
Hopkins, J. B., and R. E. Thorne, 2016, J. Appl. Crystallogr. **49**, 880.
Hoppe, W., 1969, Acta Crystallogr. Sect. A **25**, 495.
Horiba, K., Y. Nakamura, N. Nagamura, S. Toyoda, H. Kumigashira, M. Oshima, K. Amemiya, Y. Senba, and H. Ohashi, 2011, Rev. Sci. Instrum. **82**, 113701.
Hosoda, M., Y. Kishimoto, M. Sato, S. Nashima, K. Kubota, S. Saravanan, P. O. Vaccaro, T. Aida, and N. Ohtani, 2003, Appl. Phys. Lett. **83**, 1017.
Howells, M. R., *et al.*, 2009, J. Electron Spectrosc. Relat. Phenom. **170**, 4.
Hrauda, N., *et al.*, 2011, Nano Lett. **11**, 2875.
Hruszkewycz, S. O., M. J. Highland, M. V. Holt, D. Kim, C. M. Folkman, C. Thompson, A. Tripathi, G. B. Stephenson, S. Hong, and P. H. Fuoss, 2013, Phys. Rev. Lett. **110**, 177601.
Huang, M. H., C. Boone, M. Roberts, D. E. Savage, M. G. Lagally, N. Shaji, H. Qin, R. Blick, J. A. Nairn, and F. Liu, 2005, Adv. Mater. **17**, 2860.
Huang, Z. F., *et al.*, 2015, Nat. Mater. **14**, 691.
Hubbell, J. H., P. N. Trehan, N. Singh, B. Chand, D. Mehta, M. L. Garg, R. R. Garg, S. Singh, and S. Puri, 1994, J. Phys. Chem. Ref. Data **23**, 339.
Hue, F., M. Hytch, H. Bender, F. Houdellier, and A. Claverie, 2008, Phys. Rev. Lett. **100**, 156602.
Ibn al-Haytham, 1989, *Optics*, Books I–III on Direct Vision translated with introduction and commentary by A. I. Sabra of Harvard University (The Warburg Institute, London).
Ice, G. E., J. D. Budai, and J. W. L. Pang, 2011, Science **334**, 1234.
Ice, G. E., and E. D. Specht, 2012, J. Nucl. Mater. **425**, 233.
Ikonen, E., 2010, Opt. Rev. **17**, 239.
Ingham, B., 2015, Crystallography Reviews **21**, 229.
Inomata, K., T. Kawae, K. Nakajima, S. J. Kim, and T. Yamashita, 2003, Appl. Phys. Lett. **82**, 769.
Isaji, T., T. Wakasugi, K. Fukumi, and K. Kadono, 2012, Chem. Phys. Lett. **522**, 72.
Ito, S., H. Namba, T. Hirata, K. Ando, S. Koyama, N. Ikezawa, T. Suzuki, T. Saitoh, and T. Horiuchi, 2002, Microelectron. Reliab. **42**, 201.
Jacobsen, S. D., J. F. Lin, R. J. Angel, G. Y. Shen, V. B. Prakapenka, P. Dera, H. K. Mao, and R. J. Hemley, 2005, J. Synchrotron Radiat. **12**, 577.
Janssens, K., W. De Nolf, G. Van Der Snickt, L. Vincze, B. Vekemans, R. Terzano, and F. E. Brenker, 2010, Trac Trends Anal. Chem. **29**, 464.
Janssens, T. V. W., *et al.*, 2015, ACS Catal. **5**, 2832.
Jeffries, C. M., M. A. Graewert, D. I. Svergun, and C. E. Blanchet, 2015, J. Synchrotron Radiat. **22**, 273.
Jeong, D. S., R. Thomas, R. S. Katiyar, J. F. Scott, H. Kohlstedt, A. Petraru, and C. S. Hwang, 2012, Rep. Prog. Phys. **75**, 076502.
Jeschke, H. O., M. E. Garcia, and K. H. Bennemann, 1999, Appl. Phys. A **69**, S49.
Jiang, H. D., *et al.*, 2010, Proc. Natl. Acad. Sci. U.S.A. **107**, 11234.
Johansson, S. A. E., J. L. Campbell, and K. G. Malmqvist, 1995, *Particle-Induced X-Ray Emission Spectrometry (PIXE)* (Wiley, Chichester).
Johansson, T. B., R. Akselsson, and S. A. E. Johansson, 1970, Nucl. Instrum. Methods **84**, 141.
Joyce, H. J., *et al.*, 2011, Prog. Quantum Electron. **35**, 23.
Jurek, Z., G. Faigel, and M. Tegze, 2004, Eur. Phys. J. D **29**, 217.
Kada, W., T. Satoh, A. Yokoyama, M. Koka, and T. Kamiya, 2014, Nucl. Instrum. Methods Phys. Res., Sect. B **318**, 42.
Kalinin, S. V., and A. Gruverman, 2011, *Scanning Probe Microscopy of Functional Materials: Nanoscale Imaging and Spectroscopy* (Springer, New York).
Kalirai, S., U. Boesenberg, G. Falkenberg, F. Meirer, and B. M. Weckhuysen, 2015, ChemCatChem **7**, 3674.
Kamat, P. V., 2002, J. Phys. Chem. B **106**, 7729.
Kamiya, T., K. Takano, T. Satoh, Y. Ishii, H. Nishikawa, S. Seki, M. Sugimoto, S. Okumura, and M. Fukuda, 2011, Nucl. Instrum. Methods Phys. Res., Sect. B **269**, 2184.
Kanaya, K., and S. Okayama, 1972, J. Phys. D **5**, 43.
Karpinski, J., *et al.*, 1999, Supercond. Sci. Technol. **12**, R153.
Karydas, A. G., D. Sokaras, C. Zarkadas, N. Grlj, P. Pelicon, M. Zitnik, R. Schutz, W. Malzer, and B. Kanngiesser, 2007, J. Anal. At. Spectrom. **22**, 1260.
Katoh, T., N. Nishi, M. Fukagawa, H. Ueno, and S. Sugiyama, 2001, Sens. Actuators, A **89**, 10.
Katsaros, G., P. Spathis, M. Stoffel, F. Fournel, M. Mongillo, V. Bouchiat, F. Lefloch, A. Rastelli, O. G. Schmidt, and S. De Franceschi, 2010, Nat. Nanotechnol. **5**, 458.
Kelly, K. L., E. Coronado, L. L. Zhao, and G. C. Schatz, 2003, J. Phys. Chem. B **107**, 668.
Kern, J., *et al.*, 2012, Proc. Natl. Acad. Sci. U.S.A. **109**, 9721.
Kerssens, M. M., A. Wilbers, J. Kramer, P. de Peinder, G. Mesu, B. J. Nelissen, E. T. C. Vogt, and B. M. Weckhuysen, 2016, Faraday Discuss. **188**, 69.
Kilcoyne, A. L. D., *et al.*, 2003, J. Synchrotron Radiat. **10**, 125.
Kimmerle, B., J. D. Grunwaldt, A. Baiker, P. Glatzel, P. Boye, S. Stephan, and C. G. Schroer, 2009, J. Phys. Chem. C **113**, 3037.
Kimura, T., *et al.*, 2014, Nat. Commun. **5**, 3052.
Kipp, T., H. Welsch, C. Strelow, C. Heyn, and D. Heitmann, 2006, Phys. Rev. Lett. **96**, 077403.
Kirkpatrick, P., and A. V. Baez, 1948, J. Opt. Soc. Am. **38**, 766.

Kiryukhin, V., D. Casa, J. P. Hill, B. Keimer, A. Vigliante, Y. Tomioka, and Y. Tokura, 1997, Nature (London) **386**, 813.
Kiskinova, M., M. Marsi, E. Di Fabrizio, and M. Gentili, 1999, Surf. Rev. Lett. **06**, 265.
Kleiner, R., F. Steinmeyer, G. Kunkel, and P. Muller, 1992, Phys. Rev. Lett. **68**, 2394.
Knop-Gericke, A., *et al.*, 2009, Adv. Catal. **52**, 213.
Knudsen, J., J. N. Andersen, and J. Schnadt, 2016, Surf. Sci. **646**, 160.
Kobayashi, K., 2005, Nucl. Instrum. Methods Phys. Res., Sect. A **547**, 98.
Koester, S. J., R. Hammond, J. O. Chu, P. M. Mooney, J. A. Ott, L. Perraud, K. A. Jenkins, C. S. Webster, I. Lagnado, and P. R. de la Houssaye, 2001, IEEE Electron Device Lett. **22**, 92.
Kolmakov, A., D. A. Dikin, L. J. Cote, J. X. Huang, M. K. Abyaneh, M. Amati, L. Gregoratti, S. Gunther, and M. Kiskinova, 2011, Nat. Nanotechnol. **6**, 651.
Koopmans, T., 1934, Physica (Utrecht) **1**, 104.
Kotani, A., and S. Shin, 2001, Rev. Mod. Phys. **73**, 203.
Kozhevnikov, S. V., A. Ruhm, F. Ott, N. K. Pleshanov, and J. Major, 2011, Physica B (Amsterdam) **406**, 2463.
Krause, B., C. Mocuta, T. H. Metzger, C. Deneke, and O. G. Schmidt, 2006, Phys. Rev. Lett. **96**, 165502.
Kristiansen, P., J. Horbach, R. Dohrmann, and J. Heuer, 2015, J. Synchrotron Radiat. **22**, 879.
Kuisma-Kursula, P., 2000, X-Ray Spectrom. **29**, 111.
Kumakhov, M. A., and V. A. Sharov, 1992, Nature (London) **357**, 390.
Kumar, S., Z. W. Wang, X. P. Huang, N. Kumari, N. Davila, J. P. Strachan, D. Vine, A. L. D. Kilcoyne, Y. Nishi, and R. S. Williams, 2016, ACS Nano **10**, 11205.
Kuppili, V. S. C., S. Sala, S. Chalkidis, A. M. Wise, A. D. Parsons, I. Zanette, C. Rau, and P. Thibault, 2017, J. Phys. Conf. Ser. **849**, 012031.
Kwapil, W., P. Gundel, M. C. Schubert, F. D. Heinz, W. Warta, E. R. Weber, A. Goetzberger, and G. Martinez-Criado, 2009, Appl. Phys. Lett. **95**, 232113.
Kwapil, W., M. Kasemann, P. Gundel, M. C. Schubert, W. Warta, P. Bronsveld, and G. Coletti, 2009, J. Appl. Phys. **106**, 063530.
Labiche, J. C., O. Mathon, S. Pascarelli, M. A. Newton, G. G. Ferre, C. Curfs, G. Vaughan, A. Homs, and D. F. Carreiras, 2007, Rev. Sci. Instrum. **78**, 091301.
Lambert, J. H., 1760, *Photometria sive de mensura et gradibus luminis, colorum et umbrae (On the measure and gradations of light, colors, and shade)* (Eberhardt Klett, Augsburg), p. 391.
Lamberti, C., 1996a, Comput. Phys. Commun. **93**, 53.
Lamberti, C., 1996b, Comput. Phys. Commun. **93**, 82.
Lamberti, C., 2004, Surf. Sci. Rep. **53**, 1.
Lamberti, C., S. Bordiga, M. Salvalaggio, G. Spoto, A. Zecchina, F. Geobaldo, G. Vlaic, and M. Bellatreccia, 1997, J. Phys. Chem. B **101**, 344.
Lamberti, C., E. Borfecchia, J. A. Van Bokhoven, and M. Fernández-García, 2016, in *X-Ray Absorption and X-Ray Emission Spectroscopy: Theory and Applications*, edited by J. A. van Bokhoven and C. Lamberti (John Wiley & Sons, Chichester, UK), p. 303.
Lamberti, C., E. Groppo, C. Prestipino, S. Casassa, A. M. Ferrari, C. Pisani, C. Giovanardi, P. Luches, S. Valeri, and F. Boscherini, 2003, Phys. Rev. Lett. **91**, 046101.
Lamberti, C., and J. A. van Bokhoven, 2016, in *X-ray absorption and X-ray emission spectroscopy: theory and applications*, edited by J. A. van Bokhoven and C. Lamberti (John Wiley & Sons, Chichester, UK), p. 353.
Lamberti, C., *et al.*, 2003, Nucl. Instrum. Methods Phys. Res., Sect. B **200**, 196.
Larcheri, S., F. Rocca, D. Pailharey, F. Jandard, R. Graziola, A. Kuzmin, R. Kalendarev, and J. Purans, 2009, Micron **40**, 61.
Larciprete, R., L. Gregoratti, M. Danailov, R. M. Montereali, I. Bonfigli, and M. Kiskinova, 2002, Appl. Phys. Lett. **80**, 3862.
Larson, B. C., W. Yang, G. E. Ice, J. D. Budai, and J. Z. Tischler, 2002, Nature (London) **415**, 887.
Latyshev, Y. I., T. Yamashita, L. N. Bulaevskii, M. J. Graf, A. V. Balatsky, and M. P. Maley, 1999, Phys. Rev. Lett. **82**, 5345.
Lefevre, H. W., R. M. S. Schofield, J. C. Overley, and J. D. Macdonald, 1987, Scanning Microsc. **1**, 879 [https://www.semanticscholar.org/paper/Scanning-transmission-ion-microscopy-as-it-particle-Lef%C3%A8vre-Schofield/bfdb3043d83e7f93f09582fabb5f263e0354097d].
Leite, M. S., A. Malachias, S. W. Kycia, T. I. Kamins, R. S. Williams, and G. Medeiros-Ribeiro, 2008, Phys. Rev. Lett. **100**, 226101.
Leontowich, A. F. G., and A. P. Hitchcock, 2011, Appl. Phys. A **103**, 1.
Leontowich, A. F. G., A. P. Hitchcock, B. Watts, and J. Raabe, 2013, Microelectron. Eng. **108**, 5.
Leung, B. O., J. L. Brash, and A. P. Hitchcock, 2010, Materials **3**, 3911.
Li, F., and Z. T. Mi, 2009, Opt. Express **17**, 19933.
Li, J. J., Y. A. Wang, W. Z. Guo, J. C. Keay, T. D. Mishima, M. B. Johnson, and X. G. Peng, 2003, J. Am. Chem. Soc. **125**, 12567.
Li, T., A. J. Senesi, and B. Lee, 2016, Chem. Rev. **116**, 11128.
Liao, H. W., C. L. Nehl, and J. H. Hafner, 2006, Nanomedicine **1**, 201.
Libera, J., Z. Cai, B. Lai, and S. Xu, 2002, Rev. Sci. Instrum. **73**, 1506.
Liborio, L., and N. Harrison, 2008, Phys. Rev. B **77**, 104104.
Liebermann, R. C., 2011, High Press. Res. **31**, 493.
Liekhus-Schmaltz, C. E., *et al.*, 2015, Nat. Commun. **6**, 8199.
Lifshin, E., 2008, *X-ray Characterization of Materials* (Wiley, Weinheim).
Lim, S. K., M. Brewster, F. Qian, Y. Li, C. M. Lieber, and S. Gradecak, 2009, Nano Lett. **9**, 3940.
Linic, S., U. Aslam, C. Boerigter, and M. Morabito, 2015, Nat. Mater. **14**, 567.
Linic, S., P. Christopher, H. L. Xin, and A. Marimuthu, 2013, Acc. Chem. Res. **46**, 1890.
Liu, L., N. Milas, A. H. C. Mukai, X. R. Rsende, and F. H. de Sa, 2014, J. Synchrotron Radiat. **21**, 904.
Liu, N. N., P. S. Raman, X. X. Xu, H. M. Tan, A. Khursheed, and J. A. van Kan, 2015, Nucl. Instrum. Methods Phys. Res., Sect. B **348**, 23.
Liu, Q. Q., H. Yang, X. M. Qin, Y. Yu, L. X. Yang, F. Y. Li, R. C. Yu, C. Q. Jin, and S. Uchida, 2006, Phys. Rev. B **74**, 100506.
Liu, Y. J., K. H. Cats, J. N. Weker, J. C. Andrews, B. M. Weckhuysen, and P. Pianetta, 2013, in *X-Ray Nanoimaging: Instruments and Methods*, edited by B. Lai (SPIE—Int. Soc. Optical Engineering, Bellingham, WA).
Liu, Y. J., F. Meirer, C. M. Krest, S. Webb, and B. M. Weckhuysen, 2016, Nat. Commun. **7**, 12634.
Liu, Y. J., F. Meirer, P. A. Williams, J. Y. Wang, J. C. Andrews, and P. Pianetta, 2012, J. Synchrotron Radiat. **19**, 281.
Llorens, I., *et al.*, 2014, Radiochim. Acta **102**, 957.
Lomachenko, K. A., E. Borfecchia, C. Negri, G. Berlier, C. Lamberti, P. Beato, H. Falsig, and S. Bordiga, 2016, J. Am. Chem. Soc. **138**, 12025.
London, R. A., R. M. Bionta, R. O. Tatchyn, and S. Roesler, 2001, in *Optics for Fourth-Generation X-Ray Sources*, edited by R. O. Tatchyn, A. K. Freund, and T. Matsushita (SPIE—Int. Soc. Optical Engineering, Bellingham, WA), p. 51.

Luches, P., S. D'Addato, S. Valeri, E. Groppo, C. Prestipino, C. Lamberti, and F. Boscherini, 2004, Phys. Rev. B **69**, 045412.
Macdonald, A. H., P. Schiffer, and N. Samarth, 2005, Nat. Mater. **4**, 195.
Maiden, A. M., and J. M. Rodenburg, 2009, Ultramicroscopy **109**, 1256.
Malachias, A., C. Deneke, B. Krause, C. Mocuta, S. Kiravittaya, T. H. Metzger, and O. G. Schmidt, 2009, Phys. Rev. B **79**, 035301.
Manke, I., *et al.*, 2011, Adv. Eng. Mater. **13**, 712.
Manzoli, M., F. Vindigni, T. Tabakova, C. Lamberti, D. Dimitrov, K. Ivanov, and G. Agostini, 2017, J. Mater. Chem. A **5**, 2083.
Margaritondo, G., 2013, in *Characterization of Semiconductor Heterostructures and Nanostructures*, edited by C. Lamberti and G. Agostini (Elsevier, Amsterdam), p. 603, 2nd ed..
Margaritondo, G., and F. Cerrina, 1990, Nucl. Instrum. Methods Phys. Res., Sect. A **291**, 26.
Marmiroli, B., and H. Amenitsch, 2012, Eur. Biophys. J. **41**, 851.
Marsi, M., L. Casalis, L. Gregoratti, S. Gunther, A. Kolmakov, J. Kovac, D. Lonza, and M. Kiskinova, 1997, J. Electron Spectrosc. Relat. Phenom. **84**, 73.
Martinez-Criado, G., B. Alen, A. Homs, A. Somogyi, C. Miskys, J. Susini, J. Pereira-Lachataignerais, and J. Martinez-Pastor, 2006, Appl. Phys. Lett., **89**, 221913
Martinez-Criado, G., E. Borfecchia, L. Mino, and C. Lamberti, 2013, in *Characterization of Semiconductor Heterostructures and Nanostructures*, edited by C. Lamberti and G. Agostini (Elsevier, Amsterdam), p. 361, 2nd ed.
Martinez-Criado, G., J. Segura-Ruiz, B. Alen, J. Eymery, A. Rogalev, R. Tucoulou, and A. Homs, 2014, Adv. Mater. **26**, 7873.
Martinez-Criado, G., J. Segura-Ruiz, M. H. Chu, R. Tucoulou, I. Lopez, E. Nogales, B. Mendez, and J. Piqueras, 2014, Nano Lett. **14**, 5479.
Martinez-Criado, G., A. Somogyi, A. Homs, R. Tucoulou, and J. Susini, 2005, Appl. Phys. Lett. **87**, 061913.
Martinez-Criado, G., A. Somogyi, S. Ramos, J. Campo, R. Tucoulou, M. Salome, J. Susini, M. Hermann, M. Eickhoff, and M. Stutzmann, 2005, Appl. Phys. Lett. **86**, 131927.
Martinez-Criado, G., *et al.*, 2008, Appl. Phys. Lett. **93**, 021916.
Martinez-Criado, G., *et al.*, 2012a, Nucl. Instrum. Methods Phys. Res., Sect. B **284**, 36.
Martinez-Criado, G., *et al.*, 2012b, J. Synchrotron Radiat. **19**, 10.
Martinez-Criado, G., *et al.*, 2012c, Nano Lett. **12**, 5829.
Martinez-Criado, G., *et al.*, 2016, J. Synchrotron Radiat. **23**, 344.
Martini, A., E. Borfecchia, K. A. Lomachenko, I. A. Pankin, C. Negri, G. Berlier, P. Beato, H. Falsig, S. Bordiga, and C. Lamberti, 2017, Chem. Sci. **8**, 6836.
Matsui, F., H. W. Yeom, A. Imanishi, K. Isawa, I. Matsuda, and T. Ohta, 1998, Surf. Sci. **401**, L413.
Matsuyama, S., *et al.*, 2009, X-Ray Spectrom. **38**, 89.
McNeil, B. W. J., and N. R. Thompson, 2010, Nat. Photonics **4**, 814.
Meents, A., S. Gutmann, A. Wagner, and C. Schulze-Briese, 2010, Proc. Natl. Acad. Sci. U.S.A. **107**, 1094.
Meirer, F., S. Kalirai, D. Morris, S. Soparawalla, Y. Liu, G. Mesu, J. C. Andrews, and B. M. Weckhuysen, 2015, Sci. Adv. **1**, e1400199.
Meirer, F., S. Kalirai, J. N. Weker, Y. Liu, J. C. Andrews, and B. M. Weckhuysen, 2015, Chem. Commun. (Cambridge) **51**, 8097.
Meirer, F., D. T. Morris, S. Kalirai, Y. J. Liu, J. C. Andrews, and B. M. Weckhuysen, 2015, J. Am. Chem. Soc. **137**, 102.
Melnichenko, Y. B., and G. D. Wignall, 2007, J. Appl. Phys. **102**, 021101.
Mendach, S., S. Kiravittaya, A. Rastelli, M. Benyoucef, R. Songmuang, and O. G. Schmidt, 2008, Phys. Rev. B **78**, 035317.
Mendach, S., R. Songmuang, S. Kiravittaya, A. Rastelli, M. Benyoucef, and O. G. Schmidt, 2006, Appl. Phys. Lett. **88**, 111120.
Meneghini, C., A. F. Gualtieri, and C. Siligardi, 1999, J. Appl. Crystallogr. **32**, 1090.
Menzel, S., U. Bottger, M. Wimmer, and M. Salinga, 2015, Adv. Funct. Mater. **25**, 6306.
Metzger, T. H., T. U. Schulli, and M. Schmidbauer, 2005, C.R. Phys. **6**, 47.
Meunier, F. C., 2010, Chem. Soc. Rev. **39**, 4602.
Meyerson, B. S., 1992, Proc. IEEE **80**, 1592.
Mezei, F., 1997, Solid State Phenom. **56**, 133.
Miao, J., T. Ohsuna, O. Terasaki, K. O. Hodgson, and M. A. O'Keefe, 2002, Phys. Rev. Lett. **89**, 155502.
Miao, J., D. Sayre, and H. N. Chapman, 1998, J. Opt. Soc. Am. A **15**, 1662.
Miao, J. W., P. Charalambous, J. Kirz, and D. Sayre, 1999, Nature (London) **400**, 342.
Miao, J. W., T. Ishikawa, B. Johnson, E. H. Anderson, B. Lai, and K. O. Hodgson, 2002, Phys. Rev. Lett. **89**, 088303.
Michl, J., and V. Bonačić-Koutecký, 1990, *Electronic Aspects of Organic Photochemistry* (John Wiley & Sons, New York).
Mikula, P., J. Kulda, L. Horalik, B. Chalupa, and P. Lukas, 1986, J. Appl. Crystallogr. **19**, 324.
Milanesio, M., G. Artioli, A. F. Gualtieri, L. Palin, and C. Lamberti, 2003, J. Am. Chem. Soc. **125**, 14549.
Mimura, H., *et al.*, 2007, Appl. Phys. Lett. **90**, 051903.
Mimura, H., *et al.*, 2010, Nat. Phys. **6**, 122.
Minitti, M. P., *et al.*, 2015, Phys. Rev. Lett. **114**, 255501.
Mino, L., G. Agostini, E. Borfecchia, D. Gianolio, A. Piovano, E. Gallo, and C. Lamberti, 2013, J. Phys. D **46**, 423001.
Mino, L., A. Agostino, S. Codato, and C. Lamberti, 2010, J. Anal. At. Spectrom. **25**, 831.
Mino, L., A. Agostino, S. Codato, G. Martinez-Criado, and C. Lamberti, 2012, Nucl. Instrum. Methods Phys. Res., Sect. B **284**, 6.
Mino, L., V. Bonino, A. Agostino, C. Prestipino, E. Borfecchia, C. Lamberti, L. Operti, M. Fretto, N. De Leo, and M. Truccato, 2017, Sci. Rep. **7**, 9066.
Mino, L., E. Borfecchia, A. Agostino, C. Lamberti, and M. Truccato, 2017, J. Electron Spectrosc. Relat. Phenom. **220**, 69.
Mino, L., E. Borfecchia, C. Groppo, D. Castelli, G. Martinez-Criado, R. Spiess, and C. Lamberti, 2014, Catal. Today **229**, 72.
Mino, L., D. Gianolio, G. Agostini, A. Piovano, M. Truccato, A. Agostino, S. Cagliero, G. Martinez-Criado, S. Codato, and C. Lamberti, 2010, Adv. Mater. **22**, 2050.
Mino, L., D. Gianolio, F. Bardelli, C. Prestipino, E. S. Kumar, F. Bellarmine, M. Ramanjaneyulu, C. Lamberti, and M. S. R. Rao, 2013, J. Phys. Condens. Matter **25**, 385402.
Mino, L., G. Spoto, S. Bordiga, and A. Zecchina, 2012, J. Phys. Chem. C **116**, 17008.
Mino, L., G. Spoto, S. Bordiga, and A. Zecchina, 2013, J. Phys. Chem. C **117**, 11186.
Mino, L., *et al.*, 2011, Small **7**, 930.
Miron, C., and P. Morin, 2011, in *Handbook of High-resolution Spectroscopy*(John Wiley & Sons, Ltd, New York).
Miron, C., and M. Patanen, 2014, Adv. Mater. **26**, 7911.
Mirov, S. B., V. V. Fedorov, D. Martyshkin, I. S. Moskalev, M. Mirov, and S. Vasilyev, 2015, IEEE J. Sel. Top. Quantum Electron. **21**, 1601719.
Mirov, S. B., V. V. Fedorov, I. S. Moskalev, and D. V. Martyshkin, 2007, IEEE J. Sel. Top. Quantum Electron. **13**, 810.
Misra, N. L., 2014, Spectrochim. Acta B Atom. Spectros. **101**, 134.
Mocuta, C., J. Stangl, K. Mundboth, T. H. Metzger, G. Bauer, I. A. Vartanyants, M. Schmidbauer, and T. Boeck, 2008, Phys. Rev. B **77**, 245425.
Mokkapati, S., and C. Jagadish, 2009, Mater. Today **12**, 22.

Monico, L., K. Janssens, E. Hendriks, F. Vanmeert, G. Van der Snickt, M. Cotte, G. Falkenberg, B. G. Brunetti, and C. Miliani, 2015, Angew. Chem., Int. Ed. Engl. **54**, 13923.

Mooney, P. M., 1996, Mater. Sci. Eng. R Rep. **17**, 105.

Mooney, P. M., J. L. Jordan-Sweet, I. C. Noyan, S. K. Kaldor, and P. C. Wang, 1999, Appl. Phys. Lett. **74**, 726.

Morgan, A. J., *et al.*, 2015, Sci. Rep. **5**, 9892.

Morin, P., M. Simon, C. Miron, N. Leclercq, and D. L. Hansen, 1998, J. Electron Spectrosc. Relat. Phenom. **93**, 49.

Mortensen, K. I., L. S. Churchman, J. A. Spudich, and H. Flyvbjerg, 2010, Nat. Methods **7**, 377.

Moseley, H. G. J., 1913, Philos. Mag. **26**, 1024.

Moukhametzianov, R., M. Burghammer, P. C. Edwards, S. Petitdemange, D. Popov, M. Fransen, G. McMullan, G. F. X. Schertler, and C. Riekel, 2008, Acta Crystallogr. Sect. D **64**, 158.

Muller, K. A., M. Takashige, and J. G. Bednorz, 1987, Phys. Rev. Lett. **58**, 1143.

Muller, M., T. Mey, J. Niemeyer, and K. Mann, 2014, Opt. Express **22**, 23489.

Murray, C. E., I. C. Noyan, P. M. Mooney, B. Lai, and Z. Cai, 2003, Appl. Phys. Lett. **83**, 4163.

Murray, C. E., Z. Ren, A. Ying, S. M. Polvino, I. C. Noyan, and Z. Cai, 2009, Appl. Phys. Lett. **94**, 063502.

Murray, C. E., A. Ying, S. M. Polvino, I. C. Noyan, M. Holt, and J. Maser, 2011, J. Appl. Phys. **109**, 083543.

Murray, C. E., A. J. Ying, S. M. Polvino, I. C. Noyan, and Z. Cai, 2010, Powder Diffr. **25**, 108.

Murray, R. W., 2008, Chem. Rev. **108**, 2688.

Nagashima, K., *et al.*, 2012, Nano Lett. **12**, 5684.

Nam, D., *et al.*, 2013, Phys. Rev. Lett. **110**, 098103.

Nass, K., *et al.*, 2015, J. Synchrotron Radiat. **22**, 225.

Navalon, S., A. Dhakshinamoorthy, M. Alvaro, and H. Garcia, 2016, Coord. Chem. Rev. **312**, 99.

Nazaretski, E., W. Xu, N. Bouet, J. Zhou, H. Yan, X. Huang, and Y. S. Chu, 2016, Appl. Phys. Lett. **108**, 261102.

Neilson, J. R., J. A. Kurzman, R. Seshadri, and D. E. Morse, 2010, Chem. Eur. J. **16**, 9998.

Nelson, J., Y. Yang, S. Misra, J. C. Andrews, Y. Cui, and M. F. Toney, 2013, in *X-Ray Nanoimaging: Instruments and Methods*, edited by B. Lai (SPIE—Int. Soc. Optical Engineering, Bellingham, WA).

Neuhold, A., J. Novak, H. G. Flesch, A. Moser, T. Djuric, L. Grodd, S. Grigorian, U. Pietsch, and R. Resel, 2012, Nucl. Instrum. Methods Phys. Res., Sect. B **284**, 64.

Neumann, D. A., 2006, Mater. Today **9**, 34.

Neutze, R., R. Wouts, D. van der Spoel, E. Weckert, and J. Hajdu, 2000, Nature (London) **406**, 752.

Newbury, D. E., and N. W. M. Ritchie, 2013, J. Anal. At. Spectrom. **28**, 973.

Newbury, D. E., and N. W. M. Ritchie, 2015, J. Mater. Sci. **50**, 493.

Newton, M. A., 2008, Chem. Soc. Rev. **37**, 2644.

Newton, M. A., K. W. Chapman, D. Thompsett, and P. J. Chupas, 2012, J. Am. Chem. Soc. **134**, 5036.

Ney, A., K. Ollefs, S. Ye, T. Kammermeier, V. Ney, T. C. Kaspar, S. A. Chambers, F. Wilhelm, and A. Rogalev, 2008, Phys. Rev. Lett. **100**, 157201.

Nicholson, J., C. Nave, K. Fayz, B. Fell, and E. Garman, 2001, Nucl. Instrum. Methods Phys. Res., Sect. A **467–468**, 1380.

Niehus, H., W. Heiland, and E. Taglauer, 1993, Surf. Sci. Rep. **17**, 213.

Nilsson, A., and L. G. M. Pettersson, 2004, Surf. Sci. Rep. **55**, 49.

Noguez, C., and I. L. Garzon, 2009, Chem. Soc. Rev. **38**, 757.

Nordling, C., E. Sokolowski, and K. Siegbahn, 1957, Phys. Rev. **105**, 1676.

Norskov, J. K., F. Studt, F. AbildPedersen, and T. Bligaard, 2014, *Fundamental concepts in heterogeneous catalysis* (John Wiley & Sons Inc., Hoboken).

Novotny, L., and N. van Hulst, 2011, Nat. Photonics **5**, 83.

Noyan, I. C., P. C. Wang, S. K. Kaldor, J. L. Jordan-Sweet, and E. G. Liniger, 2000, Rev. Sci. Instrum. **71**, 1991.

Nugent, K. A., 2010, Adv. Phys. **59**, 1.

Oberhuber, R., G. Zandler, and P. Vogl, 1998, Phys. Rev. B **58**, 9941.

Ohno, H., D. Chiba, F. Matsukura, T. Omiya, E. Abe, T. Dietl, Y. Ohno, and K. Ohtani, 2000, Nature (London) **408**, 944.

Oien, S., *et al.*, 2015, Chem. Mater. **27**, 1042.

Okudaira, K. K., E. Morikawa, S. Hasegawa, P. T. Sprunger, V. Saile, K. Seki, Y. Harada, and N. Ueno, 1998, J. Electron Spectrosc. Relat. Phenom. **88–91**, 913.

Opara, N., I. Martiel, S. A. Arnold, T. Braun, H. Stahlberg, M. Makita, D. A. Christian, and C. Padeste, 2017, J. Appl. Crystallogr. **50**, 909.

Orloff, J., L. W. Swanson, and M. Utlaut, 1996, J. Vac. Sci. Technol. B **14**, 3759.

Ortega, R., P. Cloetens, G. Deves, A. Carmona, and S. Bohic, 2007, PLoS One **2**, e925.

Oshikane, Y., T. Kataoka, M. Okuda, S. Hara, H. Inoue, and M. Nakano, 2007, Sci. Technol. Adv. Mater. **8**, 181.

Pachuta, S. J., and R. G. Cooks, 1987, Chem. Rev. **87**, 647.

Pagliero, A., L. Mino, E. Borfecchia, M. Truccato, A. Agostino, L. Pascale, E. Enrico, N. De Leo, C. Lamberti, and G. Martinez-Criado, 2014, Nano Lett. **14**, 1583.

Pan, F., S. Gao, C. Chen, C. Song, and F. Zeng, 2014, Mater. Sci. Eng. R-Rep. **83**, 1.

Pappas, D. K., *et al.*, 2017, J. Am. Chem. Soc. **139**, 14961.

Parikh, A., W. Yarbrough, M. Mason, S. Sridhar, P. R. Chidambaram, and Z. Cai, 2007, Appl. Phys. Lett. **90**, 172117.

Pascarelli, S., O. Mathon, M. Munoz, T. Mairs, and J. Susini, 2006, J. Synchrotron Radiat. **13**, 351.

Passarelli, M. K., and N. Winograd, 2011, Biochim. Biophys. Acta Mol. Cell Biol. Lipids **1811**, 976.

Patt, M., C. Wiemann, N. Weber, M. Escher, A. Gloskovskii, W. Drube, M. Merkel, and C. M. Schneider, 2014, Rev. Sci. Instrum. **85**, 113704.

Pellegrini, C., A. Marinelli, and S. Reiche, 2016, Rev. Mod. Phys. **88**, 015006.

Pezzagna, S., D. Rogalla, H. W. Becker, I. Jakobi, F. Dolde, B. Naydenov, J. Wrachtrup, F. Jelezko, C. Trautmann, and J. Meijer, 2011, Phys. Status Solidi A **208**, 2017.

Pfeifer, M. A., G. J. Williams, I. A. Vartanyants, R. Harder, and I. K. Robinson, 2006, Nature (London) **442**, 63.

Pfeiffer, F., 2018, Nat. Photonics **12**, 9.

Pietsch, U., V. Holý, and T. Baumbach, 2004, *High-Resolution X-Ray Scattering: From Thin Films to Lateral Nanostructures* (Springer-Verlag, Berlin/Heidelberg).

Plass, L., and S. Reimelt, 2007, Chem. Ing. Tech. **79**, 561.

Poccia, N., G. Campi, M. Fratini, A. Ricci, N. L. Saini, and A. Bianconi, 2011, Phys. Rev. B **84**, 100504.

Poccia, N., M. Fratini, A. Ricci, G. Campi, L. Barba, A. Vittorini-Orgeas, G. Bianconi, G. Aeppli, and A. Bianconi, 2011, Nat. Mater. **10**, 733.

Pollock, C. J., and S. DeBeer, 2015, Acc. Chem. Res. **48**, 2967.

Polvino, S. M., C. E. Murray, O. Kalenci, I. C. Noyan, B. Lai, and Z. G. Cai, 2008, Appl. Phys. Lett. **92**, 224105.

Pontoni, D., S. Finet, T. Narayanan, and A. R. Rennie, 2003, J. Chem. Phys. **119**, 6157.

Popova-Gorelova, D., and R. Santra, 2015, Phys. Rev. B **92**, 184304.

Portale, G., and A. Longo, 2013, in *Characterization of Semiconductor Heterostructures and Nanostructures*, edited by

C. Lamberti and G. Agostini (Elsevier, Amsterdam), p. 289, 2nd ed.

Potts, P. J., A. T. Ellis, P. Kregsamer, J. Marshall, C. Streli, M. West, and P. Wobrauschek, 2002, J. Anal. At. Spectrom. **17**, 1439.

Poulsen, H. F., 2004, *Three-Dimensional X-Ray Diffraction Microscopy: Mapping Polycrystals and Their Dynamics* (Springer-Verlag, Berlin).

Powell, C. J., and M. P. Seah, 1990, J. Vac. Sci. Technol. A **8**, 735.

Pradeep, T., and Anshup, 2009, Thin Solid Films **517**, 6441.

Prasai, B., Y. Ren, S. Y. Shan, Y. G. Zhao, H. Cronk, J. Luo, C. J. Zhong, and V. Petkov, 2015, Nanoscale **7**, 8122.

Prasai, B., A. R. Wilson, B. J. Wiley, Y. Ren, and V. Petkov, 2015, Nanoscale **7**, 17902.

Prewitt, C. T., and R. T. Downs, 1998, in *Ultrahigh-Pressure Mineralogy: Physics and Chemistry of the Earth's Deep Interior*, edited by R. J. Hemley (Mineralog. Soc. Am., Washington), p. 283.

Prezado, Y., G. Fois, M. Edouard, C. Nemoz, M. Renier, H. Requardt, F. Esteve, J. F. Adam, H. Elleaume, and A. Bravin, 2009, Med. Phys. **36**, 725.

Price, S. W. T., K. Geraki, K. Ignatyev, P. T. Witte, A. M. Beale, and J. F. W. Mosselmans, 2015, Angew. Chem., Int. Ed. Engl. **54**, 9886.

Price, S. W. T., K. Ignatyev, K. Geraki, M. Basham, J. Filik, N. T. Vo, P. T. Witte, A. M. Beale, and J. F. W. Mosselmans, 2015, Phys. Chem. Chem. Phys. **17**, 521.

Prins, R., and D. C. Koningsberger, 1988, in *X-Ray Absorption: Principles, Applications, Techniques of EXAFS, SEXAFS and XANES*, edited by D. C. Koningsberger and R. Prins (John Wiley & Sons, New York), p. 321.

Prinz, V. Y., A. V. Chekhovskiy, V. V. Preobrazhenskii, B. R. Semyagin, and A. K. Gutakovsky, 2002, Nanotechnology **13**, 231.

Prinz, V. Y., V. A. Seleznev, A. K. Gutakovsky, A. V. Chehovskiy, V. V. Preobrazhenskii, M. A. Putyato, and T. A. Gavrilova, 2000, Physica E (Amsterdam) **6**, 828.

Pushie, M. J., I. J. Pickering, M. Korbas, M. J. Hackett, and G. N. George, 2014, Chem. Rev. **114**, 8499.

Qian, Q., J. Ruiz-Martinez, M. Mokhtar, A. M. Asiri, S. A. Al-Thabaiti, S. N. Basahel, and B. M. Weckhuysen, 2014, Catal. Today **226**, 14.

Quartieri, S., 2003, in *Synchrotron Radiation: Fundamentals, Methodologies and Applications*, edited by S. Mobilio and V. G. (Italian Physical Society, Bologna), p. 427.

Rajkovic, I., S. Grubel, W. Quevedo, and S. Techert, 2011, in *Advances in X-Ray Free-Electron Lasers: Radiation Schemes, X-Ray Optics, and Instrumentation*, edited by T. Tschentscher and D. Cocco (SPIE—Int Soc Optical Engineering, Bellingham, WA).

Randolph, S. J., J. D. Fowlkes, and P. D. Rack, 2006, Crit. Rev. Solid State Mater. Sci. **31**, 55.

Rasmussen, S. G. F., *et al.*, 2007, Nature (London) **450**, 383.

Rasmussen, S. G. F., *et al.*, 2011, Nature (London) **477**, 549.

Regli, L., S. Bordiga, C. Busco, C. Prestipino, P. Ugliengo, A. Zecchina, and C. Lamberti, 2007, J. Am. Chem. Soc. **129**, 12131.

Resch-Genger, U., M. Grabolle, S. Cavaliere-Jaricot, R. Nitschke, and T. Nann, 2008, Nat. Methods **5**, 763.

Ricchiardi, G., A. Damin, S. Bordiga, C. Lamberti, G. Spanò, F. Rivetti, and A. Zecchina, 2001, J. Am. Chem. Soc. **123**, 11409.

Ricci, A., *et al.*, 2011, Phys. Rev. B **84**, 060511.

Ricci, A., *et al.*, 2015, Phys. Rev. B **91**, 020503.

Richard, P., T. Qian, and H. Ding, 2015, J. Phys. Condens. Matter **27**, 293203.

Rim, K. K., J. L. Hoyt, and J. F. Gibbons, 2000, IEEE Trans. Electron Devices **47**, 1406.

Ritchie, N. W. M., D. E. Newbury, and J. M. Davis, 2012, Microsc. Microanal. **18**, 892.

Robisch, A. L., J. Wallentin, A. Pacureanu, P. Cloetens, and T. Salditt, 2016, Opt. Lett. **41**, 5519.

Rodenburg, J. M., A. C. Hurst, and A. G. Cullis, 2007, Ultramicroscopy **107**, 227.

Rodenburg, J. M., A. C. Hurst, A. G. Cullis, B. R. Dobson, F. Pfeiffer, O. Bunk, C. David, K. Jefimovs, and I. Johnson, 2007, Phys. Rev. Lett. **98**, 034801.

Rodrigues, M. S., T. W. Cornelius, T. Scheler, C. Mocuta, A. Malachias, R. Magalhaes-Paniago, O. Dhez, F. Comin, T. H. Metzger, and J. Chevrier, 2009, J. Appl. Phys. **106**, 103525.

Roman, E. L., J. L. Desegovia, R. L. Kurtz, R. Stockbauer, and T. E. Madey, 1992, Surf. Sci. **273**, 40.

Rosenbaum, D. M., *et al.*, 2007, Science **318**, 1266.

Rothe, J., *et al.*, 2012, Rev. Sci. Instrum. **83**, 043105.

Rothermel, M., T. Reinert, T. Andrea, and T. Butz, 2010, Nucl. Instrum. Methods Phys. Res., Sect. B **268**, 2001.

Rout, B., *et al.*, 2013, in *Radiation Physics: Ix International Symposium on Radiation Physics*, edited by C. Vazquez Lopez, G. Espinosa Garcia, and J. I. Golzarri (Amer. Inst. Physics, Melville, NY), p. 11.

Rubio-Zuazo, J. R., and G. R. Castro, 2005, Nucl. Instrum. Methods Phys. Res., Sect. A **547**, 64.

Rupprechter, G., and C. Weilach, 2007, Nano Today **2**, 20.

Rupprechter, G., and C. Weilach, 2008, J. Phys. Condens. Matter **20**, 184019.

Ryan, C. G., 2000, Int. J. Imaging Syst. Technol. **11**, 219.

Ryan, C. G., D. R. Cousens, S. H. Sie, and W. L. Griffin, 1990, Nucl. Instrum. Methods Phys. Res., Sect. B **49**, 271.

Ryan, C. G., R. Kirkham, R. M. Hough, G. Moorhead, D. P. Siddons, M. D. de Jonge, D. J. Paterson, G. De Geronimo, D. L. Howard, and J. S. Cleverley, 2010, Nucl. Instrum. Methods Phys. Res., Sect. A **619**, 37.

Sabra, A. I., 2007, in *Inside the Camera Obscura: Optics and Art under the Spell of the Projected Image*, edited by W. Lefèvre (Max-Planck-Institut für Wissenschaftsgeschichte, Berlin).

Sakai, T., T. Kamiya, M. Oikawa, T. Sato, A. Tanaka, and K. Ishii, 2002, Nucl. Instrum. Methods Phys. Res., Sect. B **190**, 271.

Sakdinawat, A., and D. Attwood, 2010, Nat. Photonics **4**, 840.

Sala, S., B. J. Daurer, M. F. Hantke, T. Ekeberg, N. D. Loh, F. Maia, and P. Thibault, 2017, J. Phys. Conf. Ser. **849**, 012032.

Sala, S., V. S. C. Kuppili, S. Chalkidis, D. J. Batey, X. Shi, C. Rau, and P. Thibault, 2018, J. Synchrotron Radiat. **25**.

Salassa, L., E. Borfecchia, T. Ruiu, C. Garino, D. Gianolio, R. Gobetto, P. J. Sadler, M. Cammarata, M. Wulff, and C. Lamberti, 2010, Inorg. Chem. **49**, 11240.

Salbu, B., *et al.*, 2001, Nucl. Instrum. Methods Phys. Res., Sect. A **467–468**, 1249.

Salmeron, M., and R. Schlogl, 2008, Surf. Sci. Rep. **63**, 169.

Salmon, P. S., and A. Zeidler, 2015, J. Phys. Condens. Matter **27**, 133201.

Salviati, G., F. Fabbri, F. Detto, F. Rossi, L. Lazzarini, and T. Sekiguchi, 2013, in *Characterization of Semiconductor Heterostructures and Nanostructures*, edited by C. Lamberti and G. Agostini (Elsevier, Amsterdam), p. 557, 2nd ed.

Sankar, G., T. Okubo, W. Fan, and F. Meneau, 2007, Faraday Discuss. **136**, 157.

Sanles-Sobrido, M., W. Exner, L. Rodriguez-Lorenzo, B. Rodriguez-Gonzalez, M. A. Correa-Duarte, R. A. Alvarez-Puebla, and L. M. Liz-Marzan, 2009, J. Am. Chem. Soc. **131**, 2699.

Sato, M., H. Tanida, K. Kato, T. Sasaki, Y. Yamamoto, S. Sonoda, S. Shimizu, and H. Hori, 2002, Jpn. J. Appl. Phys. **41**, 4513.

Sau, T. K., A. L. Rogach, F. Jackel, T. A. Klar, and J. Feldmann, 2010, Adv. Mater. **22**, 1805.

Sawaya, M. R., *et al.*, 2007, Nature (London) **447**, 453.
Sayre, D., 1952, Acta Crystallogr. **5**, 843.
Schattke, W., and M. A. Van Hove, 2003, *Solid-State Photoemission and Related Methods: Theory and Experiment* (Wiley, Weinheim).
Scheler, T., M. Rodrigues, T. W. Cornelius, C. Mocuta, A. Malachias, R. Magalhaes-Paniago, F. Comin, J. Chevrier, and T. H. Metzger, 2009, Appl. Phys. Lett. **94**, 023109.
Schmidt, O. G., C. Deneke, S. Kiravittaya, R. Songmuang, H. Heidemeyer, Y. Nakamura, R. Zapf-Gottwick, C. Muller, and N. Y. Jin-Phillipp, 2002, IEEE J. Sel. Top. Quantum Electron. **8**, 1025.
Schmidt, O. G., and K. Eberl, 2001, Nature (London) **410**, 168.
Schneider, C. M., *et al.*, 2012, J. Electron Spectrosc. Relat. Phenom. **185**, 330.
Schreiber, S., B. Faatz, J. Feldhaus, K. Honkavaara, R. Treush, and M. Vogt, 2012, "Status of the FLASH facility," in *Proceedings of FEL2012, Nara, Japan*, edited by T. Tanaka and V. R. W. Schaa (Joint Accelerator Conferences, CERN, Geneva), p. 37.
Schroer, C. G., and G. Falkenberg, 2014, J. Synchrotron Radiat. **21**, 996.
Schroer, C. G., and B. Lengeler, 2005, Phys. Rev. Lett. **94**, 054802.
Schroer, C. G., *et al.*, 2005, Appl. Phys. Lett. **87**, 124103.
Schropp, A., *et al.*, 2013a, Sci. Rep. **3**, 1633.
Schropp, A., *et al.*, 2013b, in *X-Ray Lasers and Coherent X-Ray Sources: Development and Applications X*, edited by A. Klisnick and C. S. Menoni (SPIE—Int. Soc. Optical Engineering, Bellingham, WA).
Scott, J. H. J., 2003, Anal. Bioanal. Chem. **375**, 38.
Seah, M. P., and W. A. Dench, 1979, Surf. Interface Anal. **1**, 2.
Sears, V. F., 1989, *Neutron Optics* (Oxford University Press, New York).
Seenivasan, K., E. Gallo, A. Piovano, J. G. Vitillo, A. Sommazzi, S. Bordiga, C. Lamberti, P. Glatzel, and E. Groppo, 2013, Dalton Trans. **42**, 12706.
Segura-Ruiz, J., G. Martinez-Criado, M. H. Chu, S. Geburt, and C. Ronning, 2011, Nano Lett. **11**, 5322.
Seiboth, F., *et al.*, 2017, Nat. Commun. **8**, 14623.
Senoner, M., and W. E. S. Unger, 2012, J. Anal. At. Spectrom. **27**, 1050.
Serrano, D. P., J. M. Escola, and P. Pizarro, 2013, Chem. Soc. Rev. **42**, 4004.
Sezen, H., B. Aleman, M. Amati, M. Dalmiglio, and L. Gregoratti, 2015, ChemCatChem **7**, 3665.
Shimizu, H. M., 2006, Physica B (Amsterdam) **385–386**, 989.
Sibillano, T., *et al.*, 2014, Sci. Rep. **4**, 6985.
Siegele, R., A. G. Kachenko, M. Ionescu, and D. D. Cohen, 2009, Nucl. Instrum. Methods Phys. Res., Sect. B **267**, 2054.
Silvestrelli, P. L., A. Alavi, M. Parrinello, and D. Frenkel, 1997, Phys. Rev. B **56**, 3806.
Singh, J., C. Lamberti, and J. A. van Bokhoven, 2010, Chem. Soc. Rev. **39**, 4754.
Sirenko, A. A., A. Kazimirov, R. Huang, D. H. Bilderback, S. O'Malley, V. Gupta, K. Bacher, L. J. P. Ketelsen, and A. Ougazzaden, 2005, J. Appl. Phys. **97**, 063512.
Sirenko, A. A., *et al.*, 2006, Appl. Phys. Lett. **88**, 081111.
Sitaud, B., P. L. Solari, S. Schlutig, I. Llorens, and H. Hermange, 2012, J. Nucl. Mater. **425**, 238.
Sitko, R., 2009, Spectrochim. Acta B Atom. Spectros. **64**, 1161.
Smith, C. S., 1954, Phys. Rev. **94**, 42.
Snigirev, A., V. Kohn, I. Snigireva, and B. Lengeler, 1996, Nature (London) **384**, 49.
Snigirev, A., V. Kohn, I. Snigireva, A. Souvorov, and B. Lengeler, 1998, Appl. Opt. **37**, 653.
Snigirev, A., and I. Snigireva, 2008, C.R. Phys. **9**, 507.
Sokolowski, E., C. Nordling, and K. Siegbahn, 1957, Ark. Fys. **12**, 301 [https://www.osti.gov/biblio/4353113?pg=1&lname=&fname=].
Somogyi, A., G. Martinez-Criado, A. Homs, M. A. Hernandez-Fenollosa, D. Vantelon, and O. Ambacher, 2007, Appl. Phys. Lett. **90**, 181129.
Somogyi, A., F. Polack, and T. Moreno, 2010, AIP Conf. Proc. **1234**, 395.
Songmuang, R., N. Y. Jin-Phillipp, S. Mendach, and O. G. Schmidt, 2006, Appl. Phys. Lett. **88**, 021913.
Sorieul, S., P. Alfaurt, L. Daudin, L. Serani, and P. Moretto, 2014, Nucl. Instrum. Methods Phys. Res., Sect. B **332**, 68.
Sosnowska, I. M., and B. T. M. Willis, 1999, J. Alloys Compd. **286**, 174.
Stangl, J., C. Mocuta, A. Diaz, T. H. Metzger, and G. Bauer, 2009, ChemPhysChem **10**, 2923.
Stankus, B., J. M. Budarz, A. Kirrander, D. Rogers, J. Robinson, T. J. Lane, D. Ratner, J. Hastings, M. P. Minitti, and P. M. Weber, 2016, Faraday Discuss. **194**, 525.
Stanley, H. B., *et al.*, 2014, CrystEngComm **16**, 9331.
Starr, D. E., Z. Liu, M. Havecker, A. Knop-Gericke, and H. Bluhm, 2013, Chem. Soc. Rev. **42**, 5833.
Stefani, G., *et al.*, 2004, J. Electron Spectrosc. Relat. Phenom. **141**, 149.
Stensgaard, I., 1992, Rep. Prog. Phys. **55**, 989.
Stockmar, M., I. Zanette, M. Dierolf, B. Enders, R. Clare, F. Pfeiffer, P. Cloetens, A. Bonnin, and P. Thibault, 2015, Phys. Rev. Applied **3**, 014005.
Strelow, C., H. Rehberg, C. M. Schultz, H. Welsch, C. Heyn, D. Heitmann, and T. Kipp, 2008, Phys. Rev. Lett. **101**, 127403.
Stubbs, A. W., L. Braglia, E. Borfecchia, R. J. Meyer, Y. Roman-Leshkov, C. Lamberti, and M. Dinca, 2018, ACS Catal. **8**, 596.
Susi, T., T. Pichler, and P. Ayala, 2015, Beilstein J. Nanotechnol. **6**, 177.
Susini, J., R. Barrett, J. Chavanne, P. Fajardo, A. Gotz, J. L. Revol, and L. Zhang, 2014, J. Synchrotron Radiat. **21**, 986.
Suzuki, Y., A. Takeuchi, and Y. Terada, 2007, Rev. Sci. Instrum. **78**, 053713.
Suzuki, Y., and Y. Terada, 2016, in *X-Ray Absorption and X-Ray Emission Spectroscopy: Theory and Applications*, edited by J. A. van Bokhoven and C. Lamberti (John Wiley & Sons, Chichester, UK), p. 251.
Tada, M., and N. Ishiguro, 2017, in *XAFS Techniques for Catalysts, Nanomaterials, and Surfaces*, edited by Y. Iwasawa, K. Asakura, and M. Tada (Springer, Switzerland), p. 133.
Tada, M., N. Ishiguro, T. Uruga, H. Tanida, Y. Terada, S. Nagamatsu, Y. Iwasawa, and S. Ohkoshi, 2011, Phys. Chem. Chem. Phys. **13**, 14910.
Takahashi, Y., A. Suzuki, S. Furutaku, K. Yamauchi, Y. Kohmura, and T. Ishikawa, 2013, Phys. Rev. B **87**, 121201.
Takata, Y., *et al.*, 2005, Nucl. Instrum. Methods Phys. Res., Sect. A **547**, 50.
Takman, P. A. C., H. Stollberg, G. A. Johansson, A. Holmberg, M. Lindblom, and H. M. Hertz, 2007, J. Microsc. **226**, 175.
Tanaka, M., M. Takeguchi, and K. Furuya, 2008, Ultramicroscopy **108**, 1427.
Tanner, B. K., and D. K. Bowen, 1980, Eds., *Characterization of Crystal Growth Defects by X-Ray Methods* (Plenum Press, New York).
Tavares, P. F., S. C. Leemann, M. Sjostrom, and A. Andersson, 2014, J. Synchrotron Radiat. **21**, 862.
Thibault, P., M. Dierolf, A. Menzel, O. Bunk, C. David, and F. Pfeiffer, 2008, Science **321**, 379.
Thibault, P., M. Guizar-Sicairos, and A. Menzel, 2015, J. Synchrotron Radiat. **22**, 469.

Thiess, S., C. Kunz, B. C. C. Cowie, T. L. Lee, M. Renier, and J. Zegenhagen, 2004, Solid State Commun. **132**, 589.

Thompson, S. E., *et al.*, 2004, IEEE Electron Device Lett. **25**, 191.

Tilinin, I. S., A. Jablonski, and W. S. M. Werner, 1996, Prog. Surf. Sci. **52**, 193.

Tonner, B. P., G. R. Harp, S. F. Koranda, and J. Zhang, 1992, Rev. Sci. Instrum. **63**, 564.

Torsello, D., L. Mino, V. Bonino, A. Agostino, E. Borfecchia, E. Vittone, C. Lamberti, and M. Truccato, 2018, Phys. Rev. Mater. **2**, 014801.

Toyoshima, R., and H. Kondoh, 2015, J. Phys. Condens. Matter **27**, 083003.

Tremsin, A. S., J. F. Pearson, A. P. Nichols, A. Owens, A. N. Brunton, and G. W. Fraser, 2001, Nucl. Instrum. Methods Phys. Res., Sect. A **459**, 543.

Tromp, M., 2015, Phil. Trans. R. Soc. A **373**, 20130152.

Truccato, M., *et al.*, 2016, Nano Lett. **16**, 1669.

Trushin, M., W. Seifert, O. Vyvenko, J. Bauer, G. Martinez-Criado, M. Salome, and M. Kittler, 2010, Nucl. Instrum. Methods Phys. Res., Sect. B **268**, 254.

Tseng, A. A., 2005, Small **1**, 924.

Tseng, A. A., A. Notargiacomo, and T. P. Chen, 2005, J. Vac. Sci. Technol. B **23**, 877.

Tsuji, K., K. Nakano, H. Hayashi, K. Hayashi, and C. U. Ro, 2008, Anal. Chem. **80**, 4421.

Tsuji, K., K. Nakano, Y. Takahashi, K. Hayashi, and C. U. Ro, 2012, Anal. Chem. **84**, 636.

Tucoulou, R., G. Martinez-Criado, P. Bleuet, I. Kieffer, P. Cloetens, S. Laboure, T. Martin, C. Guilloud, and J. Susini, 2008, J. Synchrotron Radiat. **15**, 392.

Tulchinsky, Y., *et al.*, 2017, J. Am. Chem. Soc. **139**, 5992.

Turner, D. W., and M. I. A. Jobory, 1962, J. Chem. Phys. **37**, 3007.

Tyrsted, C., N. Lock, K. M. O. Jensen, M. Christensen, E. D. Bojesen, H. Emerich, G. Vaughan, S. J. L. Billinge, and B. B. Iversen, 2014, IUCrJ **1**, 165.

Tyrsted, C., *et al.*, 2016, Catal. Sci. Technol. **6**, 8314.

Tyryshkin, A. M., S. A. Lyon, W. Jantsch, and F. Schaffler, 2005, Phys. Rev. Lett. **94**, 126802.

Valenza, R. A., and G. T. Seidler, 2016, Phys. Rev. B **93**, 115135.

van Bokhoven, J. A., and C. Lamberti, 2014, Coord. Chem. Rev. **277–278**, 275.

van Bokhoven, J. A., and C. Lamberti, 2016, *X-Ray Absorption and X-Ray Emission Spectroscopy: Theory and Applications* (John Wiley & Sons, Chichester, UK).

Van der Laan, G. P., and A. Beenackers, 1999, Catal. Rev. Sci. Eng. **41**, 255.

Van der Snickt, G., K. H. Janssens, J. Dik, W. De Nolf, F. Vanmeert, J. Jaroszewicz, M. Cotte, G. Falkenberg, and L. Van der Loeff, 2012, Anal. Chem. **84**, 10221.

van Kan, J. A., P. G. Shao, P. Molter, M. Saumer, A. A. Bettiol, T. Osipowicz, and F. Watt, 2005, Nucl. Instrum. Methods Phys. Res., Sect. B **231**, 170.

Vegard, L., 1921, Z. Phys. **5**, 17.

Vickerman, J. C., 2011, Analyst **136**, 2199.

Vila-Comamala, J., S. Gorelick, E. Farm, C. M. Kewish, A. Diaz, R. Barrett, V. A. Guzenko, M. Ritala, and C. David, 2011, Opt. Express **19**, 175.

Villanova, J., *et al.*, 2017, Mater. Today **20**, 354.

Vogt, E. T. C., and B. M. Weckhuysen, 2015, Chem. Soc. Rev. **44**, 7342.

Vurgaftman, I., J. R. Meyer, and L. R. Ram-Mohan, 2001, J. Appl. Phys. **89**, 5815.

Vyvenko, O. F., T. Buonassisi, A. A. Istratov, H. Hieslmair, A. C. Thompson, R. Schindler, and E. R. Weber, 2002, J. Appl. Phys. **91**, 3614.

Wallander, H., and J. Wallentin, 2017, J. Synchrotron Radiat. **24**, 925.

Wang, J., C. Morin, L. Li, A. P. Hitchcock, A. Scholl, and A. Doran, 2009, J. Electron Spectrosc. Relat. Phenom. **170**, 25.

Wang, J. J., Y. C. K. Chen-Wiegart, and J. Wang, 2014, Angew. Chem., Int. Ed. Engl. **53**, 4460.

Wang, K. L., 2002, J. Nanosci. Nanotechnol. **2**, 235.

Wang, Y., and M. Nastasi, 2009, *Handbook of Modern Ion Beam Materials Analysis* (Material Research Society, Pittsburgh, PA), 2nd ed.

Waser, R., R. Dittmann, G. Staikov, and K. Szot, 2009, Adv. Mater. **21**, 2632.

Weckert, E., 2015, IUCrJ **2**, 230.

Weiland, C., A. K. Rumaiz, P. Pianetta, and J. C. Woicik, 2016, J. Vac. Sci. Technol. A **34**, 030801.

Weissman, S., F. Balibar, and J.-F. Petroff, 1984, *Applications of X-Ray Topographic Methods to Materials Science* (Plenum Press, New York).

Wernet, P., *et al.*, 2015, Nature (London) **520**, 78.

West, M., A. T. Ellis, P. J. Potts, C. Streli, C. Vanhoof, and P. Wobrauschek, 2014, J. Anal. At. Spectrom. **29**, 1516.

West, M., A. T. Ellis, P. J. Potts, C. Streli, C. Vanhoof, and P. Wobrauschek, 2015, J. Anal. At. Spectrom. **30**, 1839.

Wiebach, T., M. Schmidbauer, M. Hanke, H. Raidt, R. Kohler, and H. Wawra, 2000, Phys. Rev. B **61**, 5571.

Wilde, M., and K. Fukutani, 2014, Surf. Sci. Rep. **69**, 196.

Williams, G. J., H. M. Quiney, B. B. Dhal, C. Q. Tran, K. A. Nugent, A. G. Peele, D. Paterson, and M. D. de Jonge, 2006, Phys. Rev. Lett. **97**, 025506.

Willmott, P., 2011, *An Introduction to Synchrotron Radiation: Techniques and Applications* (John Wiley & Sons, Singapore).

Willumeit, R., 2011, Adv. Eng. Mater. **13**, 747.

Wilson, C. C., 2005, Z. Kristallogr. **220**, 385.

Wirth, A., *et al.*, 2011, Science **334**, 195.

Wobrauschek, P., 2007, X-Ray Spectrom. **36**, 289.

Woicik, J. C., 2016, *Hard X-ray Photoelectron Spectroscopy (HAXPES)* (Springer, Berlin).

Wolverson, D., 2013, in *Characterization of Semiconductor Heterostructures and Nanostructures*, edited by C. Lamberti and G. Agostini (Elsevier, Amsterdam), p. 753, 2nd ed.

Wu, Y., J. Xiang, C. Yang, W. Lu, and C. M. Lieber, 2004, Nature (London) **430**, 61.

Xu, W. H., N. Schlossberger, W. Xu, H. F. Yan, X. J. Huang, Y. S. Chu, and E. Nazaretski, 2017, Meas. Sci. Technol. **28**, 127001.

Yabashi, M., and H. Tanaka, 2017, Nat. Photonics **11**, 12.

Yamauchi, K., M. Yabashi, H. Ohashi, T. Koyama, and T. Ishikawa, 2015, J. Synchrotron Radiat. **22**, 592.

Yamauchi, K., *et al.*, 2011, J. Phys. Condens. Matter **23**, 394206.

Yamazaki, H., *et al.*, 2013, J. Phys. Conf. Ser. **425**, 052001.

Yan, H. F., H. C. Kang, R. Conley, C. Liu, A. T. Macrander, G. B. Stephenson, and J. Maser, 2010, X-Ray Opt. Instrum. **2010**, 401854.

Yan, H. F., J. Maser, A. Macrander, Q. Shen, S. Vogt, G. B. Stephenson, and H. C. Kang, 2007, Phys. Rev. B **76**, 115438.

Yan, H. F., C. E. Murray, and I. C. Noyan, 2007, Appl. Phys. Lett. **90**, 091918.

Yao, Y., and J. A. van Kan, 2015, Nucl. Instrum. Methods Phys. Res., Sect. B **348**, 203.

Yin, G. C., *et al.*, 2016, AIP Conf. Proc. **1741**, 030004.

Yoshida, H., S. Nonoyama, Y. Yazawa, and T. Hattori, 2005, Phys. Scr. T **115**, 813.
Yu, J. G., Y. R. Su, and B. Cheng, 2007, Adv. Funct. Mater. **17**, 1984.
Yu, L. H., *et al.*, 2000, Science **289**, 932.
Yuhas, B. D., S. Fakra, M. A. Marcus, and P. D. Yang, 2007, Nano Lett. **7**, 905.
Yumoto, H., *et al.*, 2005, Rev. Sci. Instrum. **76**, 063708.
Zalm, P. C., 1995, Rep. Prog. Phys. **58**, 1321.
Zdora, M. C., P. Thibault, T. Zhou, F. J. Koch, J. Romell, S. Sala, A. Last, C. Rau, and I. Zanette, 2017, Phys. Rev. Lett. **118**, 203903.
Zewail, A. H., and J. M. Thomas, 2010, *4D Electron Microscopy: Imaging in Space and Time* (Imperial College Press, Singapore).
Zhang, J., E. Fretwurst, R. Klanner, I. Pintilie, J. Schwandt, and M. Turcato, 2012, J. Instrum. **7**, C12012.
Zhang, J. J., *et al.*, 2010, Phys. Rev. Lett. **105**, 166102.
Zhao, P. X., X. W. Feng, D. S. Huang, G. Y. Yang, and D. Astruc, 2015, Coord. Chem. Rev. **287**, 114.
Zhaunerchyk, V., *et al.*, 2013, J. Phys. B **46**, 164034.
Ziegler, J. F., and J. P. Biersack, 1985, in *Treatise on Heavy-Ion Science*, Astrophysics, Chemistry, and Condensed Matter, Vol. 6, edited by D. A. Bromley (Springer US, Boston, MA), p. 93.

See Supplemental Material at http://link.aps.org/supplemental/10.1103/RevModPhys.90.025007 for a detailed description of the different refractive, reflective, and diffractive optics and for the list and the technical characteristics of beam lines equipped with microbeam and nanobeam setups operating at ESRF, APS, Spring-8, PETRA-III, Diamond, MAX-IV, ALBA, CLS, Soleil, SLS, and ELETTRA synchrotrons.